Doctoral Dissertation

Doctoral Program in Civil and Environmental Engineering (38th Cycle)

Climate change impacts on landslide susceptibility in the Alpine region using a machine learning approach

By

Amirreza Pourfatollah

******

Supervisors:

Prof. Marco Barla, Supervisor

Prof. Valerio De Biagi, Co-Supervisor

Dr. Alessandra Insana, Co-Supervisor

Doctoral Examination Committee:

Prof. Wan-Huan Zhou, Referee, University of Macau

Prof. Diana Salciarini, Referee, University of Perugia

Prof. Marta Castelli, Politecnico di Torino

Politecnico di Torino

April 30, 2026

This document is part of the project NODES which has received funding from the MUR on PNRR funding programme - *Missione 4, Componente 2, Investimento 1.5 – Creazione e rafforzamento di"Ecosistemi dell'innovazione", costruzione di "leader territoriali di R&S"* with grant agreement no.ECS00000036.

I hereby declare that the contents and organisation of this dissertation constitute my own original work and do not in any way compromise the rights of third parties, including those relating to the security of personal data.

Turin, April 2026

…….....

Amirreza Pourfatollah

Abstract

Assessing the effects of climate change on the natural environment poses significant challenges for the scientific community and decision-makers, particularly in understanding how it influences geo-hydrological hazards such as landslides. This Thesis investigates the potential impacts of climate change on landslide susceptibility in the Aosta Valley, Italy, and evaluates the associated implications for critical infrastructure. The primary objective is to develop spatially and temporally landslide susceptibility maps that account for monthly climatic variability and to apply these results to support infrastructure resilience assessment. Monthly landslide susceptibility maps were produced for a present-day baseline period and for a near future scenario. Climatic inputs for the current scenario were derived from a twenty-year dataset of daily precipitation and temperature with high spatial and temporal resolution. Since the timing of landslide events was available from regional inventories, precipitation and temperature values were accurately extracted at each landslide location to characterize both antecedent and event related conditions. The predictor variables included three dynamic factors, namely mean monthly precipitation, mean monthly temperature, and mean seven-day precipitation, one semi dynamic factor represented by land cover, and nine static factors including slope, soil type, lithology, aspect, profile curvature, plan curvature, Normalized Difference Vegetation Index, Stream Power Index, and Sediment Transport Index. These variables were assigned to each recorded landslide event to construct twelve-month specific datasets. A supervised machine learning algorithm was trained and tested separately for each month to generate twelve monthly landslide susceptibility maps. The results indicate that during the last twenty years, in the analysed study area, the highest proportions of areas classified as high and very high susceptibility occur in spring, particularly in April, May, and June, which is consistent with the observed seasonal distribution of landslide occurrences. To represent the worst-case conditions, the monthly susceptibility maps were combined by selecting, for each grid cell, the maximum susceptibility value across all months, producing an envelope susceptibility map. This envelope map was validated using an independent landslide dataset to evaluate

its predictive performance and spatial reliability. Future projections were developed by first comparing multiple climate scenarios for the next twenty years. Among the available scenarios, Shared Socioeconomic Pathways 5-8.5 (SSP5-8.5) exhibited the most critical temperature and precipitation patterns. The trained monthly models were then used to asses projected monthly precipitation and temperature data for the period 2021 to 2040 under the high emission SSP5-8.5 scenario to generate future monthly susceptibility maps and a corresponding future envelope map. The results suggest that under this scenario the proportion of areas classified as high and very high susceptibility is expected to increase, especially in autumn. Finally, power transmission towers within the study area were digitized from aerial imagery and overlaid on both current and future envelope susceptibility maps to quantify infrastructure exposure and identify network segments at elevated landslide risk. For a selected area, the cascading impacts of power outages were also evaluated and combined with landslide risk at the tower level, providing an integrated assessment of direct and indirect impacts.

Keywords: Landslide susceptibility, Climate change impacts, Spatio-temporal modelling, Critical infrastructure, Risk assessment.

Acknowledgment

I wish to express my sincere gratitude to my supervisors, Professors Marco Barla, Alessandra Insana, and Valerio De Biagi. Their continuous guidance, expertise, and support throughout this research journey have been invaluable, and I deeply appreciate the trust they have placed in my work.

I would also like to express my appreciation to Professors Hannah Zhou, Diana Salsiarini, and Marta Castelli for dedicating their valuable time to reviewing this thesis. Their insightful comments, constructive feedback, and careful evaluation have significantly contributed to improving the quality of this work.

I gratefully acknowledge the CIMA Research Foundation for providing the high-resolution temperature and precipitation datasets that significantly enhanced the robustness and reliability of this study.

My sincere thanks to the ELGIP network for providing invaluable opportunities to connect with researchers across Europe.

I thank my ROCKMECH colleagues and friends: Ward, Diogo, Giacomo, Paola, Francesco, Maria, Simone, Juliana, Chonyang, Yisha, and Martina. Our shared discussions and camaraderie deeply enriched my professional growth and made this journey highly rewarding. Furthermore, I extend my heartfelt gratitude to my dear friend Parviz. For over fifteen years, he has been much more than a close friend. He has been a true brother, always ready to listen when I needed to discuss my challenges and always offering his unwavering help and guidance whenever I sought it.

Finally, my deepest and most heartfelt gratitude is reserved for my parents, Zohreh and Alireza. Though distance has kept us apart during much of this journey, and I have missed their comforting presence deeply, their love and unwavering belief in me have always transcended the miles. Their constant encouragement and unconditional support have been the absolute foundation of my achievements. I am profoundly thankful to them for always inspiring me to aim higher and pursue my aspirations with determination, even from afar.

I would like to dedicate

this Thesis to my parents

to my beautiful mom Zohreh and lovely dad Alireza whom I missed the most.

Contents

List of figures

List of Tables

Chapter 1

Introduction

1.1 Framework

Landslides are a form of mass movement that occurs on both natural and engineered slopes. They involve the downward movement of rock, debris, or soil under the influence of gravity. This movement can manifest in various forms, such as flowing, sliding, toppling, falling, or spreading, and many landslides exhibit a combination of these movements either simultaneously or throughout their duration. Present across all continents, landslides significantly shape landscapes but also pose considerable risks to populations in many regions.

Rainfall-induced shallow landslides are particularly common and hazardous due to their frequent occurrence, causing numerous fatalities and substantial economic losses worldwide each year. Concerns about these hazards are escalating as the impacts of climate change are expected to exacerbate landslide activity in some areas of the world. Global warming leads to increased air moisture content, which may, in turn, raise the frequency and intensity of heavy precipitation events. Despite high confidence that variations in heavy rainfall affect landslide activity, the site-specific responses of local environments remain uncertain, especially when coupled with rising temperatures.

In mountainous areas, temperature changes also play a significant role in the occurrence of shallow landslides. Melting ice can destabilize slopes by reducing soil shear strength while increasing pore pressure as water infiltrates into the soil. This dual effect heightens the likelihood of landslides.

Moreover, landslide activity is governed not only by hydrometeorological triggers but also by a range of controlling factors such as soil shear strength, land cover, and slope gradient. The interaction of these parameters is complex and

spatially variable, making it difficult to reliably assess slope stability using simplified approaches. Therefore, a robust methodological framework is required that is capable of integrating multiple influencing factors while capturing their combined effect on slope behaviour across different environmental conditions.

In addition, when the study area is large, a methodology is required that can efficiently handle and process large volumes of spatial data. This ensures that landslide susceptibility can be reliably assessed across extensive regions without loss of consistency or accuracy.

In this context, a comprehensive framework is proposed to identify potentially unstable areas by integrating key conditioning and triggering factors associated with landslide occurrence. These maps are essential tools for making informed decisions regarding infrastructure management and development.

1.2 Research goal and questions

This Doctoral research aims to develop a methodological framework for incorporating climate change effects into landslide susceptibility assessment using machine learning techniques. The approach integrates monthly-scale climate variability to produce dynamic susceptibility maps that better capture evolving hazard conditions. The Aosta Valley, which is in northwestern part of Italy, is used as a case study to show how the method can be applied in practice. The ultimate aim is to provide a method that can be applied to different regions to support risk-informed decision-making and infrastructure resilience planning.

To achieve this goal, the research is guided by the following key questions:

- What climatic, geomorphological, and environmental factors contribute to the occurrence of landslides in the study area?
- Which of these factors are the most critical for explaining spatial and temporal patterns of susceptibility?
- What do present-day, monthly landslide susceptibility maps reveal about current conditions?
- How will landslide susceptibility evolve under future climate scenarios?
- How is the exposure of linear infrastructure to landslide hazards expected to change under future climate scenarios, and, specifically, which sections of high-voltage transmission networks are currently exposed and how might this exposure evolve?

1.3 Research methodology

To address the research questions, the study adopts a machine learning approach applied to both present and future climate conditions. The methodological framework consists of the following steps:

i. **Data compilation and predictor variables**: A comprehensive dataset is built by integrating climatic, geomorphological, and environmental information with recorded landslide events. A 20-year daily dataset of precipitation and temperature serves as the climatic input. Using a landslide inventory containing the exact dates and locations of landslides, data related to these aspects are extracted:
    - Dynamic features: mean monthly precipitation, mean monthly temperature, mean seven-day precipitation.
    - Semi-static feature: land cover.
    - Static features**:** slope, soil type, lithology, aspect, profile curvature, plan curvature, NDVI, SPI, and STI.

ii. **Data analysis:** After preparing the datasets, a thorough analysis is conducted to ensure data quality and consistency. Missing values are identified and appropriately treated to avoid biases in model training. Then the same number of non-landslide events are added to the dataset to have a balanced dataset.

iii. **Model training and testing:** Twelve month-specific datasets are created, each of which was split into 70% training and 30% testing subsets. A supervised machine learning algorithm is then trained and evaluated on each dataset to generate monthly susceptibility maps. Model performance for each month is assessed using ROC–AUC curves. The resulting maps are combined into an envelope map by selecting, at each grid cell, the maximum susceptibility value across all months, representing the worst-case monthly scenario. Finally, the envelope map is validated against an independent set of landslide locations to evaluate its predictive performance and spatial accuracy.

iv. **Future projections:** The trained models are applied to precipitation and temperature projections for the near-future period 2021–2040 under the high-emission SSP5-8.5 scenario. This produces a new set of monthly susceptibility maps and a future envelope map that reflects the potential influence of climate change on landslide susceptibility.

v. **Infrastructure exposure analysis:** The susceptibility maps developed in this study are used to assess their interaction with critical infrastructure networks. As an example, we use high-voltage transmission lines within the study area, which are digitized from aerial imagery and spatially overlaid on both present and projected susceptibility maps. This enables the identification of network segments most exposed to landslide hazards under current and future conditions. Finally, the combined effects of cascading and landslide risks are evaluated for a selected area within the region.

This integrative methodology combines climate data, geomorphological and environmental predictors, and machine learning techniques to produce spatially and

temporally detailed landslide susceptibility assessments. The results directly inform the evaluation of climate-related risks to high-voltage transmission infrastructure in the Aosta Valley, while also providing a transferable framework that can be applied to other study areas and to different types of linear infrastructure, thereby allowing its application beyond the specific case study considered.

This Doctoral Thesis advances the state of the art through several methodological and application-oriented contributions:

- Integration of temperature as a conditioning factor: temperature is incorporated as an explicit landslide conditioning factor, allowing the models to capture climatic influences beyond precipitation alone.
- Inclusion of antecedent precipitation: the research incorporates seven-day cumulative precipitation as a conditioning factor, enabling the assessment of short-term rainfall accumulation effects on landslide occurrence.
- Event-specific climate information: instead of relying on aggregated or generalized climatic statistics, the study uses the exact precipitation and temperature values associated with each recorded landslide event for both model training and testing.
- Monthly landslide susceptibility mapping: landslide susceptibility maps are generated on a monthly basis rather than as a single static product, providing a more temporally resolved representation of susceptibility.
- Development of an envelope susceptibility map: an envelope map is produced to summarize and integrate the susceptibility information across multiple temporal scenarios.
- Model interpretability through SHAP analysis: SHAP (SHapley Additive exPlanations) is applied to each machine-learning model to quantify the contribution of individual conditioning factors and improve the transparency of model predictions.
- Monthly assessment of factor importance: the study evaluates how the relative importance of conditioning factors changes from month to month, offering insights into seasonal controls on landslide activity
- Future landslide susceptibility prediction: the methodology is extended to predict landslide susceptibility under future climate conditions, providing a framework for assessing potential climate change impacts.
- Integration of cascading infrastructure failure analysis: the research combines landslide susceptibility assessment with the analysis of cascading failures of power transmission towers, thereby linking geohazard prediction with critical infrastructure vulnerability.

1.4 Thesis structure

This Thesis is divided into seven chapters. Following this introductory chapter, Chapter 2 examines the threats posed by climate change on natural hazards from a global perspective, with a particular focus on landslide hazard.

Chapter 3 reviews various methodologies employed in the literature to develop landslide susceptibility maps, categorizing them into three broad groups: qualitative, semi-quantitative and quantitative methods.

Chapter 4, the core of this Doctoral work, introduces the area of interest, details the methodology used in this research, and explains the parameters considered as contributing factors to landslides.

Chapter 5 presents susceptibility maps for both current and future periods.

Chapter 6 presents the analysis of infrastructures at risk from potential landslide impacts.

Finally, Chapter 7 provides conclusions and discusses future research directions to implement and/or take advantage of the developed model.

Chapter 2

Natural hazards and climate change

2.1 Introduction

The year 2023 represented a significant climatic anomaly, establishing a new record for global mean temperatures. During this period, numerous nations faced a series of catastrophic phenomena, including lethal wildfires, severe landslides, and pervasive flooding (NASA.gov). These events caused extensive socio-economic disruption, affecting millions of individuals and resulting in billions of dollars in capital losses. Within the current trajectory of the climate crisis, there is a measurable trend regarding the heightened intensity and recurrence of extreme meteorological events, which frequently transition into large-scale disasters. Recent assessments by the Intergovernmental Panel on Climate Change (IPCC) indicate that climate-induced disasters are manifesting with greater severity than was forecasted in earlier scientific models (IPCC, 2022). Emerging empirical evidence further suggests that a specific threshold of additional warming is now unavoidable. This implies that disaster risks will continue to amplify even if international initiatives to curb greenhouse gas emissions prove effective. In this context, understanding how climate change influences the occurrence and spatial distribution of natural hazards is essential.

In this chapter, different climate scenarios are first introduced, followed by an explanation of projected changes in precipitation and temperature. Furthermore, the impacts of climate change on natural hazards, with particular emphasis on landslides, are discussed.

2.2 Climate scenarios

Scenarios play a central role in climate change research and assessment, as they provide a structured way to examine the long-term implications of decisions made in the near term. By outlining a range of plausible future pathways, scenarios allow researchers to investigate how climate and societal systems might evolve under deep uncertainty.

Equally important, scenarios have historically enabled collaboration across diverse research communities by offering a shared framework for analyzing mitigation strategies, climate impacts, adaptation measures, and responses of the physical Earth system. Well known examples include earlier scenario sets developed by the IPCC, such as SA90, IS92, and SRES, as well as the more recent Representative Concentration Pathways (RCPs) (Moss et al., 2010; van Vuuren et al., 2011). These widely used community scenarios are required to capture multiple dimensions, including a range of possible climate trajectories and internally consistent socioeconomic pathways. Previous studies have demonstrated that socioeconomic conditions are as influential as climatic factors in shaping climate impacts, adaptation potential, and mitigation outcomes (IPCC, 2014; Morita et al., 2000).

Moss et al. (2010) introduced a so-called parallel process for the development of new climate change scenarios within the research community. This approach led to the creation of the RCPs, which represent the climate forcing component of alternative future trajectories (van Vuuren et al., 2011) and formed the foundation for the climate projections evaluated in the IPCC Fifth Assessment Report (IPCC, 2012; Taylor et al., 2012). Building on two initial proposals by Kriegler et al. (2012) and van Vuuren et al. (2012), the structure of the socioeconomic dimension of the scenario framework was subsequently defined. Following that, researchers introduced updated Shared Socio-economic Pathways (SSPs) narratives (O'Neill et al., 2017) together with corresponding quantitative representations of major scenario drivers, including population dynamics (KC and Lutz, 2017), economic development (Crespo Cuaresma, 2016), and patterns of urbanization (Jiang and O'Neill, 2017). These narratives and projections form the core components of the SSP framework and have subsequently been applied to construct integrated scenarios. Such scenarios extend the SSPs by explicitly accounting for changes in energy systems (Figure 2-1) and land use (Figure 2-2), as well as the associated air pollutant emissions (Figure 2-3), greenhouse gas emissions (Figure 2-4) and atmospheric concentration pathways.

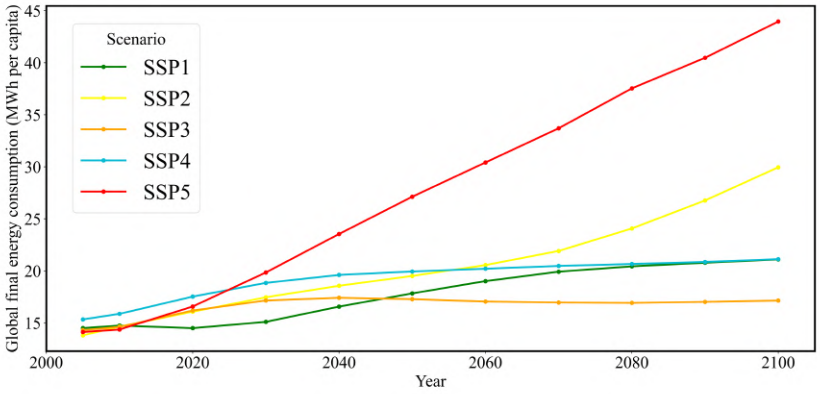

Figure 2-1 Global final energy consumption. Final energy refers to the energy supplied to end users for direct consumption, such as electricity used in homes or fuel like petrol sold at service stations (Riahi et al. 2017).

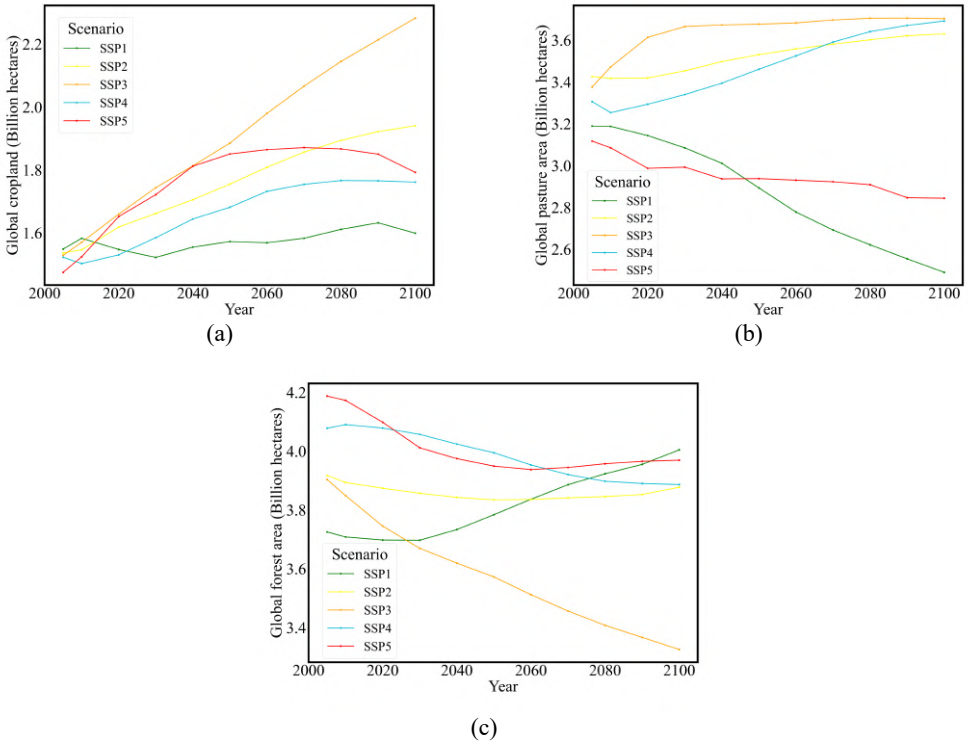

Figure 2-2 Global land cover changes, (a) Cropland, (b) Pasture, and (c) Forest areas (Riahi et al. 2017).

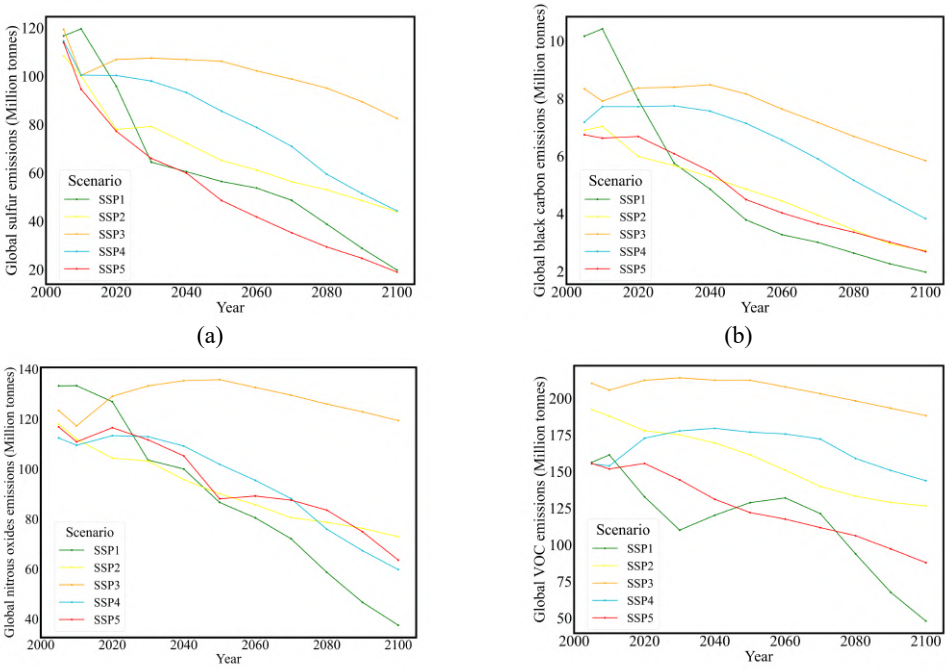

Figure 2-3 Global air pollution changes, (a) Sulfur, (b) Black carbon, (c) Nitrous oxides, and (d) Volatile organic compounds (VOC) emissions (Riahi et al. 2017).

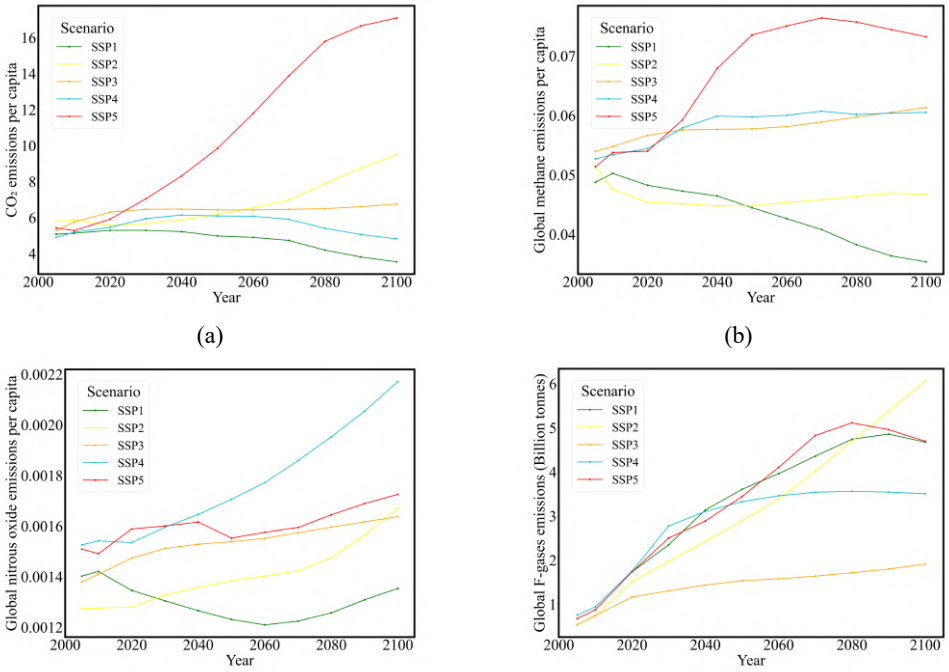

Figure 2-4 Global greenhouse gas emissions for (a) Carbon dioxide, (b) Methane, (c) Nitrous oxide, and (d) Fluorinated gases (F-gases) (Riahi et al. 2017).

2.2.1 Socio Economic Pathways (SSPs) developments

The SSPs were developed to outline five clearly distinct pathways of potential future socioeconomic developments, assuming no additional policies or measures are implemented to limit climate forcing or enhance adaptive capacity. They are intended to support climate change research and policy analysis and are structured to cover a wide spectrum of challenges related to both mitigation and adaptation. Beyond these dimensions, the storylines also incorporate elements that correspond closely with scenarios from earlier analyses, reflecting continuity with past exercises (van Vuuren and Carter, 2014). The process of developing the SSPs involved five main steps:

- Development of the narratives, establishing the core logic for each SSP and addressing aspects of socioeconomic change that are often difficult to capture in formal models.
- Translation of the narratives into model "input tables", qualitatively describing the key characteristics and assumptions of each SSP.
- Quantitative representation of the fundamental SSP components, including demographic and economic drivers, using appropriate models.
- Assessment of changes in energy systems, land use, and emissions of greenhouse gases and air pollutants for the SSP baseline scenarios through a set of Integrated Assessment Models (IAMs).
- Application of IAMs to further detail these components for the SSP mitigation scenarios.

2.2.2 SSP narratives

The SSP narratives (O'Neill et al., 2017) provide a textual portrayal of how societal trends might develop in the future. Their primary purpose is to establish an internally consistent logic of key causal relationships, including aspects of change that are typically difficult to represent in quantitative models. In this way, the narratives serve as a valuable complement to model-based projections. By outlining major socioeconomic, demographic, technological, lifestyle, policy, institutional, and other trends, they offer essential context for a wide range of users to better interpret the quantitative SSP projections.

The narratives have also played a critical role in the modeling process, guiding the assumptions and quantifications used for socioeconomic projections as well as for SSP energy and land-use transitions. Following the overall scenario framework, the narratives cover a spectrum of potential futures in terms of the socioeconomic challenges they imply for climate mitigation and adaptation. Two SSPs depict futures where both adaptation and mitigation challenges are either low (SSP1) or

high (SSP3). Two "asymmetric" SSPs combine high mitigation challenges with low adaptation challenges (SSP5) and the reverse (SSP4). Finally, one scenario represents a central case with intermediate challenges for both mitigation and adaptation (SSP2). A summary of the global narratives is provided in Table 2-1.

Table 2-1 SSP narratives.

SSP1	Sustainability – Taking the Green Road (Low challenges to mitigation and adaptation) The world gradually moves toward a more sustainable trajectory, focusing on inclusive development that respects environmental limits. Global commons are managed more effectively over time, investments in education and health speed up demographic transitions, and economic priorities shift from pure growth to broader human well-being. Strong commitment to development goals helps reduce inequality both between and within countries. Consumption patterns favor lower material growth and reduced resource and energy intensity.
SSP2	Middle of the Road (Medium challenges to mitigation and adaptation) The world continues along a trajectory where social, economic, and technological trends largely follow historical patterns. Progress in development and income growth is uneven, with some countries advancing steadily while others lag behind. Both global and national institutions work toward sustainable development goals, but progress is slow. Environmental systems experience some degradation, though modest improvements occur, and the overall intensity of resource and energy use gradually declines. Global population growth is moderate, stabilizing in the latter half of the century. Income inequality persists or improves only gradually, leaving ongoing challenges in reducing vulnerability to societal and environmental changes.
SSP3	Regional Rivalry – A Rocky Road (High challenges to mitigation and adaptation) Rising nationalism, concerns over competitiveness and security, and regional conflicts drive countries to concentrate primarily on domestic or regional priorities. Policies gradually become more focused on national and regional security. Nations prioritize achieving energy and food security within their own borders, often at the expense of broader development goals. Investment in education and technological innovation declines, economic growth remains slow, consumption is resource-intensive, and inequalities persist or worsen. Population growth is low in industrialized nations but high in developing countries. Environmental issues receive low international attention, resulting in significant degradation in some regions.
SSP4	Inequality – A Road Divided (Low challenges to mitigation, high challenges to adaptation) Unequal investments in human capital, along with growing disparities in economic opportunities and political influence, drive increasing inequality and social stratification within and between countries. Over time, a divide emerges between a globally connected society engaged in knowledge- and capital-intensive sectors, and a fragmented set of lower-income, less-educated populations working in labor-intensive, low-tech economies. Social cohesion weakens, and conflicts and unrest become more frequent. Technological advancement is concentrated in the high-tech sectors, while the global energy system becomes more diverse, combining

	investments in carbon-intensive fuels like coal and unconventional oil with low-carbon energy sources. Environmental policies primarily target local concerns in middle- and high-income regions.
SSP5	Fossil-fueled Development – Taking the Highway (High challenges to mitigation, low challenges to adaptation) In this scenario, strong confidence in competitive markets, innovation, and participatory societies drives rapid technological advancement and human capital development as a path toward sustainable development. Global markets become increasingly interconnected, supported by substantial investments in health, education, and institutions to strengthen human and social capital. Simultaneously, economic and social development relies heavily on abundant fossil fuel resources and widespread adoption of energy- and resource-intensive lifestyles. These factors fuel rapid global economic growth, while the world population peaks and declines during the 21st century. Local environmental issues, such as air pollution, are effectively managed, reflecting a broader confidence in the ability to govern social and ecological systems, potentially including geo-engineering interventions if needed.

Finally, Figure 2-5 illustrates global average temperature increases calculated for different scenarios from 2005 to 2100.

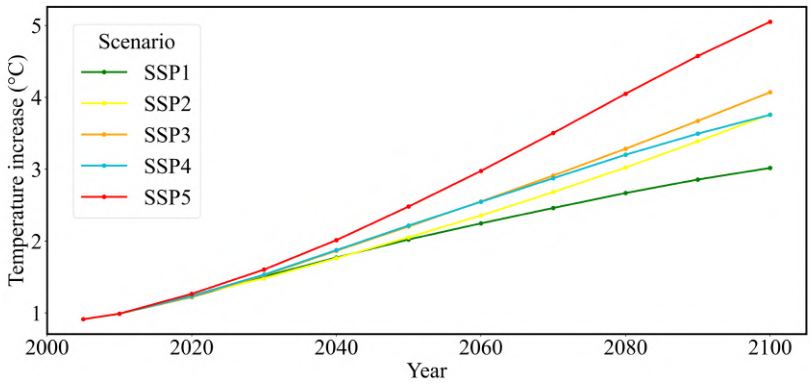

Figure 2-5 Global average temperature increases relative to the pre-industrial era (Riahi et al., 2017).

The numbers following the SSP designations, such as 2.6, 4.5, 6.0, and 8.5, represent specific targets for anthropogenic radiative forcing measured in watts per square meter (W/m^2) by the year 2100. These values correspond to the RCPs, which define the magnitude and rate of change in the Earth's energy imbalance. By combining a SSP with a specific forcing level, researchers can evaluate the mitigation stringency and adaptation challenges required to reach that climate outcome (Arnell et al., 2011).

2.3 Observed and projected changes in climate extremes

According to the IPCC Special Report on Managing the Risks of Extreme Events and Disasters to Advance Climate Change Adaptation (SREX), observational evidence indicates that several types of extreme events have changed since the mid-

20th century. Some of these changes have been attributed to human influences, and similar trends are expected to persist in the future. In addition, further changes may arise from natural climate variability as global warming intensifies (IPCC, 2012).

2.3.1 Temperature extremes

At both global and, to a lesser extent, regional scales, many observed and projected changes in extreme events can be attributed to increased radiative forcing and the resulting global warming. These processes are linked to a higher moisture-holding capacity of the atmosphere, as well as changes in vertical atmospheric stability and meridional temperature gradients that influence climate dynamics. Consistent with ongoing warming, hot extremes have become more frequent and intense, while cold extremes have generally declined in both frequency and severity (Figure 2-6). Temperature extremes over land typically increase more rapidly than the global mean temperature (Figure 2-6), largely due to the land–sea warming contrast and additional regional feedback mechanisms. Projections indicate that the intensity of temperature extremes increases in a robust and generally linear manner with global mean temperature rise across different regions up to 2100, with only limited sensitivity to the chosen emissions scenario (Kharin et al., 2018).

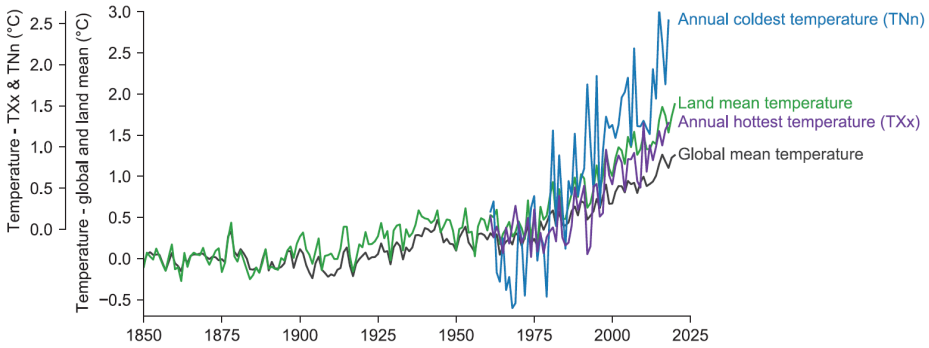

Figure 2-6 Trends in global and land temperature anomalies (1850–2020). This time series compares the annual mean temperatures (global and land) against extremes in land temperatures, specifically the annual hottest daily maximum (TXx) and coldest daily minimum (TNn) (Dunn et al., 2020).

Figure 2-7a illustrates the anomalies in daily maximum temperatures modeled by Centro Euro-Mediterraneo sui Cambiamenti Climatici – Earth System Model (CMCC-ESM2) which is a coupled climate model used to simulate the Earth's climate system (Cherchi et al., 2019; Vichi et al., 2011). The most significant increases are visible in the high northern latitudes, particularly across the Arctic Ocean, where daytime highs are projected to rise by more than 4°C. While most continental landmasses in the mid-latitudes show a moderate warming of approximately 1.5°C to 2.5°C, a notable "cold spot" or warming hole is evident in the North Atlantic, where temperatures actually show a slight decrease.

Figure 2-7b shows the anomalies for daily minimum temperatures, typically representing nighttime lows. The spatial pattern is similar to the maximum temperatures but displays even higher intensity in the Arctic and sub-Arctic regions, with anomalies peaking near 6°C. This indicates that nighttime temperatures are rising more rapidly than daytime temperatures in the north, a phenomenon often linked to changes in snow cover and atmospheric moisture. Like the first map, the North Atlantic remains the only major region resisting the warming trend, while the Southern Hemisphere oceans show a more uniform, albeit slower, rate of warming compared to the Northern Hemisphere's land-heavy geography.

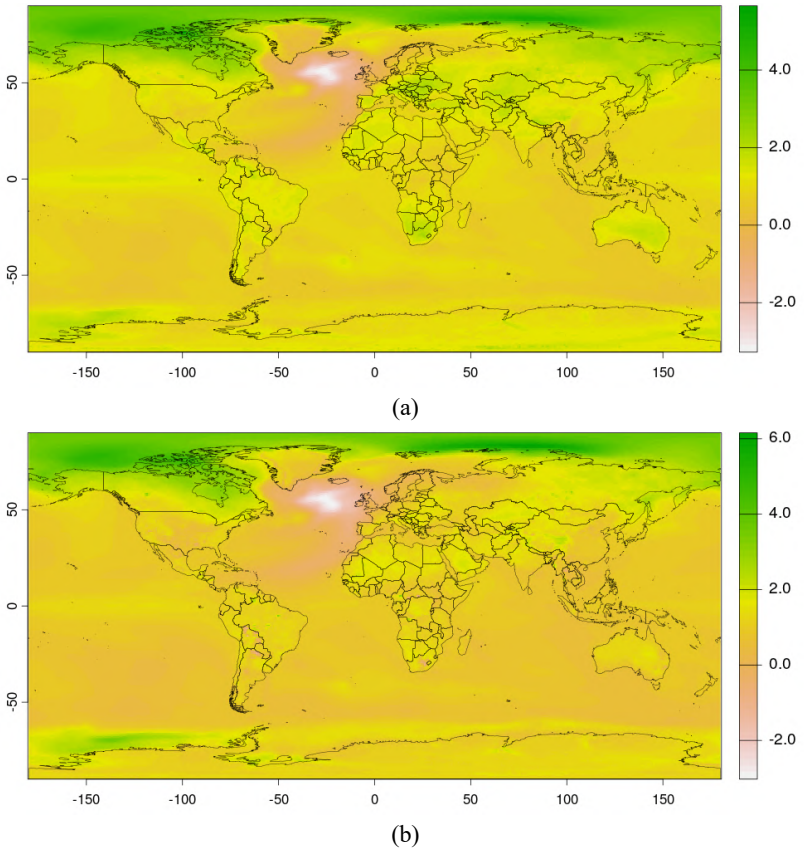

Figure 2-7 CMIP6 temperature anomalies relative to historical values (1970-2000) from the CMCC-ESM2 model for 2021-2040: (a) Maximum temperature and (b) Minimum temperature, in °C, under the SSP5-8.5 scenario (Fick et al., 2017).

The occurrence of hot temperature extremes, along with the number of heatwave days and the duration of heatwave seasons across different regions, also shows a strong relationship with increases in global mean temperature. This relationship is generally nonlinear, mainly due to threshold effects (Sun et al., 2018; Wartenburger et al., 2017).

Figure 2-8 illustrates the projected changes in the frequency of extreme temperature events over global land areas and selected regions. In each box plot, the central line represents the median, the box indicates the central 66% uncertainty range, and the whiskers extend to the 90% range of the multi-model ensemble. The

dotted line denotes no change in event frequency. These results are based on simulations from the Coupled Model Intercomparison Project Phase 6 (CMIP6) under different Shared Socioeconomic Pathway scenarios and are adapted from Li et al. (2021). For example, for Western and Central Europe, two sets of bars are shown: one for 10-year events and another for 50-year events. The charts illustrate that 10-year events occur more frequently across all temperature ranges, while 50-year events are rarer but can reach higher temperature anomalies.

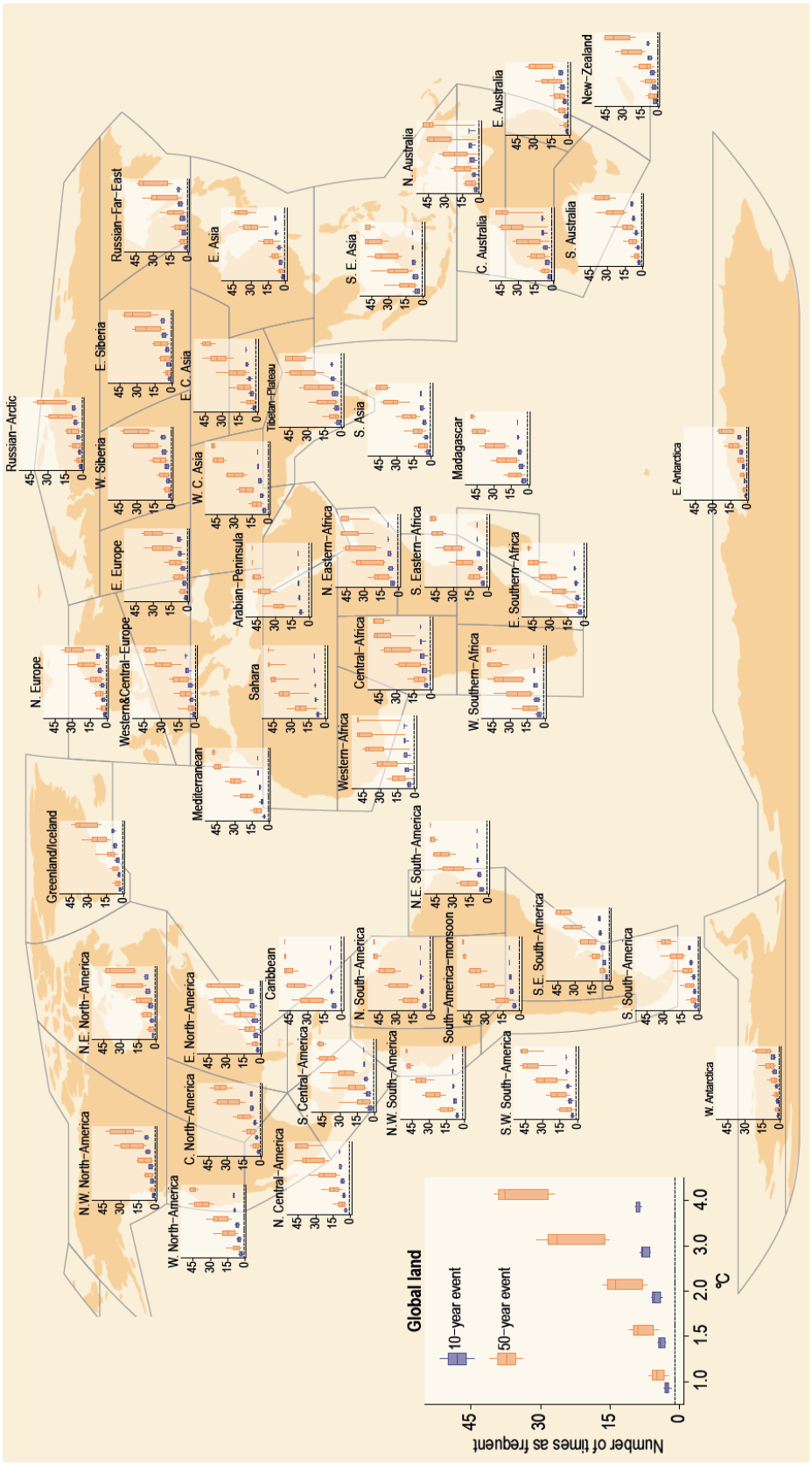

Figure 2-8 Projected changes in the frequency of extreme maximum daily temperature events (10-year and 50-year events) under 1°C-4°C global warming relative to the 1850-1900 baseline. (Li et al., 2021).

In overall, at the global scale, and in many regions where observational records are sufficient, there is medium confidence that the duration and/or occurrence of warm spells and heatwaves has increased since the mid-20th century. Anthropogenic influences are likely to have contributed to the warming of both daily minimum and maximum temperature extremes worldwide. Climate model projections indicate pronounced increases in temperature extremes by the end of the 21st century. It is virtually certain that warm days and nights will become more frequent and intense, while cold days and nights will continue to decline globally throughout the century. These changes are largely associated with shifts in mean temperature, although variations in temperature variability are also important in some regions. Model results further suggest that the duration, frequency, and intensity of heatwaves, defined relative to present-day regional climates, will increase across most land areas. In absolute terms, the 20-year return values of annual maximum daily temperatures are projected to rise by approximately 1 to 3°C by the middle of the 21st century and by about 2 to 5°C by the end of the century, depending on region and emissions pathway (IPCC, 2012). In many regions and seasons, moderate temperature extremes over land are expected to warm more rapidly than the global annual mean temperature. However, projections at subcontinental scales remain more uncertain than global estimates, and regional responses of temperature extremes may differ substantially from the global mean, as global warming does not translate uniformly across all regions and seasons.

2.3.2 Precipitation extremes

Figure 2-9 illustrates the projected changes in mean precipitation for the period 2021-2040 under the SSP5-8.5 scenario as simulated by the CMCC-ESM2 climate model. The map shows the spatial distribution of precipitation change relative to the reference period (1970-2000), with values generally indicating an intensification of the global hydrological cycle. Pronounced increases in precipitation are evident along the equatorial regions, particularly over the tropical Pacific, parts of the Indian Ocean, and equatorial Africa, reflecting enhanced convection and moisture availability under warming conditions. Mid-latitude regions exhibit more moderate and spatially heterogeneous changes, while some subtropical areas show relatively smaller increases.

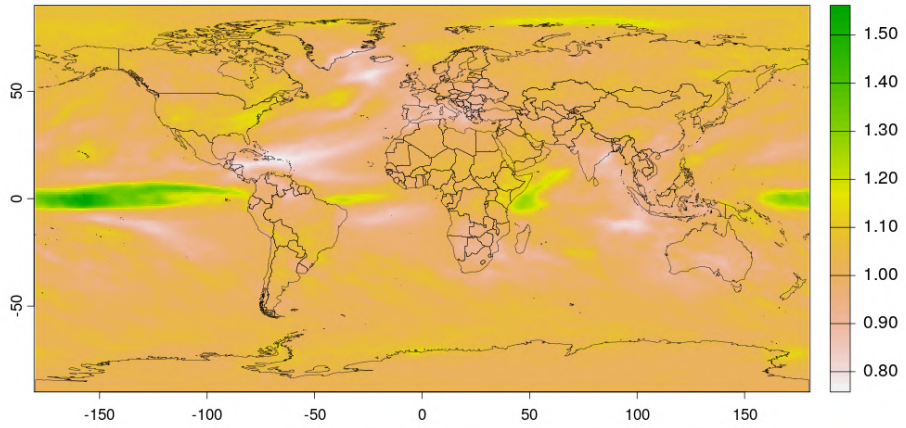

Figure 2-9 CMIP6 precipitation relative to historical values (1970-2000) from the CMCC-ESM2 model for 2021-2040 under the SSP5-8.5 scenario (Fick et al., 2017).

Moreover, changes in annual maximum one-day precipitation (Rx1day) are proportional to mean global surface temperature changes, increasing by about 7% per 1°C of warming, consistent with the Clausius–Clapeyron relation (Allen and Ingram, 2002; Boer, 1993). Equation (2-1) determines the relationship between saturation vapor pressure and temperature:

$$\frac{d \ln e_s}{dT} = \frac{L_v}{R_v T^2} \tag{2-1}$$

where e_s is saturation vapor pressure, T temperature (in Kelvin), L_v latent heat of vaporization of water, R_v is gas constant for water vapor. Equation (2-1) is observed in both historical data (Westra et al., 2013) and future projections (Kharin et al., 2013) on a global scale. At local and regional scales, however, changes in extreme events are strongly influenced by regional forcings and feedback processes. Some of these forcings, such as those related to land-use and land-cover changes or aerosol emissions, may also exert non-local or spatially heterogeneous effects at the global scale. Overall, there is high confidence in changes in extremes driven by large-scale thermodynamic processes, including global warming and the associated increase in atmospheric moisture, as these mechanisms are well understood. In contrast, confidence is considerably lower for changes linked to dynamic processes or regional and local forcings, including regional thermodynamic influences, due to their complexity and the multiple interacting factors involved. Figure 2-10 shows projected increases in the frequency of extreme precipitation events (10-year and 50-year) across most global land regions under 1°C to 4°C warming relative to the 1850–1900 baseline. For example, for Western and Central Europe, it can be seen that the frequency of 10-year events increases progressively with rising warming levels across all temperature thresholds. In contrast, 50-year events, while less frequent, exhibit a more pronounced relative increase at higher warming levels, indicating a substantial amplification of rare and intense precipitation extremes.

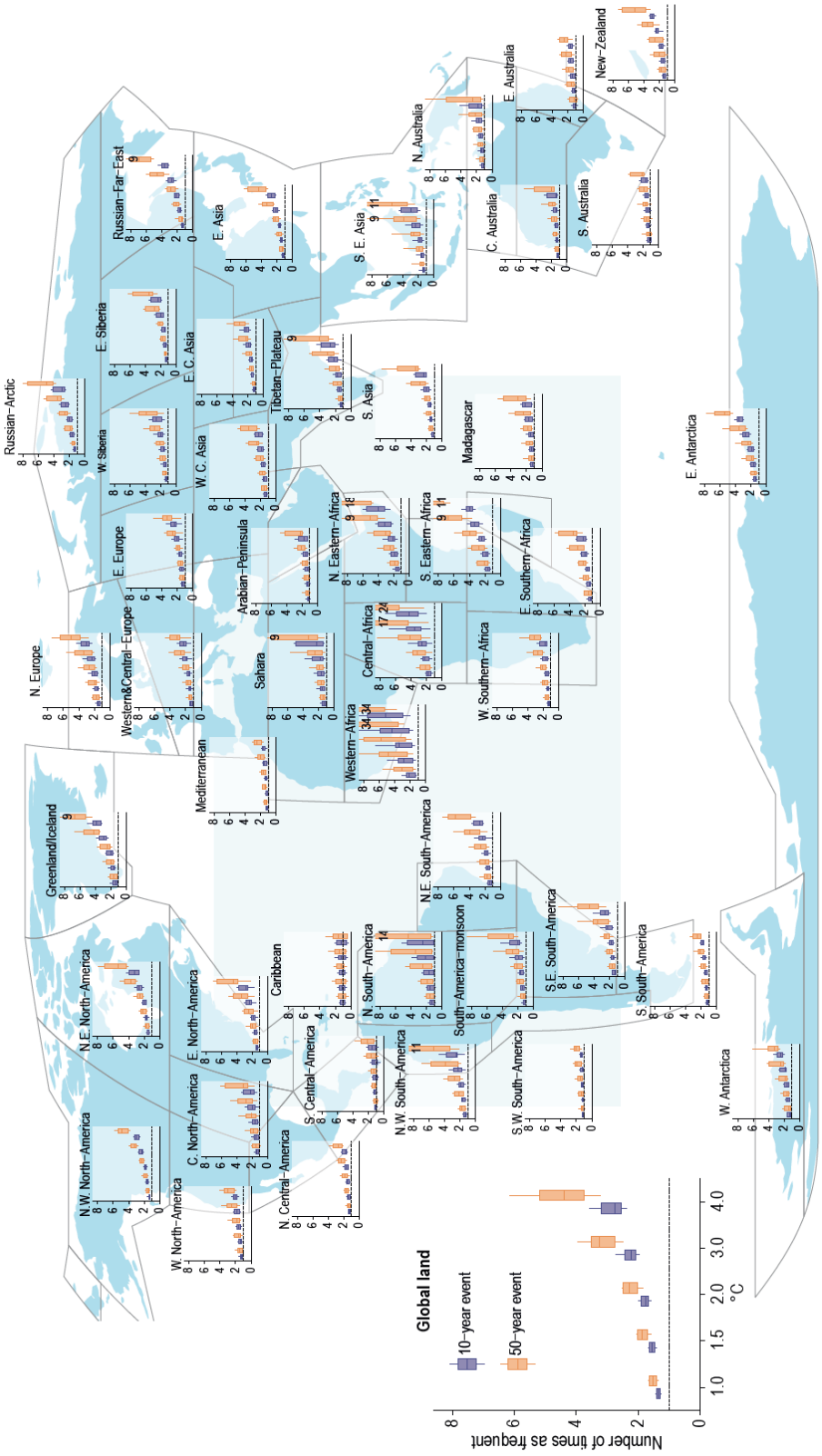

Figure 2-10 Projected changes in the frequency of extreme precipitation events (10-year and 50-year events) under 1°C–4°C global warming relative to the 1850–1900 baseline. (Li et al., 2021).

Results from both global- and regional-scale studies suggest that, during the 21st century, the frequency of heavy precipitation events and the share of total rainfall contributed by such events are likely to increase across large parts of the world. These increases are particularly evident in high-latitude regions, the tropics, and the northern mid-latitudes during winter. In several regions, heavy precipitation is projected to intensify even where total precipitation is expected to decline, although confidence in this pattern is medium. Model projections further indicate that precipitation events currently associated with a 20-year return period for annual maximum 24-hour rainfall may occur much more frequently by the end of the century, potentially becoming events with return periods of approximately 5 to 15 years in many regions. However, in some areas, projected changes in return periods remain small or statistically insignificant (IPCC, 2022).

2.4 Climate-related natural hazards and associated risk

Anthropogenic climate change has fundamentally reshaped the temporal frequency and magnitude of diverse natural hazards. Consequently, a comprehensive understanding of these shifts is imperative for the formulation of robust risk management frameworks and adaptive policy interventions (IPCC, 2022). Principal climate-sensitive hazards encompass a broad spectrum of phenomena, including wildfires, hurricanes, tornadoes, and flooding. Within the scope of this section, these broader meteorological and climatological hazards are briefly characterized to establish the environmental context. However, landslides are accorded a more rigorous and detailed analysis in the subsequent subsections.

Wildfires represent a critical component of socio-ecological dynamics and are central to the regulation of energy exchange within terrestrial ecosystems (Bousfield et al., 2023; Potter et al., 2020). While they are a natural part of ecosystem process, contemporary anthropogenic influences and accelerated climatic shifts have precipitated fire events of unprecedented scale and intensity across diverse geographic regions, most notably in Australia, the Amazon basin, and Canada (Driscoll et al., 2024; Jain et al., 2024; Mataveli et al., 2022). These escalating fire regimes present a dual threat to biodiversity conservation objectives and the stability of human socio-economic systems. The long-term outlook for wildfire activity remains highly concerning within the context of global thermal escalation. Projections indicate that the occurrence of extreme wildfire events is likely to increase by approximately 30% by the middle of the century, with a potential surge of 50% by the year 2100 (UNEP and GRID-Arendal, 2022). Furthermore, there is a prevailing scholarly consensus that fire regimes will undergo a significant transition, characterized by heightened severity and increased recurrence intervals across a variety of global biomes (Sayedi et al., 2024).

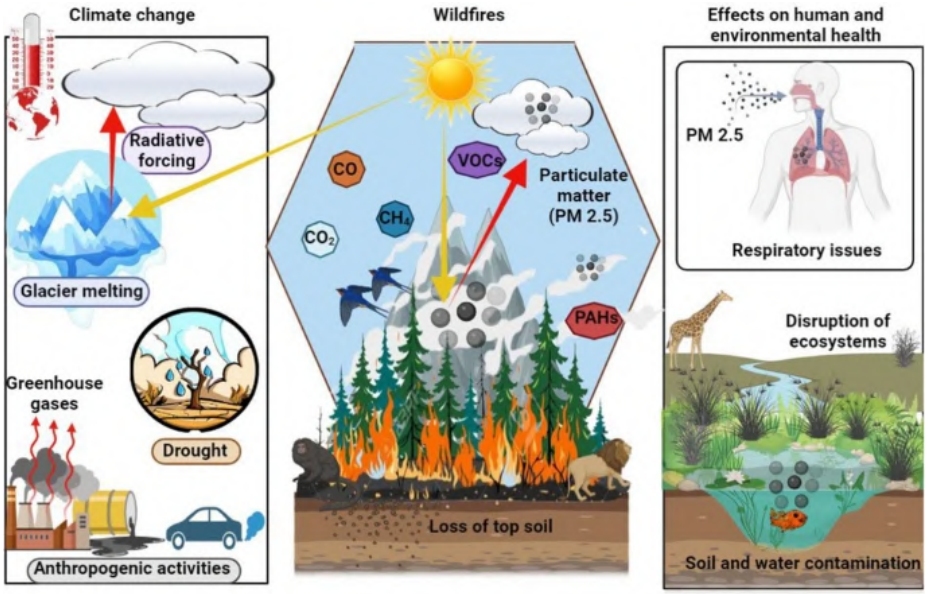

Figure 2-11 Climate change impacts om wildfire and its consequences (Bolan et al., 2025).

Hurricanes are defined as high-magnitude tropical cyclones originating over warm oceanic basins, categorized by sustained wind velocities exceeding 119 kilometers per hour. Recent climatological shifts have exacerbated the destructive potential of these systems by elevating sea surface temperatures, atmospheric moisture capacity, and total ocean heat content (Peterson et al., 2006). These anthropogenically induced modifications facilitate the intensification of storm surges, increased precipitation rates, and the deceleration of translational storm speed, which collectively precipitate catastrophic flooding and the degradation of critical coastal infrastructure (Camelo et al., 2020; Kossin, 2018). While empirical projections do not suggest a substantial increase in the absolute frequency of tropical cyclogenesis, there is significant evidence indicating an upward trajectory in storm intensity and associated hydrological output. Consequently, the future risk profile for vulnerable coastal regions is expected to deteriorate as these high-intensity events result in escalating socio-economic damages and increased mortality rates (Gutmann et al., 2018). Figure 2-12 shows the impact of hurricane on power lines.

Figure 2-12 Downed power lines in Holly Beach, Louisiana, caused by Hurricane Laura on 27 August 2020 (NBC News, 2020).

Hazardous convective phenomena, including severe windstorms, large hail, and tornadoes, represent a major threat to public safety and built environments and contribute substantially to the number of weather-related disasters exceeding one billion dollars in the United States when adjusted for inflation (NOAA National Centers for Environmental Information). Anthropogenic climate change is altering the atmospheric processes that influence tornado development by enhancing low-level heat and moisture, thereby increasing convective available potential energy. At the same time, broader warming trends are diminishing pole-to-equator temperature contrasts, which may contribute to a reduction in vertical wind shear (Gensini and Brooks, 2018). Recent advances in climate modeling across multiple spatial scales suggest that tornado strength, particularly during the cool season, may become increasingly responsive to human-induced climate forcing, although projected changes in overall tornado occurrence remain uncertain (Woods, 2023). Figure 2-13 presents tornado impacts on houses.

Figure 2-13 Destroyed Houses in Florida by a tornado in the wake of Hurricane Milton in 2024 (Sobel and Emanuel, 2025).

Projected global warming is expected to amplify the intensity of extreme precipitation over large regions, largely due to thermodynamic constraints described by the Clausius–Clapeyron relationship. As mentioned earlier, it suggests that the atmosphere's capacity to retain moisture increases by roughly 6–7% per degree of temperature rise (Ingram, 2016). Nevertheless, these precipitation responses are not spatially uniform, as they are shaped by multiple interacting climatic and environmental factors (Tabari et al., 2019). As a result, the relationship between extreme rainfall and land surface temperature differs across regions; in certain warm environments, inverse scaling has been documented, potentially linked to limited surface moisture availability or increased aridity (Roderick et al., 2019). In moisture-rich regions, enhanced atmospheric moisture transport may intensify rainfall extremes, whereas in arid areas, gains in precipitation may be counterbalanced by elevated evaporation rates. From an infrastructure perspective, flooding inflicts considerable structural damage on roadways, leading to broader system-level consequences such as traffic disruptions and reduced network performance (Kasmalkar et al., 2020). Transportation networks, which play a vital role in sustaining regional and national connectivity, are particularly vulnerable to flood-related hazards (Koks et al., 2019). Climate change further amplifies these risks by increasing both the occurrence and severity of flood events, thereby elevating the exposure of transportation assets (Kimura et al., 2023; Raymond et al., 2020). Consequently, strengthening the resilience of urban transport systems to flood hazards has emerged as a key priority for cities worldwide (Garcia et al., 2025; Haraguchi et al., 2022; Shen et al., 2023). Figure 2-14 shows an example of flooding consequences in Valencia, spain.

Figure 2-14 Consequences of the November 2024 floods in Valencia, Spain (Earth.Org, 2025).

2.5 Landslides

Reporting 17% of all natural hazards, landslides are the 7th life-threatening natural geo-environmental hazard in the world (Petley, 2012). Landslides are ubiquitous in the hills, mountains, and high coasts that constellate the landmasses (Guzzetti et al., 2012), and in many areas they cause significant human, societal, economic, and environmental damage and costs (Rossi et al., 2019; Salvati et al., 2018). Since the focus of this study is on landslides, the following sections present an overview of landslide classification, triggering factors, the impacts of climate change on landslide occurrence, and the effects of landslides on infrastructure systems.

2.5.1 Landslides classifications

Landslides are categorized based on both the type of material involved and the nature of movement, which reflects the underlying failure process. The widely adopted international classification framework proposed by Cruden and Varnes (1993) uses a two-part naming convention: the first term identifies the material, while the second specifies the movement mechanism (Table 2-2). Movement types encompass a broad range of failure processes (Figure 2-15), and the concept of "landsliding" may also extend to ground subsidence and surface collapse phenomena. Comparable physical processes occur in snow and ice avalanches. Many landslides exhibit complex, multi-phase behavior in which an initial mode of movement evolves into another. These events are therefore described using compound terminology. For instance, the term "rockfall–debris flow" refers to an initial detachment and fall of rock blocks that subsequently fragment upon impact, forming debris that is then transported downslope as a flowing mass.

Table 2-2 Landslide types Cruden and Varnes (1993).

Movement type	Material type		
	bedrock	Engineering soils	
		Predominantly coarse	Predominantly fine
Falls	Rockfall	Debris fall	Earth fall
Topples	Rock topple	Debris topple	Earth topple
Slides			
Rotational	Rock slide	Debris slide	Earth slide
Translational			
Lateral spreads	Rock spread	Debris spread	Earth spread
Flows	Rock flow	Debris flow	Earth flow
Complex combination of two or more principal movement types			

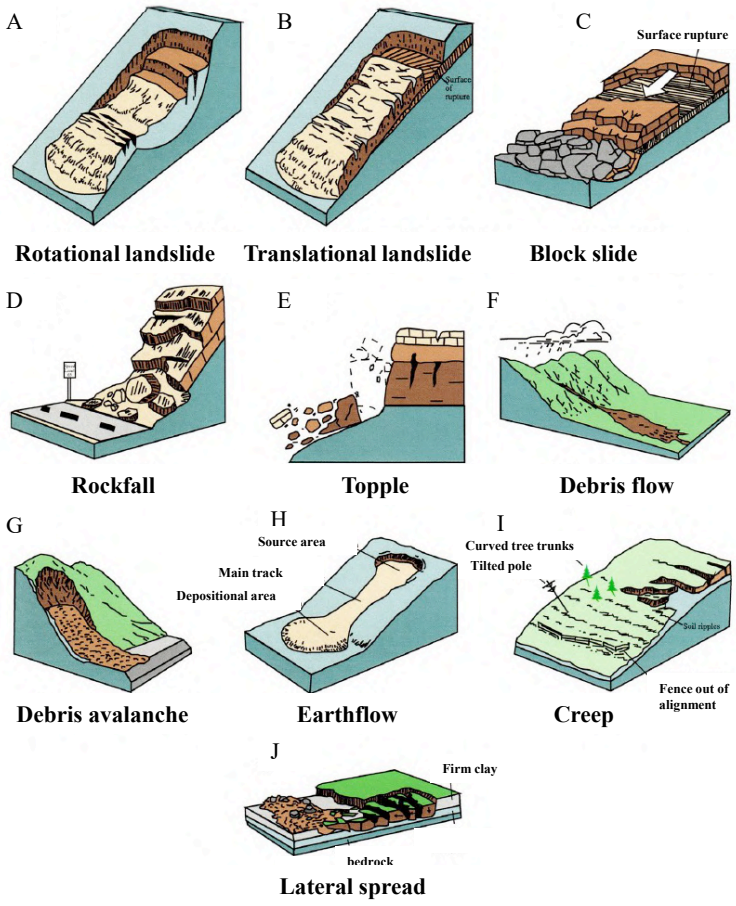

Figure 2-15 Schematic illustration of the major landslide movement types (Highland and Bobrowsky, 2008).

2.5.2 Landslides triggering factors

This category includes several primary triggering factors that may act independently or in combination: (1) hydrological conditions, (2) seismic events, (3) volcanic processes, and (4) temperature-related effects. The impact of these triggers varies considerably depending on site-specific conditions, including slope gradient, landform characteristics, soil properties, geological structure, and the presence of human settlements or infrastructure within the affected area.

2.5.2.1 Hydrological conditions

Water infiltration leading to slope saturation is one of the dominant drivers of landslide initiation. Saturation may result from prolonged or intense rainfall, snowmelt, fluctuations in groundwater levels, or changes in surface-water levels along coastlines, earth dams, and the margins of lakes, reservoirs, canals, and rivers (Miao et al., 2019; Saha and Bera, 2026; Wang et al., 2026). Changes in groundwater or surface-water levels raise pore water pressures inside the slope, which reduces the effective stress that actually holds the soil together, leading to a loss of shear strength. At the same time, the gradual disappearance of matric suction in unsaturated soils, along with additional seepage forces, further weakens the slope and makes failure more likely.

Landslide occurrence is strongly linked to flooding, as both processes are influenced by precipitation, runoff, and soil moisture conditions. Flood events can promote slope failure by eroding stream and river banks or by saturating hillslopes through overland flow. Additionally, debris flows and mudflows commonly develop within narrow, steep channels and are frequently misidentified as flood events; in many cases, both hazards occur concurrently within the same area.

Landslides can also act as a trigger for flooding when displaced rock and debris obstruct waterways, forming temporary natural dams that impound water upstream. The subsequent failure of such blockages can generate sudden downstream flooding. Furthermore, landslide-derived sediment can increase the volume and density of streamflow or obstruct channels, leading to altered flow paths, localized erosion, and flood-like conditions. Landslides may also generate tsunamis (Dohmen et al., 2025), cause overtopping of reservoirs (Barla and Paronuzzi, 2013), and reduce reservoir storage capacity through sediment accumulation.

Slopes affected by wildfire are particularly susceptible to landslide due to vegetation loss, post-fire soil property changes, and enhanced water infiltration from rainfall and other sources. On burned terrain, debris flows represent the most frequently observed landslide type (Highland and Bobrowsky, 2008).

Figure 2-16a–d illustrates the 2009 Valgrisenche landslide in the Aosta Valley, where an estimated 35,000 m^3 of debris was mobilized along the SR25 road. The

failure was preceded by prolonged rainfall during the spring season, which significantly increased slope saturation and contributed to the progressive mobilization of colluvial and morainic deposits on a steep slope (35°–40°). The presence of protective structures such as the counterscarp wall and an anchored retaining wall influenced the landslide evolution by limiting its downslope propagation and partially preventing a deeper failure beneath the road level.

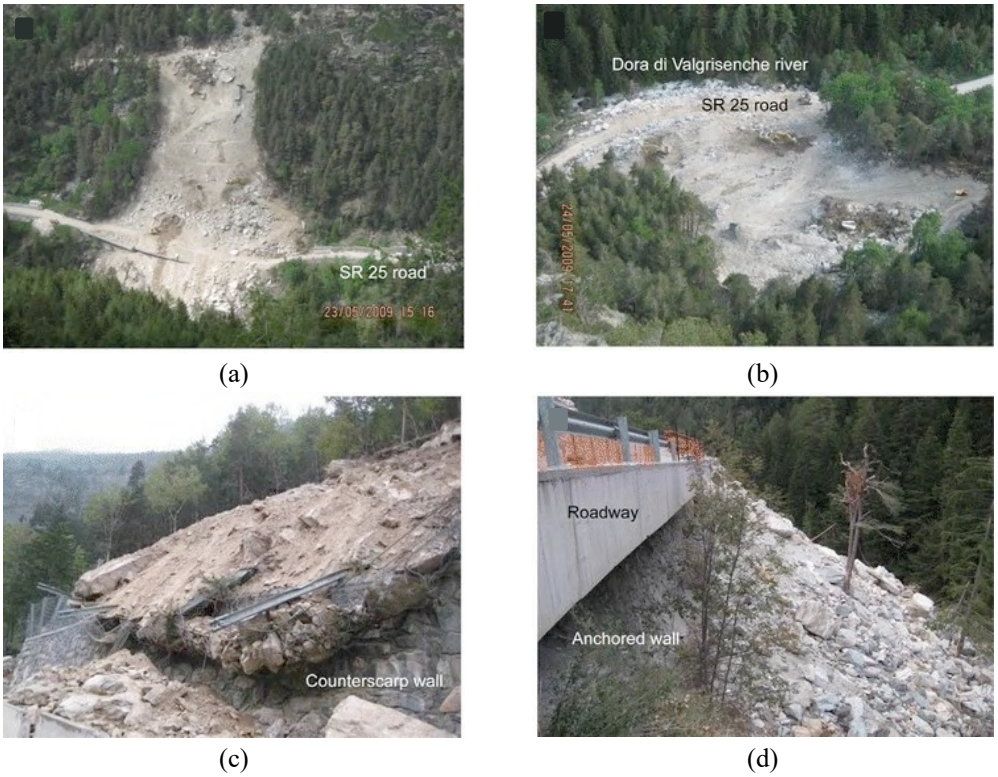

Figure 2-16 Valgrisenche landslide: (a) Overview of the landslide from the opposite side of the valley (May 2009), (b) View of the failure from the crown zone, and (c) Close-up of the counterscarp wall partially overtopped by the moving mass. d Detailed view of the SR25 road section and the anchored retaining structure (Barla et al., 2013).

2.5.2.2 Landslides and seismic activity

Earthquake-induced landslides are characterized by their abrupt initiation and their ability to affect large geographic areas simultaneously. Recent seismic events, including the 6 February 2023 Türkiye–Syria earthquake, have triggered over 3,000 landslides, demonstrating the scale of this hazard (Figure 2-17) (Görüm et al., 2023; Kocaman et al., 2025). Seismic activity can significantly modify slope stability and subsurface conditions, leaving affected regions vulnerable to prolonged instability. Intense ground shaking disrupts rock and soil structures, increasing their susceptibility to subsequent failures both during the main seismic event and in later rainfall episodes (Tanyaş et al., 2021).

Seismic ground motion weakens slope materials by reducing their shear strength, thereby increasing their susceptibility to failure during subsequent rainfall

or later seismic activity. In tectonically active mountainous regions, co-seismic landslides contribute substantially to societal and infrastructural losses while also reshaping the physical landscape (Tang et al., 2017). Analyses of sequential post-earthquake landslide inventories indicate that landslide occurrence and erosion rates typically rise sharply in the years immediately following a major earthquake before gradually returning to background levels (Fan et al., 2019). Because the elevated risk of earthquake-related landsliding can persist for extended periods, assessing the temporal evolution of post-seismic landslide activity and its consequences are essential for improving understanding of triggering processes, refining hazard evaluations, and supporting disaster risk reduction strategies (Shafique, 2020). Figure 2-17 illustrates a landslide event that was initiated by an earthquake.

Figure 2-17 Landslide caused by earthquakes in İdilli, Turkey (Kocaman et al., 2025).

2.5.2.3 Landslides and volcanic activity

Explosive volcanic eruptions significantly alter landscapes and ecosystems through the widespread deposition of tephra on hillslopes, which buries vegetation, degrades soil structure, disrupts habitats, and modifies hydrological processes by reducing infiltration and increasing surface runoff (Major and Yamakoshi, 2005; Pierson et al., 2013). The subsequent remobilization of these unconsolidated materials by runoff and lahars produces some of the highest sediment yields observed in fluvial systems, causing rapid channel aggradation, lateral channel shifts, and extensive floodplain burial (Korup, 2012). The combined effects of added surface loading weakened soil cohesion, and enhanced pore-water pressures

substantially increase slope instability, thereby elevating landslide susceptibility both immediately following eruptions and over longer post-eruptive periods as volcanic deposits continue to be reworked. Figure 2-18 presents an example of a landslide caused by volcanic activity at the Mount Meager massif, located approximately 150 km north of Vancouver, British Columbia (Parizia et al., 2024). This deeply eroded volcanic complex is composed of about 20 km³ of mainly andesitic and dacitic rocks, with geological units ranging in age from the Pliocene to the Holocene period.

Figure 2-18 The 2010 Mount Meager landslide deposit in British Columbia, Canada (Parizia et al., 2024).

2.5.2.4 Landslides and temperature

Research on the influence of temperature on soil mechanical properties began in the 1960s, yet this relationship remains insufficiently understood. Early studies reported negligible variation in soil strength across a temperature range of approximately 10 °C to 60 °C (Mitchell, 1969), a finding later supported by experimental work (Saffer et al., 2001). Subsequent research has revealed that soil behavior under thermal loading is strongly dependent on stress history and thermo-hydraulic conditions. Observed responses include thermally enhanced consolidation (Laloui, 2001) and increased hydraulic conductivity resulting from reduced pore-water viscosity at higher temperatures (Fredlund and Rahardjo, 1993). In highly porous clays, heating-induced pore fluid loss has been shown to trigger structural collapse and significant settlement. Numerous studies have reported pronounced volumetric strains during heating and cooling cycles, while corresponding changes in shear strength were comparatively minor, leading to greater research emphasis on volumetric behavior rather than shear response (He et al., 2021; Hueckel et al., 2009; Liu et al., 2018).

Freeze–thaw cycling, a widespread natural process, has attracted increasing research attention in recent years (Zhang et al., 2020; Zhang et al., 2023b). Seasonal frozen soils are characterized by repeated freezing and thawing, during which a portion of pore water transitions into ice as temperatures fall below freezing. This phase change alters the original three-phase soil system of solids, liquids, and gases into a four-phase structure (Qi et al., 2008), resulting in microstructural reorganization and corresponding changes in mechanical strength (Zhou et al., 2018). Triaxial test results on silty soils indicate that cohesion, internal friction angle, and elastic modulus decrease markedly following freeze–thaw cycles, with the most significant degradation occurring during the initial cycles (Xu et al., 2019). The effects of freeze–thaw processes vary among soil types, and in some cases, strength reduction may be minimal or absent. Nevertheless, there is broad consensus that loess exhibits notable strength deterioration after freeze–thaw cycling (Kong et al., 2023), accompanied by microstructural changes such as increased porosity and the development and widening of cracks (Ye and Li, 2019). Consequently, in mountainous environments characterized by pronounced temperature fluctuations, thermal processes represent a non-negligible control on soil strength evolution and landslide susceptibility. Figure 2-19 presents the effects of snowmelt on slope stability.

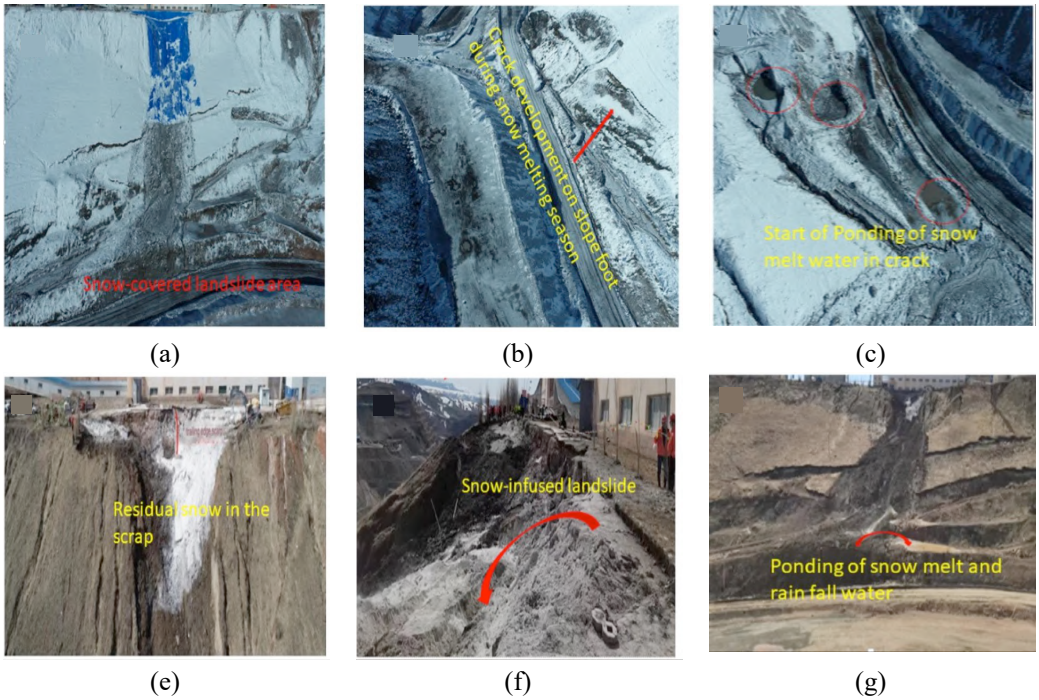

Figure 2-19 Snowmelt- and rainfall-driven slope failure processes and subsequent post-failure behavior in the Yili Valley, Xinjiang, China (Wang et al., 2025).

2.5.2.5 Methodologies for landslide mechanism

In the previous section, the main landslide triggering factors were discussed in detail. Building on this, the present section explains the methodological approaches used to investigate landslide mechanisms, which are broadly categorized into experimental, numerical, and machine learning methods.

Experimental approaches have been widely used to investigate landslide triggering mechanisms, particularly to understand the interactions between rainfall infiltration, slope deformation in unsaturated conditions, and groundwater table rise (Sasahara and Sakai, 2014; Luo et al., 2025). These investigations have employed field observations, small-scale and centrifuge model tests, as well as large-scale rainfall simulator experiments to better reproduce real slope failure conditions (Longoni et al., 2025; Take et al., 2004).

Numerical approaches provide a quantitative framework for evaluating slope stability and landslide behavior based on mechanical principles and material properties. These methods are widely used to calculate the Factor of Safety (FoS), which serves as a key indicator of slope stability under various conditions, or runout analysis. Methods such as the Limit Equilibrium Method (LEM), Finite Element Method (FEM), Boundary Element Method (BEM), Discrete Element Method (DEM), and Finite Difference Method (FDM) are commonly employed to accurately simulate the deformation and failure processes of landslides (Brideau et al., 2006; Jiang et al., 2022; La Porta et al., 2024; Napoli et al., 2023; Pasqua et al., 2025). Software platforms including, Rocscience, Geo-Studio, UDEC, and FLAC3D enable coupled analyses of seepage and stress–strain fields, thereby improving the understanding of landslide evolution.

Machine learning approaches have emerged as a tool for capturing the nonlinear relationships between multiple triggering factors and landslide displacement, especially when traditional models struggle with complexity (Han et al., 2021). These methods rely on data-driven analysis rather than explicit physical equations.

Each of numerical, experimental, and machine learning approaches present distinct strengths and limitations in landslide trigger analysis. Numerical methods are powerful in simulating the physical processes governing slope behavior and provide detailed insight into deformation and failure mechanisms; however, they are often computationally time-consuming and less suitable for large-scale regional studies due to model complexity and calibration requirements. Experimental methods offer valuable controlled environments to observe landslide processes directly, but they are generally constrained by scale limitations and difficulty in fully reproducing natural field conditions. In contrast, machine learning approaches are well-suited for handling large datasets and spatially extensive problems, making them particularly effective for regional-scale landslide prediction; nevertheless,

their reliance on data availability and limited physical interpretability remains a key challenge. Overall, the three approaches are complementary, with numerical and experimental methods emphasizing process understanding, while machine learning enhances large-scale predictive capability.

2.5.3 Climate change impacts on landslides

Due to their pronounced spatial and temporal variability, landslides can be influenced by climate change in multiple ways and across different geographical and temporal scales (Crozier 2010; Gariano and Guzzetti 2016). Beyond the direct effect of rising temperatures, global warming can alter atmospheric circulation patterns that are relevant for the triggering or reactivation of slope failures. For instance, the enhanced moisture-holding capacity of a warmer atmosphere is expected to intensify extreme precipitation events (Fowler et al. 2021), which may directly increase landslide occurrence in settings where a single intense rainfall event is sufficient to trigger failure and antecedent hydrological conditions play only a minor role (Martinez-Villalobos and Neelin 2023).

At the same time, higher temperatures can increase evapotranspiration demand, potentially reducing soil volumetric water content where moisture availability is limited. In fine-grained soils, however, drying may promote cracking, which can enhance infiltration during subsequent rainfall events. The combined effects of these processes introduce considerable complexity. Unlike other climate-related hazards such as urban flooding or hydrological drought, the response of landslides to climatic changes may involve competing mechanisms with contrasting impacts on frequency and triggering conditions, depending strongly on local characteristics. A simplified perspective might suggest an increase in fast-moving failures in coarse-grained soils and a reduction in the frequency or intensity of reactivations in slow-moving landslides within fine-grained materials. However, for soils with intermediate properties, and where opposing processes such as enhanced evapotranspiration and crack-induced infiltration interact, such generalizations are inadequate without detailed modeling (Gariano and Rianna 2025).

Furthermore, both predisposing and triggering factors are closely linked to intrinsic soil properties, including grain size distribution and state variables such as surface water and groundwater regimes, as well as land cover and land use. Even under stationary climatic conditions, separating predisposing factors from triggering mechanisms and identifying suitable indicators for their relative influence is challenging. Under climate change, this complexity increases further, as the two phases may be affected differently, and their combined response is often highly site-specific.

Comprehensive research on the influence of climate change on rainfall-induced landslides is essential, as emphasized in Action No. 6 of the Kyoto 2020

Commitment for Global Promotion of Understanding and Reducing Landslide Disaster Risk (Sassa, 2021). This action calls for systematic investigation of climate change impacts on rainfall-triggered landslides and for the advancement of effective rainfall forecasting systems to enable earlier warnings and evacuations, particularly in developing countries. The issue has also been examined in a dedicated report by the European Environment Agency (2017).

Climate projections indicate that mean annual precipitation is likely to increase in high-latitude regions and in the equatorial Pacific (Figure 2-9). In mountainous and hilly environments within these areas, an increase in the frequency or seasonal activity of deep-seated landslides, rockslides, earthflows, and mudflows is anticipated (Chiang and Chang, 2011; Jakob and Lambert, 2009). In North America, precipitation patterns are expected to diverge spatially, with increases in the northern regions and decreases in the southern regions. These contrasting trends may produce different responses in landslide activity (Jakob and Lambert, 2009). Specifically, a rise in the frequency of shallow landslides and debris flows is projected in some areas, while rainfall-triggered deep-seated landslides may become less active or exhibit slower displacement rates (Figure 2-20).

In other regions, such as the southern European Alps, total annual precipitation is projected to remain relatively stable, but rainfall is expected to be concentrated into fewer days, leading to more intense precipitation events (IPCC, 2014). This shift is likely to increase the occurrence of shallow landslides (Saez et al., 2013; Stoffel et al., 2014) while potentially reducing the frequency of deep-seated failures (Rianna et al., 2014). Changes in the number of rainy days may also alter precipitation regimes, thereby modifying the temporal distribution of rainfall-induced landslides and debris flows.

For example, Nikolopoulos et al. (2015) identified a marked north–south contrast in the seasonal occurrence of debris flows in Trentino–Alto Adige in the eastern Italian Alps. In the northern sector, characterized by substantial snowfall and comparatively lower rainfall, debris flows mainly occur during summer. In contrast, in the southern and wetter areas, most events take place in autumn. Shifts in rainfall seasonality may therefore modify this spatial and temporal pattern. Additionally, projected increases in air temperature in these regions are expected to enhance evapotranspiration, potentially reducing subsurface water content and contributing to greater slope stability.

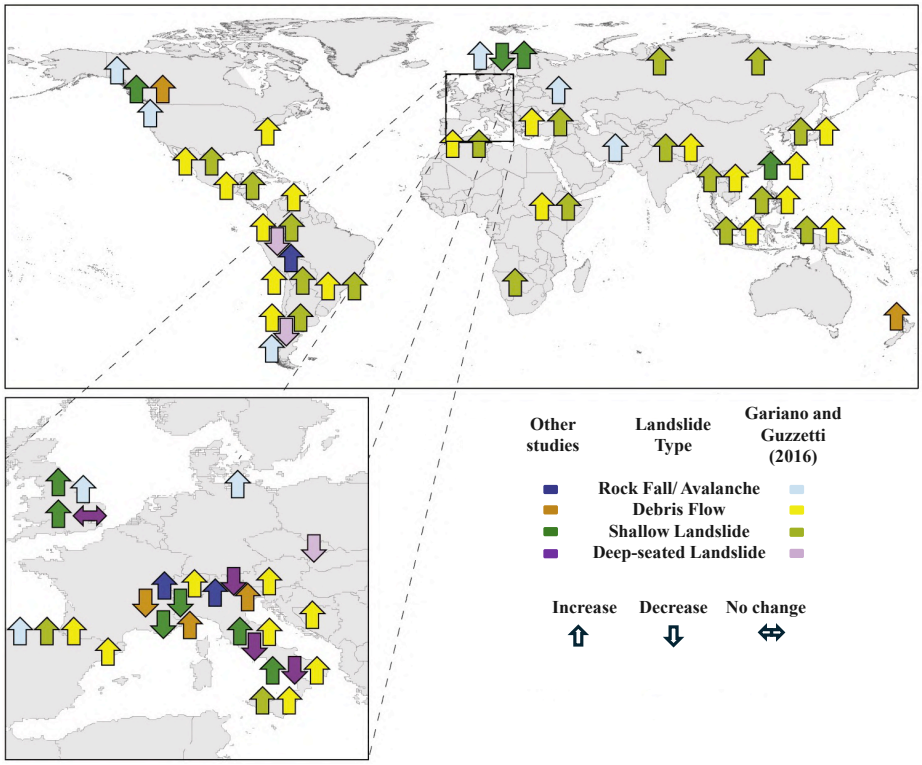

Figure 2-20 General areas where variations in the abundance or activity of four landslide types are expected under projected climate change (Gariano and Guzzetti, 2016).

A study by Insana et al. (2025) constructs a modular framework to systematically incorporate climate change considerations into the geotechnical analysis and design of both new and existing geo-structures. The framework is built on a causal chain linking climate change signals, their effects, and resulting impacts, enabling engineers to assess performance under evolving climate scenarios (Figure 2-21). The approach is illustrated through a slope stability example, where in their study they present an application to demonstrate how the framework can support the evaluation and improvement of geo-structure performance under future climate conditions.

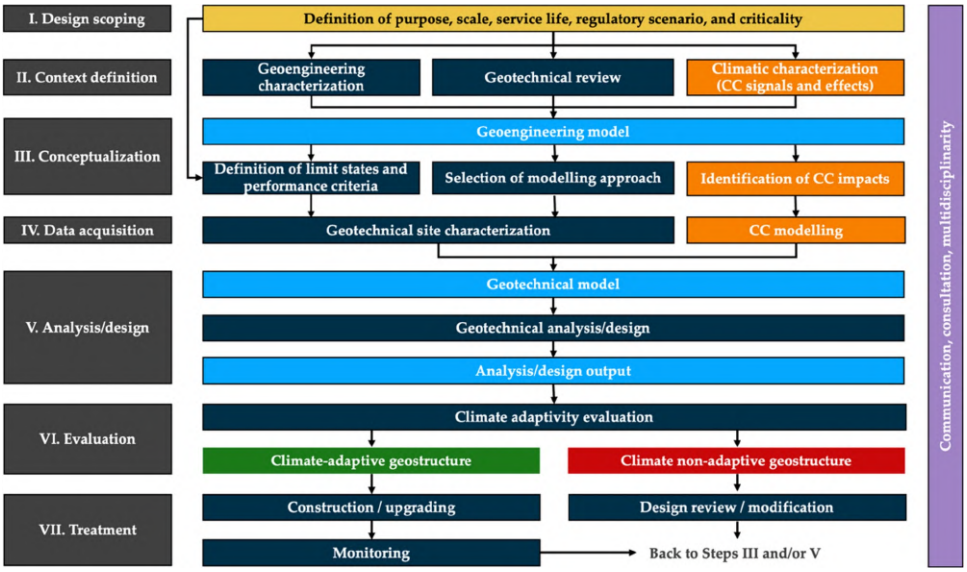

Figure 2-21 Framework for geotechnical analysis and design adapted to climate change (Insana et al., 2025).

2.5.4 Landslides impacts on infrastructures

In Europe, it has been estimated that approximately 1.3 to 3.6 million people reside in areas characterized by high landslide hazard. In addition, between 31,000 and 42,000 km of the road network and roughly 13,000 to 18,500 km of railway lines are considered exposed to landslide risk across the continent (Jaedicke et al. 2014). An increase in the frequency of rainfall events exceeding continental-scale landslide triggering thresholds has been documented across large parts of Europe during the period 1991–2018 compared with 1961–1990 (Bezak and Mikoš 2021). These trends are consistent with broader climate change impacts on geo-structures, particularly the reduced stability of slopes and embankments due to intensified hydrological processes such as extreme rainfall and flooding (Insana et al., 2021). Furthermore, a growing trend in fatal landslides was identified between 2008 and 2014, with events widely distributed throughout Europe but more concentrated in mountainous regions (Haque et al. 2016). These landslide events pose a significant threat to critical infrastructure, including energy transmission networks, highways, and bridges (Cernuto et al., 2025; Vitaletti et al., 2026).

For example, the Vajont landslide occurred on 9 October 1963 in the Dolomites of Friuli, Italy, when approximately 270–300 million m³ of rock and debris collapsed into a reservoir, generating a wave that overtopped the 261.6 m-high double-curvature arch dam constructed within a V-shaped gorge (Figure 2-22). The flood wave dropped into the Piave Valley destroying the town of Longarone and other villages nearby. More than 2,000 people were killed. The Vajont case is widely regarded as a benchmark for understanding deep-seated landslides due to the complexity of its geological and geomechanical setting. Investigations highlighted that the 1963 failure was the reactivation of a large prehistoric rockslide

involving the Mount Toc slope, characterized by a thick basal shear zone composed of heterogeneous materials including limestone debris and clay layers. Particular emphasis has been placed on the role of reservoir-induced pore pressure variations caused by repeated filling and drawdown cycles, which significantly affected slope stability by altering the effective stress conditions. This case also underlined the necessity of detailed geological, geomorphological, and hydrogeological investigations, as well as the use of advanced numerical modelling techniques to properly simulate the interaction between rock mass behavior and reservoir operations (Barla and Paronuzzi, 2013).

(a) (b)

Figure 2-22 The Vajont landslide and dam system, with (a) Presenting a panoramic view of the slip surface and (b) Showing the double-curved arch dam (Barla and Paronuzzi, 2013).

Another catastrophic event was recorded on 25 January 2026 in Niscemi, Sicily, Italy, where intense rainfall associated with Cyclone Harry triggered a severe landslide. The event generated a chasm approximately 4 km in length and up to 25 m in depth, resulting in the partial collapse of an entire slope sector of the urban area. Road infrastructure failed, vehicles were engulfed, and significant portions of the built environment were displaced downslope into the adjacent valley. Numerous residential buildings were left unstable along the landslide scarp, while additional roadway segments and vehicles continued to deteriorate due to ongoing ground instability. As a precautionary measure, authorities evacuated more than 1,600 residents. Several areas within the historic town center were identified as being at high risk, including 17th-century churches and other heritage structures potentially susceptible to further slope movement. According to geologists and environmental experts, the Niscemi landslide represents a recent example of increasing geomorphological instability in the Mediterranean region. The event has been associated with the combined effects of intensified precipitation linked to climate change and long-standing challenges related to land-use planning, building practices, and urban expansion in vulnerable areas. Figure 2-23 shows the damages on houses and infrastructures due to the landslide in Niscemi.

(a)

(b)

Figure 2-23 An aerial perspective of Niscemi showing(a) A cluster of residential buildings situated directly on a precipice, and(b) The ongoing collapse of the hillside, pulling vehicles and asphalt debris down the slope (https://www.theguardian.com).

Figure 2-24 presents a comparison of orthophotos acquired before and after the event. The post-event imagery consists of a series of drone-based photographs collected by the Municipality of Niscemi on January 18, and February 2, 2026.

(a)

(b)

Figure 2-24 Orthophotos of the study area: Before the event; (b) After the event (acquired on January 18, and February 2, 2026).

2.6 Summary

This chapter has examined the multifaceted relationship between climate change and natural hazards, with particular emphasis on landslides as a climate-sensitive geo-environmental process. It began by outlining the increasing frequency and intensity of extreme climatic events under ongoing global warming, framed within established scenario architectures such as the SSP–RCP framework. Observed and projected changes in temperature and precipitation extremes were reviewed, highlighting the thermodynamic and dynamic mechanisms that intensify heatwaves and heavy rainfall events. The chapter then characterized major climate-related hazards, including wildfires, tropical cyclones, convective storms, and flooding, before providing a detailed analysis of landslides, their classifications, triggering mechanisms, and evolving risk profiles. This was followed by an explanation of hydrological, seismic, volcanic, and temperature-related controls on slope instability, along with the complex and regionally heterogeneous influences of climate change on landslide occurrence, magnitude, and seasonality. The socio-economic implications of increasing landslide activity, particularly for infrastructure and vulnerable communities, were also discussed. Building on this conceptual and process-based understanding, the next chapter focuses on the various methodologies used to assess and delineate landslide susceptibility, with particular emphasis on machine learning approaches for identifying areas prone to failure under different environmental and climatic conditions.

Chapter 3

Landslide susceptibility mapping

3.1 Introduction

Landslide susceptibility mapping represents a fundamental step in landslide investigation, risk assessment, and prevention. Effective mitigation and management strategies require reliable evaluation and susceptibility mapping. Over recent decades, numerous methods have been developed for landslide assessment and mapping. These methods are generally categorized into qualitative, semi quantitative, and quantitative approaches. Qualitative approaches typically include geomorphological mapping and heuristic techniques, which rely heavily on expert judgment and field interpretation. In contrast, quantitative approaches encompass statistical methods, artificial intelligence techniques, probabilistic and deterministic models. Semi-quantitative methods combine expert knowledge with limited statistical analysis to assign relative weights or rankings to landslide factors. Quantitative methods estimate landslide susceptibility based on observed data and explicit analytical frameworks, thereby reducing the subjectivity inherent in qualitative assessments. Different techniques incorporate varying sets of triggering factors and apply diverse procedures for factor weighting, analysis, and interpretation. Each method presents specific advantages and limitations, depending on the context of application. Therefore, selecting an appropriate technique for landslide susceptibility evaluation and mapping is a critical decision. Key considerations include the objective of the investigation, the spatial extent of the study area, the intended map scale, the nature and quality of available data, the types of landslides under consideration.

In this chapter, first, the various methods are examined in detail, with particular emphasis on machine learning approaches, including a step-by-step explanation of

their application in landslide susceptibility mapping. Subsequently, the methodologies used in literature to assess landslide threats to infrastructure are then presented. Finally, the existing research gaps are identified and discussed.

3.2 Landslide susceptibility mapping methods

A wide range of approaches and techniques have been developed for the assessment of landslide susceptibility, including landslide inventory mapping, heuristic terrain evaluation, susceptibility zonation, statistical modeling, deterministic analysis, and probabilistic methods (Aleotti and Chowdhury, 1999; Corominas et al., 2014; Guzzetti et al., 1999; Kanungo et al., 2006; Raghuvanshi et al., 2014a; Raghuvanshi et al., 2015). These methods are generally grouped into three broad categories: qualitative and quantitative, and semi-quantitative approaches.

Qualitative approaches comprise inventory and distribution analyses, geomorphological mapping, and expert-based or heuristic evaluations that rely on the experience and judgment of the analyst (Corominas et al., 2014; Raghuvanshi et al., 2014a). Qualitative methods are often regarded as inherently subjective due to their dependence on expert interpretation (Casagli et al., 2004; Fall et al., 2006),

In contrast, quantitative approaches include statistical techniques, deterministic models, probabilistic frameworks, and distribution-free methods (Kanungo et al. 2006; Raghuvanshi et al., 2014a). They are generally considered more objective compared to qualitative methods because they rely on explicit mathematical and statistical procedures (Girma et al., 2015). In recent years, quantitative techniques have become increasingly prevalent in landslide susceptibility studies, largely due to advances in data availability, computational capacity, and modeling methodologies. Artificial intelligence methods are introduced here as part of this category and are described in detail in section 3.6, as they represent the primary methodological approach adopted in this research.

Semi-quantitative methods, on the other hand, integrate expert judgment with basic statistical techniques to allocate relative importance or scores to landslide conditioning factors (Bera et al., 2019; Erener et al., 2016). While they are less subjective than purely qualitative approaches, they still rely to some extent on expert interpretation.

3.3 Qualitative methods

Qualitative methods represent knowledge-based approaches that depend largely on expert interpretation, geomorphological analysis, and heuristic reasoning rather than on formal statistical or probabilistic frameworks. In these approaches, terrain units are assigned to susceptibility classes, typically ranging from low to high,

according to the interpreted influence of conditioning factors such as slope gradient, lithology, land use, drainage characteristics, and structural discontinuities.

In contrast to data-driven statistical or machine learning techniques, qualitative methods do not require extensive landslide inventories for calibration. Instead, they are grounded in the assumption that experienced geomorphologists and engineering geologists can assess the likelihood of future slope instability based on landscape features and an understanding of geomorphic processes. Consequently, qualitative approaches are particularly valuable in regions with limited data availability, in newly studied areas, or in contexts of environmental change where historical landslide records may not adequately reflect evolving instability patterns (Guzzetti et al., 1999; Van Westen et al., 2003)

3.3.1 Geomorphological mapping method

In this method, most of the data related to factors responsible for landslides are obtained through remote sensing, while data procurement through direct fieldwork is rarely employed. Landslide susceptibility mapping is carried out using aerial photographs (Guzzetti et al., 1999; Kanungo et al., 2009; Mandaglio et al., 2016; Verstappen, 1983) or satellite imagery (Nossin, 1989). These methods are most commonly, though not necessarily, associated with the preparation of a landslide inventory map. A landslide inventory involves mapping past landslides in an area and collecting data on their location, type, and dimensions. In addition, information on causative factors, triggering mechanisms, and frequency of occurrence is recorded (Girma et al., 2015; Dai et al., 2002; Dai and Lee, 2001). Landslide inventory mapping is considered straightforward and is required for most susceptibility and hazard zonation techniques (Dai and Lee, 2002), either to formulate general predictive rules or to validate models. However, geomorphic techniques generally do not explicitly consider the specific factors that initiate or trigger landslides. The principal factors used in landslide hazard zonation include lithology, geomorphology, land use and land cover, and the presence or absence of previous landslides. Figure 3-1 shows a Landslide Susceptibility Map (LSM) using geomorphological mapping method.

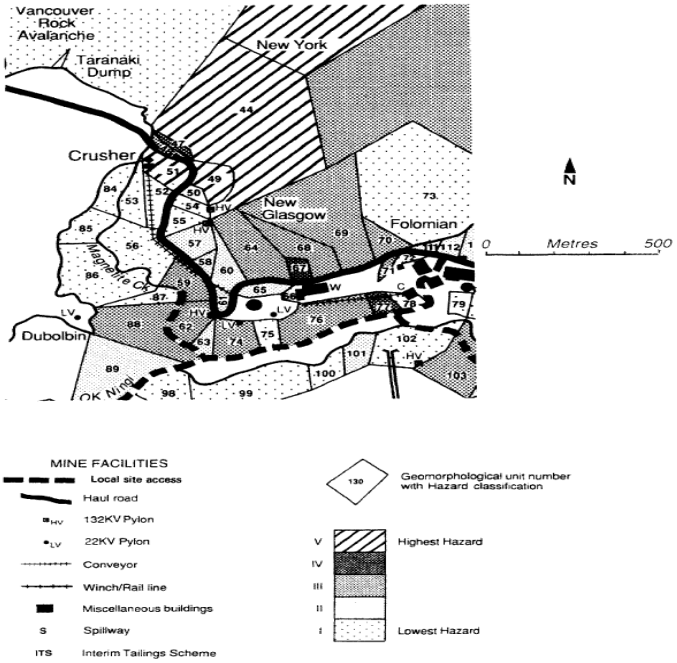

Figure 3-1 LSM for the Ok Tedi mine site (Hearn, 1995).

3.3.2 Heuristic method

In this technique, the expert determines the degree and type of hazard for a given area using either a direct or an indirect mapping approach. Landslide hazard is evaluated based on quasi-static variables , such as slope angle, aspect, soil type, and elevation (Dai and Lee 2001; Fall et al. 2006), and the assessment largely depends on the judgment and experience of the evaluator (Aleotti and Chowdhury, 1999; Carrara et al., 1995; Gorsevski et al., 2003; Guzzetti et al., 1999; Hutchinson, 1995; Raghuvanshi et al., 2014a; Van Westen et al., 1997; Varnes and IAEG, 1984). Consequently, landslide susceptibility and hazard assessments produced using heuristic techniques may vary significantly when conducted by different experts (Casagli et al., 2004; Ruff and Czurda, 2008).

Despite this limitation, these techniques remain popular due to their simplicity and practical applicability. They are primarily based on field-acquired data and are strongly supported by the evaluator's judgment and experience (Raghuvanshi et al., 2014b). Figure 3-2 presents an example of a LSM employing heuristic method.

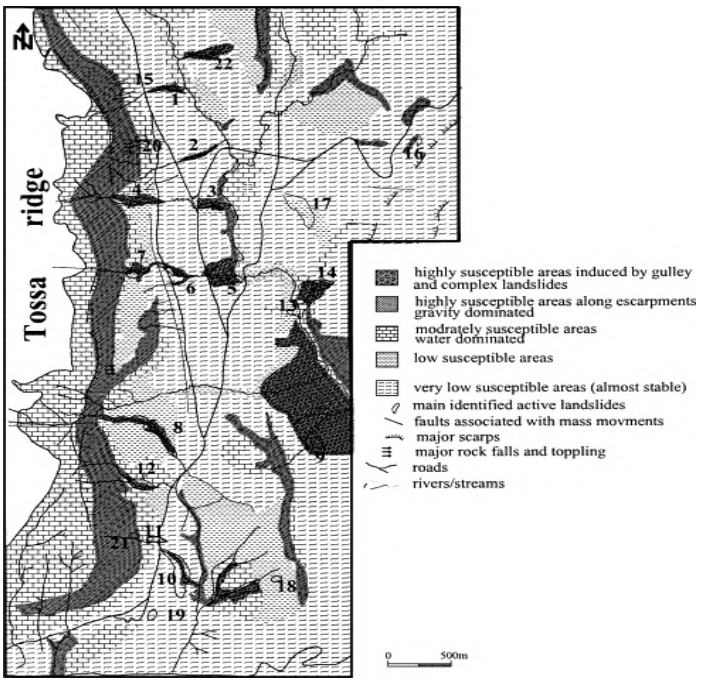

Figure 3-2 LSM and active landslide sites, Dessie, Ethiopia (Ayenewa and Barbieri, 2005).

3.4 Semi-quantitative methods

Semi-quantitative methods represent an intermediate class of landslide susceptibility assessment techniques, positioned between purely qualitative (expert-driven) approaches and fully quantitative statistical. These methods incorporate numerical scoring systems, weighting schemes, or statistical indices; however, they do not generate explicit probabilistic outputs nor rely entirely on rigorous statistical inference (Abija et al., 2019; Bera et al., 2019; Erener et al., 2016; Feizizadeh and Blaschke, 2012; Feizizadeh et al., 2014; Gorsevski and Jankowski, 2010; Milan et al., 2023).

Semi-quantitative approaches, generally classified as multi-criteria decision analysis methods, include the Analytical Hierarchy Process, the Weighted Overlay, Fuzzy Logic, Weighted Linear Combination, and the Ordered Weighted Average. In the following sections, only the first three methods, which are more widely applied in the literature, are described in detail.

3.4.1 Analytical Hierarchy Process method

The Analytical Hierarchy Process (AHP) is a multi-criteria decision-making approach widely used for landslide susceptibility. It is a systematic method that involves problem definition, identification of goals and alternatives, formulation of a pairwise comparison matrix, determination of weights, and calculation of overall priority values (Pardeshi et al., 2013; Saaty, 2008). Landslides are complex processes resulting from the combined influence of multiple causative factors

(Chimidi et al., 2017; Raghuvanshi, 2019). The AHP approach can be applied using either absolute or relative measurement to evaluate the relationship between causative factors and landslide occurrence. In absolute measurement, each alternative is compared with an ideal alternative. In contrast, relative measurement involves comparing each alternative with other alternatives. The absolute measurement approach is normative, as it is conditioned by what is considered the best standard. Conversely, the relative measurement approach is descriptive in nature, as it depends on the evaluator's experience and judgment (Saaty and Vargas, 2006).

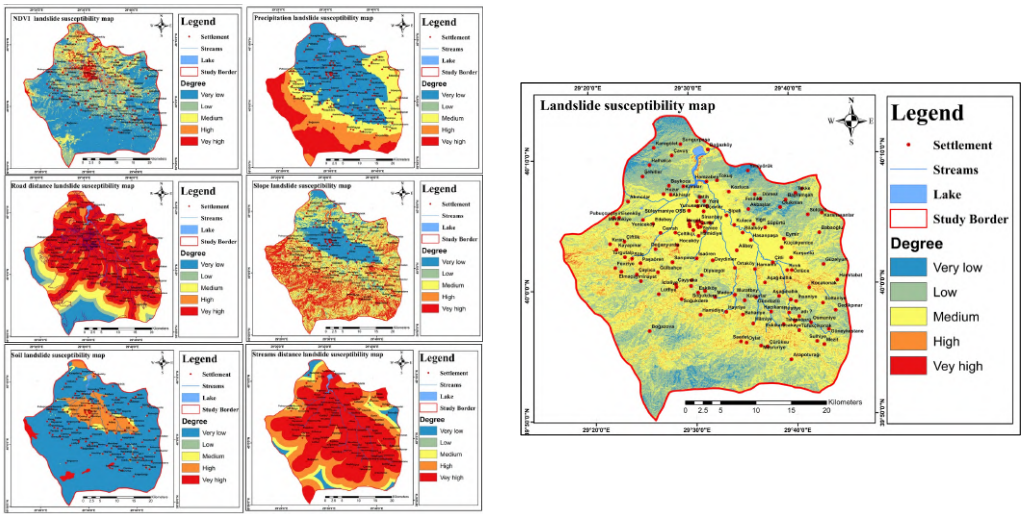

(a) (b)

Figure 3-3 AHP methodology used by Aksoy (2023) in Marmara region Türkiye: (a) A number of weighted sensitivity maps of criteria, and (b) LSM of the study area.

3.4.2 Weighted Overlay method

The Weighted Overlay is a simple approach used for evaluating landslide hazard in a given area (Ayele et al., 2014; Bachri and Shresta, 2010; Erener and Duzgun, 2012; Intarawichian and Dasananda, 2010). This method is based on the assumption that conditions responsible for past landslides, if repeated in the future in other areas, may again result in landslide occurrence. In the Weighted Overlay method, each causative factor layer is reclassified by assigning values to its classes according to their relative contribution to landslide occurrence. The preferred scale typically ranges from 1 to 9, where 9 represents the highest significance in relation to landslide occurrence. All causative factor layers are then integrated within a GIS environment using the Weighted Overlay Model (Equation (3-1)). In addition, weights are assigned to the causative factors using an ordinal scale ranging from 0 to 9. The numerical values assigned to the classes of each factor are referred to as ratings, whereas the values assigned to the causative factors themselves are termed weights (Lee et al., 2005). A higher weight or rating assigned to a factor or its

respective class indicates greater significance in contributing to landslide occurrence (Ayele et al. 2014). Equation (3-1) determines the spatial unit:

$$S = \frac{\sum W_i S_{ij}}{\sum W_i} \tag{3-1}$$

where W_i is the weight of 'ith' factor map, S_{ij} is the ith spatial class weight of 'jth' factor map, S is the spatial unit value in the output map. Figure 3-4 shows the application of Weighted Overlay method on debris slope, rock slope, and landslide susceptibility.

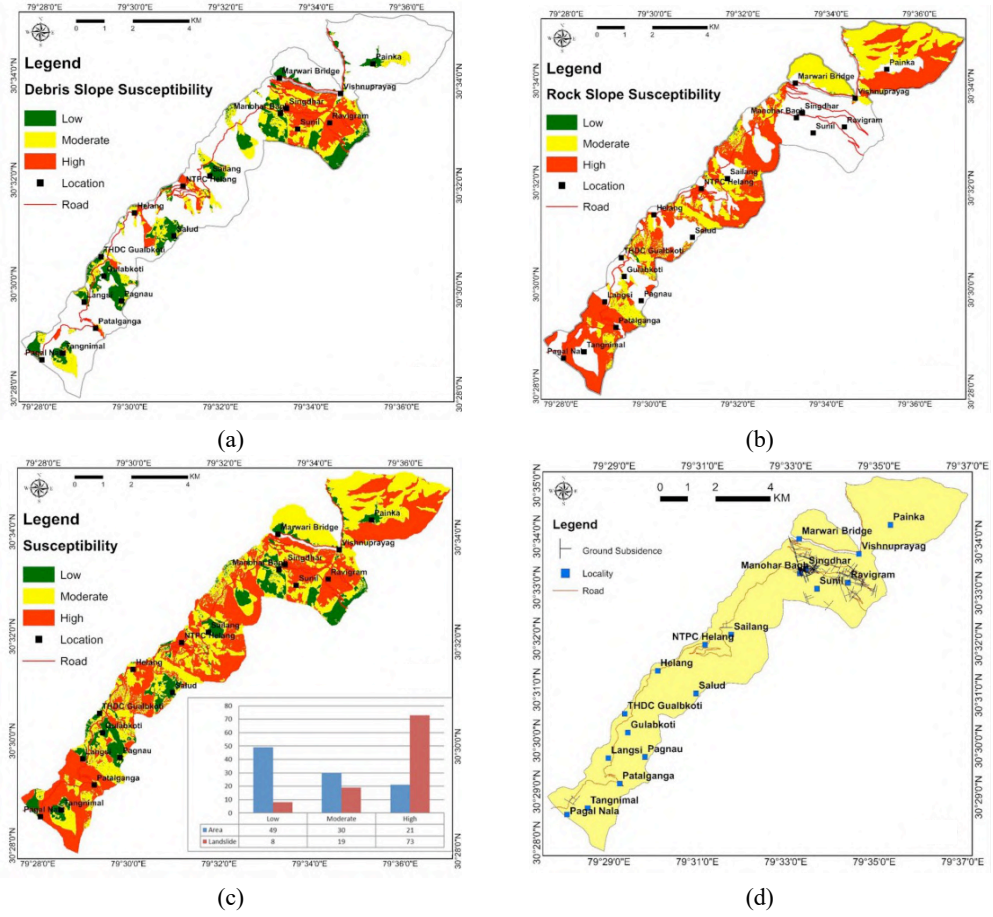

Figure 3-4 Weighted overlay method used by Rana et al (2025) for Chamoli district of Uttarakhand (a) Debris susceptibility map, (b) Rock susceptibility map, (c) LSM of the study area. (d) Ground crack map of Tangni-Vishnuprayag road corridor.

3.4.3 Fuzzy Logic method

Processes, events, or functions that change continuously cannot always be defined in terms of strictly true or false conditions; therefore, such phenomena are expressed in a fuzzy manner. Concepts that are vague or imprecise are described as fuzzy. Fuzzy Logic is considered a superset of Boolean logic and serves as an extension

to address partial truth values that lie between completely false and completely true (Chacón et al., 2006).

In landslide studies, the Fuzzy Logic method is applied to reduce subjectivity arising from the selection and evaluation of multiple causative factors (Meten et al. 2015). This method is based on fuzzy set theory, in which elements are assigned membership degrees representing varying levels of confidence within the interval [0, 1] (Kanungo et al., 2006). Several fuzzy operators can be used in analysis, including 'fuzzy OR', 'fuzzy AND', 'fuzzy algebraic product', 'fuzzy algebraic sum', and the 'gamma operator'. Among these, the 'fuzzy AND' operator is equivalent to the Boolean AND (logical intersection) operation in classical set theory (Anbalagan et al., 2015; Razifard et al., 2018) which can be obtained by Equation (3-2):

$$\mu_{combination} = MIN(\mu_A, \mu_B, \mu_C \ldots.) \tag{3-2}$$

where $\mu_{combination}$ is the fuzzy membership function, μ_A represents the membership value of map 'A' at specified location, and μ_B represents the value of map 'B' at specified location, likewise μ_C and so on. Similarly, the fuzzy OR operator corresponds to the classical Boolean OR (logical union), but it operates within a framework of graded membership rather than binary logic. In this context, the resulting membership value is determined by selecting the maximum membership value among the input sets. Accordingly, the fuzzy OR operator can be mathematically expressed as described by Lee (2007) by Equation (3-3):

$$\mu_{combination} = MAX(\mu_A, \mu_B, \mu_C \ldots.) \tag{3-3}$$

Further, the 'fuzzy algebraic product' operator can be expressed as Equation (3-4) (Bonham-Carter, 1994; Zimmermann, 1996):

$$\mu_{combination} = \prod_{i=1}^{n} \mu i \tag{3-4}$$

where μi denotes the fuzzy membership value associated with the ith map, and i = 1, 2, …, n identifies the set of maps included in the combination process. In a similar manner, the fuzzy algebraic sum serves as a complementary operator to the fuzzy algebraic product and can be formulated as presented by Lee (2007), Zimmermann (1996), and Bonham-Carter (1994) by Equation (3-5):

$$\mu_{combination} = 1 - \prod_{i=1}^{n} (1 - \mu i) \tag{3-5}$$

where μi denotes the fuzzy membership value corresponding to the ith map, and i = 1, 2, …, n indicates the total number of maps involved in the combination. Finally, the gamma operation is formulated as a function of both the fuzzy algebraic product and the fuzzy algebraic sum, integrating their effects through a parameterized relationship. This has been defined by Equation (3-6) (Anbalagan et al., 2015; Zimmermann, 1996):

$$\mu_{combination} = (Fuzzy\ algebric\ sum)^{\lambda} * (Fuzzy\ algebric\ product)^{1-\lambda} \quad (3\text{-}6)$$

in this formula, λ represents a parameter constrained within the interval (0, 1). The fuzzy algebraic sum is computed using Equation (3-5), whereas the fuzzy algebraic product is determined according to Equation (3-6). When λ =1, the fuzzy gamma operation becomes equivalent to the fuzzy algebraic sum; conversely, when λ = 0, it reduces to the fuzzy algebraic product. Therefore, an appropriate selection of λ enables a balanced integration of the decreasing behavior associated with the fuzzy algebraic product and the increasing tendency characteristic of the fuzzy algebraic sum. In landslide susceptibility assessments, Lee (2007) and Ahmed et al., (2014) adopted a range of λ values between 0 and 1, specifically 0.025, 0.05, 0.1, 0.2, 0.3, 0.4, 0.5, 0.6, 0.7, 0.8, 0.9, 0.95, and 0.975.

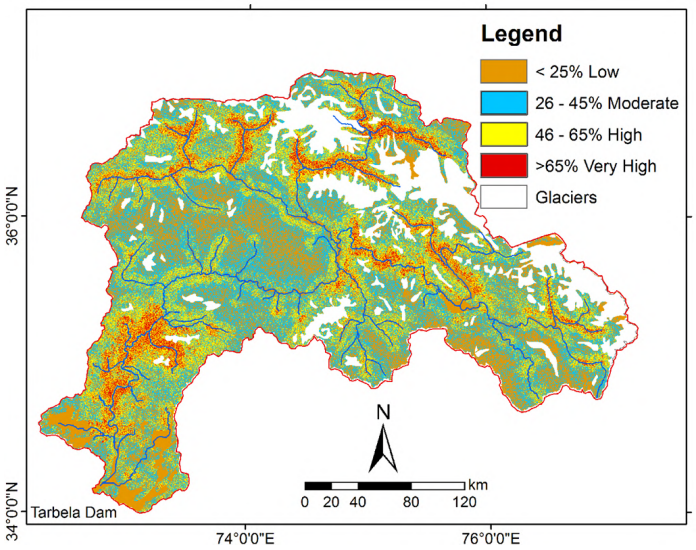

Figure 3-5 LSM in Pakistan compiled by employing the Fuzzy Logic approach (Ahmed et al., 2014).

3.5 Quantitative methods

Quantitative approaches to landslide susceptibility assessment are data-driven techniques that employ statistical analysis, probabilistic frameworks, or machine learning algorithms to derive empirical relationships between landslide occurrence and relevant conditioning factors. In contrast to qualitative or semi-quantitative methods, these techniques seek to generate objective, reproducible, and frequently probabilistic estimates of susceptibility grounded in observed data. Such

approaches require a comprehensive landslide inventory along with a set of explanatory variables, including slope gradient, lithology, curvature, land cover, drainage density, and precipitation. Statistical or computational models are subsequently calibrated to quantify the association between landslide occurrence or non-occurrence and the selected conditioning factors. Given that machine learning constitutes the principal methodology adopted in this study, it is examined in greater depth following a brief overview of other quantitative approaches.

3.5.1 Statistical methods

Statistical techniques represent the most widely applied approaches for landslide susceptibility assessment and hazard zonation (Mengistu et al., 2019). Over time, certain early techniques have been abandoned, others have undergone modification, and new approaches continue to emerge. A detailed examination of the literature indicates that statistical methods employed for landslide susceptibility mapping can generally be categorized into bivariate and multivariate approaches. These methods exhibit considerable variability in terms of the thematic factors considered, the spatial scale adopted, the statistical modeling tools applied, and the procedures used for performance evaluation and validation.

Bivariate statistical methods are based on inductive reasoning, assuming that relationships observed under past and present conditions can be generalized to future scenarios (Dai and Lee, 2001). In landslide studies, these approaches evaluate the relationship between each causative factor and historical landslide occurrence independently (Chimidi et al., 2017; Lan et al., 2004). The contribution of each factor is quantified using a density ratio derived from overlay analysis between thematic factor layers and the landslide inventory, comparing landslide presence and absence within each factor class.

Multivariate statistical methods assess landslide susceptibility by analyzing the combined and relative contributions of multiple causative factors simultaneously (Kanungo et al., 2009; Nandi and Shakoor, 2009). These approaches model landslide presence or absence at the pixel level through statistical relationships between predictor variables and landslide occurrence. Common techniques include logistic regression, multiple regression, and discriminant analysis.

Although some statistical models may demonstrate superior predictive performance under specific conditions, no single method has consistently proven to be universally optimal. Indeed, integrating multiple approaches into a composite or hybrid model, while utilizing the same thematic datasets and landslide inventory, may yield improved predictive capability compared to a single-model framework. Moreover, the effectiveness of any statistical approach largely depends on the expertise, experience, and technical competence of the practitioner applying it (Corominas et al., 2014; Reichenbach et al., 2018). Consequently, selecting an

appropriate methodological framework remains a persistent challenge. In addition, uncertainties inevitably arise regarding the reliability and credibility of the results generated (Guzzetti et al., 2006; Reichenbach et al., 2018).

A fundamental limitation of statistical approaches is that they do not explicitly model the physical mechanisms controlling slope failure. Instead, they rely on the assumption that future landslide-prone areas can be inferred from combinations of variables that were associated with past events (Safaei et al., 2011). In the following section, selected bivariate methods, including Frequency Analysis, Weights of Evidence, and Information Value, as well as multivariate approaches such as Logistic Regression and Discriminant Analysis, are introduced.

3.5.1.1 Frequency Analysis method

Within bivariate statistical approaches, frequency analysis is the most widely applied method (Li et al., 2017). This technique evaluates the relationship between each class of causative factors and the spatial distribution of historical landslides in the study area (Malsawmzuali et al., 2026; Moung-Jin et al., 2014). The frequency analysis method computes the ratio of landslides within a given factor class as a percentage of total landslides relative to the proportion of the study area occupied by that factor class. This frequency ratio is normalized to a value of 1. A frequency ratio exceeding 1 indicates a strong association between the factor class and landslide occurrence, whereas a ratio below 1 suggests a weaker correlation (Khan et al., 2026). Figure 3-6 shows an obtained LSM with this method. Mathematically, the frequency ratio (FR_d) can be expressed as follows in Equation (3-7):

$$FR_d = \frac{Ls}{Am} \tag{3-7}$$

where FR_d denotes the frequency ratio associated with a specific causative factor class, Ls represents the percentage of landslides occurring within that class, and Am corresponds to the proportion of the study area occupied by the same class, expressed as a percentage of the total map area. Subsequently, the Landslide Susceptibility Index (LSI) for each pixel is calculated as the cumulative sum of the frequency ratio values corresponding to all overlapping factor classes at that location, as expressed in Equation (3-8):

$$LSI = \sum_{n=1}^{d} FR_d \tag{3-8}$$

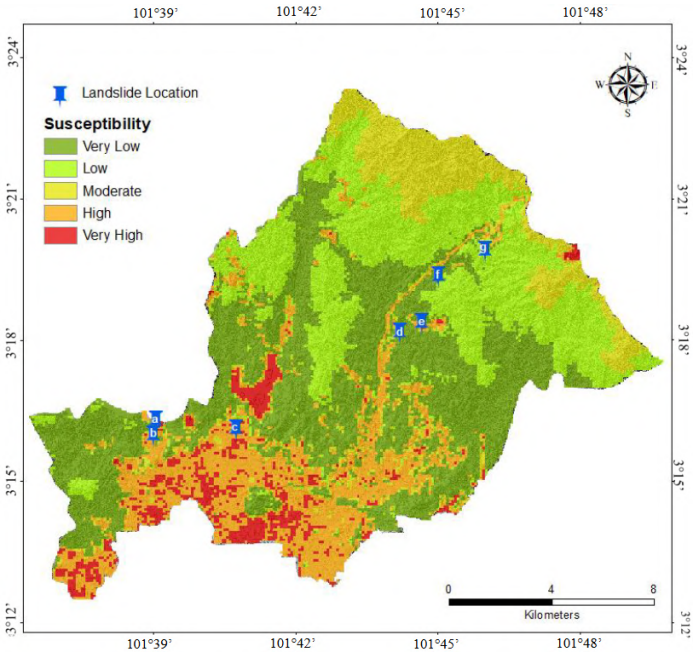

Figure 3-6 LSM of Selayang (Klang Valley), Malaysia, using FR model (Mustapa and Tahar, 2026).

3.5.1.2 Weights of Evidence method

Another bivariate statistical approach is the Weights of Evidence, which has been extensively applied to identify areas susceptible to landslides (Hong et al., 2017; Ilia and Tsangaratos, 2015; Süzen and Doyuran, 2004). This method employs a quantitative, data-driven probabilistic framework to integrate landslide inventory information with conditioning factors. Within the model, the prior probability ($Prior_p$), conditional probabilities ($Cond_p$), and the corresponding positive and negative weights related to landslide occurrence are calculated. The prior probability reflects the overall landslide density in the study area and is determined as the ratio of the total number of pixels affected by landslides to the total number of pixels within the entire study region. Accordingly, the $Prior_p$ can be formulated as presented in Equation (3-9):

$$Prior_p = P\{S\} = \frac{N_{Pix(slide)}}{N_{Pix(total)}} \tag{3-9}$$

where $P\{S\}$ represents the probability of landslide occurrence (S), $N_{Pix(slide)}$ is the total number of pixels located within mapped landslides in the study area, and $N_{Pix(total)}$ corresponds to the total number of pixels in the entire study region. The conditional probability ($Cond_P$) is defined as the ratio between the number of pixels belonging to a specific factor class that fall within landslide areas and the total number of pixels of that same factor class across the entire study area (Van Westen, 2002). This relationship can be expressed as shown in Equation (3-10):

$$Cond_P = P\left\{\frac{S}{B}\right\} = \frac{P\{S \cap B\}}{P\{B\}} = \frac{N_{Pix}\{S \cap B\}}{N_{Pix}\{B\}} \quad (3\text{-}10)$$

where $Cond_P$ denotes the conditional probability of landslide occurrence S within a specific parameter class B; $N_{Pix}\{S \cap B\}$ represents the total number of pixels belonging to class B that are located within mapped landslides; and $N_{Pix}\{B\}$ corresponds to the total number of pixels of that same factor class B across the entire study area. This method subsequently calculates weights for each predictive causative factor (B) by evaluating their statistical association with the presence or absence of landslides in the study region by Equation (3-11) and Equation (3-12) (Bonham-Carter, 1994; Mohammady et al., 2012):

$$W_i^+ = \ln\left(\frac{P\left\{\frac{B_i}{S}\right\}}{\left\{\frac{B_i}{\bar{S}}\right\}}\right) \quad (3\text{-}11)$$

$$W_i^- = \ln\left(\frac{P\left\{\frac{\bar{B}_i}{S}\right\}}{\left\{\frac{\bar{B}_i}{\bar{S}}\right\}}\right) \quad (3\text{-}12)$$

where, P represents probability Bi indicates the presence of a potential landslide conditioning factor, whereas $\bar{B}_i$ denotes its absence. Similarly, S refers to the presence of a landslide, and $\bar{S}$ represents the absence of a landslide. The term W_i^+corresponds to the positive weight, indicating that the predictive factor is associated with landslide occurrence. Conversely, W_i^-denotes the negative weight, reflecting the absence of the predictive factor in relation to landslide occurrence. Figure 3-7 illustrates an LSM, obtained by weight of evidence method.

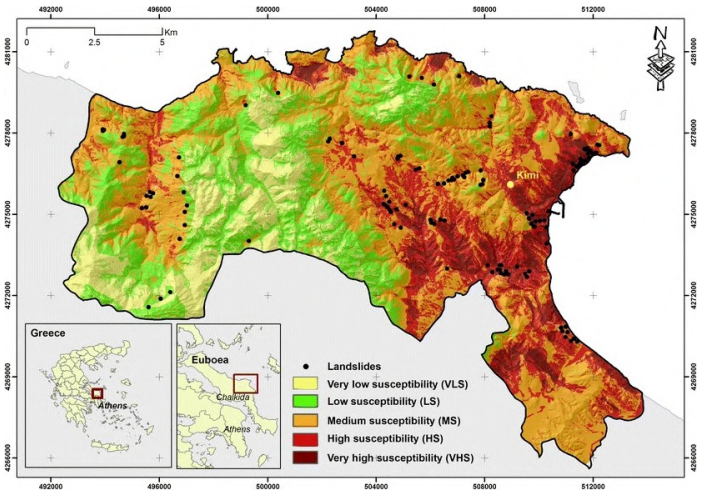

Figure 3-7 Example of an LSM obtained by applying weight of evidence method for Euboea Island, Greece (Ilia and Tsangaratos, 2015).

3.5.1.3 Information Value method

The Information Value (IV) method represents another bivariate statistical approach in which the weight assigned to each factor class is derived from the density of landslides associated with that class. This technique has been widely applied in spatial landslide prediction and hazard zonation studies (Balasubramani and Kumaraswamy, 2013; Lin and Tung, 2004; Mengistu et al., 2019; Yalcin, 2008; Zêzere et al., 2004). In this method, the calculated information values of different causative factor classes are used to delineate areas with varying probabilities of landslide occurrence, thereby supporting susceptibility mapping. The IV for each class is determined based on the presence or absence of that class within previously mapped landslides. To compute the class weights, the landslide inventory map is overlaid with each causative factor map, allowing the estimation of landslide density within individual subclasses (Mengistu et al., 2019). According to Yin and Yan (1990), a positive information value indicates a strong association between a specific factor class and landslide occurrence. Van Westen et al. (1997) defined the class weight as the natural logarithm of the ratio between the landslide density within a given factor class and the overall landslide density across the entire study area. For this reason, the IV method is also referred to as the Landslide Index (LI) method.

The IV can be calculated using Equations (3-13) to (3-16), as proposed by Yin and Yan (1990):

$$CP = \frac{N_{Pix}\{S \cap Bi\}}{N_{Pix}\{Bi\}} \tag{3-13}$$

$$PP = \frac{N_{Pix}\{TS\}}{N_{Pix}\{A\}} \tag{3-14}$$

$$WBi = \frac{CP}{PP} \tag{3-15}$$

$$IV = \log WBi \tag{3-16}$$

where CP and PP denote the conditional probability and prior probability, respectively; WBi represents the weight assigned to a specific factor class; and IV refers to the IV. Furthermore, $N_{Pix}\{S \cap B_i\}$ indicates the number of landslide pixels within factor class Bi, $N_{Pix}\{Bi\}$ is the total number of pixels belonging to that factor class; $N_{Pix}\{TS\}$ represents the total number of landslide pixels across the entire study area; and $N_{Pix}\{A\}$ corresponds to the total number of pixels within the study region.

Once the IVs are calculated, the corresponding IV weights are assigned to each factor class to generate weighted causative factor maps. These maps are

subsequently processed within a GIS environment, where the LSI for each pixel is computed using a raster calculator (Equation (3-17)). Equation (3-17) is the resulting LSI, which serves as the basis for producing the final LSM (Mengistu et al., 2019):

$$LSI = \sum IVB \tag{3-17}$$

where, LSI is the landslide susceptibility index and $\Sigma\, IVB$ is the sum total of IVs for all causative factors. Figure 3-8 illustrates an LSM obtained by IV method.

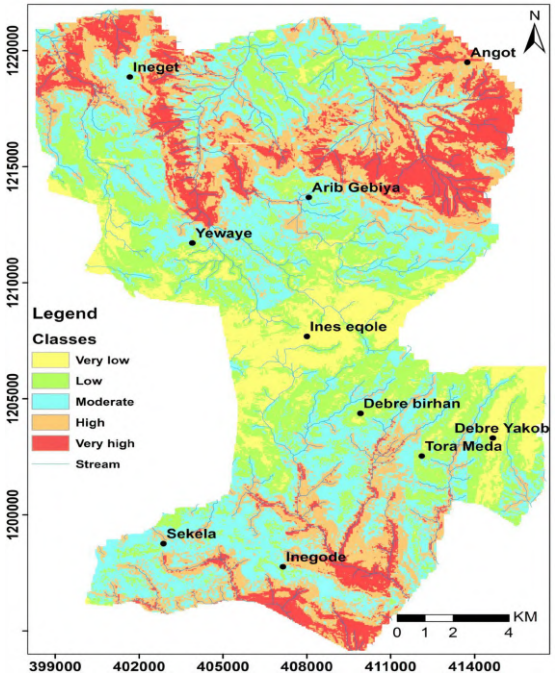

Figure 3-8 LSM using IV method in for Goncha Siso Eneses, Ethiopia (Wubalem and Meten, 2020).

3.5.1.4 Logistic Regression method

Among the range of multivariate statistical techniques, Logistic Regression (LR) remains one of the most extensively applied approaches for spatial modeling of landslide susceptibility (Schicker and Moon, 2012; Wu et al., 2015). This technique is particularly suitable for modeling dichotomous outcome variables, such as the presence or absence of landslides, by incorporating both categorical and continuous predictor variables (Goetz et al., 2015; Steger et al., 2016; Xing et al., 2021). Within this framework, the probability of landslide occurrence is estimated through logistic regression analysis. The statistical relationship between landslide occurrence and its controlling factors can be formally expressed by Equation (3-18):

$$P = \frac{1}{1 + e^{-z}} \tag{3-18}$$

where P is the estimated probability of a landslide occurrence, ranging from 0 to 1 on a 'S shaped' curve. The term z identifies a linear combination. The LR utilizes fitting of an Equation (3-19) to the data set:

$$z = b_0 + b_1 x_1 + b_2 x_2 + \cdots + b_n x_n \tag{3-19}$$

where, b_0 denotes the model intercept, bi (i = 0, 1, 2, …, n) represent the regression coefficients associated with each predictor variable, and x_i (i = 0, 1, 2, …, n) correspond to the independent variables included in the model. LR can be employed in cases where predictor variables are continuous, categorical, or a combination of both, which constitutes one of its principal advantages. Nevertheless, this method does not explicitly quantify the relative contribution of individual classes to landslide occurrence. For the implementation of logistic regression, the dependent variable must be dichotomous in nature, such as yes or no, 0 or 1, or absence or presence (Chen and Wang, 2007; Lee, 2015).

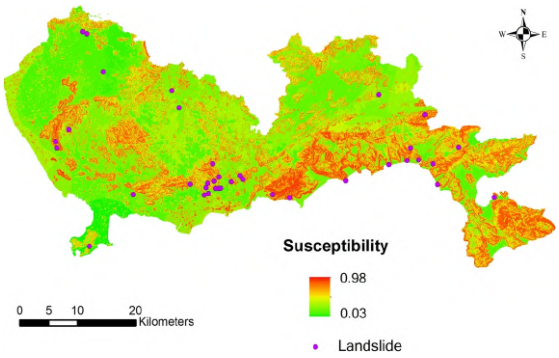

Figure 3-9 LSM employing logistic regression method for Shenzhen, China (Xing et al., 2021).

3.5.1.5 Discriminant method

Discriminant analysis is widely applied in landslide susceptibility assessment and hazard zonation studies. It represents a multivariate statistical approach in which the dependent variable is treated as categorical rather than continuous (Gorsevski et al. 2000). This method enables the identification of the maximum separation between landslide and non-landslide groups based on the set of causative factors (independent variables). Consequently, it provides a foundation for assigning relative weights to these conditioning factors (Lee et al., 2008; Pardeshi et al., 2013).

Using this approach, slope units can be classified into landslide-affected and landslide-free categories. Moreover, the relative importance of each predictor variable can be quantified through the Standardized Discriminant Function Coefficient, which expresses the contribution of each variable within the discriminant function used to predict potential slope instability. Variables associated with higher standardized coefficients exhibit stronger relationships with the presence or absence of landslides (Guzzetti et al., 2005b; Pardeshi et al., 2013).

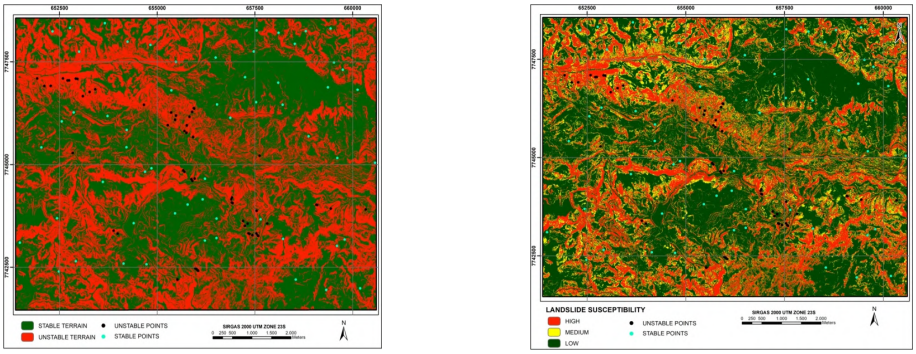

(a) (b)

Figure 3-10 Maps for Minas Gerais, Brazil indicating (a) Stable and unstable terrains (b) LSM using discriminant method (Eiras et al., 2021).

3.5.2 Probabilistic approach

In order to evaluate landslide susceptibility, the degree of relationship between the past landslide distribution and the causative factors is converted to a value which is based on a probability distribution function. Probabilistic approach helps in prediction of spatial and temporal landslide distribution probability in the given area (Guzzetti et al., 2005b; Lari et al., 2014). The approach utilizes the comparison of spatial landslide distribution with the considered causative factors (explanatory variables) in a framework of probabilistic theory (Lari et al., 2014; Straub and Schubert, 2008).

A study by Salciarini et al. (2016) performed a probabilistic analysis of slope stability under projected climate conditions using the PG_TRIGRS model. The analysis incorporated statistically downscaled rainfall projections derived from multiple GCM scenarios and time horizons to evaluate the impact of climate change on landslide activity.

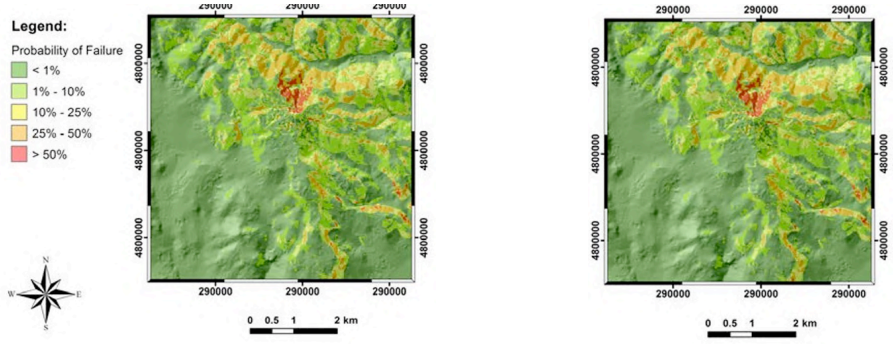

(a) (b)

Figure 3-11 Map of probability of failure (Pof) for: (a) Rainfall intensity I=1.01×10e−6 m/s (current scenario) and (b) Rainfall intensity I=1.77×10e−6 m/s (future scenario) (Salciarini et al., 2016).

Figure 3-12a-d presents another study in which the LSMs derived from the factor of safety analysis and the probabilistic approach, evaluated under three different coefficients of variation (COVs).

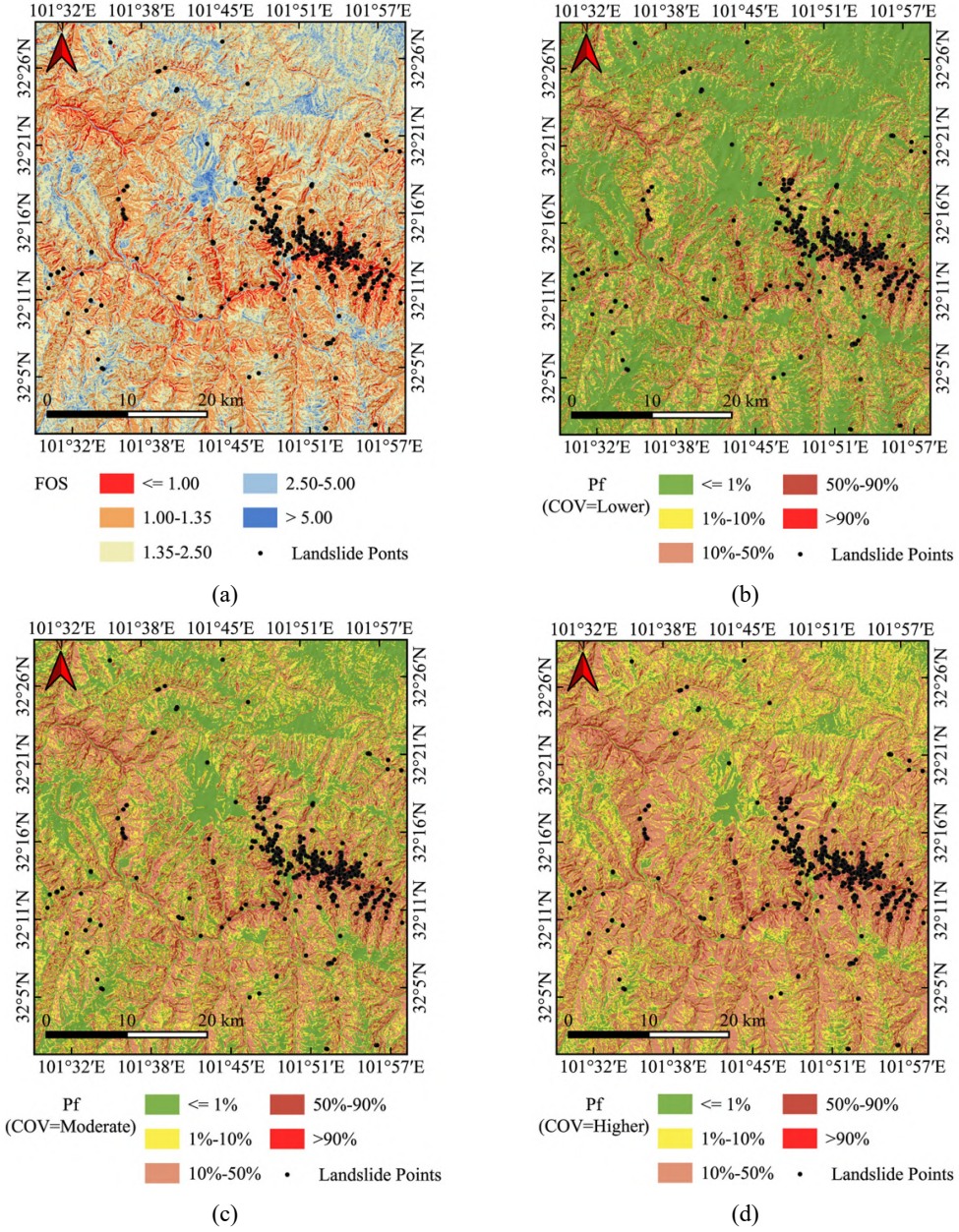

Figure 3-12 The LSMs of Maerkang, China: (a) Factor of Safety (FOS), (b) P_f with lower COV, (c) P_f with moderate COV, and (d) P_f with higher COV (Ji et al., 2025).

3.5.3 Deterministic approach

The deterministic approach to landslide hazard assessment is grounded in mechanical principles governing slope stability. These methods encompass empirical approaches (Liu and Chen, 2007; Raghuvanshi, 2019), kinematic analyses (Karaman et al., 2013 ; ZainAlabideen and Helal, 2016), static infinite slope models (Dietrich et al., 1995; Pack et al., 1998), dynamic infinite slope models (Simoni et al., 2008), as well as two-dimensional (Sharma et al., 1995) and three-dimensional limit equilibrium and numerical modeling techniques (Gitirana Jr. et al., 2012; Stead et al., 2006; Tang et al., 2016).

Deterministic methods typically consider key controlling factors such as slope geometry, discontinuity properties and their orientation relative to the slope, groundwater conditions, and surface drainage characteristics (Bednarik and Kralovičová, 2024). Additional triggering or contributing factors include rainfall, seismic activity, and anthropogenic influences (Dahal et al., 2006; Wang and Niu, 2009). The combined interaction of these parameters is considered responsible for slope instability and landslide occurrence. Figure 3-13 illustrates the susceptibility map using deterministic method.

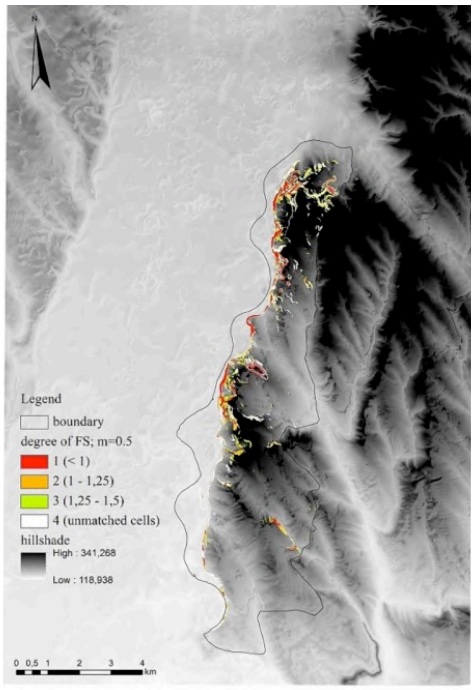

Figure 3-13 LSM calculated by a deterministic approach in Trnava region, Slovakia (Bednarik and Kralovičová, 2024).

3.6 Artificial intelligence and its application in geotechnical engineering

Artificial intelligence (AI) is concerned with the development of computational systems capable of replicating aspects of human cognitive processes. Its primary objective is to design machines that can perceive their surroundings, reason logically, learn from experience, and make data-driven decisions based on identified patterns (Russell and Norvig, 2010). AI includes Machine Learning (ML), computer vision, and robotics. Within ML, several specialized branches exist, including deep learning (DL), Bayesian methods, reinforcement learning (RL), each targeting distinct dimensions of intelligent behavior (Figure 3-14).

ML constitutes a core component of intelligent system design, focusing on the development of algorithms and statistical models that enable systems to improve task performance through exposure to training data. DL, a subset of ML,

emphasizes the construction and training of artificial neural networks inspired by the structure and operation of the human brain. By employing multiple interconnected layers of neurons, DL models can automatically extract hierarchical feature representations, allowing the handling of increasingly complex tasks through progressive abstraction.

RL investigates how autonomous agents learn optimal behaviors through iterative interaction with an environment. In this framework, agents refine their decision-making strategies over time by responding to feedback in the form of rewards or penalties.

Bayesian machine learning methods are widely employed to explicitly account for both aleatoric and epistemic uncertainties in modeling and decision-making processes. In geotechnical engineering contexts, such uncertainties may arise from material variability, spatial heterogeneity, parameter estimation errors, numerical model limitations, as well as measurement and data quality issues (Girolami et al., 2021; Kennedy and O'Hagan, 2001; MacKay, 2003). Figure 3-14 Presents AI subfields.

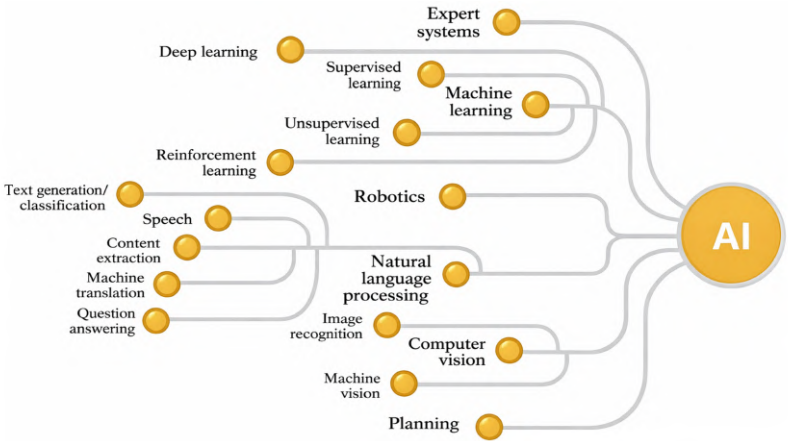

Figure 3-14 Map of AI sub-fields (Sheil et al., 2026).

The use of AI in geotechnical engineering has expanded significantly in recent years. These applications can be broadly categorized into: (i) inverse analysis, such as the estimation of geotechnical parameters from field measurements; (ii) prediction of material behavior, for example during pile installation; (iii) prediction of structural performance, such as tunnel boring machine (TBM) control; (iv) enhancement of deterministic modeling approaches, including improvements to constitutive models; and (v) landslide susceptibility mapping. While the first four categories are briefly introduced for completeness, the primary emphasis of this study is on landslide susceptibility mapping, which is discussed in greater detail in the following sections.

ML techniques have been extensively adopted in geotechnical engineering for data-driven ground modeling, supporting foundation design and optimizing

sampling strategies for site investigation programs (Hu et al., 2021; Yoshida et al., 2022; Zhao and Wang, 2019). These data-driven ground models are typically developed using site investigation data, including Cone Penetration Test (CPT) and Dynamic Penetration Test (DPT) measurements. In general, two primary predictive tasks are involved: identification of soil stratigraphy and spatial prediction or interpolation of geotechnical properties.

A variety of ML techniques have been applied to the identification of soil stratigraphy and the detection of layer boundaries. These approaches include Gaussian Process Regression (GPR), which is mathematically equivalent to kriging (Li et al., 2016), Bayesian model class selection (Wang et al., 2013), changepoint detection methods (Ching et al., 2015; Suryasentana et al., 2023a), Bayesian compressive sampling (Wang et al., 2020), and random field modeling approaches (Gong et al., 2020). Additional techniques involve lasso-based regression (Shuku et al., 2020) and clustering algorithms (Zhao and Wang, 2020). More recently, DL methods have also been introduced for this purpose (Zhou et al., 2024). Representative examples of soil layer boundary identification using DPT and CPT data are illustrated in Figure 3-15.

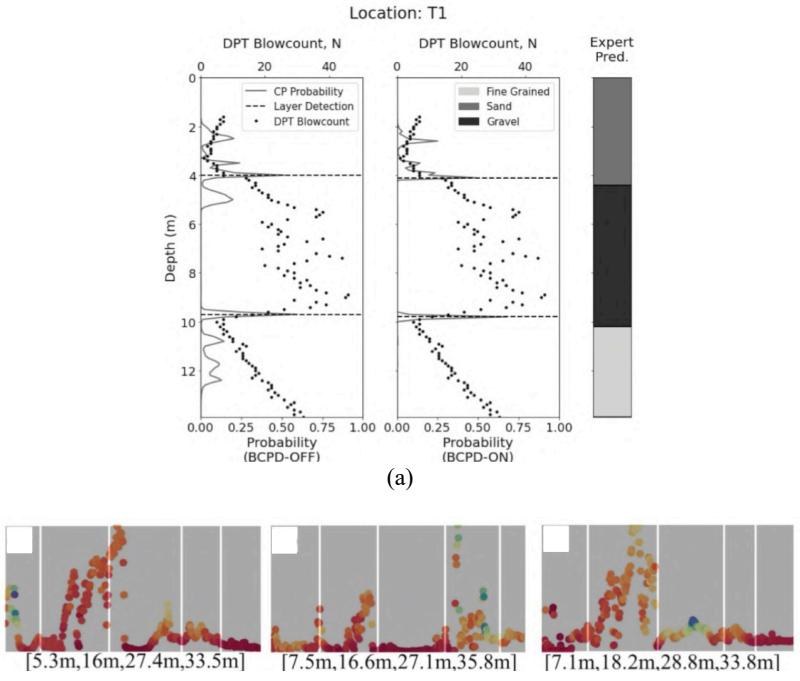

Figure 3-15 Soil layer boundaries predictions employing (a) DPT data (Suryasentana et al. 2023b), and (b) CPT data (Zhou et al. 2024).

Another important application of AI in geotechnical engineering is predictive modelling of soil behaviour. In conventional constitutive modelling, soil response is described through mathematical formulations defined by a set of parameters and state variables. However, attempts to represent increasingly complex soil

behaviours have resulted in highly sophisticated constitutive models with numerous material parameters. For instance, the SANISAND model (Dafalias and Manzari, 2004) incorporates multiple fabric tensors and internal variables. While such models are capable of reproducing complex soil responses, they also increase calibration difficulty and reduce model interpretability.

With the growing availability of AI tools during the early 1990s, researchers began investigating AI techniques, particularly Artificial Neural Networks (ANNs), as alternative approaches for modelling material behaviour (e.g., Ghaboussi et al., 1991). Early studies by Ellis et al. (1992) and Ghaboussi et al. (1990) introduced Neural Network Constitutive Models (NNCMs) for soils. Following these pioneering efforts, a significant number of AI-based constitutive models were developed (Penumadu and Zhao, 1999). The development of intelligent constitutive models later expanded beyond neural networks to include other AI techniques such as evolutionary regression. Subsequently, research efforts focused on the numerical implementation of these AI-based material models within computational frameworks (Hashash et al., 2004; Javadi and Rezania, 2009).

Despite their promise, the performance of early purely data-driven AI-based constitutive models was often inconsistent. These limitations were primarily related to poor interpretability and the large datasets required for effective training. Moreover, such models frequently demonstrated weak generalisation capabilities, with predictive accuracy deteriorating when applied outside the range of the training data.

However, the recent resurgence of AI in geotechnical engineering has renewed interest in the development of intelligent constitutive models. In particular, Physics-Informed Machine Learning (PIML) approaches have emerged as a major research direction (Masi et al., 2021; Masi and Stefanou, 2022). These methods integrate prior physical knowledge, such as empirical relationships or governing physical laws, with machine learning techniques to constrain predictions within physically realistic limits (Cuomo et al., 2022). Although such hybrid approaches significantly improve model generalisation, they still require large, high-quality datasets to achieve predictive performance comparable to traditional constitute models.

These challenges have encouraged the development of interpretable machine learning approaches designed to operate effectively with sparse geotechnical datasets (Zhang et al., 2023c). For example, Zhang et al. (2025) introduced a Prior information-based Neural network (PiNet) that incorporates three theoretical frameworks, namely incremental nonlinearity, hyperelasticity, and elastoplasticity (Figure 3-16). The proposed PiNet models were subsequently applied to simulate real soil behaviour using a multi-fidelity framework that maximises the use of limited high-fidelity data.

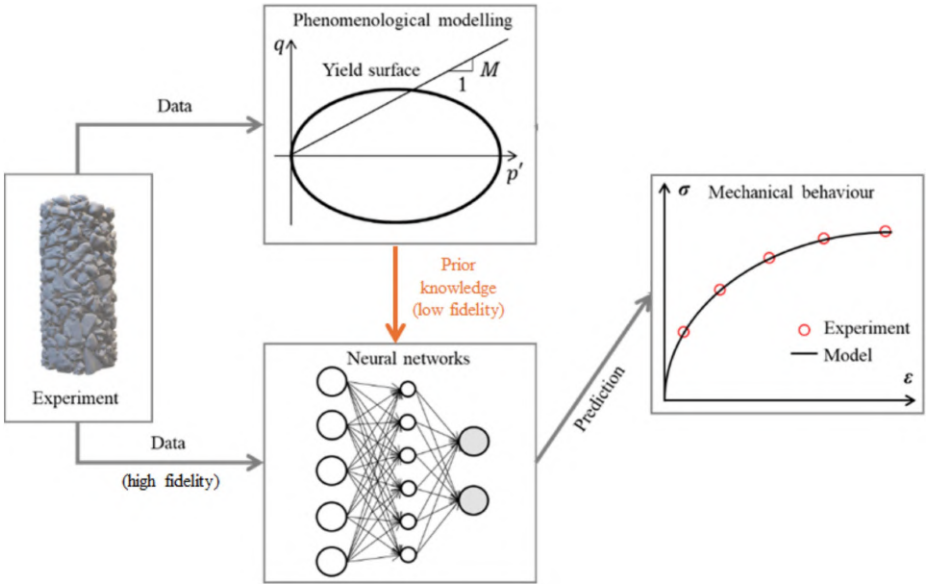

Figure 3-16 Multi-fidelity modelling framework proposed by Zhang et al. (2023c), integrating a data-driven neural network with traditional phenomenological constitutive models.

Geotechnical design and construction are increasingly incorporating AI to address the limitations of traditional methods based on manual calculations, empirical correlations, and simplified models. In foundation engineering, ML techniques have been used to predict the bearing capacity (Lawal and Kwon, 2023) and settlement (Zhang et al., 2022b) of shallow footings. AI methods have also been applied to improve pile design, including predictions of driveability (Buckley et al., 2023), axial resistance (Alexander et al., 2024), lateral resistance (Taherkhani et al., 2023), settlements and displacements (Ge et al., 2023), and pile group behaviour (Khatti et al., 2023).

Beyond foundation engineering, AI applications in geotechnical construction are largely focused on tunnelling, particularly tunnel boring machine (TBM) performance prediction, tunnel-induced settlement estimation, geological forecasting, and cutterhead design optimization (He et al., 2025). Additional applications include tunnel-induced building damage prediction (Cao et al., 2020; Ninić et al., 2024), TBM automation (Mokhtari and Mooney, 2019), tunnel condition assessment (Zhu et al., 2020), anomaly detection (Sheil et al., 2021), tunnel profile measurement (Xue and Zhang, 2019), resilience assessment (Khetwal et al., 2019), structural defect identification (Ding et al., 2019), tunnel face stability (Hayashi et al., 2019), rockburst prediction (Liu and Hou, 2019), and intelligent building information modelling (Zhao et al., 2019). Figure 3-17 presents real-time control of TBM face pressure for three different scenario, scenario (1) (black line) is the baseline case with unchanged face support pressure leading to severe damage, scenario (2) (green line) increases the face pressure early at step 26 to 180 kPa resulting in reduced settlements and moderate damage, and scenario (3) (blue line)

applies a delayed pressure increase at step 29, which slightly reduces settlement but still leads to severe damage.

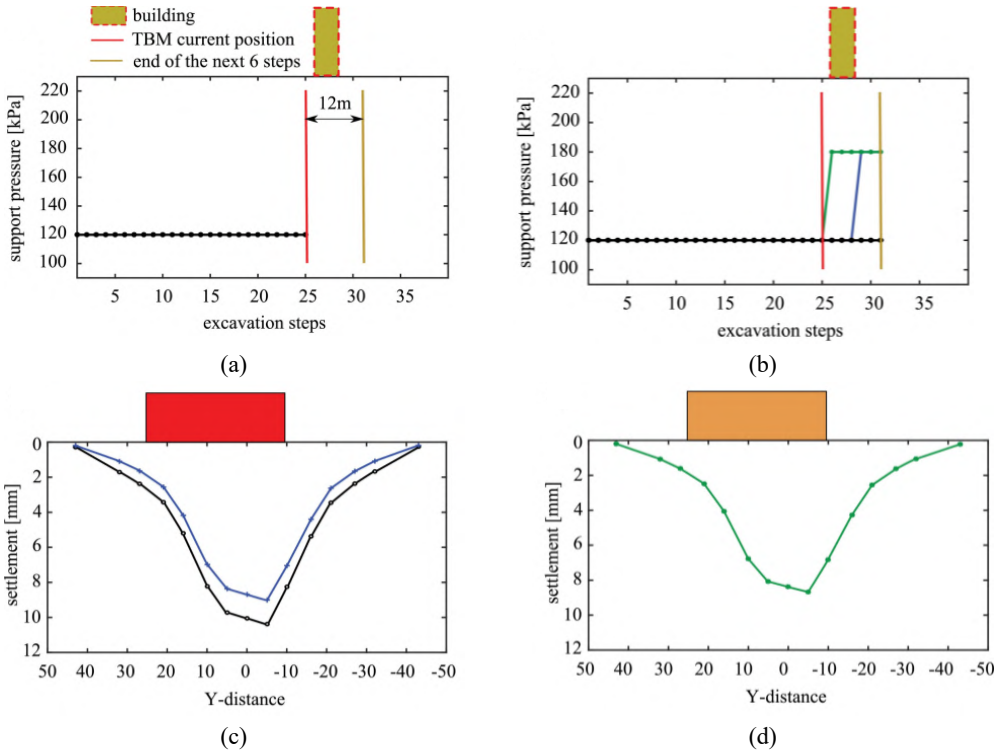

Figure 3-17 Real-time control of TBM face pressure to minimize damage to a nearby building: (a) Recorded face support pressure data up to time step 25; (b) Three potential pressure adjustment scenarios; (c) Resulting settlement trough and building damage categories for scenarios (1) and (2); (d) Resulting settlement trough and building damage categories for scenario (3) (Cao et al., 2020).

AI can also support interdisciplinary applications by enabling advanced numerical models to be used in regional-scale planning (Charles et al., 2023). This is typically achieved through surrogate models (Previtali et al., 2022; Guardiani et al., 2022), which approximate the results of complex simulations at much lower computational cost, for example in rockfall risk mitigation (Figure 3-18).

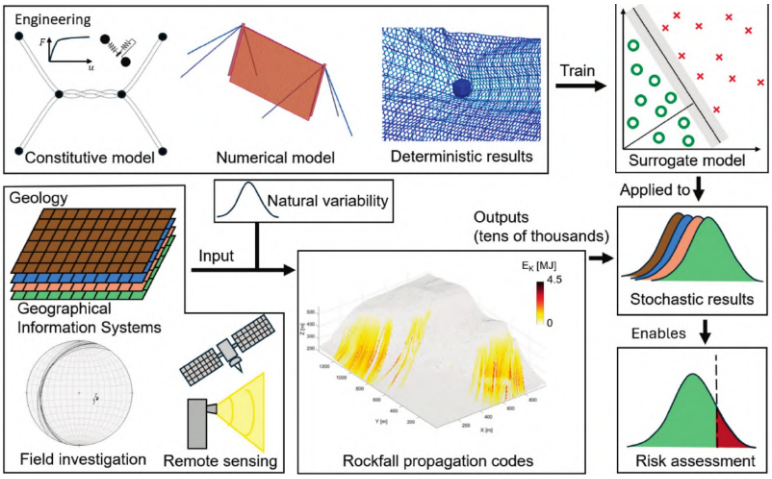

Figure 3-18 Flowchart illustrating the use of AI-based surrogate models to combine the accuracy of advanced numerical simulations with the computational efficiency required for large-scale planning (Previtali et al., 2022).

Moreover, AI has been widely applied in slope stability design, particularly for optimising failure mechanisms and estimating factors of safety (Aminpour et al., 2023; Mahmoodzadeh et al., 2022), predicting failure timing (Zhang et al., 2022a), employing InSAR images to identify early deformation signals (Bayaraa et al., 2023), and ML-assisted stochastic analyses (Zeng et al., 2022). Another recent application of ML in landslide studies is the generation of landslide susceptibility maps, which will be discussed in detail in the following sections.

3.7 ML application in LSMs

A key application of AI in geohazard studies is the production of LSMs, which serve as valuable references for planners and policymakers in development planning. Landslide susceptibility reflects the probability of landslides occurring within a given area. Numerous machine learning-based approaches have also been employed in this field (Ado et al., 2026; Chen, 2025; Janizadeh et al., 2023; Lee et al., 2025; Ren et al., 2024), highlighting the renewed interest of researchers in leveraging ML methods to capture the complex relationships between landslides and their conditioning factors.

Implementing these methods requires several key steps, irrespective of the specific algorithm used. First, the necessary data must be collected, cleaned, and processed. Next, ML algorithms are applied to model the relationships between conditioning factors and landslide occurrence. Finally, after algorithm optimization, their predictive performance must be rigorously evaluated. The required steps and data for applying machine learning to landslide susceptibility mapping are described in the following section.

3.7.1 Defining the area of interest

The first step is to define the study area of interest by establishing its spatial boundaries. It is essential to ensure that sufficient data are available within the selected area, including records of past landslide occurrences as well as relevant landslide conditioning factors, which will be described in subsequent sections.

3.7.2 Landslide inventory

The landslide inventory is a fundamental component of landslide susceptibility mapping, as its accuracy directly affects the quality of the samples used to train and test machine learning models. Typically, a landslide inventory is stored as a dataset (e.g., CSV format) containing information such as the location, date, causes, magnitude, and potential damage associated with landslide events. These inventories can be developed from multiple sources, including historical records, satellite imagery, Google Earth interpretation, and aerial photograph analysis.

3.7.2.1 Field survey

Field surveys are considered the most accurate approach for generating landslide inventories, as they involve detailed investigation of affected areas to identify and measure individual slope failures (Bornaetxea et al., 2018; Chen et al., 2014). They are also frequently used to complement or validate inventories derived from other sources, such as satellite imagery, Google Earth interpretation, and aerial photographs. However, field investigations are often time-consuming and labour-intensive, and some landslides may be physically inaccessible, making surveys costly or impractical.

3.7.2.2 Satellite image

Advances in satellite technology over recent decades have significantly increased the number of satellites and created extensive networks capable of capturing high-resolution images of the Earth's surface. Landslide inventories can therefore be developed by analysing and comparing satellite images acquired at different times (König et al., 2019). This approach effectively addresses the accessibility limitations associated with field surveys. However, it can still be relatively expensive, and cloud cover may sometimes interfere with the acquisition and quality of satellite imagery.

3.7.2.3 Google earth interpretation

To reduce the cost and technical barriers associated with satellite imagery, Google Earth interpretation has become increasingly popular in recent landslide susceptibility studies (Broeckx et al., 2018; Conoscenti et al., 2016), mainly due to

its free access and ease of use. However, similar to satellite imagery, its effectiveness can be limited by cloud cover, which may reduce image quality and hinder accurate interpretation.

3.7.2.4 Aerial photograph interpretation

Aerial photograph interpretation is considered one of the most economical and versatile remote sensing methods (Li et al., 2013) and has been widely used for landslide detection and susceptibility assessment (Chen et al., 2025). With the support of drones, this approach can effectively capture landslide information in areas with limited accessibility. Moreover, unlike many satellite images, aerial photography can provide near real-time observations, making it suitable for certain applications. However, its use can be constrained by the time required for data collection as well as the need for specialised equipment and trained personnel.

3.7.3 Landslide conditioning factors

Identifying appropriate landslide conditioning factors (LCFs) is a fundamental step in developing reliable landslide prediction models and remains a major challenge in landslide susceptibility assessment (Zhang et al., 2022c). The difficulty largely arises from the complex nature of landslide processes. In fact, as many as 596 variables potentially influencing landslide occurrence have been reported in the literature (Reichenbach et al., 2018). Incorporating all of these variables in practical engineering applications is unrealistic because it requires considerable time and computational effort. Consequently, earlier studies (Janizadeh et al, 2023; Nhu et al., 2020; Zhou et al., 2021) have focused on a limited number of representative categories that play dominant roles in landslide formation. These commonly include topographic, hydrological, geological, land cover, natural, and anthropogenic factors, together with their most frequently used sub-indicators.

Rainfall is widely regarded as the principal triggering factor for landslides, especially in mountainous environments (Lee et al., 2014). Because long-term precipitation records are generally easy to obtain, mean annual precipitation is frequently incorporated into landslide susceptibility modelling (Yang et al., 2026; Shi et al.,2026; Zhou et al.,2025). Temperature is another environmental variable that may influence landslide activity (Insana et al., 2021). Variations in temperature can alter soil moisture conditions by affecting evapotranspiration processes and the resulting soil moisture deficit (Dixon and Brook, 2007). Increasing temperatures may also enhance atmospheric moisture content and potentially intensify precipitation events. In mountainous areas, rising temperatures can contribute to permafrost degradation, which reduces ground stability and increases the likelihood of slope failure (Barla and Barla, 2001). To the best of the author’s knowledge,

temperature has rarely, if ever, been explicitly considered in LSMs, with elevation commonly adopted as a proxy due to its accessibility.

Land-cover conditions also influence landslide development. Vegetation can enhance slope stability by extracting water from the soil through root uptake. As a result, vegetated slopes are typically drier and exhibit significantly higher matric suction compared with bare or fallow slopes, with reported average reductions in moisture content of approximately 12.84% (Gonzalez-Ollauri and Mickovski, 2017). The magnitude of this effect varies depending on vegetation type. For this reason, the normalized difference vegetation index (NDVI) is widely adopted as an indicator of vegetation cover in landslide studies. In contrast, certain anthropogenic land-cover changes may adversely affect slope stability (Promper et al., 2014), making land-use classification another relevant variable.

Hydrological conditions are also critical because variations in soil moisture strongly influence slope stability. Several indices are commonly used to represent hydrological characteristics, including the aridity index, the topographic wetness index, and the moisture index. In addition, the proximity of slopes to river channels can significantly affect landslide occurrence due to the combined effects of long-term erosion and soil weakening caused by water infiltration (Wang et al., 2017).

Using GIS-based tools, various terrain-related variables can be rapidly derived from digital elevation models (DEM). Parameters such as slope, aspect, profile curvature, plan curvature, and topographic wetness index (TWI) can be automatically generated through built-in spatial analysis functions. In addition, proximity-related variables, including distance to rivers and distance to roads, can be calculated efficiently using spatial analysis operations such as the near-distance function based on the geographic location of the corresponding features.

At the final stage, all LCFs must be collected and imported into a GIS environment. It is essential to ensure that all datasets share a consistent coordinate reference system (CRS) to enable accurate spatial analysis. The data are then extracted as CSV files for further processing and inspection.

3.7.4 Data processing

After extracting pixel-based data and generating the corresponding CSV file, the dataset must be further processed. This involves verifying all values and addressing any missing data to ensure completeness. Given the typically large size of such datasets, the identification and treatment of missing values should be carried out using programming tools such as MATLAB or Python to ensure both efficiency and accuracy. The number of columns corresponds to the selected LCFs, along with an additional column representing landslide occurrence. A value of 1 is assigned to pixels at which landslide initiation occurs, whereas a value of 0 is assigned to all

other pixels. The number of rows is determined based on the sampling ratio, which is discussed in the following section.

3.7.4.1 Sampling ratio

The proportion of positive (landslide events) and negative (non-landslide events) samples used during model training is another factor that can significantly influence modelling performance. In landslide susceptibility studies, researchers frequently adopt a balanced sampling strategy in which the number of landslide and non-landslide samples is equal (0.5:0.5) (Behnia and Blais-Stevens, 2017; Janizadeh et al., 2023; Wu et al., 2020). However, the optimal sampling proportion may vary depending on the characteristics of the dataset and the type of machine learning algorithm employed. Adjusting this ratio appropriately can lead to improvements in predictive accuracy. Yang et al. (2023) investigated the influence of sampling proportions in machine learning-based landslide susceptibility assessment using a Bayesian optimization approach. Their results showed that optimizing the sampling ratio, which was 1:1.55 (positive to negative), improved the performance of all tested models. The most notable improvements were observed for the random forest (RF) and gradient boosting decision tree (GBDT) models, each showing an accuracy increase of approximately 1.3%.

3.7.5 Training to testing ratio

After data cleaning and preprocessing, the prepared dataset is typically extracted and randomly divided into two subsets according to a predefined proportion: a training dataset used to build the model and a testing dataset used to evaluate its performance. The selection of the training–testing split can substantially affect the predictive capability of the resulting model. Therefore, choosing an appropriate ratio between these two subsets is important for improving modelling performance.

Previous studies have investigated the influence of different training–testing ratios on landslide susceptibility modelling. For example, Sahin et al. (2018) examined the impact of nine different ratios ranging from 0.1:0.9 to 0.9:0.1. Model performance was evaluated using several indicators, including root-mean-square error (RMSE), overall accuracy (OA), the Kappa coefficient (KC), success rate curves, receiver operating characteristic (ROC) curves, and the corresponding area under the curve (AUC). Their results indicated that the 0.9:0.1 ratio produced the highest RMSE, whereas the 0.7:0.3 split resulted in the lowest error. Similarly, Saha et al. (2021) also identified 0.7:0.3 as the optimal ratio for landslide data from the East Sikkim Himalayan region in India.

However, the optimal ratio is not universal and may vary depending on the characteristics of the dataset, since different subsets may contain varying amounts of information. For instance, Xu et al. (2024) reported that a 0.8:0.2 training–testing

ratio resulted in better model performance, showing that the most suitable split can differ across studies and datasets.

3.7.6 Machine learning algorithms

To capture the complex non-linear relationships between landslide occurrence and conditioning factors, a wide range of ML approaches have been increasingly applied in landslide susceptibility assessment. In addition to conventional algorithms such as logistic regression (LR), support vector machines (SVM), and random forest (RF), recent studies have explored hybrid and ensemble strategies that combine multiple machine learning techniques to enhance predictive performance.

Furthermore, the rapid growth in data availability has encouraged the adoption of more advanced approaches, including deep learning and transfer learning, which are gradually gaining attention in this domain. Most of these models fall within the category of supervised learning, where model performance strongly depends on the quality and reliability of labeled training data (Chang et al., 2020).

3.7.6.1 Artificial neural network

Artificial neural networks (ANNs) are among the most widely used machine learning techniques and are conceptually inspired by the functioning of the human brain and biological nervous systems. An ANN typically consists of three main components: an input layer, one or more hidden layers, and an output layer (Figure 3-19). Each layer is composed of interconnected units, commonly referred to as neurons, which contain adjustable parameters that are optimized during the training process to map inputs to outputs. Due to their flexible structure and strong capability in capturing complex non-linear relationships, ANNs can learn patterns directly from data without requiring explicit prior assumptions about the underlying problem. This characteristic has contributed to their widespread application in landslide susceptibility modelling (Behera et al., 2026; Harmouzi et al., 2019). However, a major limitation of ANNs is their reliance on large training datasets, as the high number of parameters requires substantial data to achieve reliable performance.

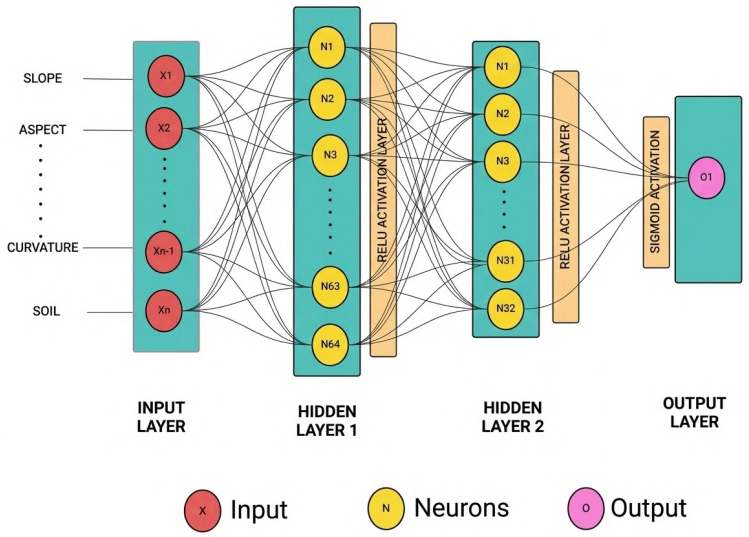

Figure 3-19 Artificial neural network architecture used for landslide susceptibility modelling (Behera et al., 2026).

3.7.6.2 Logistic regression

Logistic regression (LR) can be considered an extension of linear regression that incorporates a nonlinear activation function to constrain model outputs within the range of 0 to 1 (Figure 3-20). This transformation enables LR to handle binary classification problems, where outcomes are represented by dichotomous variables such as 0 and 1 or true and false (Menard, 1995). In the context of landslide susceptibility modelling, LR aims to establish the relationship between landslide occurrence (presence or absence) and a set of conditioning factors, including variables such as slope, elevation, and aspect (Ayalew and Yamagishi, 2005). The method typically involves fitting the dependent variable using a logistic function, as expressed in Equations (3-20) and (3-21):

$$Z = C_0 + C_1X_1 + C_2X_2 + \cdots + C_nX_n \tag{3-20}$$

$$p = \frac{1}{1 + e^{-Z}} \tag{3-21}$$

where Z is the logistic regression for landslide probability, C_0 is the intercept, and C_1, C_2, C_3… are coefficients, which measure the contribution of independent factors (X_1, X_2, X_3), and is the probability of landslide.

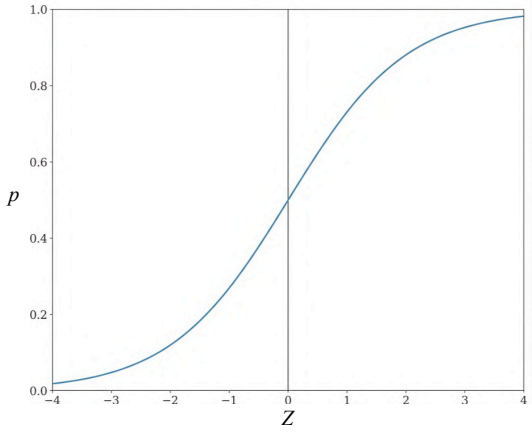

Figure 3-20 Sigmoid function (Næs et al., 1993)

3.7.6.3 Support vector machines (SVM)

Support vector machine (SVM) is a supervised learning algorithm that can be applied to both classification and regression tasks and has been used in LSM (El Brahimi et al., 2026; Chen et al.,2016). It was originally introduced by Vapnik (1995) based on statistical learning theory and the principle of structural risk minimization. To address nonlinearity, SVM employs kernel functions, such as Gaussian and polynomial kernels, to implicitly project input data into a higher-dimensional feature space. Within this transformed space, the algorithm determines an optimal hyperplane that separates different classes by maximizing the margin between them (Abe, 2005). More specifically, the objective of SVM is not merely to classify data points, but to identify a decision boundary that maximizes the separation between classes (Figure 3-21). Given training data $\{(x_i, y_i)\}_{i=1}^{m}$, where x_i is the feature vector of conditioning factors and y_i denotes landslide presence or absence, the decision function is expressed by Equation (3-22):

$$f(x) = sign(\sum_{i=1}^{m} \alpha_i y_i K(x_i, x) + b) \quad (3\text{-}22)$$

where b is the parameters of the hyper-plane, k is the kernel, and $sign$ denotes the sign function.

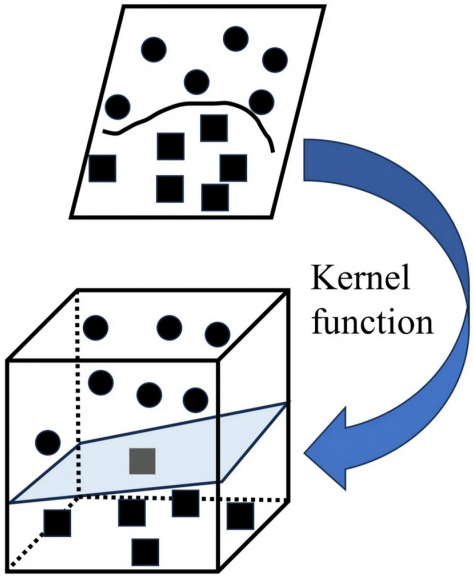

Figure 3-21 SVM optimal separating (The dots and squares indicate the two types of samples) (Huang and Zhao 2018).

3.7.6.4 Decision trees

Decision tree (DT) is one of the earliest and most widely used machine learning techniques, characterized by a hierarchical structure that represents decision rules in a flowchart-like form (Figure 3-22). The model is constructed by recursively partitioning the dataset, starting from the root node and selecting, at each step, the attribute that provides the highest contribution to classification accuracy (Yeon et al., 2010).

Owing to its simplicity, interpretability, and computational efficiency, as well as its flexibility in handling different types of input data, DT has been extensively applied in landslide susceptibility modelling over the past years (Thai Pham et al., 2018; Tsangaratos et al, 2016).

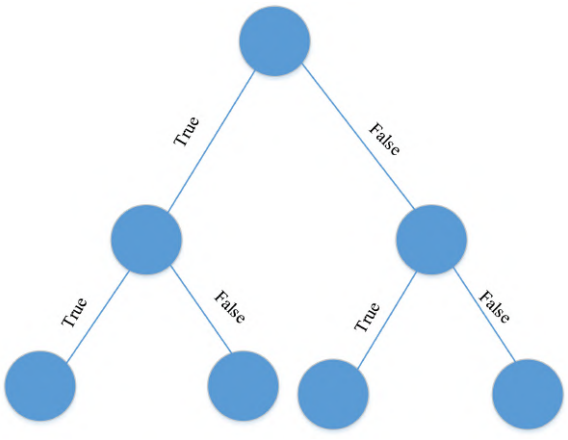

Figure 3-22 Basic decision tree architecture

3.7.6.5 Ensemble techniques

Ensemble learning was developed based on the idea that combining multiple models can lead to more accurate and robust predictions, similar to how collective decision-making can outperform individual judgments in complex problem-solving scenarios (Rokach, 2010). An ensemble model consists of several individual ML algorithms, often referred to as weak learners. Each learner produces its own prediction, and the final output is obtained by combining these predictions according to a specific aggregation rule. Ensemble learning methods are typically classified into two distinct categories: bootstrap aggregating (bagging) and boosting.

Bagging (bootstrap aggregating) is one of the most widely used approaches. It involves generating multiple models, typically DTs, using different bootstrap samples drawn from the original dataset. The final prediction is then determined by averaging or majority voting across all models. Although originally designed for classification tasks, bagging can also be extended to regression problems.

Random forest (RF) is one of the most well-known bagging-based methods, introduced by Breiman (2001) and further developed by Cutler (2005). It offers several advantages, including relatively low computational cost, ease of hyperparameter tuning, and strong performance in modelling complex nonlinear relationships. As a result, RF has been widely applied in landslide susceptibility modelling (Feng et al., 2015; Youssef et al., 2015).

During the training process (Figure 3-23), multiple decision trees are constructed as independent estimators using randomly selected subsets of the data. In addition, each tree is trained using a random subset of input features at each split. The final prediction of the RF model is obtained by aggregating the outputs of all trees, typically through majority voting. This combination of data and feature randomness introduces diversity among the individual trees, which enhances model robustness and reduces sensitivity to noise and outliers.

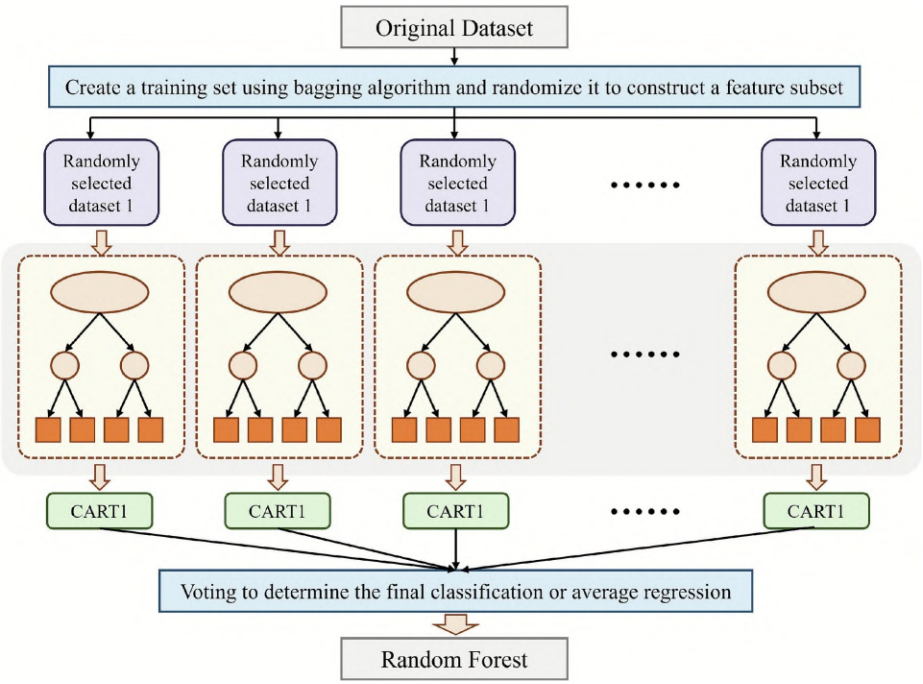

Figure 3-23 Random forest classifier algorithm description (Xu et al., 2026).

While bagging can be interpreted as a group of independent models working in parallel and combining their predictions through voting, boosting follows a sequential learning strategy in which models are trained to address the errors made by previous ones. In this sense, boosting can be viewed as a cooperative process where each learner focuses on improving specific aspects of the overall prediction.

In general, boosting methods consist of a series of weak learners, typically decision trees, which are combined to form a strong predictive model. Several tree-based boosting algorithms have been developed following this concept, including gradient boosting machine (GBM), extreme gradient boosting (XGBoost), light gradient boosting machine (LightGBM), and categorical boosting (CatBoost). Owing to their strong predictive capabilities, these approaches have attracted considerable attention in landslide susceptibility modelling (Kim et al., 2017; Sahin, 2022).

XGBoost is an advanced implementation of the gradient boosting framework and has been widely applied in classification, regression, and ranking problems (Zhang et al., 2023a). Similar to other boosting methods, XGBoost constructs multiple weak learners in a sequential manner, where each new model is trained to improve upon the errors of the previous ones. The final prediction is obtained by combining the outputs of all learners through a weighted summation (Friedman, 2001). The estimated probability of the positive class ($\hat{p}$) for a given input vector X in XGBoost binary classification is expressed as Equation (3-23)(Chen et al., 2015; Chen and Guestrin, 2016):

$$\hat{p} = \frac{1}{1 + e^{-(w^T X + b)}} \tag{3-23}$$

where w denotes the weight vector, b represents the bias term, and the superscript T indicates the transpose of the vector. The parameters w and T are estimated during the training process by minimizing a regularized objective function, defined as Equation (3-24):

$$\min_{w,b} \sum_{i=1}^{n} L\,(y_i, \hat{y}) + \Omega(f) \tag{3-24}$$

where L denotes the loss function, y_i and $\hat{y}$ represent the i-th observed and predicted values, respectively, and $\Omega(f)$ is the regularization term that penalizes model complexity. The regularization term is defined as Equation (3-25):

$$\Omega(f) = \gamma T + \frac{1}{2}\lambda \sum_{j=1}^{T} w_j^2 \tag{3-25}$$

where T represents the number of leaves in the decision trees, w_j denotes the weight associated with the j-th leaf, and γ and λ are regularization parameters controlling model complexity.

The fundamental idea of XGBoost is to iteratively reduce model bias by minimizing a predefined objective function, which includes both a loss term and a regularization component. This regularization mechanism helps control model complexity and prevents overfitting, thereby improving generalization performance. In addition, XGBoost incorporates several optimization techniques, such as parallel processing and efficient handling of missing data, which contribute to its high computational efficiency and predictive accuracy. Figure 3-24 presents the XGBoost architecture, specifically showing how multiple Classification and Regression Trees (CART) are trained sequentially, which helps to minimize residual errors and produce a final weighted output.

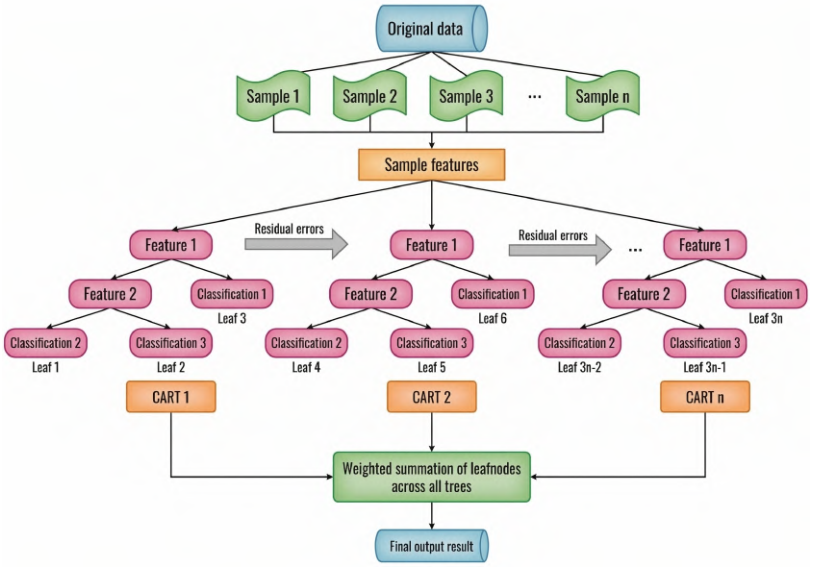

Figure 3-24 XGBoost classifier algorithm description (Lin et al., 2026).

3.7.6.6 Deep learning

With the rapid growth in data generation and availability, deep learning techniques have attracted increasing attention in recent years. Among these approaches, convolutional neural networks (CNNs) are one of the most widely used architectures (Figure 3-25). A typical CNN consists of several layers, including input, convolutional, pooling, fully connected, and output layers, which work together to automatically extract and learn hierarchical features from data.

Although CNNs were originally developed for image processing tasks, their capability to efficiently handle two-dimensional data structures has enabled their application in numerical and spatial analyses. This is particularly relevant in landslide susceptibility modelling, where DEMs can be represented as 2D arrays. For instance, Wang et al. (2021) developed a hybrid CNN–LSTM model based on object-based 2D representations derived from high-resolution DEMs, achieving a high predictive performance with an AUC value of 0.972.

In addition to 2D CNNs, one-dimensional CNN (1D-CNN) architectures have also been applied in landslide susceptibility modelling (Azarafza et al., 2021). These models have demonstrated superior predictive accuracy compared with traditional machine learning methods, such as LR and SVM, particularly when sufficient and high-quality training data are available.

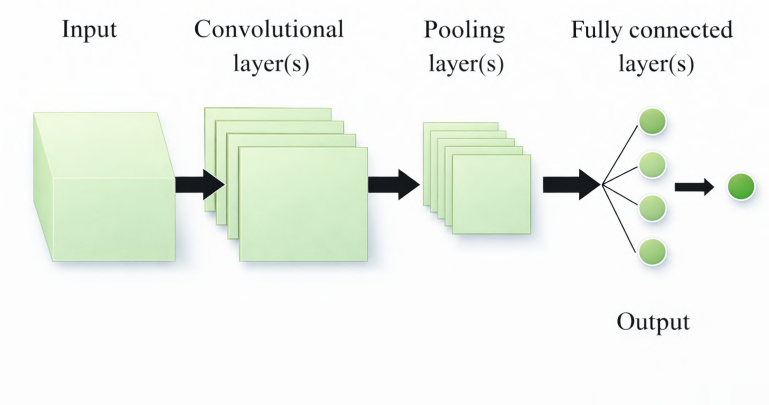

Figure 3-25 CNN architecture.

3.7.7 Multicollinearity

Multicollinearity occurs when two or more variables are linearly related, indicating that they are not statistically independent or orthogonal from one another (Alin, 2010). Some authors also refer to this relationship as collinearity or describe it as a case of ill conditioning (Chattefuee and Hadi, 2006). Multicollinearity poses challenges when constructing a model that relates the response variable y to the explanatory variables X. The multiple linear regression model between y and X is given in Equation (3-26):

$$y = X\beta + \varepsilon \tag{3-26}$$

Here, y represents the n×1 vector of response values, and X denotes the matrix of explanatory variables with dimensions $n \times (k+1)$, where the first column is a vector of ones to account for the intercept. The vector β is of size $(k+1) \times 1$, containing the regression coefficients, while ε is the $n \times 1$ error vector, assumed to have a mean of zero and a variance-covariance matrix equal to σ^2I. If the explanatory variables are mean-centered, the model in Equation (3-26) excludes the intercept term. As a result, there is no need to include a column of ones in the X matrix. In this case, the X matrix has k columns corresponding to the k centered predictors, and the coefficient vector β has k rows. The least squares estimate of β is then computed as Equation (3-27):

$$\beta = (X^T X)^{-1} X^T y \tag{3-27}$$

where, in the presence of multicollinearity, the estimated coefficients β for i=1, 2,…, k may exhibit incorrect signs, meaning they might differ from the signs of the simple correlations between the respective explanatory variables and the response

variable. However, it's also possible for the coefficient signs to appear correct despite severe multicollinearity, or to appear incorrect even when multicollinearity is minimal (Wold et al., 2001). The most significant consequence of multicollinearity is that the standard errors of the coefficients ($\sigma^2_{\beta i}$) tend to be large, indicating high sampling variability. This, in turn, undermines the reliability of the coefficient estimates and reduces their precision.

The effects of multicollinearity may provide preliminary indications of its presence. However, the most commonly applied method for detecting multicollinearity involves examining the correlation matrix of the explanatory variables. It should be noted that correlation and collinearity are not equivalent; therefore, low pairwise correlations do not necessarily imply the absence of multicollinearity. Consequently, relying solely on the correlation matrix R is insufficient.

The determinant of the correlation matrix, denoted as $\det(R)$, can also be used as a diagnostic measure, but it suffers from similar limitations, as multicollinearity may still be present even when the determinant is close to one. Furthermore, neither pairwise correlations nor $\det(R)$ provides insight into the number or structure of collinear relationships among variables. A more widely used diagnostic is the Variance Inflation Factor (VIF), defined in Equation (3-28):

$$\text{VIF}=\frac{1}{1-R_i^2} \text{ for i=1, 2, …, k} \tag{3-28}$$

where R^2 represents the coefficient of multiple determination for regressing x_i on the remaining explanatory variables. When the X matrix is standardized, the diagonal elements of $(X^T X)^{-1}$ correspond to the VIFs. The VIF quantifies how much the variance of the estimated coefficient σ_{bi} is increased due to multicollinearity, compared to what it would be if there were no multicollinearity. A higher VIF indicates a greater inflation of variance. A large VIF_i suggests that x_i is involved in some form of linear dependence, though it does not identify which specific variables are involved. Commonly, a VIF value greater than 10 is considered indicative of problematic multicollinearity (Alin, 2010).

3.7.8 Hyperparameter

Most machine learning models are capable of attaining high predictive accuracy using their default hyperparameter configurations; however, careful tuning of these parameters can further enhance model performance. Manually identifying the optimal set of hyperparameters for a given problem is impractical, as it requires an exhaustive and potentially infinite process of trial and error. Consequently, automated hyperparameter optimization techniques have been developed, and the

fundamental principles of the most widely adopted approaches in this domain are outlined below.

3.7.8.1 Grid search

Grid search is commonly considered the most straightforward and intuitive approach for hyperparameter optimization and has been extensively applied in landslide susceptibility modelling (Zhang et al., 2022c). This method systematically evaluates all possible combinations of predefined hyperparameter values in order to identify the optimal configuration. Nevertheless, such an exhaustive exploration results in high computational costs, particularly when the number of hyperparameters and their potential values increase significantly.

3.7.8.2 Random search

To mitigate the high computational demands of exhaustive searches, various random search-based algorithms have been developed. Rather than evaluating every possible combination of hyperparameters, these methods employ strategies such as Simulated Annealing, Genetic Algorithms, Gravitational Search Algorithms, and Ant Colony Clustering Algorithms (Zhang et al., 2022c) to explore only a subset of combinations, thereby significantly reducing computation time. As a result, these approaches have also gained popularity in landslide susceptibility modelling (Rong et al., 2020; Sameen et al., 2020). However, a limitation of these methods is that they do not guarantee identification of the truly optimal hyperparameter combination.

3.7.9 Validation methods

Several metrics are available to assess the performance of machine learning models, and their applicability depends on the type of task, namely classification or regression.

For regression tasks, where the objective is to predict continuous values, typical metrics include root mean square error (RMSE), mean absolute error (MAE), and coefficient of determination (R^2). These metrics quantify the difference between predicted and observed continuous values.

For classification tasks, commonly used evaluation metrics include accuracy, precision, recall, F1-score, ROC-AUC, and logarithmic loss (log-loss). These metrics evaluate the model's ability to correctly assign instances to predefined classes and, in some cases, its probabilistic predictions.

In the context of landslide susceptibility modelling, which is generally treated as a binary classification problem (landslide vs. non-landslide), the most commonly

employed evaluation metrics are accuracy and ROC-AUC, which are described in detail below.

3.7.9.1 Accuracy

Accuracy is among the most widely used metrics for evaluating the predictive performance of machine learning models, particularly in binary classification tasks such as landslide susceptibility modelling with balanced positive and negative samples. It is defined in Equation (3-29), with higher values generally indicating superior model performance:

$$Accuracy = \frac{(TP + TN)}{(TP + FP + TN + FN)} \tag{3-29}$$

In this context, TP (true positive) refers to correctly predicted landslides, while TN (true negative) denotes correctly predicted non-landslides. Conversely, FP (false positive) represents instances where the predicted class is positive, but the actual class is negative, and FN (false negative) indicates cases where the predicted class is negative while the actual class is positive.

3.7.9.2 Receiver Operating Characteristic Curve

When dealing with imbalanced datasets, accuracy often fails to reflect the true predictive performance of a machine learning model. For instance, if a dataset contains 9,999 positive samples and only 1 negative sample, a model that predicts all instances as positive would achieve an accuracy of 99.99%, despite completely failing to identify the negative case. To address this limitation, the Receiver Operating Characteristic (ROC) curve is employed, plotting the true positive rate $\frac{(TP)}{(TP+FN)}$ versus false positive rate $\frac{(FP)}{(FP+TN)}$ across different threshold values. The area under the ROC curve (AUC) quantifies model performance, with higher AUC values indicating better predictive capability. Figure 3-26 illustrates a ROC curve.

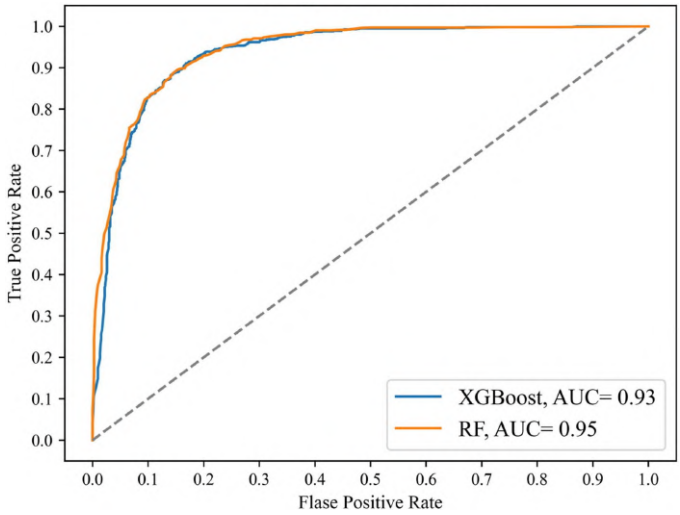

Figure 3-26 ROC curve and AUC results for XGBoost and RF models (Janizadeh et al., 2023).

3.7.10 Feature importance and Shapley additive explanation

The occurrence of landslides is governed by a variety of influencing factors, each contributing differently to the overall process. As a result, it is essential to examine both the relative importance of these factors and the mechanisms through which they affect landslide initiation. Such analysis can support more reliable prediction and mitigation of landslide hazards.

At the same time, landslide occurrence represents a highly complex and nonlinear phenomenon. Advanced machine learning models, such as ANN, XGBoost, and RF, are capable of achieving high predictive performance, but they often lack transparency. To address this limitation, the field of explainable artificial intelligence (XAI) has emerged, aiming to make the outputs of complex models more interpretable (Linardatos et al., 2021). One widely used XAI method is Shapley Additive Explanations (SHAP). SHAP enables the interpretation of model predictions by quantifying the contribution of each input feature to a given output. However, within geotechnical applications, there is still limited understanding of how input variables influence the predictions of machine learning models (Kannangara et al., 2022).

SHAP is a Python-based framework developed by Lundberg and Lee (2017) to interpret machine learning predictions by assigning a contribution value to each feature. The method is based on Shapley values from cooperative game theory (Shapley, 1953), which quantify the contribution of individual players to a collective outcome. These values satisfy two key properties: additivity, meaning that the sum of individual contributions equals the final prediction, and consistency, meaning that features with greater influence are assigned higher importance (Kannangara et al., 2022). For a given feature i, the Shapley value (ϕ_i) is computed

as the average marginal contribution of that feature across all possible subsets *S* of the feature set *N*, excluding *i*, and can be determined as follows:

$$\varphi_i = \frac{1}{n!}\sum_{S\subseteq N\setminus\{i\}} |S|!\,(n-1-|S|)!\,[f(S\cup\{i\}) - f(S)] \tag{3-30}$$

where f represents the original prediction model, S denotes a subset of input features, N is the complete set of features, i refers to the feature of interest, and n is the total number of features. Within the SHAP framework, the prediction for an individual observation x, given by $f(x)$, is approximated using an interpretable linear function g, which can be expressed as follows:

$$f(x) = g(\acute{x}) = \varphi_0 + \sum_{i=1}^{M} \varphi_i\,\acute{x}_i \tag{3-31}$$

where x represents the instance being explained, while x' denotes the corresponding simplified input. These two are connected through a mapping function, such that $x = h_x(x')$. The term ϕ_0 refers to the base value of the model output when no input features are present, and M indicates the number of simplified input features.

3.8 Advantages and limitation of methods

Different methods for landslide susceptibility analysis present distinct advantages and limitations depending on their application, data requirements, and the spatial scales at which they can be implemented.

Geomorphological methods are cost-effective and can be applied over relatively short periods. They are suitable for relatively large areas (small-scale mapping) and can cover inaccessible regions through multi-temporal satellite image interpretations (Guzzetti et al., 1999). However, because these methods are generally applied at small scales, the geomorphological details they capture are limited, restricting the reliability and applicability of results for specific purposes. Similarly, landslide inventories are constrained by subjectivity and by the challenges of assessing their reliability, which largely depends on the quality and abundance of available data sources (Guzzetti et al., 2005a; Raghuvanshi et al., 2014a).

Heuristic evaluation techniques are valued for their simplicity. Experts assign weights to causative factors based on relative contributions without relying on historical datasets, making them easy to implement. These approaches often combine field-acquired data with expert judgment and experience. The main drawback is the inherent subjectivity in assigning weights and ratings, which can result in significant variability when different experts evaluate the same area (Delmonaco et al., 2013).

Statistical approaches rely on quantitative relationships between past landslides and causative factors, deriving factor weights from landslide inventory data. These methods can cover large areas, and the factor ratings are statistically determined from historical landslide occurrences. The limitation lies in the need for extensive, well-distributed past landslide data; without it, results may be unreliable. Additionally, collecting and validating such datasets requires substantial effort, and collaboration between geomorphologists and statisticians is often necessary to avoid unrealistic outputs. Statistical models can also be sensitive to study area extent, complicating comparisons between regions, and their results may be difficult for non-specialists, such as planners or policymakers, to interpret (Fall et al., 2006). Deterministic and probabilistic approaches are based on physical laws governing slope instability. These methods provide detailed quantitative analyses but are generally limited to small areas due to the challenges of collecting high-resolution geotechnical data over large regions.

AI approaches offer advantages in reliability, cost-effectiveness, and the ability to handle uncertainty and complex interactions between variables. ML methods do not require statistical assumptions and allow integration of heterogeneous data sources such as remote sensing and GIS. They are computationally efficient, permit pixel-by-pixel analysis, and can handle incomplete or imperfect data, as well as nonlinear interactions between variables. The limitations of this approach include the inherent complexity of the processes occurring within hidden layers, which can make model interpretation challenging. Additionally, acquiring high-quality and comprehensive datasets is often time-consuming and resource-intensive, slowing down analysis. Table 3-1 compares the three main approaches in terms of their methodological basis, data and computational needs, objectivity, and predictive performance.

Table 3-1 Comparison of qualitative, semi-quantitative, and quantitative methods to build landslide susceptibility maps.

Criterion	Qualitative methods	Semi-quantitative methods	Quantitative methods
Basis of analysis	Expert knowledge and field interpretation	Combination of expert judgment and numerical weighting	Statistical, mathematical, or computational modeling
Subjectivity	High	Moderate	Low
Reproducibility	Low	Moderate	High
Data requirements	Low	Moderate	High
Computational requirements	Low	Low-moderate	Moderate-high
Ease of implementation	High	High	Low

Criterion	Qualitative methods	Semi-quantitative methods	Quantitative methods
Ability to handle large datasets	Limited	Moderate	High
Ability to model complex relationships	Low	Moderate	High
Predictive capability	Low	Moderate	High
Model transparency	High	High	Moderate
Future climate scenario integration	Limited	Limited	High
Suitability for regional-scale mapping	Moderate	High	High

3.9 Selection criteria

The selection of an appropriate technique for landslide susceptibility assessment and hazard zonation depends on several factors, including the purpose of the study, spatial extent, mapping scale, type of landslides, data availability, and the expertise and resources of the investigator. Different applications require different methodological approaches. For instance, site-specific investigations for construction projects demand detailed and quantitative slope stability analyses, typically achieved through deterministic methods. These studies are conducted at large or detailed scales and rely on high-quality geotechnical and geological data.

For regional land-use planning and hazard zonation, the choice of method is influenced by the size of the study area and available data. Heuristic approaches, which depend heavily on expert judgment and field observations, are generally suitable for smaller, accessible areas where sufficient field data can be collected. In contrast, statistical methods are more appropriate for medium-scale analyses, provided that reliable landslide inventory data is available. In some cases, hybrid approaches combining multiple techniques are used to improve the robustness of the results.

Mapping scale is closely linked to the study objective and data resolution. Large-scale maps are used for detailed site investigations and engineering design, while medium-scale maps support regional planning by identifying susceptible zones. Small-scale or national-level studies cover extensive areas but provide only generalized information, often intended for policy-making rather than detailed analysis.

Data availability plays a critical role in method selection. Statistical and probabilistic techniques require comprehensive and high-quality historical landslide inventories, which are often incomplete due to limitations in data collection, vegetation cover, or erosion processes. Deterministic methods, on the other hand, require detailed geotechnical data and are therefore limited to smaller areas where such data can be obtained. Heuristic methods require less inventory data but still depend on substantial field-based information.

ML approaches have emerged as powerful alternatives, particularly for small-medium scale studies. These methods can efficiently handle large datasets, integrate numerous conditioning factors, and model non-linear relationships that are difficult to capture using traditional techniques. AI-based models are especially suitable for generating dynamic landslide susceptibility maps, allowing continuous updates as new data becomes available. This makes them highly effective for regional to national-scale assessments, where conventional methods may be limited by data complexity, scale, and variability.

3.10 Landslide susceptibility and infrastructures

Modern risk management approaches emphasize the explicit integration of landslide susceptibility or hazard maps with infrastructure networks, enabling the assessment of exposure and vulnerability of assets such as roads, bridges, and pipelines. This integration supports more informed planning and design aimed at risk mitigation. In general, methodologies that combine infrastructure systems with landslide susceptibility can be broadly classified into two categories: probabilistic risk modelling and spatial overlay techniques.

3.10.1 Probabilistic risk modeling

Probabilistic approaches estimate landslide risk by integrating the likelihood of hazard occurrence with the vulnerability of infrastructure elements. In such frameworks, landslide occurrence is represented probabilistically, often incorporating spatial, temporal, and magnitude components, while infrastructure systems (e.g., roads, railways, and pipelines) are characterized using fragility functions or vulnerability curves.

For instance, Liu et al. (2022) proposed a comprehensive probabilistic framework to evaluate the risk to regional road networks exposed to landslides by explicitly linking landslide hazard with road vulnerability. In this approach, landslide hazard is formulated as a conditional probability that captures interdependence among spatial, temporal, and magnitude factors, thereby overcoming the common assumption of independence. The spatial probability component is derived using a CNN trained on historical landslide inventories and relevant conditioning factors, resulting in a susceptibility map (Figure 3-27a) that

highlights high-probability zones primarily in the central and southeastern parts of the study area. The magnitude probability is modeled using a Weibull distribution (Figure 3-27b), while the temporal occurrence of landslides is represented through a modified Poisson process.

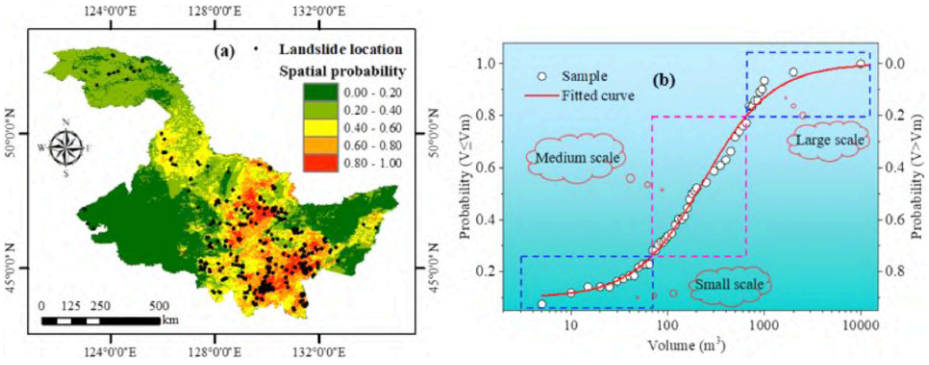

Figure 3-27 Landslide probability, (a) Space probability distribution, (b) Magnitude probability measure and classification (Liu et al., 2022)

Road vulnerability is quantified within a probabilistic framework by integrating both the system-level vulnerability of the road network and the fragility of infrastructure to landslides. The system vulnerability is assessed using the Traffic Consequence Index (TCI), which represents the increase in travel time resulting from the failure of specific road segments and is spatially depicted in Figure 3-28a. In parallel, the resistance of the road network to landslide impacts is illustrated in Figure 3-28b.

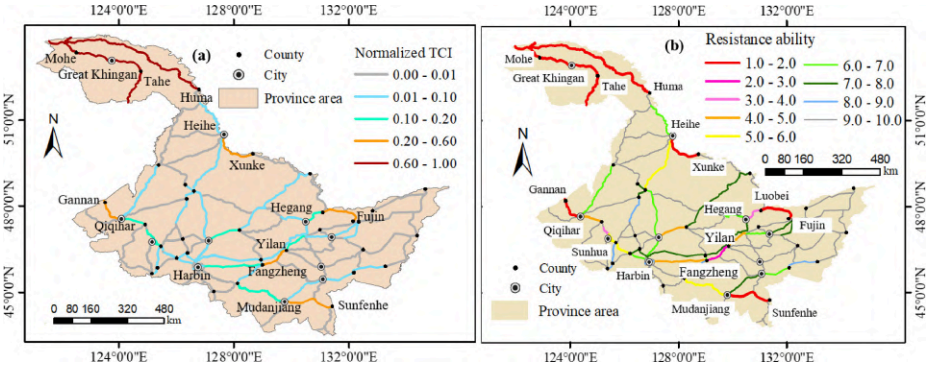

Figure 3-28 Road vulnerability, (a) TCI value, (b) Road resistance (Liu et al., 2022).

Another study by Uzielli et al. (2018) presents a probabilistic framework for landslide risk assessment by integrating hazard characterization and infrastructure vulnerability within a unified approach. In this framework, landslide hazard is defined as the probability of occurrence conditioned on spatial susceptibility and triggering factors and is modeled using a Poisson-based temporal process combined with a magnitude distribution function. Infrastructure vulnerability is represented through fragility relationships, which express the probability of exceeding specific damage states as a function of landslide intensity. Figure 3-29 illustrates the temporal variation of P_L across ten 30-year periods spanning from 1981–2010 to

2071–2100 under both RCP 4.5 and RCP 8.5 scenarios. Specifically, model outputs and ensemble averages are presented for RCP4.5 (Figure 3-29a), RCP8.5 (Figure 3-29b), and the combined concentration scenarios (Figure 3-29c). Additionally, Figure 3-29d shows the sample coefficient of variation for both scenarios.

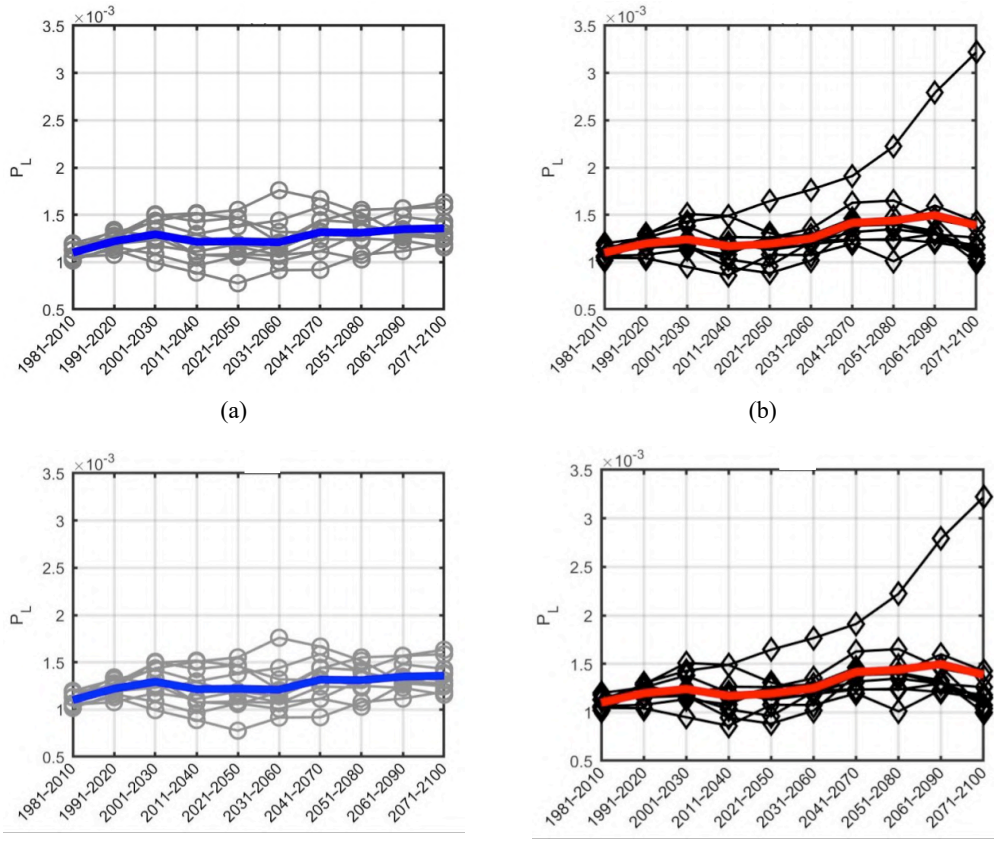

Figure 3-29 Second-moment statistical analysis of landslide occurrence probability (PL) (Uzielli et al., 2018).

Figure 3-30a and b present the quantile regression–based fitting of the modified geometric model to samples of occurrence probability corresponding to exceedance probabilities of 50% (Q50) and 10% (Q90), for the RCP4.5 and RCP8.5 scenarios, respectively.

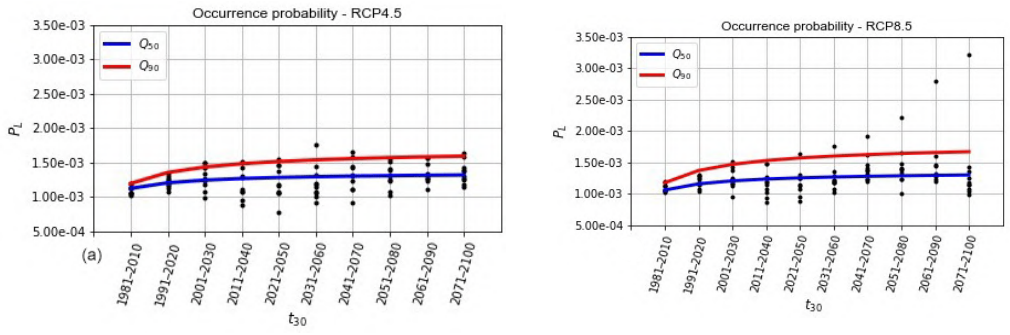

Figure 3-30 Fitting of modified geometrical models to landslide occurrence probability ensemble data for quantiles Q50 and Q90: (a) RCP4.5 and (b) RCP8.5 (Uzielli et al., 2018).

The study further addresses the spatial variability of flow-like landslide hazards by incorporating the modeling of downslope propagation (runout). In this framework, reach probability is defined as the likelihood, ranging from 0 (no impact) to 1 (certain impact), that a specific location within the spatial domain will be affected during the runout process (Figure 3-31).

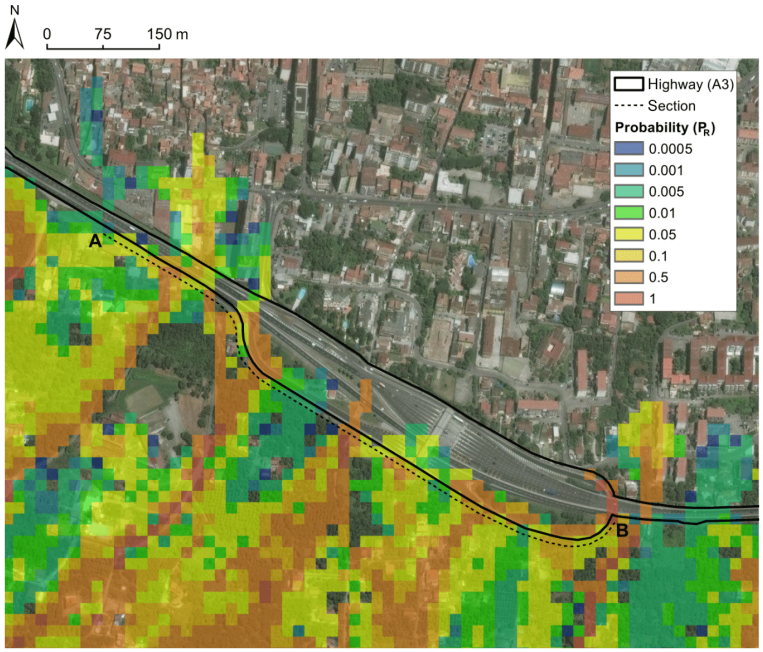

Figure 3-31 Spatial distribution of reach probability at infrastructure scale (Uzielli et al., 2018).

3.10.2 Spatial overlay

This approach involves overlaying a landslide susceptibility map with spatial layers of infrastructure to determine which assets are located within high-risk zones. For instance, Biswas et al. (2026) produced a landslide susceptibility map using a deep learning method and subsequently overlaid road networks onto the map to identify areas of vulnerability (Figure 3-32).

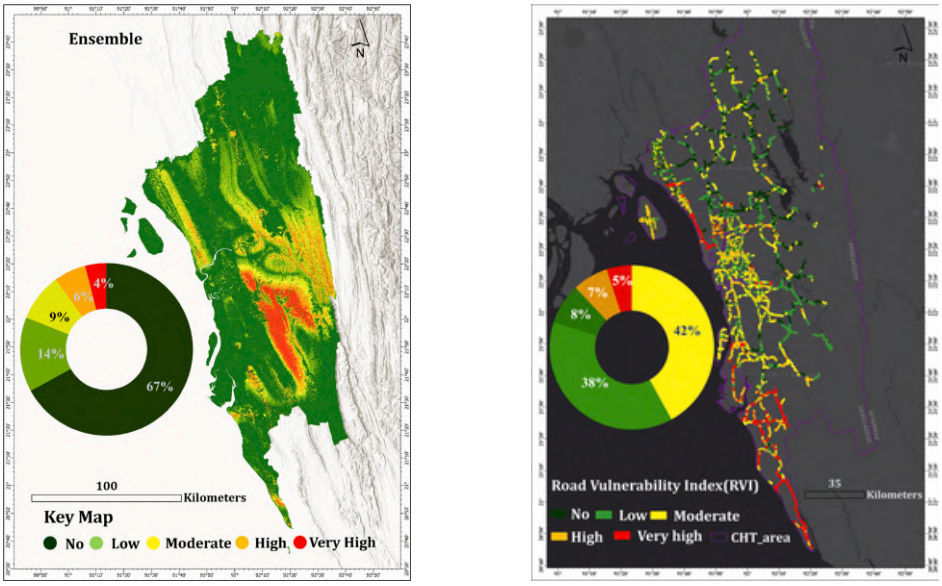

(a) (b)

Figure 3-32 Maps of (a) LSM, and (b) Road vulnerability index for Chittagong Hill Tracks, Bangladesh (Biswas et al., 2026).

Also, Zhang et al. (2026), first buffered the area around the road and generated the LSM for the buffered area, and then locate the susceptible areas around the highway with XGBoost and RF algorithms (Figure 3-33).

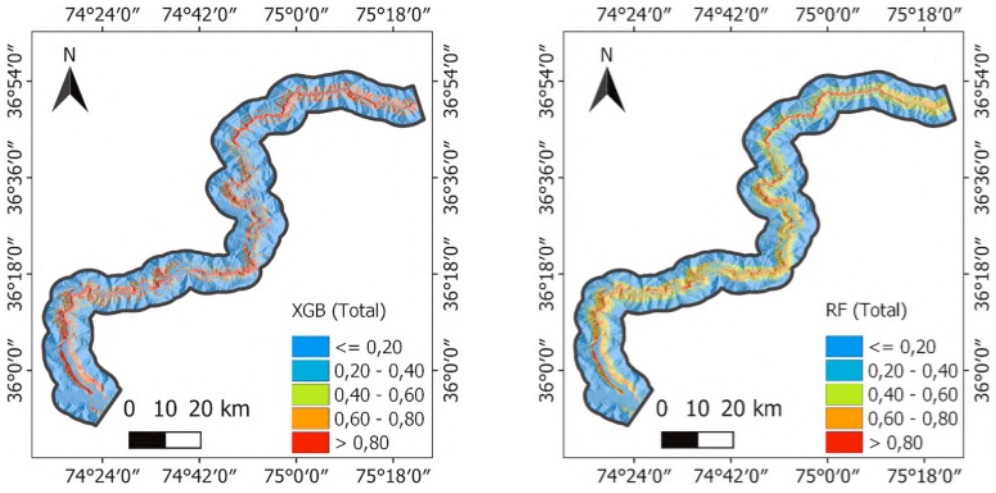

(a) (b)

Figure 3-33 Integration of LSM with the Karakoram Highway, Pakistan, (a) XGBoost, and (b) RF algorithms (Zhang et al, 2026).

Finally, Gnyawali et al. (2023) reclassified the landslide susceptibility map into ten classes and similarly categorized critical infrastructure based on intensity on a scale from 1 to 10. The two indices were then combined to assess overall risk. Figure 3-34 highlights the individual classes exceeding class 5.

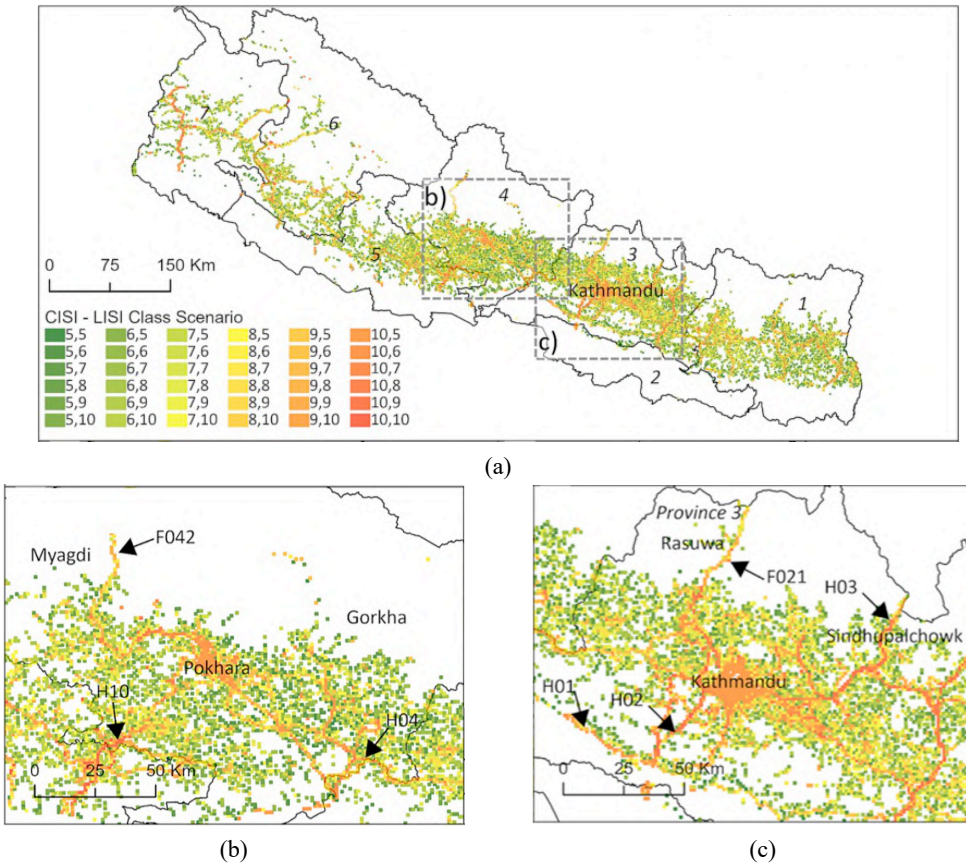

Figure 3-34 Interaction LSM with infrastructures by merging Critical Infrastructure Spatial Index (CISI) and Landslide Intensity Spatial Index (LISI), Nepal (Gnyawali et al., 2023).

3.11 Research gaps and limitations

Despite numerous efforts in landslide susceptibility mapping and the assessment of vulnerable infrastructure, several gaps and limitations persist in existing studies.

A first set of limitations relates to the methodological treatment of landslide susceptibility modelling. Some studies apply regression-based approaches to landslide occurrence, even though it is inherently a classification problem, making regression unsuitable in this context. In addition, multicollinearity among landslide conditioning factors is often overlooked, which can introduce bias into model outcomes. The handling of input variables also presents issues: categorical factors such as soil type, land cover, and lithology are sometimes assigned arbitrary numerical values, potentially misleading algorithms that are designed to treat them as categorical. Conversely, continuous variables are occasionally discretized into arbitrary classes, which may oversimplify underlying relationships and reduce model accuracy.

A second major limitation concerns the representation of triggering factors, particularly precipitation. Although rainfall is widely recognized as a primary driver of landslides, it is frequently neglected in susceptibility analyses. When

included, most studies rely on average annual accumulated precipitation, which fails to capture short-term extreme events that are often responsible for landslide initiation. For instance, intense rainfall over a period of several days may trigger a landslide, while the corresponding annual total may remain relatively low, leading to underestimation of hazard. Notably, no study to date has incorporated actual precipitation data immediately preceding landslide events.

Closely related to this is the insufficient consideration of temperature effects. Temperature is largely ignored in existing studies, and in some cases, elevation is used as a proxy. While this assumption may be acceptable in static analyses, it becomes inadequate in the context of climate change, where temperature varies dynamically over time and cannot be reliably represented by elevation alone.

Another set of limitations involves model interpretability and validation practices. Only a limited number of studies employ SHAP (Shapley Additive Explanations) analysis to quantify the contribution of individual conditioning factors to landslide probability. Furthermore, model evaluation is typically restricted to standard metrics such as ROC and AUC using testing datasets, without incorporating post-event landslide occurrences to assess model robustness under real-world conditions.

In terms of risk assessment, the integration of infrastructure with LSM remains overly simplistic. Most studies rely on spatial overlay techniques, which do not account for cascading effects that may arise from infrastructure failure, thereby underestimating the broader consequences of landslide events.

To address these limitations, this study proposes a novel framework for generating landslide susceptibility maps for the 2003–2022 period, while incorporating climate change projections for 2021–2040. The methodology produces LSMs on a monthly basis, enabling the capture of temporal variations in accumulated precipitation and average temperature. In addition, the study evaluates the risk to power towers and explicitly considers cascading effects associated with electricity failure, providing a more comprehensive assessment of landslide-related risks.

3.12 Summary

This chapter presents a comprehensive review of the techniques used to identify landslide-susceptible areas. In general, these methods can be classified into three main categories: qualitative, semi-quantitative, and quantitative approaches. AI and ML methods, which fall under the quantitative category, are discussed in greater detail due to their increasing application and effectiveness. Figure 3-35 illustrates different LSM techniques.

The implementation of machine learning approaches begins with data collection and the selection of appropriate landslide conditioning factors, which represent the most critical and time-intensive stage of the process. The collected data must then be preprocessed to ensure consistency, including harmonizing coordinate reference systems (CRS) and addressing missing values. Following this, the dataset is divided into training and testing subsets, and various algorithms are applied. Since no single algorithm can be universally considered superior, model selection depends on the specific characteristics of the study area and dataset. Hyperparameter optimization is subsequently performed to identify the most suitable model configuration. Finally, model performance is evaluated using appropriate validation techniques.

Each methodological group presents distinct advantages and limitations. Geomorphological methods are cost-effective and suitable for large-scale applications, including inaccessible areas; however, they lack detailed representation and may produce less reliable results. Heuristic approaches are simple and easy to implement without requiring historical data, but they are highly subjective and dependent on expert judgment. Statistical methods allow for quantitative analysis over large areas and derive factor importance from historical data, yet they require extensive and well-distributed landslide inventories and may be difficult to interpret for non-specialists. Deterministic approaches provide physically based and detailed analyses, although their application is generally limited to smaller areas due to data requirements. In contrast, AI and ML methods are powerful in handling complex, nonlinear relationships, integrating diverse datasets, and managing incomplete data; however, they often suffer from limited interpretability, high data requirements, and restricted applicability in certain contexts such as runout analysis.

The chapter further outlines the criteria for selecting appropriate methods based on data availability, study scale, and research objectives. It also reviews approaches for integrating landslide susceptibility with infrastructure systems to identify vulnerable assets. Finally, key gaps and limitations in existing literature are discussed, providing the foundation for the methodological developments proposed in this study.

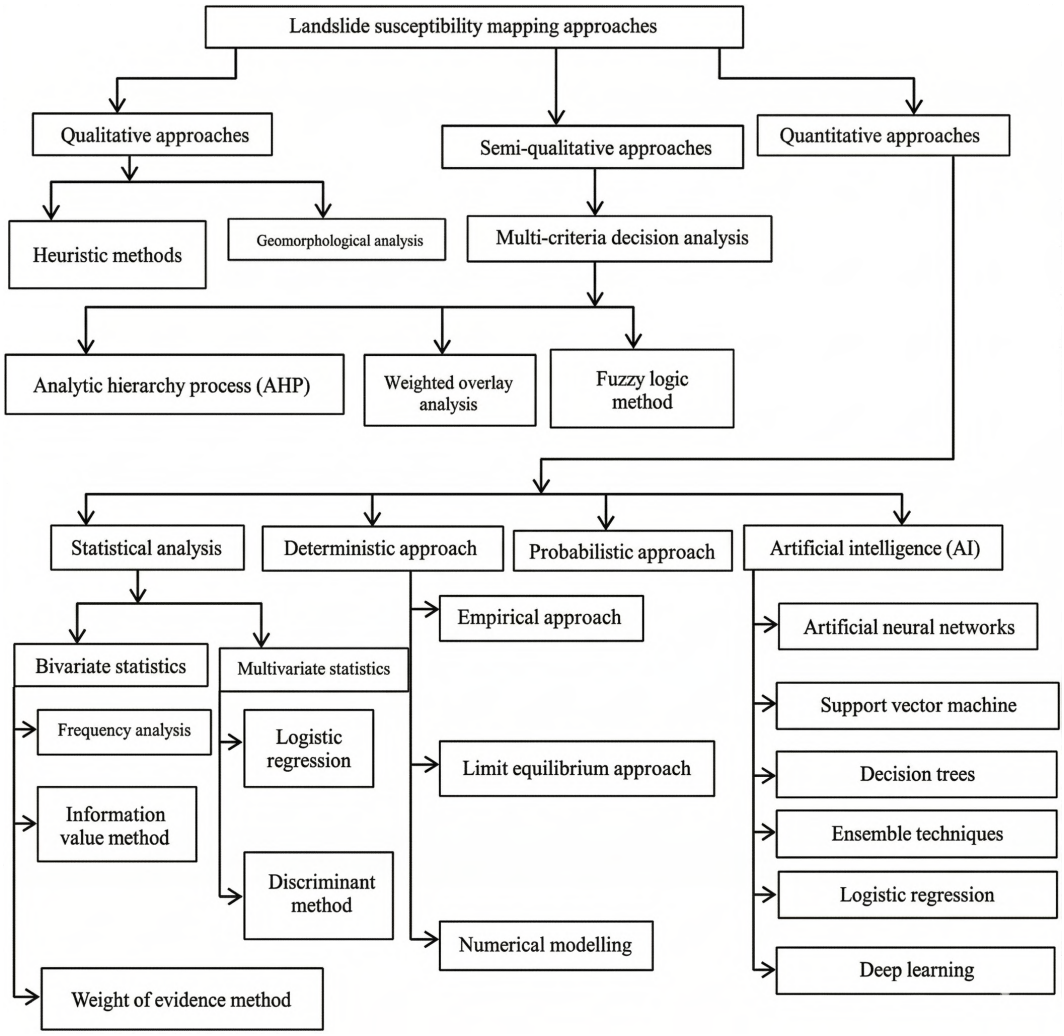

Figure 3-35 Landslide susceptibility techniques.

Chapter 4

Machine learning based methodological framework

4.1 Introduction

This chapter presents the methodological framework adopted in this Thesis to develop monthly landslide susceptibility maps under both current and future climate conditions. The approach integrates climatic, topographic, and environmental variables within a data-driven framework to capture the temporal variability of landslide occurrence. The analysis focuses on the Aosta Valley, located in Northwestern Italy, selected to demonstrate the practical applicability of the proposed approach and to enable comparison between present and projected conditions.

Landslide susceptibility is modelled using a machine learning approach based on the Extreme Gradient Boosting (XGBoost) algorithm. This method was selected for its strong predictive capability and, based on comparative tests with other algorithms, its superior performance in this study. Future projections of landslide susceptibility describe its evolution under changing climatic conditions, obtained by forcing the model with climate variables derived from climate projections. Among the scenarios discussed in this Chapter, the SSP5-8.5 pathway is adopted to assess the potential impact of high-emission conditions on landslide susceptibility.

The chapter begins with an introduction to the study area and its main characteristics, including the landslide inventory that serves as the primary data source. It then describes the machine learning method applied, which was trained and tested on the landslide dataset to generate the susceptibility maps. The methodological steps presented in this chapter follow the same sequence introduced

in the previous chapter (section 3.7), where the required data and procedures for applying machine learning in landslide susceptibility mapping were described step by step. The methodology described in this chapter builds upon approaches previously published in Pourfatollah et al. (2025a, 2025b) and Barla (2024).

4.2 Description of the study area: Aosta Valley (Italy)

The Aosta Valley, situated in the northwestern Italian Alps, is the country's smallest autonomous region, covering an area of 3,262 km². It borders Switzerland to the north and France to the west. The territory is entirely Alpine, characterized by rugged mountain landscapes and traversed by the east-west course of the Dora Baltea River, which originates at Monte Bianco. Monte Bianco, also known as Mont Blanc, is Italy's highest peak, rising to 4,810 m on the border with France. Other notable summits along the northern frontier include Monte Cervino (the Matterhorn, 4,478 m) and Monte Rosa (4,634 m). The region's elevation varies from 305 m to the highest Alpine peaks, with nearly 80% of its surface lying above 1,500 m a.s.l.. Figure 4-1 provides an overview of the Aosta Valley and its elevation distribution.

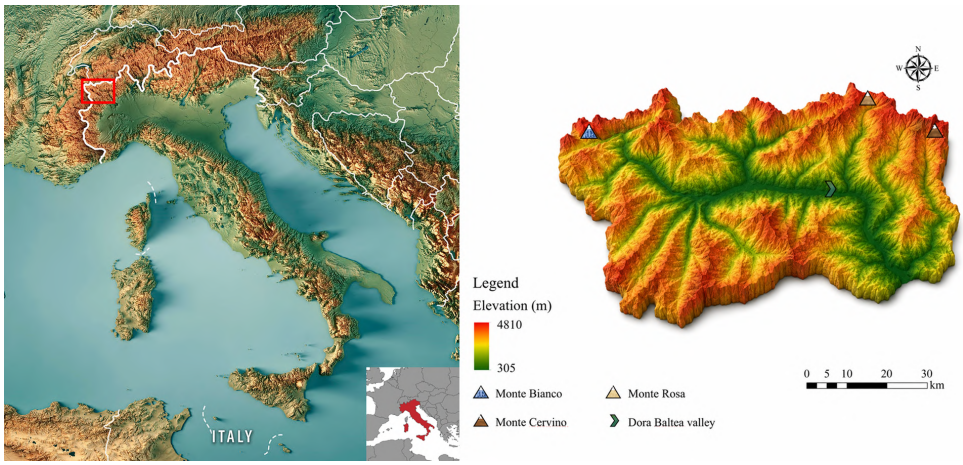

Figure 4-1 The Aosta Valley region.

In the Aosta Valley, the rainfall regime is characterized by two seasonal peaks, one in spring and another in autumn. The spatial distribution of precipitation is highly variable and influenced by factors such as elevation, the orientation of lateral valleys, and the slope and exposure of the mountain sides. Two distinct climatic conditions can be observed in the region. In the mountainous and peripheral areas, temperature ranges are wider and precipitation is abundant, often occurring as snow, with annual averages between 1000 and 1100 millimetres. In contrast, the Dora Baltea valley is marked by a milder climate, with occasional dry winds and limited rainfall, with yearly averages below 600 millimetres (Ratto et al., 2003).

Due to its complex mountainous topography, the Aosta Valley is particularly prone to slope instability. Landslide events in the region are primarily induced by intense rainfall, rapid snowmelt, and freeze–thaw cycles, which increase pore water pressures and reduce the effective stress in slope materials, thereby diminishing shear strength and promoting slope failure.

In many alpine regions, including this area, rock slides and landslides are often associated with permafrost thawing (Barla and Barla, 2001; Deline et al., 2015; Gruber and Haeberli, 2007; Huggel, 2009). Figure 4-2 shows an example of a glacier retreat in the Aosta Valley.

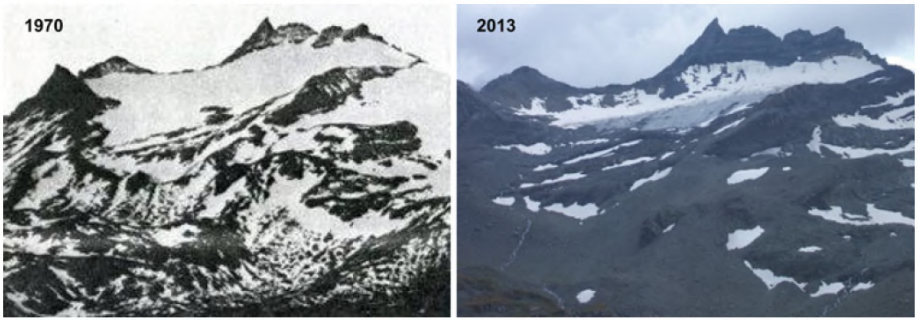

Figure 4-2 Arguerey Meridionale Glacier (Aosta Valley): comparison between two photographs taken from the same vantage point illustrates the marked glacier retreat (Chiarle et al., 2015).

Landslide occurrence is largely influenced by conditioning factors, which reflect the intrinsic characteristics of the terrain and predispose slopes to instability. These factors are described in detail in section 4.4.

4.3 Landslide inventory

Landslide inventory is the collection of the landslides that occurred in Aosta Valley, which was obtained from Inventario dei Fenomeni Franosi in Italia (IFFI). This inventory was compiled using a combination of field surveys, satellite imagery, and aerial photographs, and was organized in an Excel database. The inventory contains 3627 points from different categories of hazards (landslides, rockfalls, floods, potential instabilities, floods, hydrological alerts, generic events, debris flows and hydraulic phenomena) that occurred from 1981 onwards (Figure 4-3a). However, many of the records did not include the exact date of occurrence and reported only the year. Since this study requires precise event dates to extract the corresponding meteorological conditions preceding each landslide, these records were excluded from the analysis. In addition, although the inventory initially contained several types of slope movements, including debris flows, creep, and block slides, these events were removed because their kinematic mechanisms and controlling factors differ from those of the landslide types considered in this study. Consequently, only events classified as flaws, translational, rotational, or complex landslides were retained for the analysis (according to Cruden and Varnes, 1993). Following these

filtering, a total of 369 landslide events occurring between 2003 and 2022 were selected (Figure 4-3b).

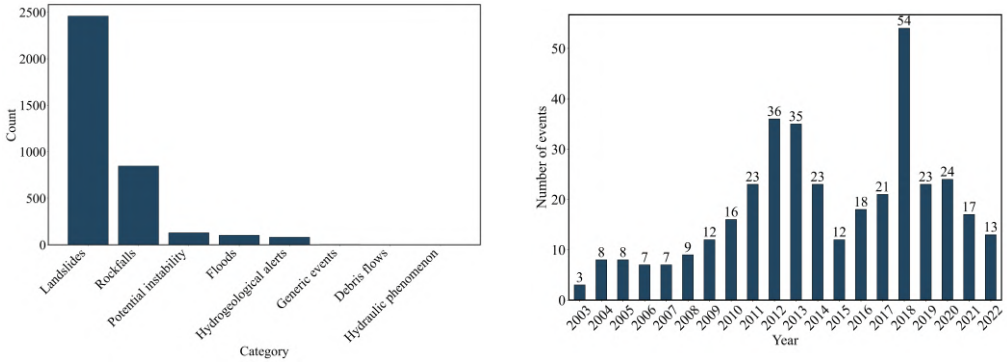

(a) (b)

Figure 4-3 Recorded (a) Natural hazard events since 1981 by type, and (b) Number of selected landslide events occurred in Aosta Valley from 2003 to 2022.

The methodology requires the inclusion of negative samples, representing non-landslide events. Therefore, in addition to landslide occurrences (assigned a probability of 1), non-landslide points were included to represent locations with a probability of 0. This allows the algorithm to distinguish between susceptible and stable areas. Several studies have examined the selection of non-landslide points and their influence on model performance (Chang et al., 2023; Gu et al., 2023; Khabiri et al., 2023). For example, Nocentini et al. (2023) showed that selecting non-landslide points from different locations and times, particularly when dynamic variables are considered, improves model predictive performance.

To generate the non-landslide points, areas located at least 500 m away from any recorded landslide were considered as safe zones (Janizadeh et al, 2023). Within these safe zones, 369 points, equal to the number of landslide points, were randomly selected, and the corresponding LCF values were extracted to form a balanced dataset of landslide and non-landslide points.

For dynamic parameters, non-landslide points were assigned values that vary by month. This temporal variation allows the model to learn the differences in environmental conditions across months and improves its ability to differentiate between susceptible and non-susceptible areas. Figure 4-4 shows the selected landslide and non-landslide points in the region.

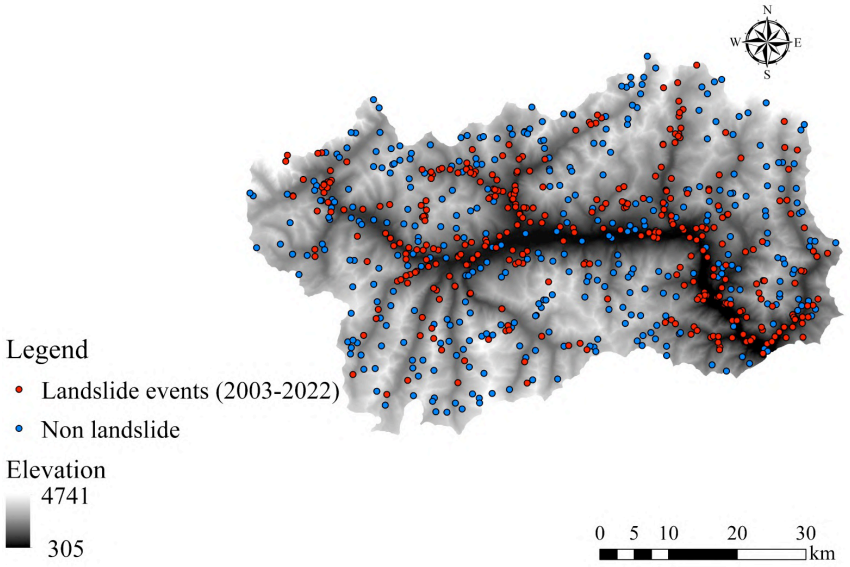

Figure 4-4 Landslide events occurred from 2003 to 2022 in the Aosta Valley and non-landslide points.

It is worth mentioning that a polygon-based landslide inventory was also available for the study area, which could potentially provide a more realistic representation of the spatial extent of landslide events. However, most of the polygon dataset did not include precise dates of occurrence. Since methodology in this Doctoral Thesis requires exact event timing to extract corresponding precipitation and temperature values prior to each landslide, the polygon inventory could not be used. Therefore, the analysis was conducted using the point-based inventory, which contains reliably dated landslide events.

It should also be noted that, although the objective of this study is to generate monthly landslide susceptibility maps, the same landslide inventory is used to train all monthly models. This is because when the inventory is disaggregated by month, some months contain only a limited number of recorded landslide events. For example, January and February contain approximately ten landslide occurrences each, which are insufficient for robust machine-learning model training and may lead to unstable or unreliable predictions. This methodology ensures a consistent training dataset while allowing the influence of seasonal climatic variability on landslide susceptibility to be assessed. Therefore, although the landslide inventory is multi-temporal and the predictions are generated on a monthly basis, the comparison remains meaningful because the monthly maps primarily reflect temporal changes in the triggering climatic conditions rather than changes in the underlying landslide inventory.

4.4 Landslide conditioning factors

Based on the environmental characteristics of the study area and the existing scientific literature, 13 landslide conditioning factors were selected. These include: (i) topographic factors such as slope, aspect, plan curvature, profile curvature, sediment transport index (STI), and stream power index (SPI); (ii) geological and soil-related factors such as lithology and soil type; (iii) climatic factors including average monthly precipitation, seven-day precipitation, and average monthly temperature; and (iv) environmental factors such as land cover and the normalized difference vegetation index (NDVI). Some of these factors vary over time and are therefore considered dynamic, such as the climatic variables. Land cover is treated as semi-dynamic, since in this work a single land cover map for 2018 was used to represent the period 2003–2022, while an updated map for 2024 was adopted to represent the period 2021–2040. All the remaining conditioning factors are assumed to be constant over time and are treated as static. Table 4-1 illustrates the LCFs classification.

Table 4-1 Landslide conditioning factors (LCFs) classification.

Number	LCFs	Controlling factor type	Temporal classification
1	Aspect	Topographic	Static
2	Slope	Topographic	Static
3	SPI	Topographic	Static
4	Plan curvature	Topographic	Static
5	Profile curvature	Topographic	Static
6	STI	Topographic	Static
7	Lithology	Geological	Static
8	Soil type	Geological	Static
9	NDVI	Environmental	Static
10	Land cover	Environmental	Semi-static
11	Monthly accumulated precipitation	Climatic	Dynamic
12	Seven-day accumulated precipitation	Climatic	Dynamic
13	Mean monthly temperature	Climatic	Dynamic

These LCFs were selected as they play a key role in the calculation of the factor of safety Equation (4-1), in the rock mass failure criterion Equation (4-2), in the Universal Soil Loss Equation (4-3), and in average flow velocity Equation (4-4). These equations are presented only as representative examples among the many formulations used in slope stability analysis, illustrating the range of potential controlling factors that may influence slope behavior and stability.

$$F = \frac{\left(\frac{c'}{\gamma z}\right) + (1 - r_u)\cos^2\theta \tan\varphi'}{\sin\theta \cos\theta} \quad (4\text{-}1)$$

(Skempton and Delory, 1957)

$$\sigma_1' = \sigma_3' + \sigma_{ci}\left(m_b \frac{\acute{\sigma}_3}{\sigma_{ci}} + s\right)^a \quad (4\text{-}2)$$

(Hoek and Brown, 1980)

$$A = R \cdot K \cdot LS \cdot C \cdot P \quad (4\text{-}3)$$

(Wischmeier and Smith, 1960)

$$V = \frac{R^{2/3} \cdot S_f^{1/2}}{n} \quad (4\text{-}4)$$

(Manning, 1891)

In Equation (4-1), F is the factor of safety, c' is the effective cohesion, γ is the bulk unit weight of the soil, z is the depth of the potential failure surface, r_u is the pore-water pressure ratio, θ is the slope angle, and $\varphi'$is the effective angle of internal friction. In Equation (4-2), σ_1' is the major effective principal stress at failure, σ_3' is the minor effective principal stress at failure, C is the uniaxial compressive strength of the intact rock, m is the Hoek–Brown material constant, and s is the Hoek–Brown constant describing rock mass quality. In Equation (4-2), σ_1' and σ_3' are the major and minor effective principal stress at failure, σ_{ci} is the uniaxial compressive strength of the intact rock, m_b is the reduced value of the material constant m_i and s and a are the Hoek–Brown constants for the rock mass. In Equation (4-3), A is the computed average annual soil loss, R is the rainfall–runoff erosivity factor, K is the soil erodibility factor, LS is the slope length steepness factor, C is the cover-management factor, and P is the support-practice factor. In Equation (4-44-4), V is the mean flow velocity, R is the hydraulic radius, S_f is the energy slope (hydraulic gradient), and n is Manning's roughness coefficient.

Geotechnical and geomechanical parameters include c', γ, φ' in Equation (4-1), σ_1' and σ_3' in Equation (4-2), and K in Equation (4-3). These parameters describe the material properties of the soil or rock and can be represented by LCFs such as soil type and lithology.

Topographic or geometric parameters include z, $\sin\theta$ and $\cos\theta$ in Equation (4-1), LS in Equation ((4-34-3), and R , S_f and n in Equation (4-4). These parameters describe slope geometry and landscape features and can be represented by LCFs such as slope, aspect, plan curvature, profile curvature, SPI, and STI.

Hydrological and climate-related parameters include r_u in Equation (4-1) and R in Equation (4-3). These parameters describe the effects of precipitation and temperature on slope stability and can be represented by LCFs such as average monthly precipitation, seven-day precipitation, and average monthly temperature, which indirectly affect groundwater conditions.

Vegetation and land cover parameters are included in c' in Equation(4-1), P and C in Equation (4-3) These parameters describe the internal stresses and

reinforcement of the slope mass and can be represented by LCFs such as land cover and NDVI.

Overall, the LCFs considered in this study can be grouped into three main categories based on their temporal variability: static factors, which remain constant over time; semi-static factors, for which one map represents the period 2003–2022 and another map represents future conditions (2021–2040); and dynamic factors, which change on a monthly basis for both the current and future periods.

By overlaying the landslide inventory with LCFs that have categorical classes (aspect, land cover, lithology, and soil type), the corresponding class values at the locations of observed landslides were extracted. This enabled the assessment of landslide occurrence frequency within each class. This analysis was performed exclusively for categorical variables and not for continuous LCFs with numerical values.

4.4.1 Static LCFs

4.4.1.1 Aspect

Aspect or dip direction of the slope identifies where the slope faces. Slope aspect can be divided into 9 groups: Flat, North, Northeastern, East, Southeast, South, Southwestern, West and Northwest. Aspect can be a parameter influencing landslide occurrence, as it controls several contributing factors such as the orientation of lineaments, rainfall distribution, wind exposure, and the degree of solar radiation received by the slope (Yalcin and Bulut, 2007).

In some studies, the East–South-facing slopes are more prone to landslides because they might be affected more by intense wetting and drying cycles (Bednarik et al., 2010; Piacentini et al., 2012; Regmi et al., 2010). The aspect map was derived from the Digital Elevation Model (DEM), calculated from Equation (4-5) (Wilson and Gallant, 2000):

$$Aspect = \left(\frac{dz/dy}{-dz/dx} \right) \tag{4-5}$$

where *dz/dy* and *dz/dx* are the partial derivatives of elevation with respect to the *y* and *x* coordinates, respectively. Figure 4-5 shows the aspect map of Aosta Valley with a spatial resolution of 10 × 10 m per pixel.

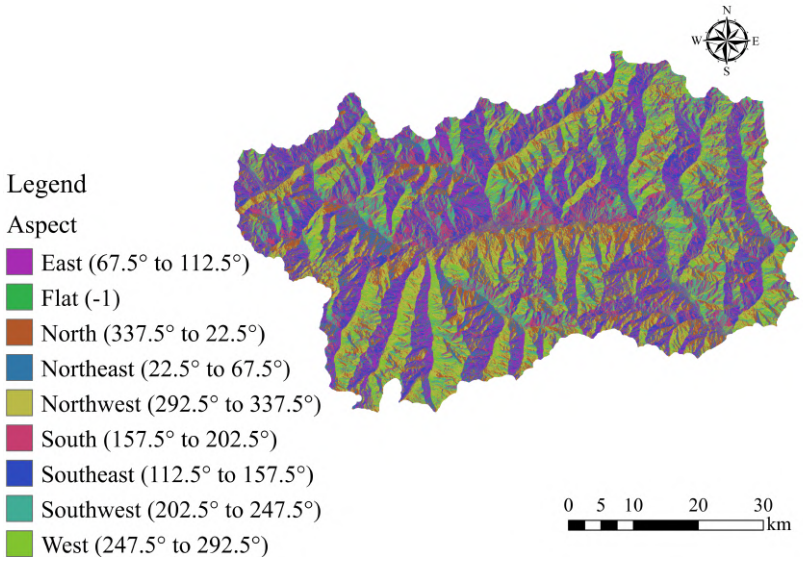

Figure 4-5 Aspect map of Aosta Valley.

Figure 4-6 illustrates the proportion of each aspect class in the region. It can be seen that all of the classes have approximately the same percentage, except for Flat (-1), which means the surface doesn't face any direction, whose share is negligible.

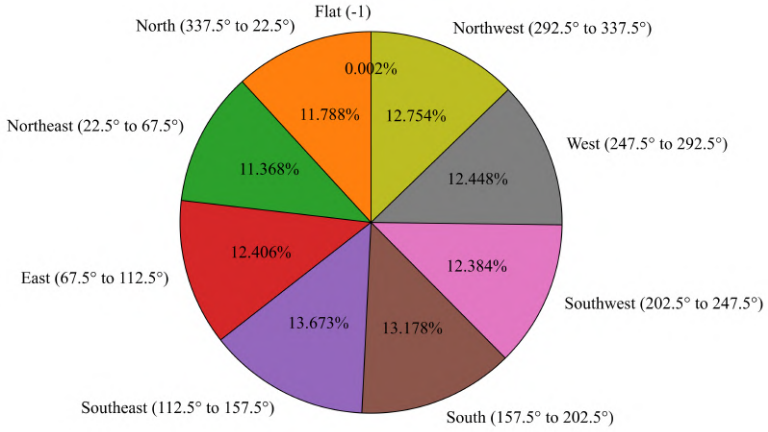

Figure 4-6 Distribution of each slope aspect group in Aosta Valley.

Figure 4-7 illustrates the number of landslides that occurred in each aspect class. It can be seen that the south-oriented slopes have more landslides in the region. Although there is no strong evidence explaining the higher occurrence of landslides on south-facing slopes, it may be attributed to the fact that east–south-facing slopes are more susceptible to intense wetting and drying cycles (Bednarik et al., 2010; Piacentini et al., 2012).

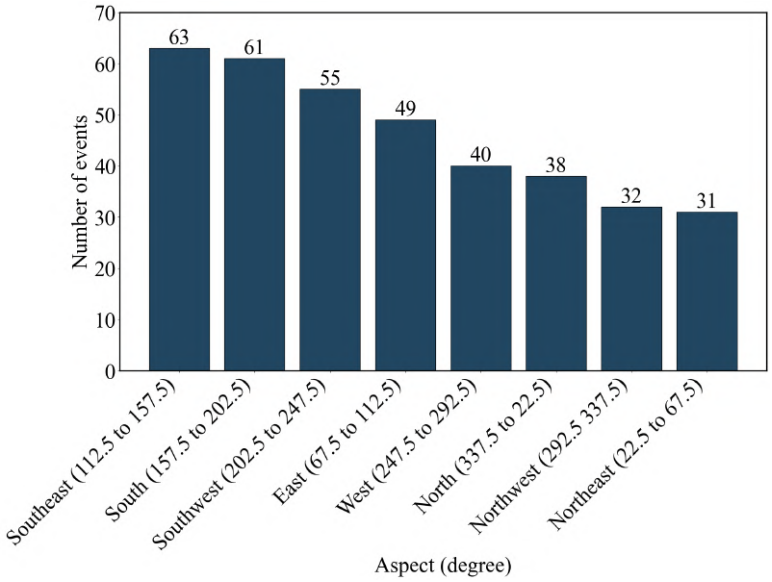

Figure 4-7 Landslide shares in each aspect class.

4.4.1.2 Lithology

The lithological map of the Aosta Valley, shown in Figure 4-8, was retrieved from the Aosta Valley Geoportal website (https://geoportale.regione.vda.it/). In its original form, the map included 17 lithological classes. For this study, these classes were simplified into four broader groups. The reduction was necessary for two main reasons.

First, several of the original classes share comparable mechanical and hydrological properties and could therefore be meaningfully combined. For example, “Slope debris”, “Glacial deposits”, “Alluvial deposits”, and “Sedimentary covers” were grouped as “Quaternary deposits”.

Second, the use of 17 classes can pose technical limitations for the machine learning analysis. Each class in the training dataset must contain both landslide and non-landslide points to allow the algorithm to properly learn the relationships between lithology and slope stability. However, some of the 17 original lithological classes contained very small areas, making them unsuitable for model training. By reducing the number of classes to four, this imbalance was resolved, ensuring that each lithological class included enough representative samples for both categories. The map has a 10 × 10 m per pixel resolution.

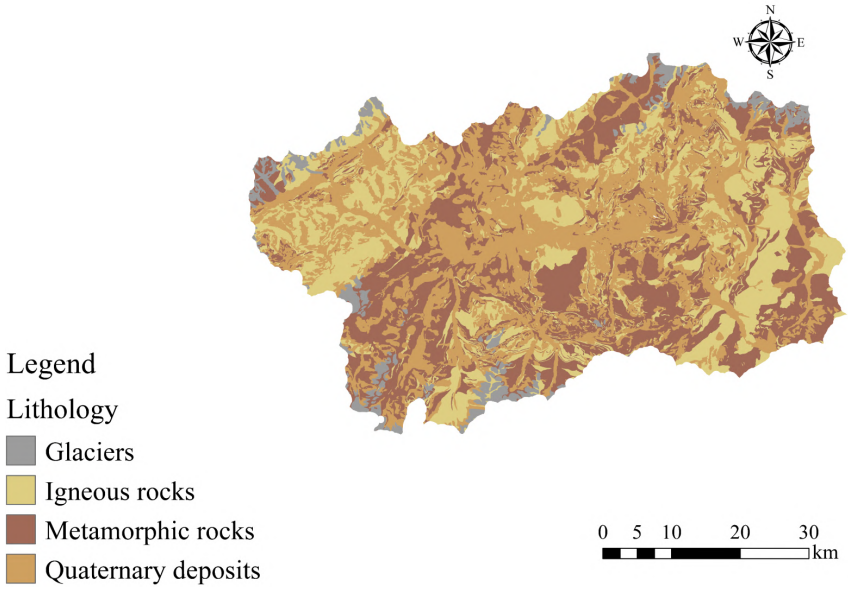

Figure 4-8 Lithology map of Aosta Valley.

The share of each class of lithology can be seen in Figure 4-9.

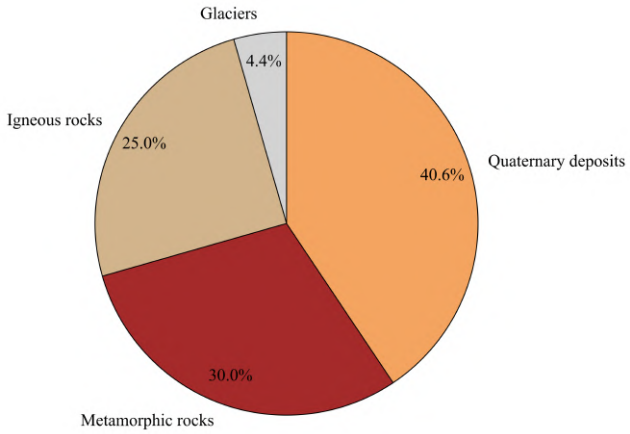

Figure 4-9 Distribution of each lithology class of in Aosta Valley.

Figure 4-10 shows that the majority of landslides occurred in areas classified as Quaternary deposits, which include landslide and glacial deposits that are generally loose and prone to failure. In contrast, during the study period, no landslides were recorded in areas classified as glaciers.

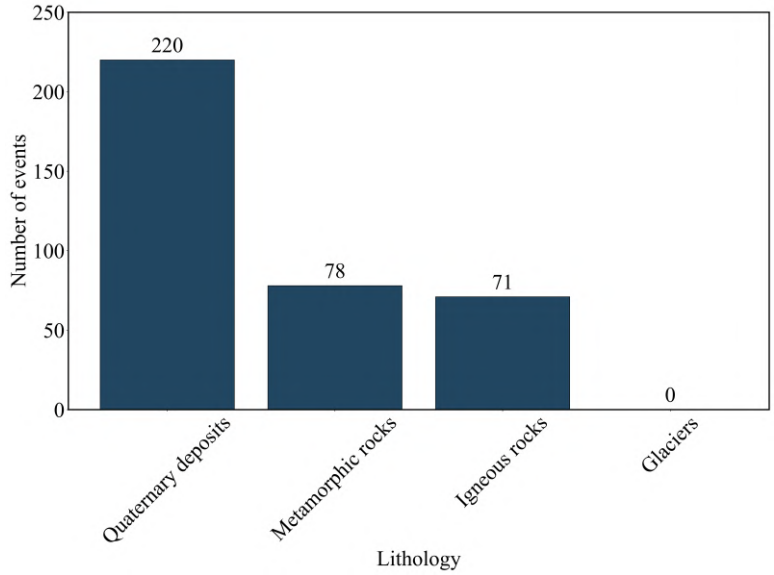

Figure 4-10 Landslide shares in each lithology class.

4.4.1.3 Normalized difference vegetation index

Normalized difference vegetation index (NDVI) is commonly employed to estimate how much vegetation exists at any given site. In some studies, NDVI is introduced as an important contributor factor, that even enhanced the machine learning model performance (Janizadeh et al., 2023; Niraj et al., 2023).

NDVI values for each pixel range between -1 and +1. Values close to -1 usually correspond to water bodies, clouds, or snow and ice surfaces (Weier and Herring, 2000). Values around zero indicate areas with little or no vegetation, such as bare soil or rocks. Higher positive values represent increasing vegetation density, with values between 0.8 and 0.9 typically indicating maximum green leaf density. The NDVI values were derived from the dataset provided by the CIMA Research Foundation, following Equation (4-6), defined in the literature (Yuan and Bauer, 2007):

$$NDVI = \frac{R_{\mathrm{NIR}} - R_{red}}{R_{\mathrm{NIR}} + R_{red}} \tag{4-6}$$

where R_{NIR} and R_{red} are the spectral reflectance in the near-infrared band and in the red band, respectively. Figure 4-11 shows the NDVI map of the region. The map has a 10 × 10 m per pixel resolution.

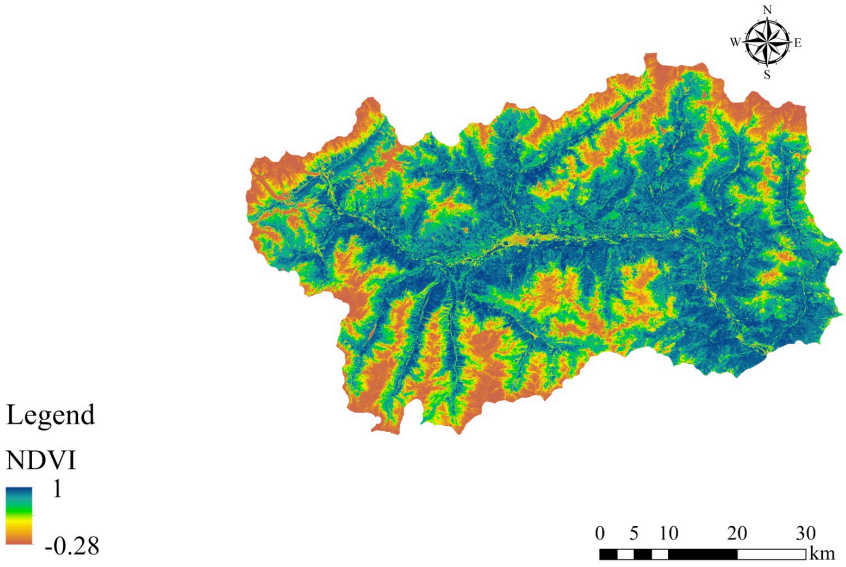

Figure 4-11 NDVI map of Aosta Valley.

4.4.1.4 Plan curvature

Curvature (plan and profile) derived from DEM represents the surface shape of the terrain. It allows to detect regions vulnerable to landslides, flooding, and other natural hazards, as well as to support the planning of transportation and infrastructure. Plan curvature is oriented perpendicular to the steepest slope direction. It reflects the convergence or divergence of flow across the terrain. As can be seen in Figure 4-12, a positive value (a) indicates the surface is laterally convex at that location, while a negative value (b) shows it is laterally concave. A value of zero represents a linear surface (c).

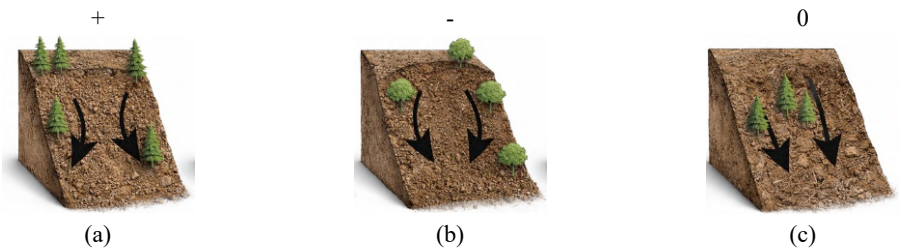

Figure 4-12 Plan curvature for (a) Positive and convex slopes (b) Negative and concave slopes, and (c) Zero and flat surface.

In the Aosta Valley, as shown in Figure 4-13, the minimum plan curvature value –379 indicates the most concave areas, while the maximum value 343

represents the most convex areas. The map has a spatial resolution of 10 x 10 m per pixel.

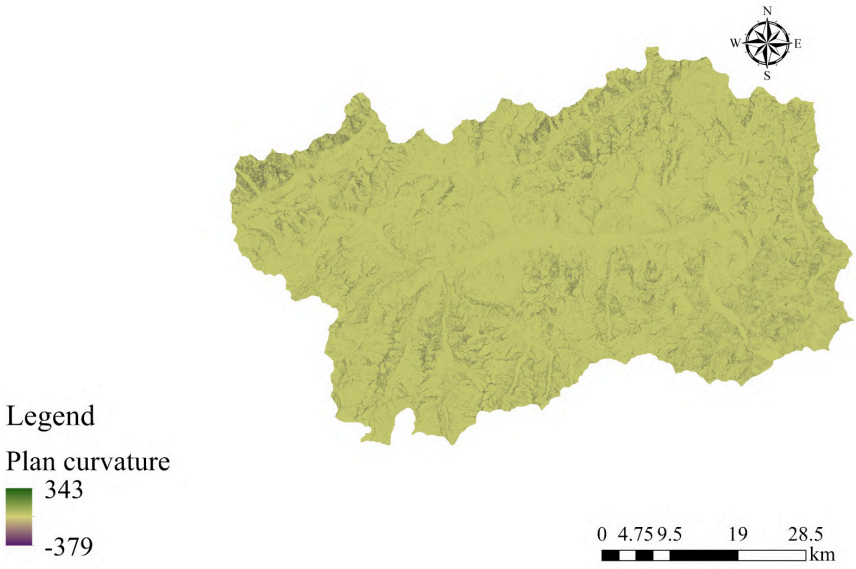

Figure 4-13 Plan curvature map of Aosta Valley.

4.4.1.5 Profile curvature

Profile curvature is also derived from DEM. It runs parallel to the slope and shows the direction of the steepest descent. It influences how flow accelerates or decelerates over the surface. As can be seen in Figure 4-14, A positive profile (a) means the surface is upwardly concave at that cell, causing flow to accelerate. A negative value (b) means the surface is upwardly convex at that cell and flow will be decelerated. A value of zero indicates a linear surface (c).

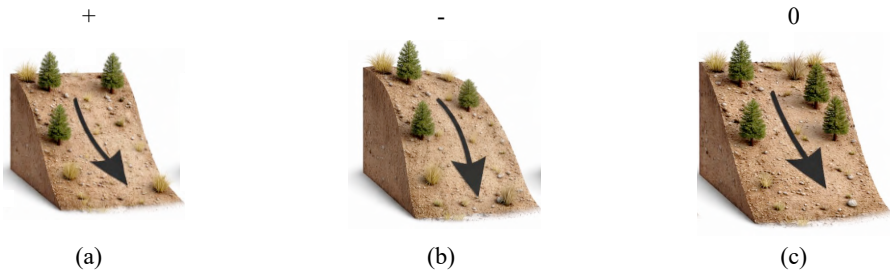

Figure 4-14 Plan curvature for (a) Positive and concave slopes, (b) Negative and convex slopes, and (c) Zero and flat surface.

Figure 4-15 illustrates profile curvature of the region. Each pixel on the map represents an area of 10 × 10 m.

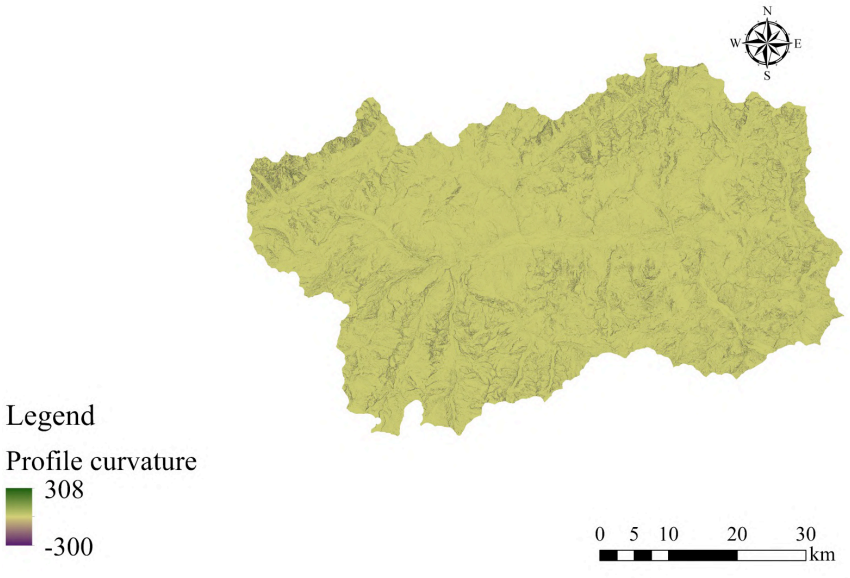

Figure 4-15 Profile curvature map of Aosta Valley.

4.4.1.6 Sediment Transport Index

The Sediment Transport Index (STI) indicates the likelihood of soil and sediment movement on slopes. Elevated STI values imply greater erosion and sediment transfer, which may play a role in triggering landslides in areas prone to instability (Mokhtari and Abedian, 2019; Öztürk, 2025). This index can be calculated from Equation (4-7) (Moore et al., 1991):

$$STI = \left(\frac{A_S}{22.13}\right)^m \cdot \left(\frac{\sin\beta}{0.0896}\right)^n \tag{4-7}$$

where A_s denotes the specific catchment area (m²/m), β is the slope angle (in radians), and m and n are empirical constants with values of 0.6 and 1.3, respectively. The Equation was implemented in GIS using the DEM of the study area to generate the STI map, as illustrated in Figure 4-16. The map's pixel size corresponds to 10 meters on each side. The generally low STI values observed in the study area indicate a relatively limited sediment transport capacity over most slopes. Since STI is a function of slope gradient and flow accumulation, higher values are concentrated along drainage networks and convergent flow paths, where the potential for sediment transport is greater.

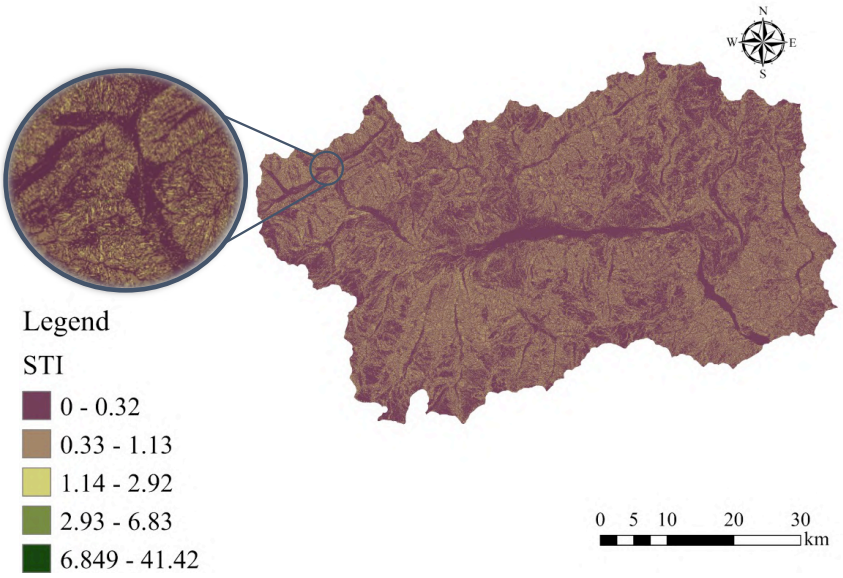

Figure 4-16 Sediment transport index map of Aosta Valley.

4.4.1.7 Slope

In mountainous areas, such as the Aosta Valley, the slope gradient plays a key role in determining landslide susceptibility. As slope angles become steeper, gravitational forces acting on slope materials intensify, leading to reduced stability and a higher likelihood of landslides. Figure 4-17 presents the slope map of Aosta Valley. Slope map is derived from DEM, and each pixel covers a 10 x 10 m area on the ground.

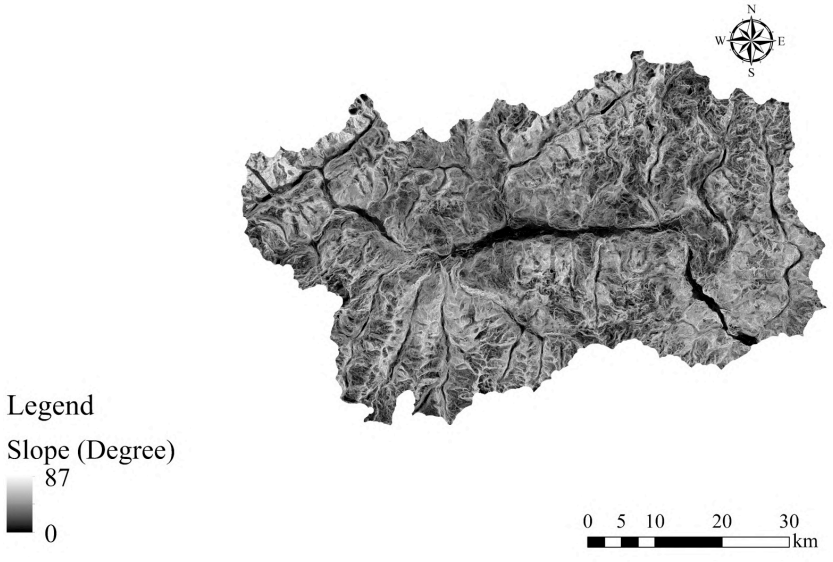

Figure 4-17 Slope map of Aosta Valley.

4.4.1.8 Soil type

Figure 4-18 shows the soil type of the region. The data was obtained from Aosta Valley Geoportal website (https://geoportale.regione.vda.it/). Soil type governs the mechanical and hydrological properties of slope materials, influencing key strength parameters such as cohesion, friction angle, and permeability, which in turn play a role in determining landslide susceptibility. The map has a spatial resolution of 10 meters by 10 meters per pixel.

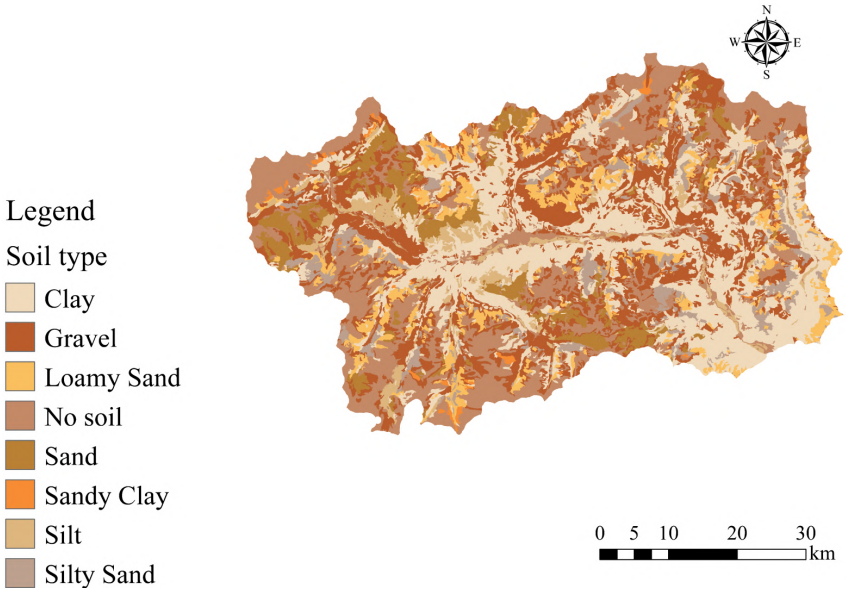

Figure 4-18 Soil type map of Aosta valley.

Figure 4-19 shows the share of each class of soil type in the region. No soil, clay, and sand comprise more than three-quarters of the area.

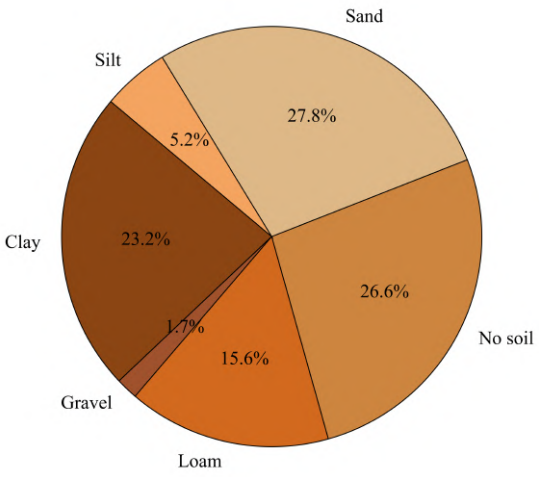

Figure 4-19 Distribution of each soil type class in Aosta Valley.

The statistics indicate that nearly 50% of landslides occurred in areas with clay soils (Figure 4-20). Although sand covers the largest portion of the region's surface (Figure 4-19), only a small proportion of landslides were associated with this soil type.

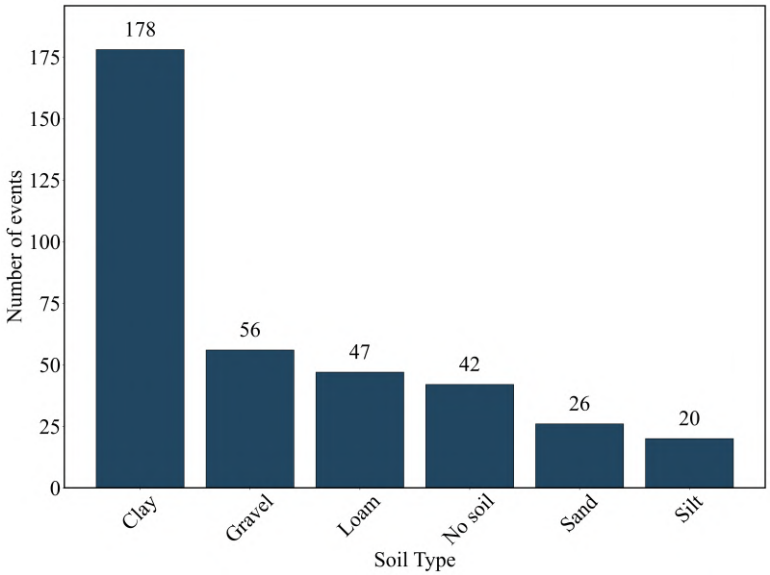

Figure 4-20 Landslide shares in soil type classes.

4.4.1.9 Stream power index

The Stream Power Index (SPI) is a derived topographic parameter that combines slope steepness with upslope contributing area. It reflects the relationship between flow pathways, flow accumulation, and terrain gradient, representing the potential erosive energy of surface water (Pawluszek and Borkowski, 2017). This parameter was also derived from DEM, which can be calculated from Equation (4-8) (Yilmaz, 2009):

$$SPI = A_s \cdot \tan(\beta) \tag{4-8}$$

where, A_s is the specific catchment area (m²/m), , and β is the local slope gradient in degrees. SPI values become negative when A_s is less than zero, which can occur for cells receiving surface runoff from outside the mapped area. Positive SPI values indicate areas where water flow has higher erosive potential due to a larger contributing area and steeper slopes, while negative values reflect boundary effects and do not represent actual erosive power within the study region (Moore et al., 1991). Figure 4-21 gives information about the SPI map of Aosta Valley. Each pixel on the map represents an area of 10 × 10 meters.

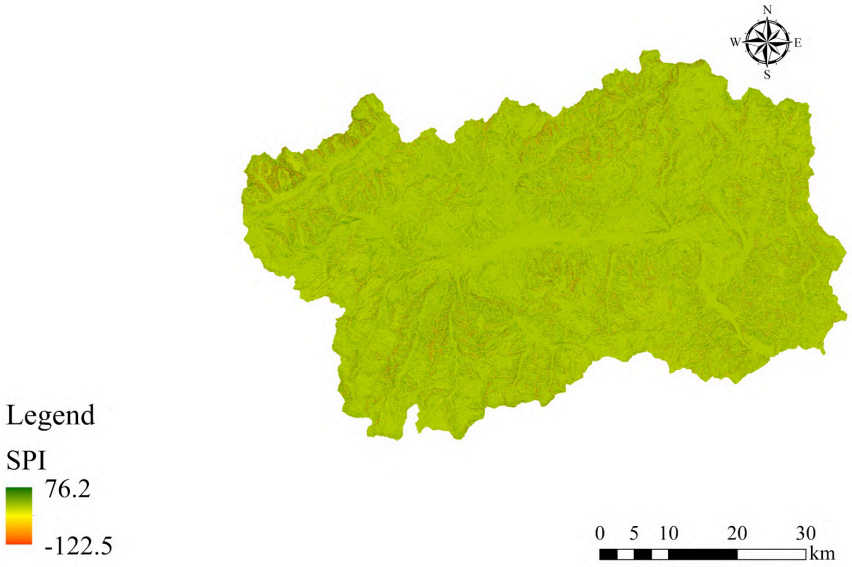

Figure 4-21 Stream Power Index of Aosta Valley.

4.4.2 Semi-static LCF

In this study, the only factor treated as semi-static is land cover. For the timeframe 2003–2022, the land cover dataset corresponding to the year 2018 is employed. The map corresponding to this dataset was used for training and testing the landslide events, and for generating the landslide susceptibility maps representing the current conditions. For the future period (2021–2040), however, the most recently updated land cover dataset available, corresponding to the year 2024, was adopted. In this way, the present susceptibility maps are based on land cover from 2018, while the future predictions rely on the updated 2024 land cover information. Both maps were obtained from ARPA Valle d'Aosta with a 10 × 10 m per pixel resolution (https://geoportale.regione.vda.it/).

4.4.2.1 Land cover

Figure 4-22 shows the land cover map of the region for 2018. Land cover can influence the mechanical strength of a slope. Vegetation, in particular, can increase the apparent soil cohesion through root reinforcement, where plant roots bind soil particles and provide additional tensile strength. In addition, vegetation can modify slope stability by altering mechanical loads (e.g., tree weight) and hydrological conditions (e.g., interception and evapotranspiration)(Likitlersuang et al., 2017; Masi et al., 2023; Pedone et al., 2016).

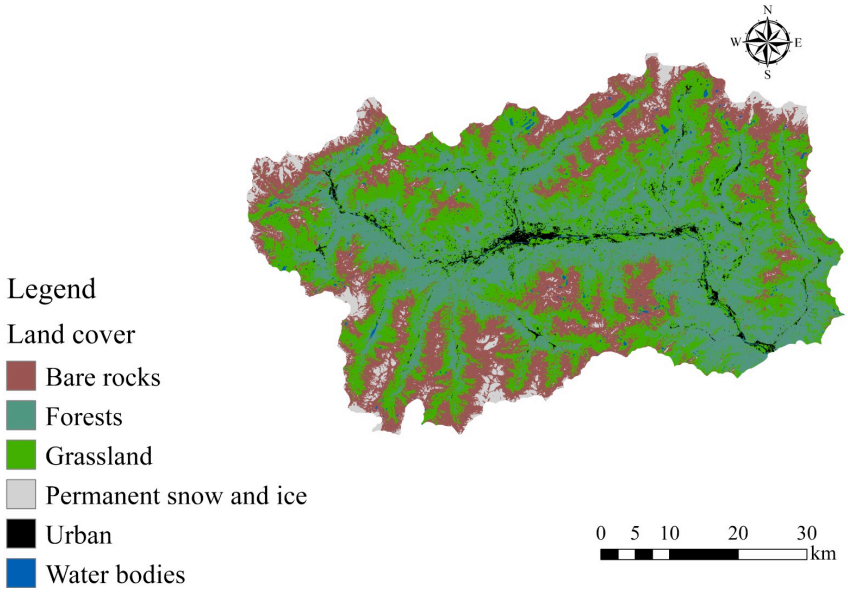

Figure 4-22 Land cover map of Aosta Valley in 2018.

Figure 4-23 presents the share of each land cover class in 2018. It can be seen that most of most of area is covered by grassland and forests (68% of total).

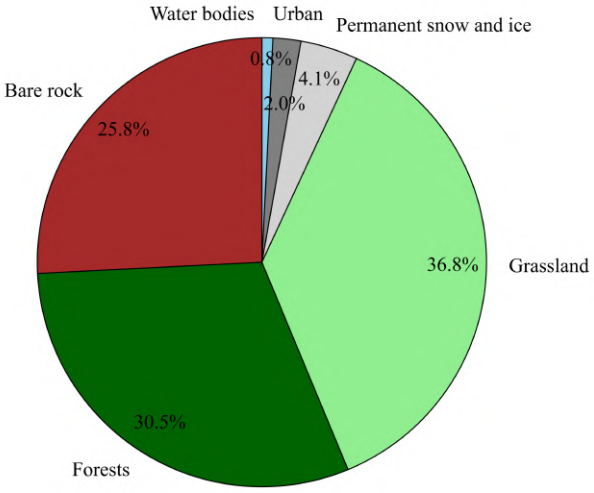

Figure 4-23 Distribution of each land cover class in Aosta Valley in 2018.

Grassland, which has the highest proportion of land cover (Figure 4-23), is the second group where landslides occurred. In fact, most of the selected landslides occurred where the land is covered with forests (Figure 4-24).

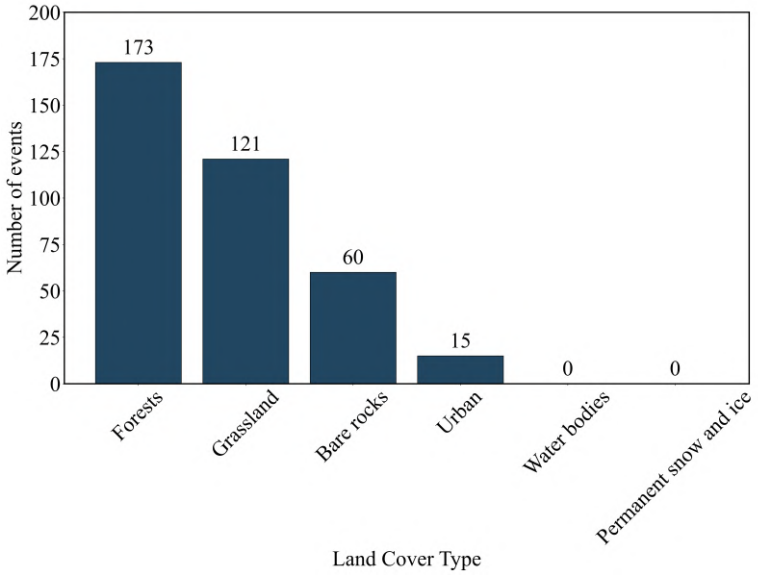

Figure 4-24 Landslide shares in land cover classes.

For the future time frame (2021–2040), the most recent land cover map available, corresponding to the year 2024, was used. Compared to the year 2018, the proportions of grassland and forest land cover types decreased to approximately 60%, while the area classified as bare rock increased by about 8%. Additionally, around 1.3% of the area previously covered by permanent snow and ice experienced melting during the same period. The changes are not clearly distinguishable in the map and show a pattern similar to Figure 4-22. Figure 4-25 presents the distribution of different land cover classes in 2024.

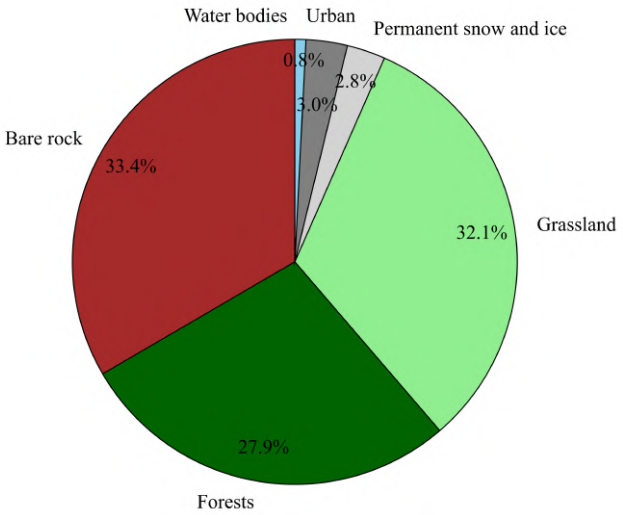

Figure 4-25 Distribution of each land cover class in Aosta Valley in 2024.

4.4.3 Dynamic LCFs

In this study, three dynamic LCFs were considered: monthly accumulated precipitation, seven-day precipitation, and monthly temperature. For the 2003-2022 period, the landslide susceptibility maps were generated using observational data obtained from meteorological stations provided by CIMA. For the near-future period (2021–2040), however, the research relies on projections from the Coupled Model Intercomparison Project Phase 6 (CMIP6), which integrates Shared Socioeconomic Pathways (SSPs) with Representative Concentration Pathways (RCPs). Specifically, the SSP 5-8.5 scenario was adopted, representing the worst-case trajectory of greenhouse gas emissions, using climate projections provided by the Centro Euro-Mediterraneo sui Cambiamenti Climatici (CMCC), the Italian institution participating in CMIP6. These future climate projections were obtained from the WorldClim version 2.1 climate database (https://www.worldclim.org/data/cmip6/cmip6_clim30s.html /).

The use of monthly precipitation maps is motivated by the limitations observed in the initial results, which were based on annual accumulated precipitation and showed lower validation accuracy. Consequently, shorter temporal intervals were adopted to better capture precipitation variability and improve model performance.

To identify the climate scenario under which precipitation and temperature changes are most critical, the different SSP scenarios were compared. The scenarios considered for the next 20 years include SSP1-2.6, SSP2-4.5, SSP3-7.0, and SSP5-8.5, each providing global-scale climate projections. To enable a regional comparison, monthly values were extracted for the Aosta Valley by masking the scenario maps to the study area.

Figure 4-26 presents the precipitation values for the historical period (2003–2022) and for the future period (2021–2040) under the different scenarios. A comparison between the two periods shows that no clear trend is observed during the first six months of the year. However, from July onward, the spatial mean precipitation values under the SSP5-8.5 scenario begin to increase. From September to December, this scenario consistently exhibits higher precipitation values compared to the other scenarios.

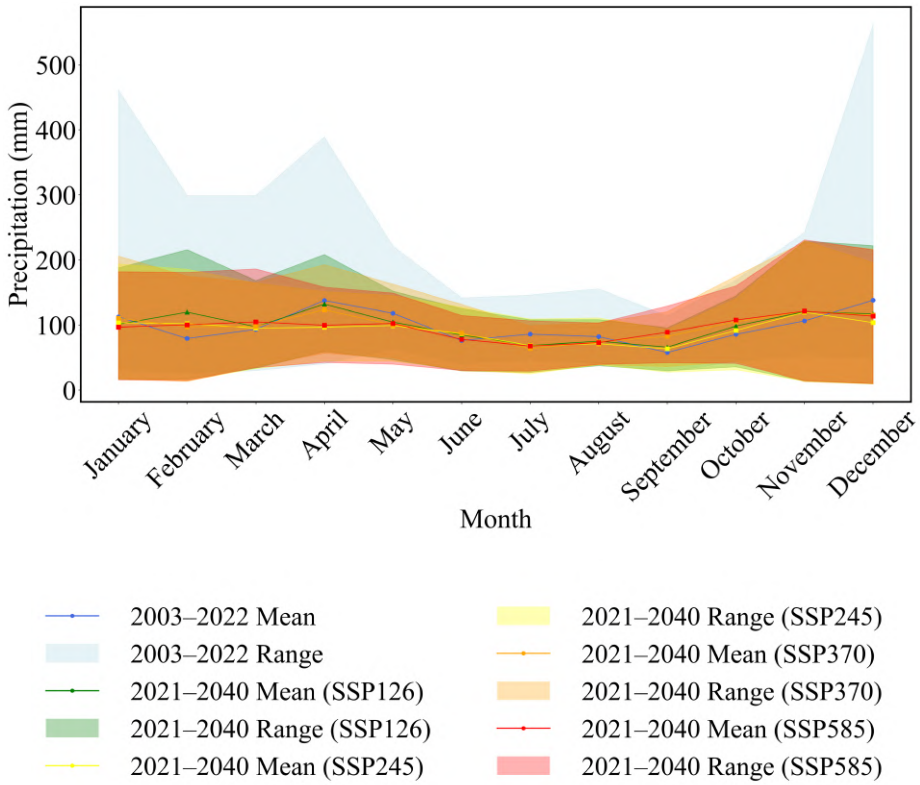

Figure 4-26 Monthly mean precipitation for the Aosta Valley during the historical period (2003–2022) and the future period (2021–2040) under different SSP scenarios. Shaded areas represent the range of spatial variability, while solid lines indicate spatial mean values.

As illustrated in Figure 4-27 for temperature, this trend becomes more pronounced. Among all scenarios, SSP5-8.5 shows the highest spatial mean temperature values. Additionally, the range between minimum and maximum temperature values in the future period becomes narrower, with both extremes shifting closer to the spatial mean compared to the 2003–2022 period.

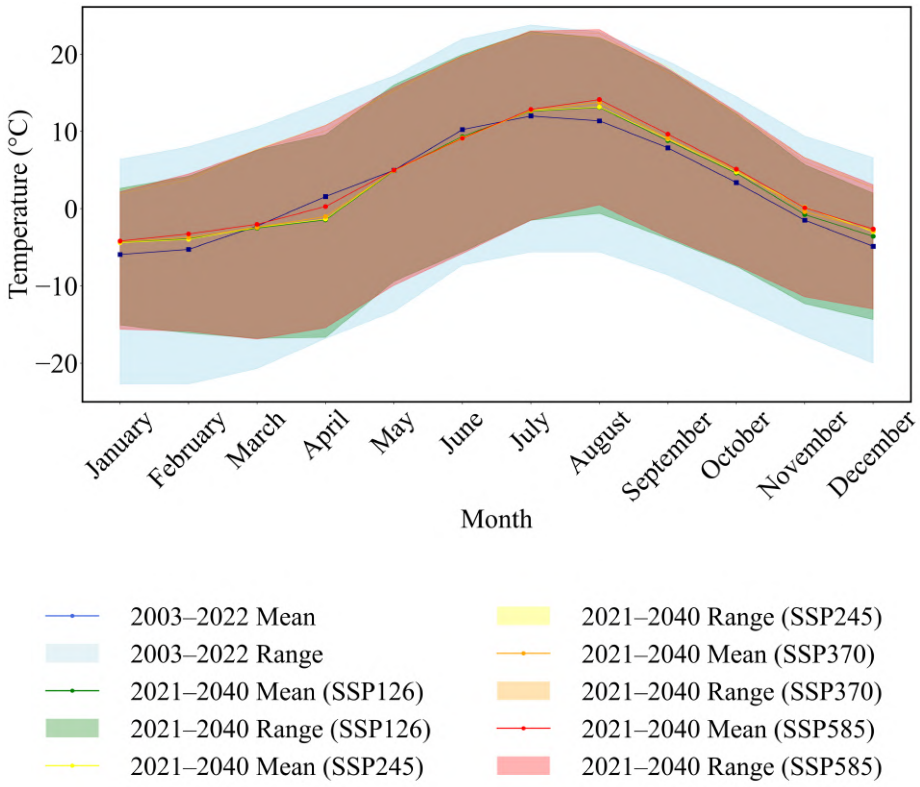

Figure 4-27 Monthly mean temperature for the Aosta Valley during the historical period (2003–2022) and the future period (2021–2040) under different SSP scenarios. Shaded areas represent the range of spatial variability, while solid lines indicate spatial mean values.

Based on the comparison of precipitation and temperature patterns across the considered scenarios, SSP5-8.5 was selected for the 2021–2040 period as the most critical scenario for further analysis. As shown in Figure 4-27, this scenario consistently exhibits higher spatial mean temperatures throughout the year compared to the other SSPs, indicating a more pronounced warming signal. In terms of precipitation, while no distinct trend is observed during the first half of the year (Figure 4-26), SSP5-8.5 shows a clear increase in spatial mean precipitation from July onward, with noticeably higher values during the second half of the year, particularly from September to December. Additionally, the reduced spread between minimum and maximum values under SSP5-8.5 suggests a more spatially consistent signal relative to the historical period. The combination of higher temperatures and increased late-year precipitation makes SSP5-8.5 the most representative scenario for assessing potential future impacts.

4.4.3.2 Monthly accumulated precipitation

This factor provides information about the total precipitation in the 30 days preceding each landslide event that occurred from 2003 to 2022. To elaborate, since the exact date of each landslide was available in the dataset, it was possible to

calculate the cumulative precipitation at the specific location of each event. This was achieved by analyzing 7,200 daily precipitation maps of the region, allowing for a precise assessment of the rainfall patterns leading up to the landslides. For all other pixels, including non-landslide events, precipitation was not associated with a specific event date. Instead, for each calendar month, a spatial map of mean monthly accumulated precipitation was generated based on the available records. Non-landslide samples were then assigned precipitation values by extracting the corresponding values from the monthly map of the same period. These monthly maps have a 288×207 m (north–south × east–west) per pixel resolution. As an example, Figure 4-28 presents the mean accumulated precipitation for January, averaged over the period 2003–2022.

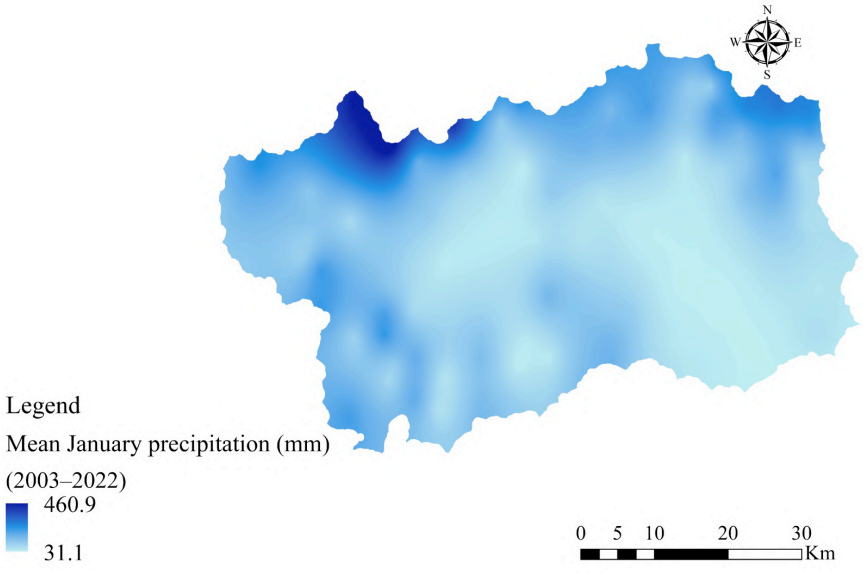

Figure 4-28 Mean January accumulated precipitation in 2003-2022.

Figure 4-29 presents the monthly maximum and minimum of mean accumulated precipitation, along with the mean spatial precipitation. The mean spatial values were calculated by averaging the pixel values across each map for every month.

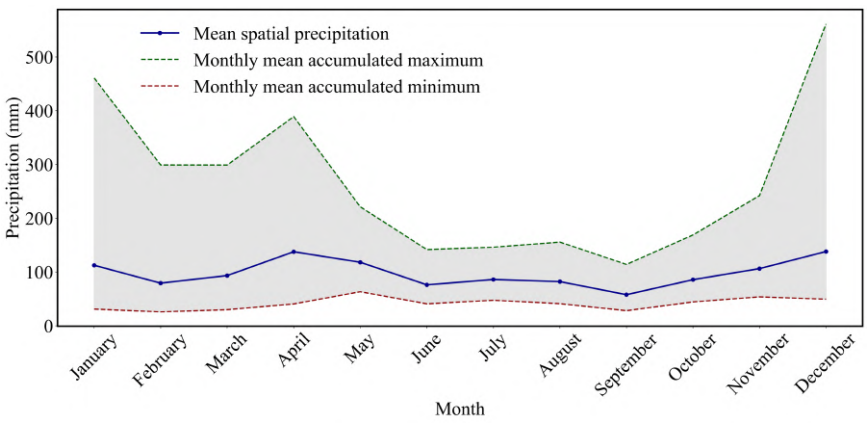

Figure 4-29 Monthly means accumulated precipitation values (mm) in 2003-2022.

Figure 4-30 shows the monthly total precipitation for January from 2021-2040. The cell size is approximately 927 m × 668 m (north–south × east–west).

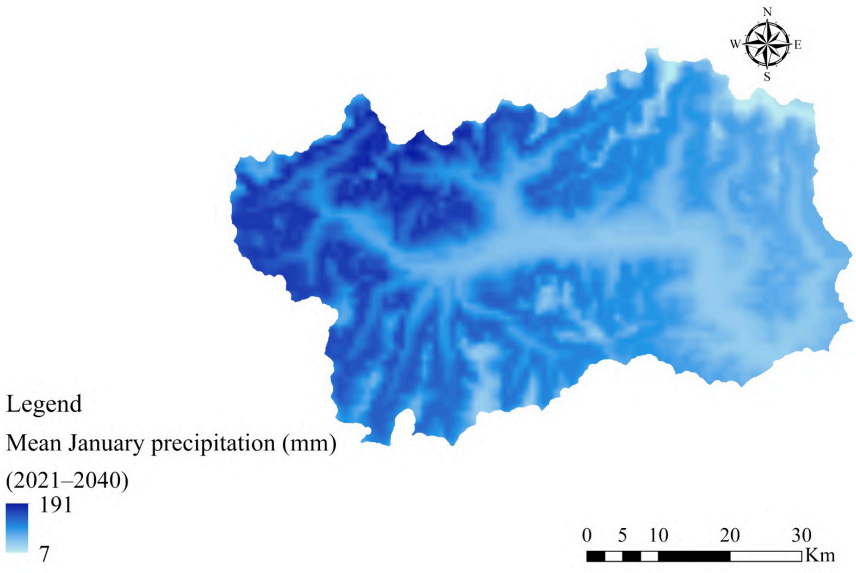

Figure 4-30 Mean January accumulated precipitation in 2021-2040.

Since Figure 4-30 is less smooth than Figure 4-28, the monthly precipitation maps were interpolated. For this purpose, a regular grid of points with a spacing of 5 km was generated over the study region, and precipitation data were extracted at each point. The extracted data were then interpolated across the entire region using the Kriging method with different semivariogram models. Among the tested models (Spherical, Exponential, Circular, Gaussian, and Linear), the Exponential model was selected because it provided the smoothest results and showed the greatest consistency with the existing precipitation data. Figure 4-31 presents the interpolated precipitation map.

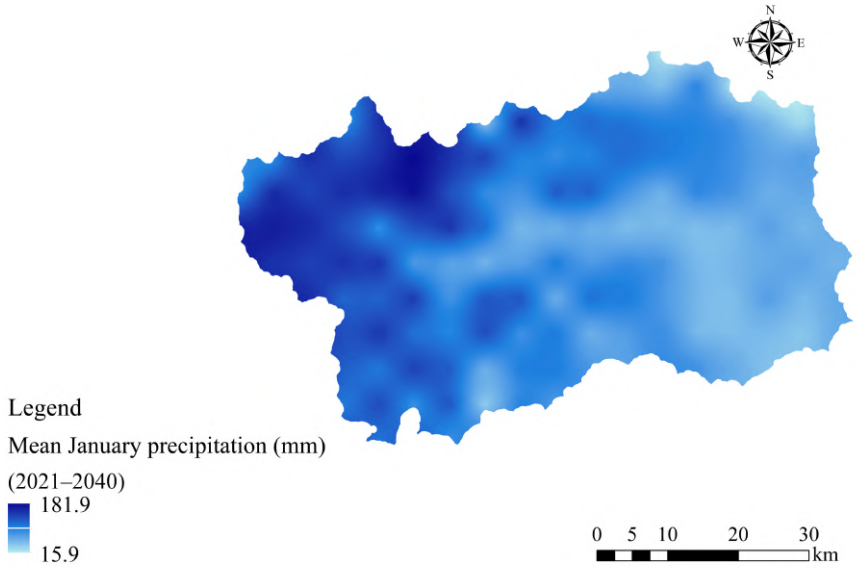

Figure 4-31 Interpolated mean January accumulated precipitation in 2021-2040.

Figure 4-32 illustrates the monthly maximum and minimum of mean accumulated precipitation, along with the mean spatial precipitation for 2021-2040 period. The mean spatial values were calculated by averaging the pixel values across each map for every month.

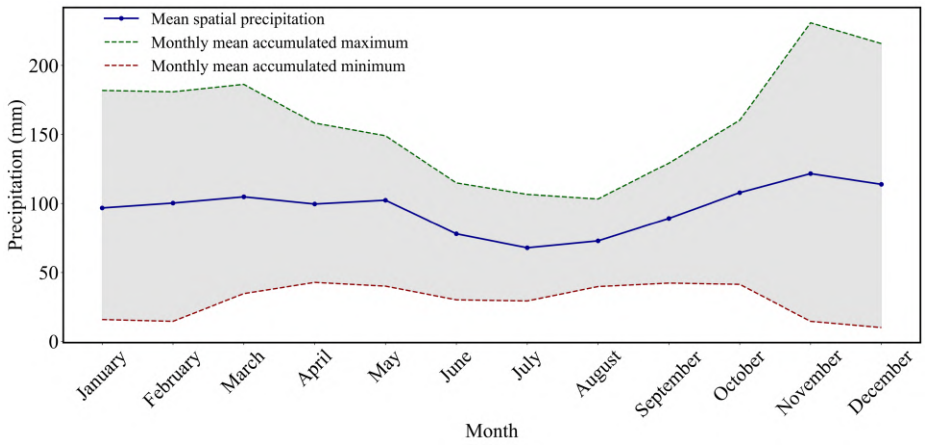

Figure 4-32 Monthly means accumulated precipitation values (mm) in 2021-2040.

4.4.3.3 Seven-day accumulated precipitation

Similar to the monthly precipitation, the seven-day precipitation was calculated by summing the precipitation totals for the seven days leading up to each landslide occurrence in the same time frame. This shorter time window provides insight into the influence of extreme precipitation events on landslide triggering. By focusing on this critical period, the analysis aims to capture the impact of intense, short-duration rainfall, which is often a key factor in slope instability and landslide

initiation. These precipitation data were also obtained from meteorological stations. The map has a spatial resolution of 288×207 meters per pixel.

For pixels where landslides occurred, the cumulative precipitation over the seven days preceding each of the 369 events was calculated using daily precipitation maps. However, to generate a spatially continuous seven-day precipitation map covering all pixels, including those without landslides, a generalized approach was adopted. Specifically, for each month, the ratio between the seven-day antecedent precipitation associated with landslide events and the corresponding total monthly precipitation was first computed (Figure 4-33). This ratio was applied to the average accumulated monthly precipitation map to estimate seven-day precipitation across the entire study area. This approach was adopted for two main reasons: (i) to derive spatially continuous precipitation values for all pixels, including non-landslide locations, and (ii) to ensure methodological consistency for future projections, where only monthly precipitation data are available rather than daily records.

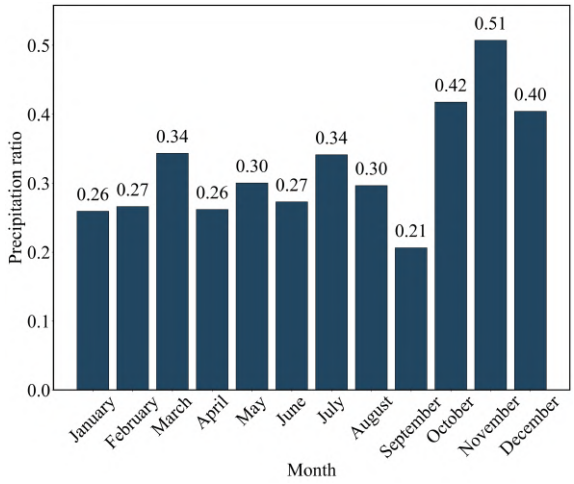

Figure 4-33 Ratio of seven-day to monthly precipitation derived from landslide events (2003-2022).

For example, Figure 4-34 shows the seven-day mean precipitation for January (2003–2022), calculated by multiplying the ratio of 0.26 from Figure 4-33 by the mean January precipitation for 2003–2022 (Figure 4-28).

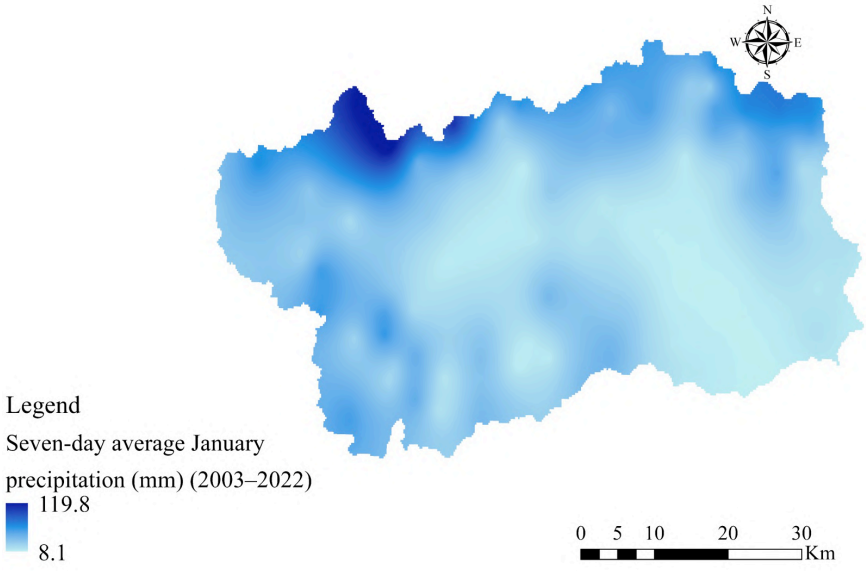

Figure 4-34 Average seven-day January precipitation in 2003-2022.

However, the ratios presented in Figure 4-33 may vary in the future under different climate scenarios. Kotlarski et al. (2023) analyzed regional climate models for the Northwestern, Northeastern, and Southern Alps under various greenhouse gas emission scenarios. As shown in Figure 4-35, the Aosta Valley falls within the Southern Alps subregion in their classification.

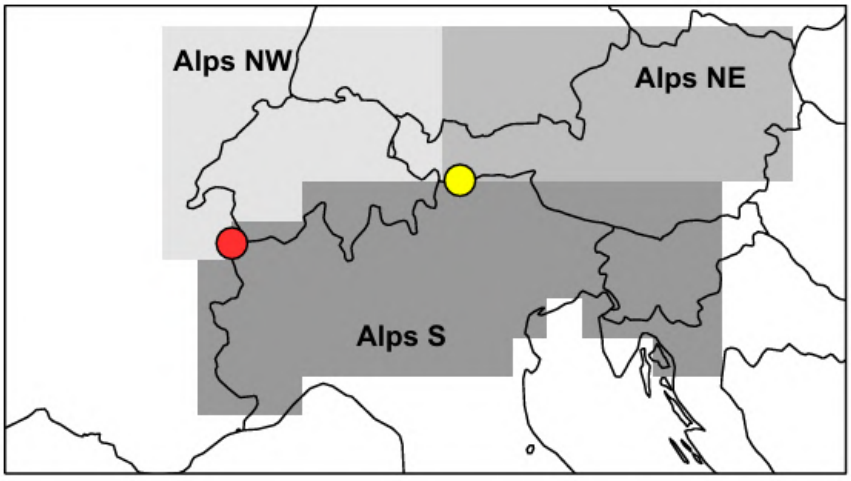

Figure 4-35 Subregions defined by Kotlarski et al. (2022) for spatially averaged analyses. Colored circles indicate the locations of the Mont-Blanc Massif (red) and the Ötztal Alps (yellow) (Kotlarski et al., 2023).

Their results indicate that wet-day frequency, precipitation intensity, and the seasonal maximum of daily precipitation events are all projected to change significantly between 1981–2010 and 2070–2099, depending on both the season and the climate scenario. Figure 4-36 shows projections for seasonal precipitation change in Alps South for different scenarios.

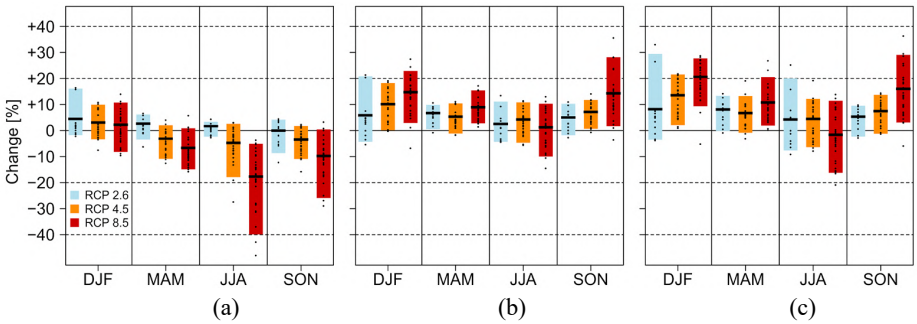

Figure 4-36 Seasonal change in precipitation characteristics [%] between 1981-2010 and 2070-2099 for the Southern Alps (Alps S) and for all three emission scenarios considered (color coding) for (a) Wet-day frequency, (b) Wet-day intensity, and (c) The average maximum daily event per season for Alps South (Kotlarski et al., 2023).

In our study, since the seven-day precipitation parameter is directly influenced by both precipitation frequency and intensity, we incorporated these two aspects under the RCP 8.5 scenario. Accordingly, by applying Equation (4-9), we adjusted the monthly ratios for 2003-2022 (Figure 4-28), to account for projected changes in frequency and intensity in 2021-2040, thereby obtaining updated ratios for the future time frame:

$$R_{7fut} = \left(1 + \Delta_{fre}\right) \times (1 + \Delta_{int}) \times R_{7hist} \tag{4-9}$$

where R_{7fut} represents the updated monthly ratio of seven-day accumulated mean precipitation to monthly accumulated mean precipitation for the near-future period (2021–2040). Δ_{fre} denotes the percentage change in precipitation frequency, while Δ_{int} represents the percentage change in precipitation intensity. R_{7hist} is the monthly ratio previously calculated for the historical period (2003–2022). Figure 4-37 shows the updated monthly ratios for 2021-2040.

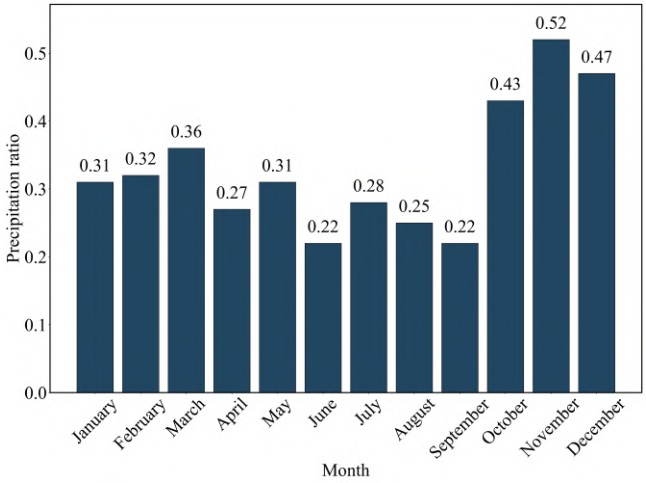

Figure 4-37 Ratio of seven-day to monthly precipitation (2021-2040).

By applying the updated ratios to the mean monthly precipitation for 2021–2040, the seven-day average precipitation for the same period was derived. Figure 4-38 illustrates this parameter for January.

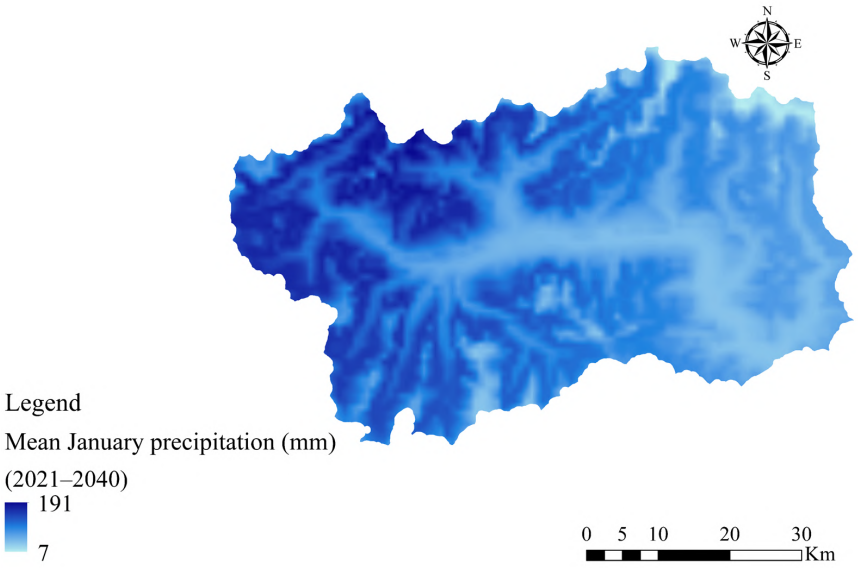

Figure 4-38 Average seven-day January precipitation in 2021-2040.

However, to ensure consistency with the approach applied to monthly precipitation, the seven-day precipitation values were interpolated. To this end, a regular grid of points with a spacing of 5 km was generated over the study region, and seven-day precipitation data were extracted at each grid point. These data were then interpolated across the entire region using the Kriging method, with an exponential semivariogram model. Figure 4-39 shows the resulting interpolated precipitation map.

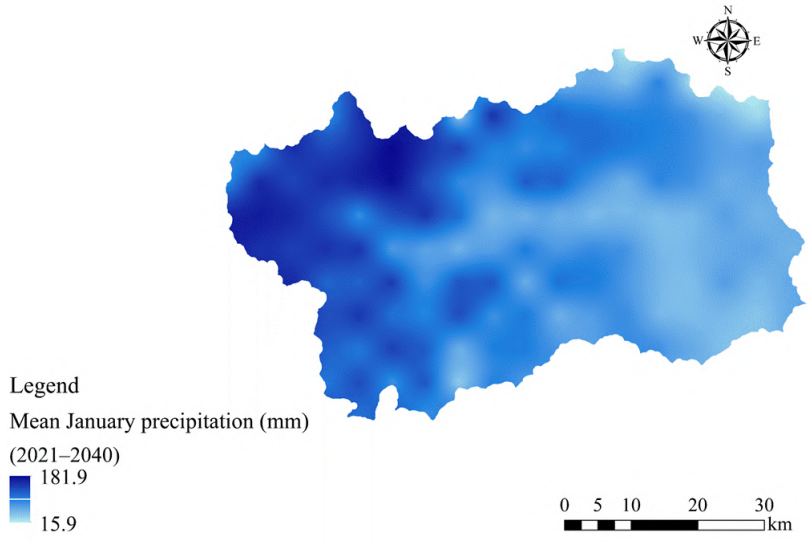

Figure 4-39 Interpolated seven day mean January accumulated precipitation in 2021-2040.

4.4.3.4 Monthly mean temperature

The average monthly temperature is another dynamic factor, defined here as the mean temperature over the 30 days preceding each landslide event that occurred between 2003 and 2022. Since the exact dates of the landslides were available, this factor was calculated by extracting and averaging the daily temperature values at each landslide location from the event date back to 30 days prior. Similar to precipitation, this calculation was based on a dataset of approximately 7,200 daily temperature maps spanning the study period. For the remaining pixels, encompassing non-landslide events, the monthly mean temperature values were used. Figure 4-40 shows January mean temperature with a 288×207 m (north–south × east–west) per pixel resolution.

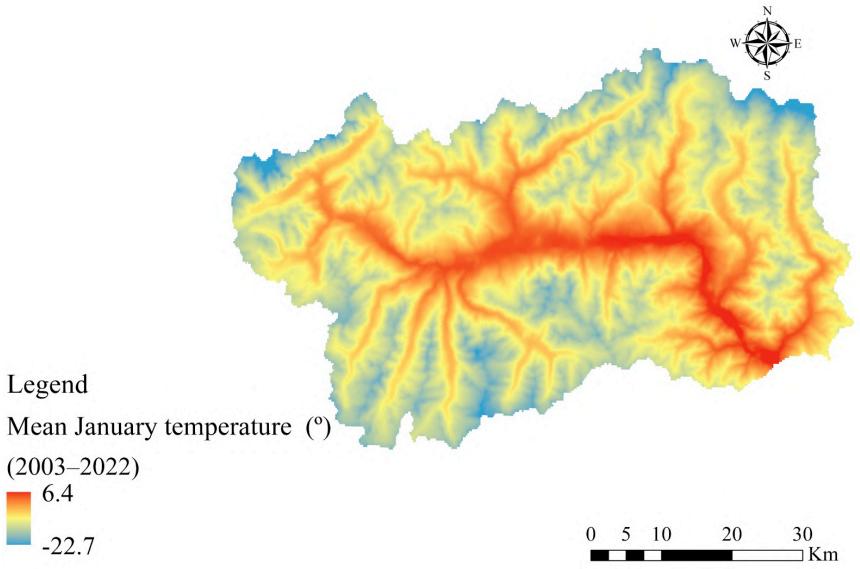

Figure 4-40 Mean January temperature in 2003-2022.

Figure 4-41 presents the monthly maximum and minimum of mean temperature, along with the mean spatial temperature in 2003-2022. The mean spatial values were calculated by averaging the pixel values across each map for every month.

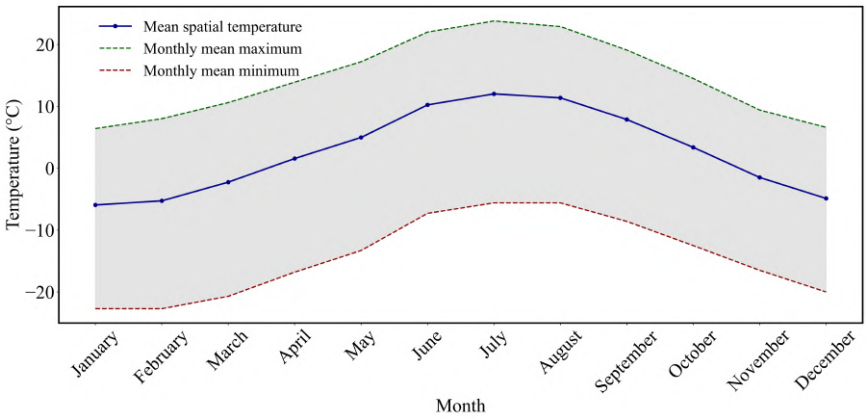

Figure 4-41 Monthly mean temperature values (°C) in 2003-2022.

Figure 4-42 shows the mean temperature for January from 2021-2040. The cell size is approximately 927 m × 668 m (north–south × east–west).

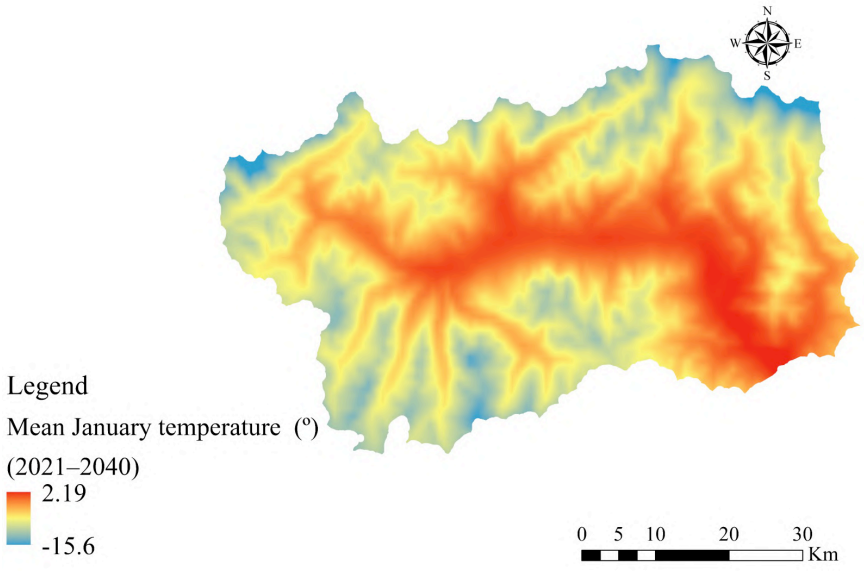

Figure 4-42 Mean January temperature in 2021-2040.

Figure 4-43 illustrates the monthly maximum and minimum of mean temperature, along with the mean spatial temperature in 2021-2040. The mean spatial values were calculated by averaging the pixel values across each map for every month.

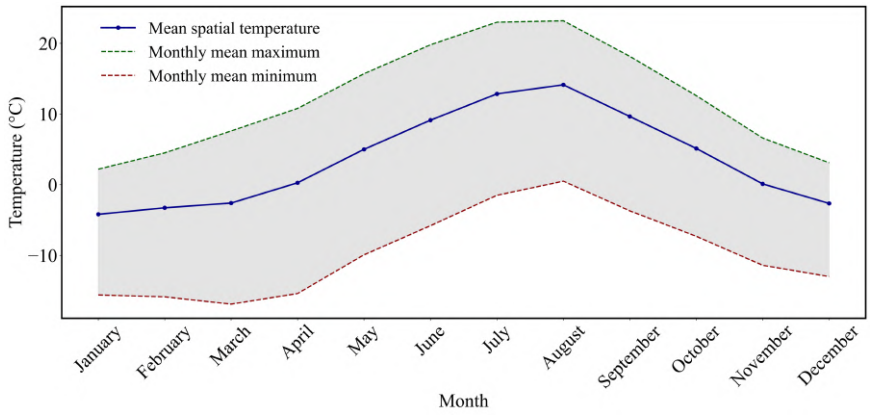

Figure 4-43 Monthly mean temperature values (°C) in 2021-2040.

4.5 Data processing

A balanced sampling ratio of 0.5:0.5 was adopted to ensure equal representation of landslide and non-landslide conditions. Given the availability of 369 mapped landslide events, an equivalent number of non-landslide points (369) was randomly selected. All LCFs were then overlaid with both landslide and non-landslide points, and the corresponding values were extracted. This procedure resulted in 12 distinct datasets, each comprising 738 rows (369 landslide and 369 non-landslide samples) and 14 columns, including 13 LCFs and one landslide occurrence variable (0 or 1).

Before splitting the dataset into training and testing sets, it is important to properly handle categorical LCFs such as “Aspect,” “Land Cover,” “Lithology,” and “Soil Type.” If these variables are simply converted into numerical values (e.g., assigning “Clay” as 6 and “Silt” as 1), the algorithm might incorrectly interpret the numerical order as implying a ranked or linear relationship. For instance, since more landslides may occur in areas with clay soil, the model could mistakenly learn that higher numeric values for soil type correspond to a higher probability of landslide occurrence. This introduces a bias that does not reflect the true nature of categorical data.

To address this issue, we applied one-hot encoding. This technique transforms each category into a separate binary feature, where a value of 1 indicates the presence of the category and 0 indicates its absence. One-hot encoding ensures that all categories are treated equally and avoids misleading assumptions about relationships between categories. It preserves the categorical nature of the data while making it suitable for machine learning algorithms.

The finest spatial resolution of the input data was 10 m × 10 m, resulting in the extraction of 30,781,552 pixels from each LCF map using GIS software. For the thirteen LCFs, this process produced a comprehensive dataset comprising 30,781,552 rows and 13 columns, which was subsequently used as input for the trained model. Although the data extraction stage was computationally intensive,

requiring approximately four hours, the subsequent model training, testing, and generation of LSMs were comparatively efficient, with each monthly LSM produced in approximately one hour.

4.6 Testing and training ratio

Each dataset was divided into training and testing subsets, with 70% of the data used for training and 30% for testing, consistent with previous studies (Janizadeh et al., 2023, 2024). To ensure temporal representativeness, the split was performed on a monthly basis. Specifically, landslide events from each month were proportionally distributed, with 70% assigned to the training set and the remaining 30% to the testing set. This approach prevents the exclusion of any month from the training phase and ensures that the model is exposed to representative samples across all temporal conditions.

4.7 XGBoost algorithm

Initial results indicated that among the three algorithms of Random Forest (RF), Support Vector Machine (SVM), and Extreme Gradient Boosting (XGBoost), the XGBoost algorithm achieved the highest validation accuracy. Therefore, XGBoost was selected for further analysis.

As explained in previous chapter (in section 3.7.6.5), XGBoost refers to a machine learning technique developed by Friedman that builds models in a sequential manner, optimizing performance through gradient descent (Friedman, 2001).

4.8 Multicollinearity

In our study, to prevent issues arising from multicollinearity, Variance Inflation Factor (VIF) was calculated for each month (see 3.7.7 Multicollinearity). “Elevation”, “Seven days temperature” and “TWI” (Topographic Wetness Index), which were initially included as LCFs, exhibited high VIF values and were therefore excluded from the analysis.

“Elevation” was strongly correlated with “Temperature,” which is expected given the known inverse relationship between altitude and temperature. Its inclusion in the model negatively influenced the estimated effect of temperature. Similarly, “Seven days temperature” exhibited high correlation with “Temperature” due to their closely aligned values. “TWI” (Topographic Wetness Index) also showed significant correlation with both “Elevation” and “Temperature”, contributing to multicollinearity in the dataset.

After assessing the VIF, these parameters were excluded from the model to mitigate multicollinearity. Since the dataset for each month is distinct and independent, VIF was calculated separately for each monthly dataset. It was ensured that all remaining variables in each month's model had VIF values below the commonly accepted threshold of 5.

4.9 Hyperparameter tuning

Each of the 12 datasets is independent of the other. Hyperparameters in each algorithm are different and tuning them makes the model work properly. Hyperparameters in XGBoost algorithm are: “n_estimators”, “learning_rate”, “max_depth”, “min_child_weight”, “subsample”, “colsample_bytree”, “reg_alpha”, “reg_lambda”,“gamma”, “scale_pos_weight”, “early_stopping_rounds”.

“n_estimators” defines the number of boosting rounds or trees to be built sequentially. A higher value can improve learning but increases training time. “learning_rate” controls how much each tree contributes to the final prediction. Lower values make the model learn slowly and more cautiously, often requiring more trees to reach good performance. “max_depth” sets the maximum depth of each decision tree. Deeper trees can model more complex patterns, but are also more likely to overfit the training data. “min_child_weight” specifies the minimum sum of instance weights (hessian) needed in a child node. Higher values lead to more conservative models by preventing the algorithm from learning relations that might be highly specific to the training data. “subsample” is the fraction of the training data randomly sampled for each tree. It helps prevent overfitting by adding randomness and reducing model variance. “colsample_bytree” is the fraction of features (columns) randomly sampled to grow each tree. Lower values help reduce overfitting and improve generalization, especially with high-dimensional data. “reg_alpha” is the L1 regularization term on weights, which adds a penalty for the absolute value of coefficients. It encourages sparsity in feature weights, effectively helping with feature selection. “reg_lambda” is the L2 regularization term on weights, penalizing large coefficients by adding the square of weights to the loss function. It helps smooth the model and control complexity to reduce overfitting. “gamma” is the minimum loss reduction required to make a further partition on a leaf node. Larger values make the algorithm more conservative by requiring greater improvement to split. “scale_pos_weight” adjusts the balance between positive and negative classes, especially useful in imbalanced datasets. It helps the model give more attention to the minority class during training. “early_stopping_rounds” stops training if the model doesn’t improve on the validation set after a fixed number of rounds. It prevents overfitting and reduces training time by avoiding unnecessary trees.

There are different methods to optimise and tune the parameters. In our study, we used the Grid Search method to find the optimal value of each hyperparameter. This method selects the combination that gives the best performance on a validation set or through cross-validation. Table 4-2 shows the range of parameter in the models.

Table 4-2 Selected hyperparameter values for XGBoost model configuration.

Hyperparameter	Range
n_estimators	100-1000
learning_rate	0.01-0.1
max_depth	3-8
min_child_weight	1-10
subsample	0.6-0.8
colsample_bytree	0.8
reg_alpha	0-1
reg_lambda	1-3
gamma	0-2
scale_pos_weight	1
early_stopping_rounds	100-200

4.10 Models' validation

Model validation was conducted using two complementary approaches. The first method employed the Receiver Operating Characteristic (ROC) curve and the corresponding Area Under the Curve (AUC), a widely used metric in similar studies. Each of the 12 models produced a distinct AUC value, reflecting variations in model performance associated with the complexity of the monthly datasets.

The second approach involved validation of the envelope susceptibility map, which is proposed specifically in this study. After generating 12 monthly landslide susceptibility maps, an envelope map was constructed by selecting the maximum susceptibility value for each pixel across all maps. This envelope map was then

validated using an independent set of landslide events that were not included in either the training or testing datasets and occurred in 2023. These events were overlaid onto the envelope map to assess whether their locations corresponded to areas classified as high or very high susceptibility.

4.11 Feature importance and SHAP

Since twelve different models are developed in this study, each model yields its own distinct feature importance ranking. Furthermore, as discussed in section 3.7.10, SHAP (Lundberg and Lee, 2017) is a recently proposed method for interpreting machine learning model predictions based on Shapley values. Because SHAP requires a trained model as input, it is also computed separately for each of the twelve models, resulting in twelve corresponding sets of SHAP values.

4.12 Summary

This chapter has outlined the methodological framework adopted in this Thesis to develop updated and enhanced monthly landslide susceptibility maps under both current and future climate conditions, using machine learning techniques. The landslide conditioning factors (LCFs) were introduced and classified into three main groups: static, semi-static, and dynamic. A summary of these factors, along with their corresponding data sources, is provided in Table 4-3.

The landslide inventory, consisting of 369 events recorded between 2003 and 2022, formed the basis of the analysis. To balance the dataset, an equal number of non-landslide points were randomly selected, resulting in 738 samples used for training and testing the XGBoost algorithm. For each sample, data corresponding to the LCF maps were extracted, enabling the model to be trained. Once trained, the model was applied to the full dataset of approximately 30 million pixels, allowing for a spatially exhaustive evaluation. The outcomes, presented as monthly landslide susceptibility maps for the period 2003–2022, will be discussed in the following chapter.

For the future projections, the analysis considered the worst-case climate scenario (SSP5-8.5). The dynamic factors for the period 2021–2040 were extracted accordingly and prepared for evaluation using the trained algorithm. The results of this analysis, namely the projected monthly landslide susceptibility maps under future climate conditions, will also be presented in the next chapter.

Table 4-3 Summary of Landslide conditioning factors (LCFs).

Number	LCFs	Source	Size
1	Aspect	DEM	10 × 10 m
2	Lithology	geoportale.regione.vda.it	10 × 10 m
3	NDVI	CIMA Research Foundation	10 × 10 m
4	Plan curvature	DEM	10 × 10 m
5	Profile curvature	DEM	10 × 10 m
6	STI	DEM	10 × 10 m
7	Slope	DEM	10 × 10 m
8	Soil type	geoportale.regione.vda.it	10 × 10 m
9	SPI	DEM	10 × 10 m
10	Land cover	arpa.vda.it	10 × 10 m
Current			
11	Monthly accumulated precipitation	Meteorological stations (Provided by CIMA Research Foundation)	288×207 m
12	Seven-day accumulated precipitation		
13	Mean monthly temperature		
Future			
11	Monthly accumulated precipitation	WorldClim.org	927×668 m
12	Seven-day accumulated precipitation		
13	Mean monthly temperature		

Chapter 5

Landslide susceptibility maps

5.1 Introduction

In this chapter, landslide susceptibility maps (LSMs) for each month, along with their future projections are presented. To represent the worst-case scenario throughout the period, a landslide susceptibility envelope map is also provided. This map is generated by assigning to each pixel the maximum susceptibility value recorded across all twelve-monthly maps. It offers a practical tool for authorities to easily identify and prioritize areas most prone to landslides.

5.2 Current period (2003-2022)

The algorithm was trained and tested using data from 369 landslides over a 20-year period, along with an equal number of non-landslide instances. For each month, monthly and seven days accumulated precipitation and monthly mean temperature data were evaluated, in addition to static variables such as slope, soil type, and other relevant factors.

Figure 5-1 to Figure 5-13 present the monthly landslide susceptibility maps. For each month, Area Under the Curve (AUC) of Receiver Operating Characteristic (ROC) values, feature importance plots, and Shapley Additive Explanations (SHAP) have been computed separately to evaluate and interpret the model's performance and the influence of individual predictors. In SHAP summary plots, the horizontal axis represents the SHAP values, while the vertical axis shows the input features used in the model prediction. The color indicates the feature value, where red represents higher values and blue represents lower values. Each point in the plot corresponds to a single observation from the training dataset.

Since the seven-day accumulated precipitation represents a fraction of the monthly accumulated precipitation (Figure 4-33), it was not included in the figures.

5.2.1 January

In January (Figure 5-1), precipitation and temperature levels generally do not pose a significant threat for slope instabilities. Although precipitation amounts are high (Figure 4-29), with a spatial mean of 112.63 mm, temperature is typically low, with spatial mean value around -6°C, for most of it to fall as snow rather than rain across much of the region.

Moreover, the results indicate that only approximately 0.53% of the area was classified as "Very high" and "High" susceptibility, whereas 96.5% was categorized as "Very low" and "Low". The AUC for this month reached a value of 0.986, which is the highest among all months, demonstrating the model's excellent ability to distinguish between landslide and non-landslide events during this period. Temperature emerged as the most influential factor in January. According to SHAP analysis, temperature exhibited a direct relationship with landslide occurrence. This finding shows that, despite significant precipitation during January, the probability of landslides increases with rising temperatures, likely due to the enhanced rainfall (as opposed to snowfall) and the accelerated melting of snow.

5.2.2 February

In February (Figure 5-2), mean monthly precipitation remains relatively high (Figure 4-29), with the mean spatial of 79 mm, while temperatures begin to rise, reaching up to a mean spatial value of -5.2 °C. The LSM reveals that approximately 1.5% of the area falls under the "Very high" and "High" susceptibility classes, compared to around 93.3% classified as "Very low" and "Low". This suggests a slight deterioration in slope stability conditions, indicating an increased potential for landslide occurrences relative to January.

The model maintains strong predictive performance during this month, with the AUC only slightly decreasing to 0.971, which still indicates excellent classification ability. Consistent with the previous month, temperature remains the most influential factor, followed by land cover and slope. SHAP analysis further confirms that temperature and slope exhibit a direct relationship with landslide occurrence. In particular, the gradual temperature increase likely contributes to snowmelt and a higher proportion of precipitation falling as rain, thereby elevating the risk of slope failures.

5.2.3 March

In March (Figure 5-3), precipitation and temperature levels increase compared to those observed in February, with a mean spatial of 93 mm and -2.2 °C, respectively (Figure 4-29 and Figure 4-41). Approximately 6% of the area is now classified under the “Very high” and “High” susceptibility categories, while the proportion of “Very low” susceptibility area decreases to 84.7%. This shift reflects a worsening of slope stability conditions as the warming trend continues.

The model's performance remains strong, with the AUC decreasing slightly to 0.970, still indicative of high predictive accuracy. Temperature continues to be the most influential factor, showing a direct relationship with landslide occurrence, as confirmed by SHAP analysis. The elevated temperatures likely accelerate snowmelt and increase rainfall, both of which enhance soil saturation and slope instability, thereby posing a greater risk for landslides.

5.2.4 April

In April (Figure 5-4), both precipitation and temperature show a significant increase, reaching up mean spatial values to 137.7 mm and 1.56 °C, respectively. These climatic conditions contribute to a marked rise in landslide susceptibility, making April one of the most critical months for slope instability. Approximately 20% of the area is classified as “Very high” and “High” susceptibility, while around 53% falls within the “Very low” and “Low” categories.

The AUC for this month experiences a more noticeable decline, dropping to 0.950. This reduction in model performance may be attributed to the similarity between the precipitation (both monthly and seven-day cumulative) and temperature values of landslide and non-landslide records in the dataset, making it more challenging for the algorithm to effectively distinguish between the two classes. For this month, land cover, slope, and NDVI emerge as the most influential factors contributing to landslide occurrence.

5.2.5 May

In May (Figure 5-5), although the mean spatial precipitation decreases by 20 mm to 118 mm, which is still a high value, the spatial mean temperatures rise significantly to 5 °C. These conditions contribute to May being identified as the most susceptible month for landslide occurrence. Over 21% of the area is classified under the “Very high” and “High” susceptibility zones, while less than 54% falls within the “Very low” and “Low” categories.

The model's predictive performance decreased gradually, reaching an AUC of 0.941 compared to April. Seven-day cumulative precipitation is the most important factor, followed by soil type and slope.

5.2.6 June

In June (Figure 5-6), temperature values continue to rise, reaching a spatial mean of 10.2°C, while precipitation levels decrease significantly to 76 mm. This decline in rainfall leads to a reduction in landslide-prone areas, with the proportion of the region classified as "Very high" and "High" susceptibility decreasing to 13.3%. Conversely, areas categorized as "Very low" and "Low" susceptibility increase to around 59%.

The model's performance shows a slight drop, with the AUC decreasing to 0.933. During this month, seven-day cumulative precipitation, slope and monthly precipitation, emerge as the most influential factors. SHAP analysis shows a direct relationship of these features with landslide occurrence. Interestingly, NDVI values suggest that areas with denser vegetation are more prone to landslides in this period, possibly due to increased soil moisture retention or vegetation type and coverage associated with vulnerable terrain.

5.2.7 July

In July (Figure 5-7), the overall environmental conditions closely resemble those of June, with spatial mean precipitation and temperature values increase marginally to 86 mm and 12 °C (Figure 4-29 and Figure 4-41). As a result, the spatial distribution of landslide susceptibility also shows minimal variation. Approximately 14% of the area is classified within the "Very high" and "High" susceptibility categories, nearly identical to the previous month. Similarly, the "Very low" and "Low" susceptibility zones cover about 57% of the region.

The model's performance exhibits a slight decline, with the AUC decreasing by 0.002, reaching 0.931 which is the lowest compared to other months. During this period, the most influential factors contributing to landslide susceptibility are monthly and seven days accumulated precipitation, and slope, respectively. These results highlight the continued importance of precipitation-related variables in controlling slope stability during the summer months.

5.2.8 August

In August (Figure 5-8), both spatial mean precipitation and temperature decreased slightly, dropping to 82 mm and 11.3 °C. These minor changes in climatic conditions result in a relatively stable landslide susceptibility distribution.

Approximately 13% of the area falls within the “Very high” and “High” susceptibility classes, while around 56% is categorized as “Very low” and “Low.”

The model's performance remains steady, with the AUC at 0.931, indicating consistently high predictive capability. The three most influential factors in landslide prediction for August are soil type, monthly precipitation, and seven-day cumulative precipitation. The presence of precipitation-related factors among the top three during the summer months highlights their dominant and consistently influential role in controlling landslide susceptibility across the region.

5.2.9 September

In September (Figure 5-9), both spatial mean precipitation and temperature declined to 58 mm and 7.9°C (Figure 4-29 and Figure 4-41), contributing to a reduction in landslide susceptibility across the region. However, localized zones of very high susceptibility persist in the northwestern part of the study area, corresponding to areas with the highest precipitation values. This can be attributed to the dominant influence of seven-day cumulative and monthly precipitation, which maintain elevated soil moisture conditions, and the still relatively moderate temperatures in September, which together create favorable conditions for slope failure. The proportion of the area classified as “Very high” and “High” susceptibility decreases to approximately 7.3%, while the share of “Very low” and “Low” susceptibility zones increases to 69%, indicating improved slope stability compared to the previous month.

The model’s performance improves accordingly, with the AUC rising to 0.948, suggesting that landslide and non-landslide events are more easily distinguishable under these conditions. Seven-day cumulative precipitation, followed by monthly precipitation and land cover, emerge as the most important contributing factors.

5.2.10 October

In October (Figure 5-105-11), although the spatial mean temperature decreased to 3.3 °C, that of precipitation increased remarkably, reaching 86 mm. This rise in precipitation contributes to heightened landslide susceptibility, with approximately 15.6% of the region classified under the “Very high” and “High” susceptibility categories. Nevertheless, a considerable portion of the area, around 54%, remains within the “Very low” and “Low” susceptibility classes.

The model’s performance experiences a slight grow, with the AUC reaching to 0.95. Soil type emerges as the most important variable, followed by seven-day cumulative precipitation and slope.

5.2.11 November

Although precipitation increases in November (Figure 5-12), reaching a spatial mean monthly value of 106 mm, the temperature drops markedly, with a spatial mean of –1.5 °C (Figure 4-29 and Figure 4-41). This substantial temperature decrease contributes to a reduction in landslide susceptibility. Consequently, the proportion of the area classified as "Very high" and "High" susceptibility declines to about 8%, while approximately 77.5% of the region falls into the "Very low" and "Low" categories.

The model's performance shows an increase in AUC to 0.968. However, the feature importance ranking changes: temperature becomes the most influential factor, while seven-day cumulative precipitation rises to second place, and monthly precipitation shifts to third.

5.2.12 December

In December (Figure 5-13), as temperature values continue to decline, with spatial mean value of -4.9 °C, monthly precipitation increases sharply, reaching the highest level of the year with a maximum of 561 mm and spatial mean value of 138 mm. Despite this substantial rise in precipitation, its overall impact on landslide susceptibility remains limited. This is because, under very low temperature conditions, even intense precipitation does not significantly contribute to slope instability. As shown in the feature importance analysis for December, precipitation does not appear among the top five influential factors.

The proportion of the area classified as "Very high" and "High" susceptibility decreases markedly to around 3%, while more than 94% of the region falls within the "Very low" and "Low" categories. The model's performance witnesses a small drop by 0.002, achieving an AUC of 0.966. Soil type, temperature and land cover are the most influential factor, whereas precipitation-related variables are no longer among the top three. This shift suggests that during colder months, soil characteristics and vegetation, play a more dominant role in controlling slope stability than precipitation alone.

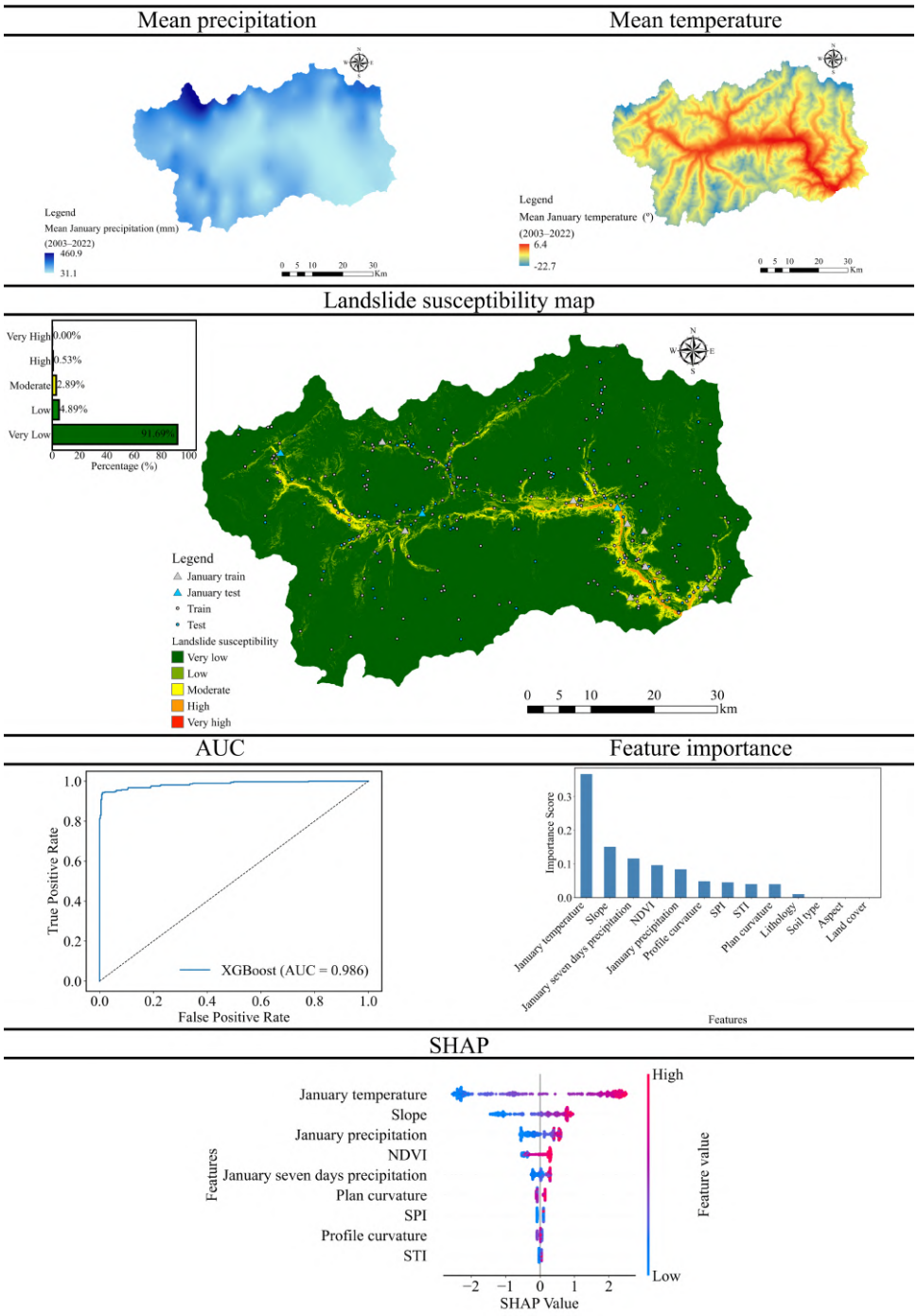

Figure 5-1 January mean precipitation (mm) and temperature (°C) maps, LSM, AUC, feature importance, and SHAP.

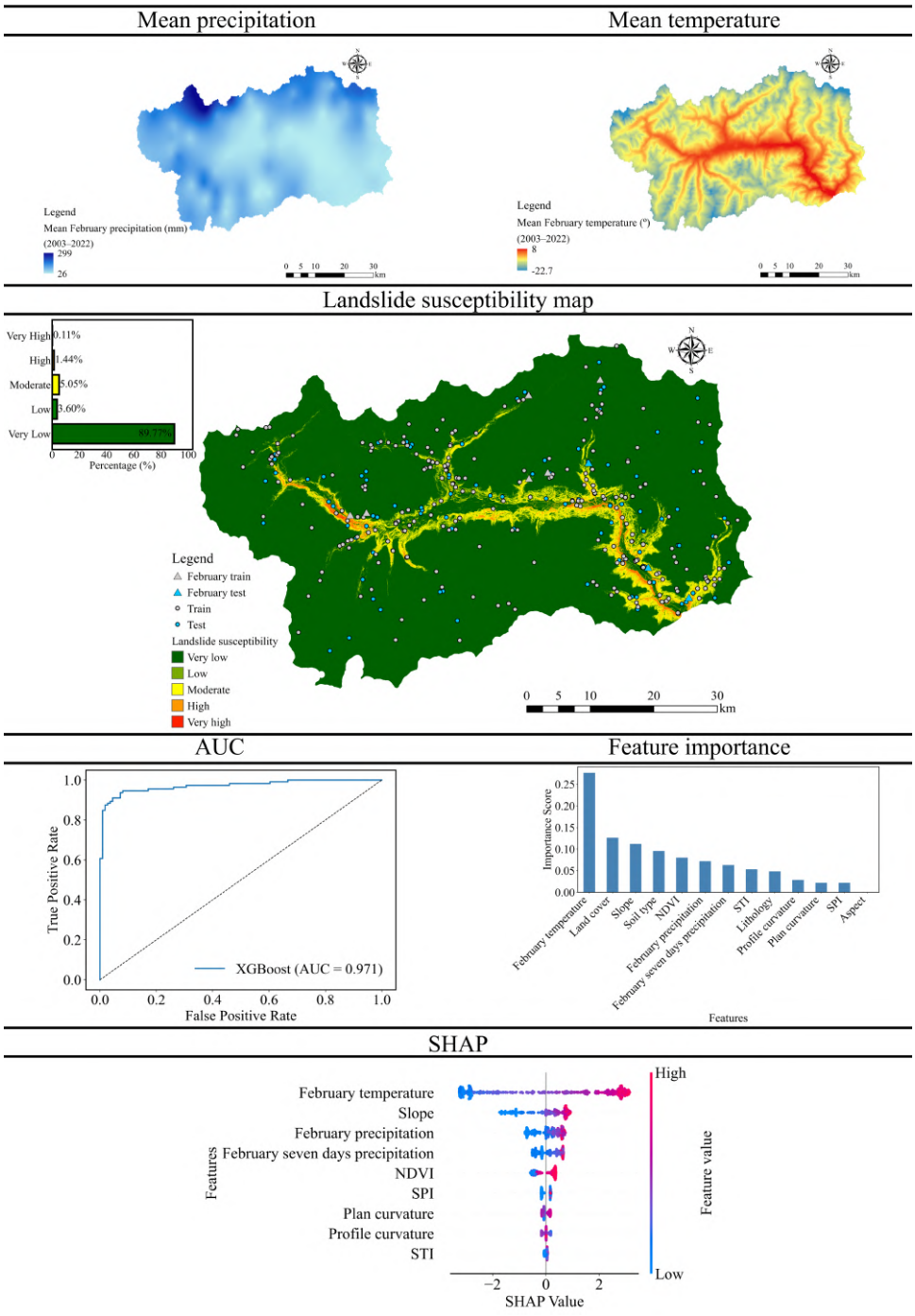

Figure 5-2 February mean precipitation (mm) and temperature (°C) maps, LSM, AUC, feature importance, and SHAP.

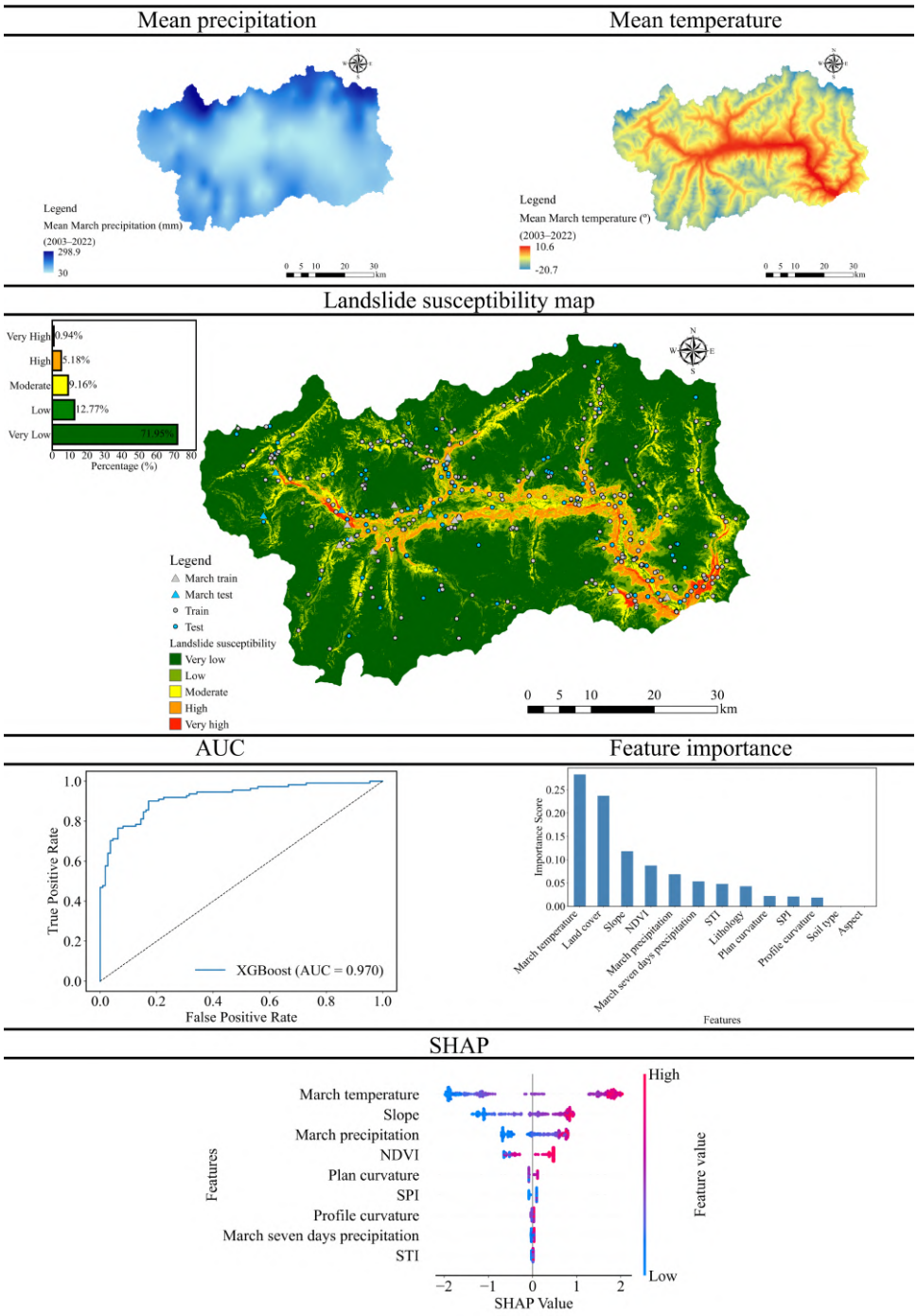

Figure 5-3 March mean precipitation (mm) and temperature (°C) maps, LSM, AUC, feature importance, and SHAP.

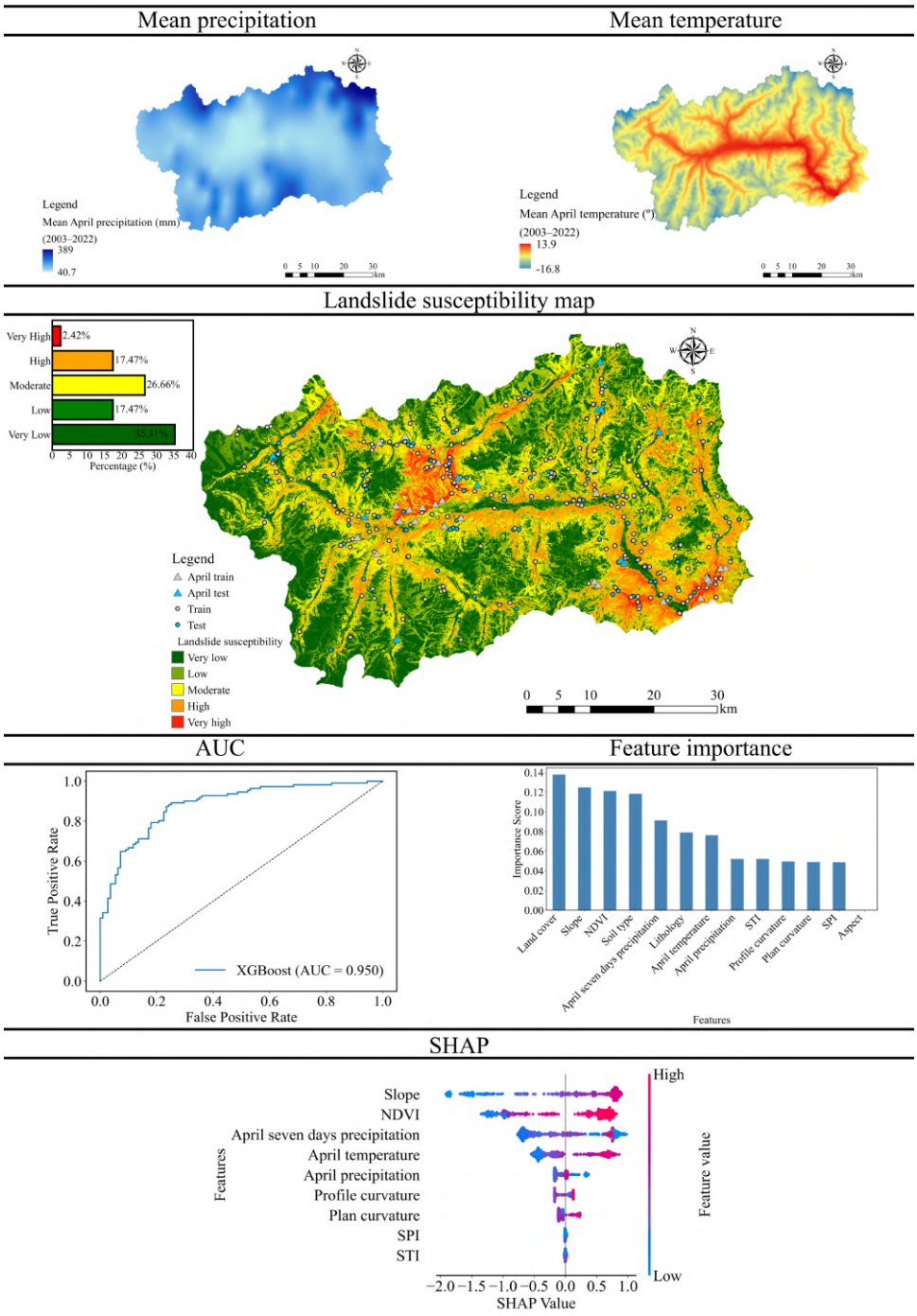

Figure 5-4 April mean precipitation (mm) and temperature (°C) maps, LSM, AUC, feature importance, and SHAP.

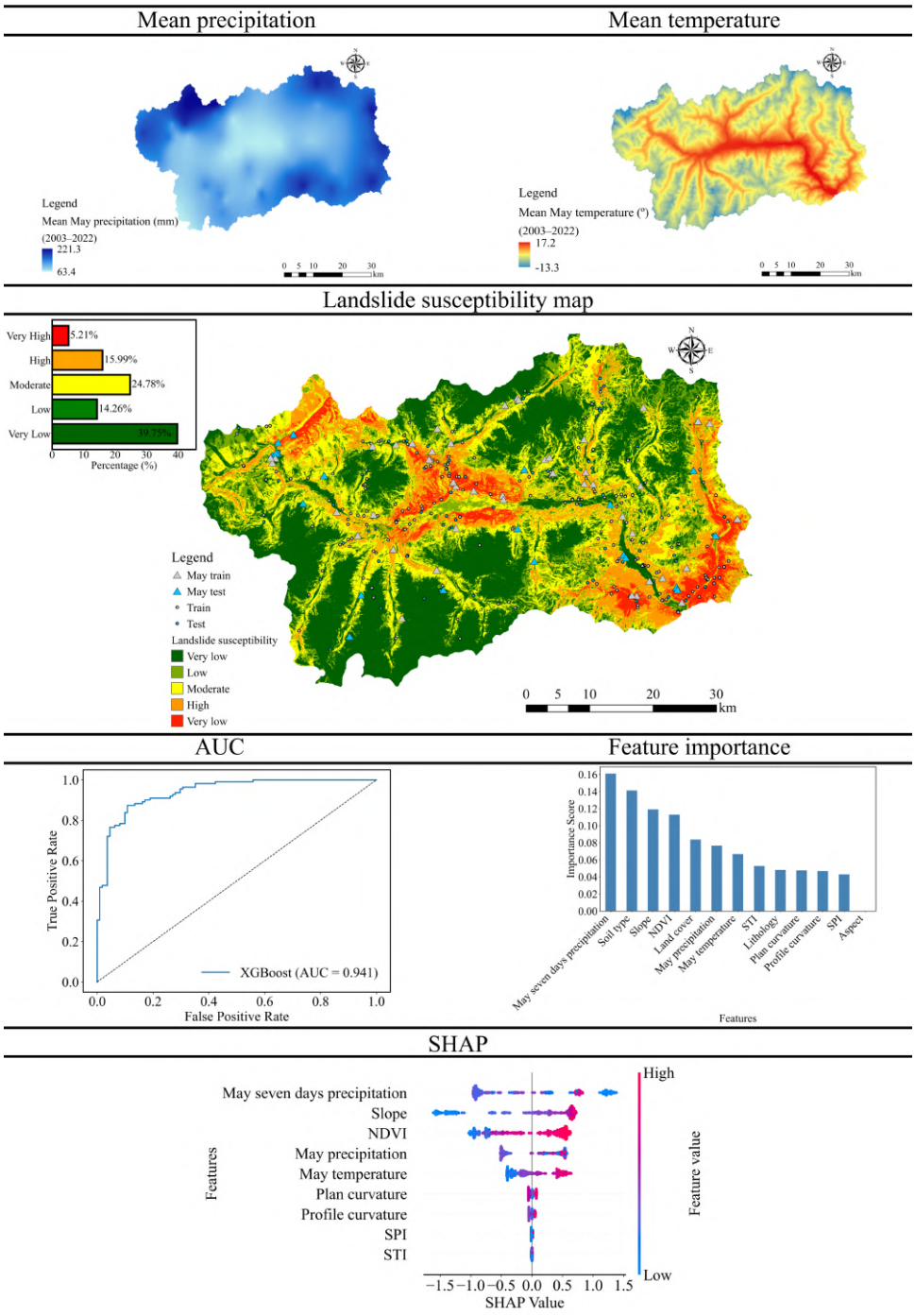

Figure 5-5 May mean precipitation (mm) and temperature (°C) maps, LSM, AUC, feature importance, and SHAP.

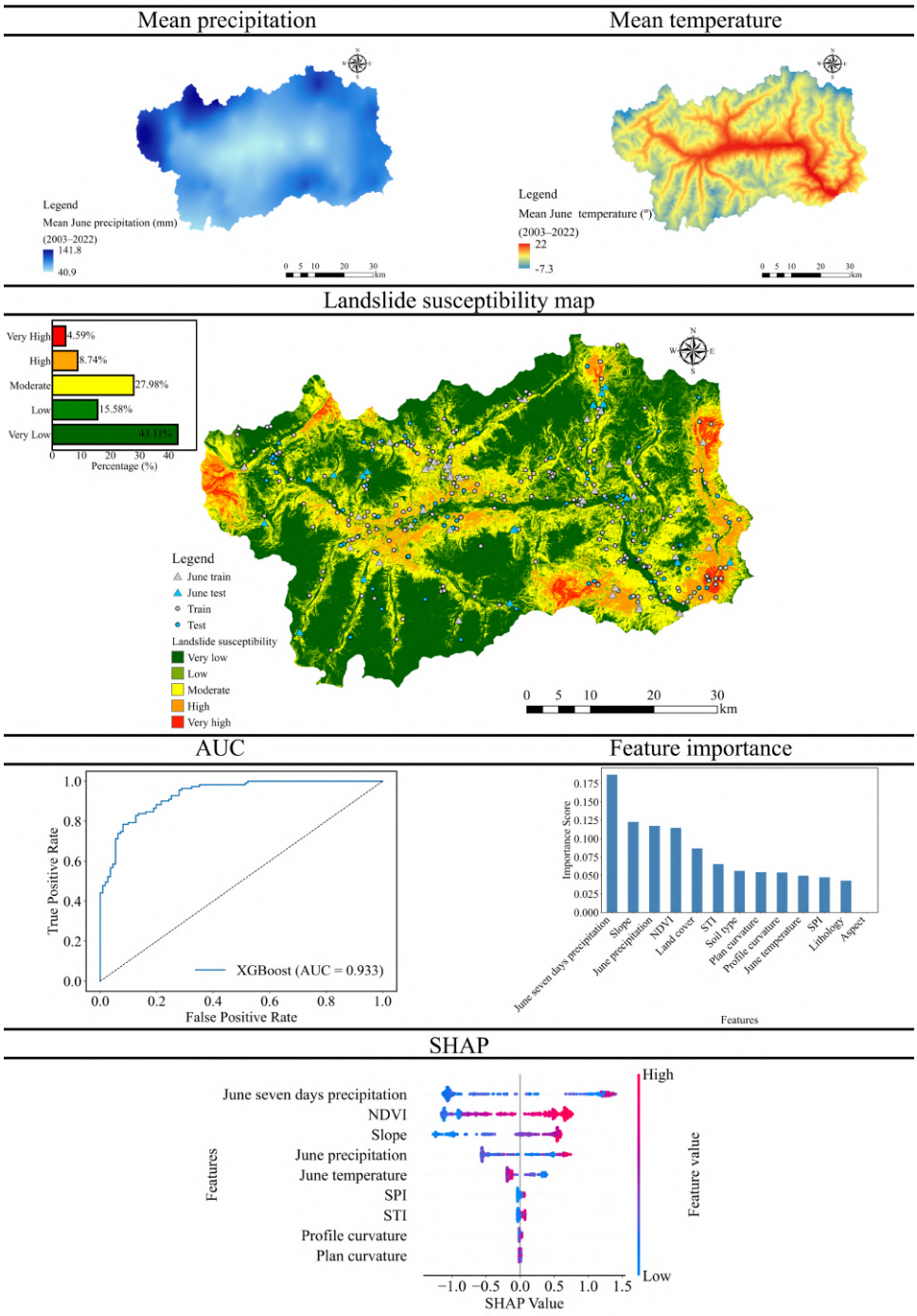

Figure 5-6 June mean precipitation (mm) and temperature (°C) maps, LSM, AUC, feature importance, and SHAP.

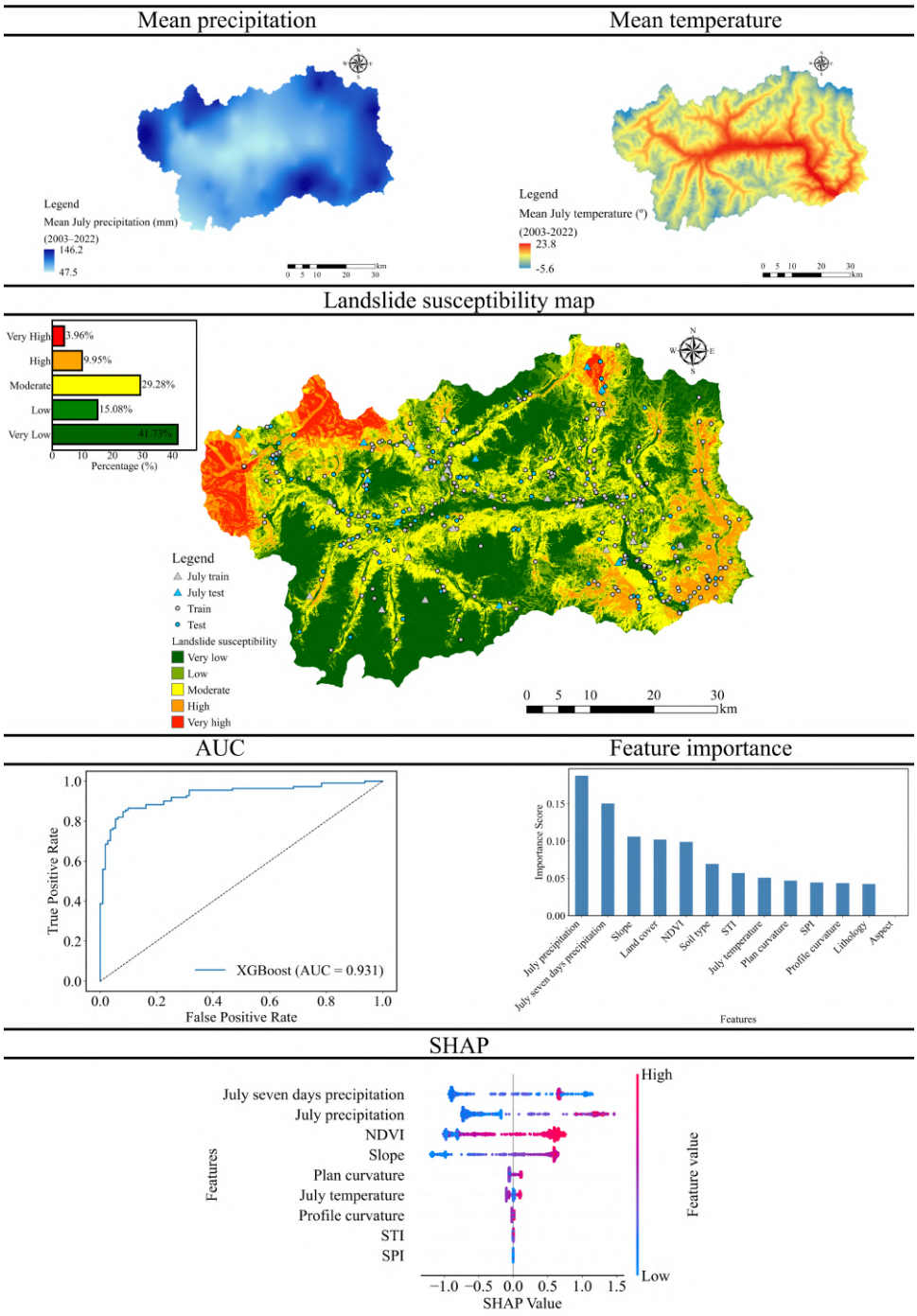

Figure 5-7 July mean precipitation (mm) and temperature (°C) maps, LSM, AUC, feature importance, and SHAP.

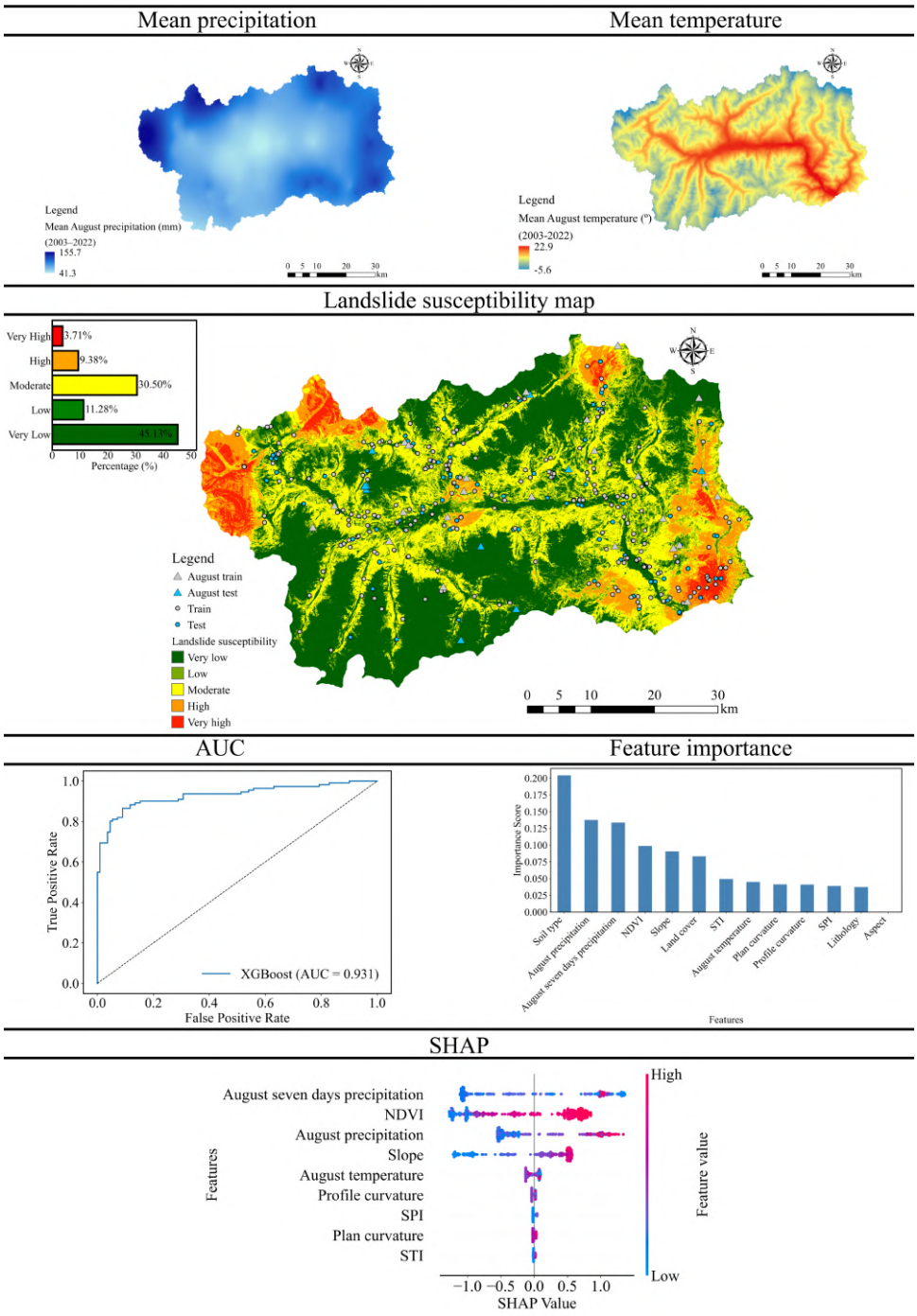

Figure 5-8 August mean precipitation (mm) and temperature (°C) maps, LSM, AUC, feature importance, and SHAP.

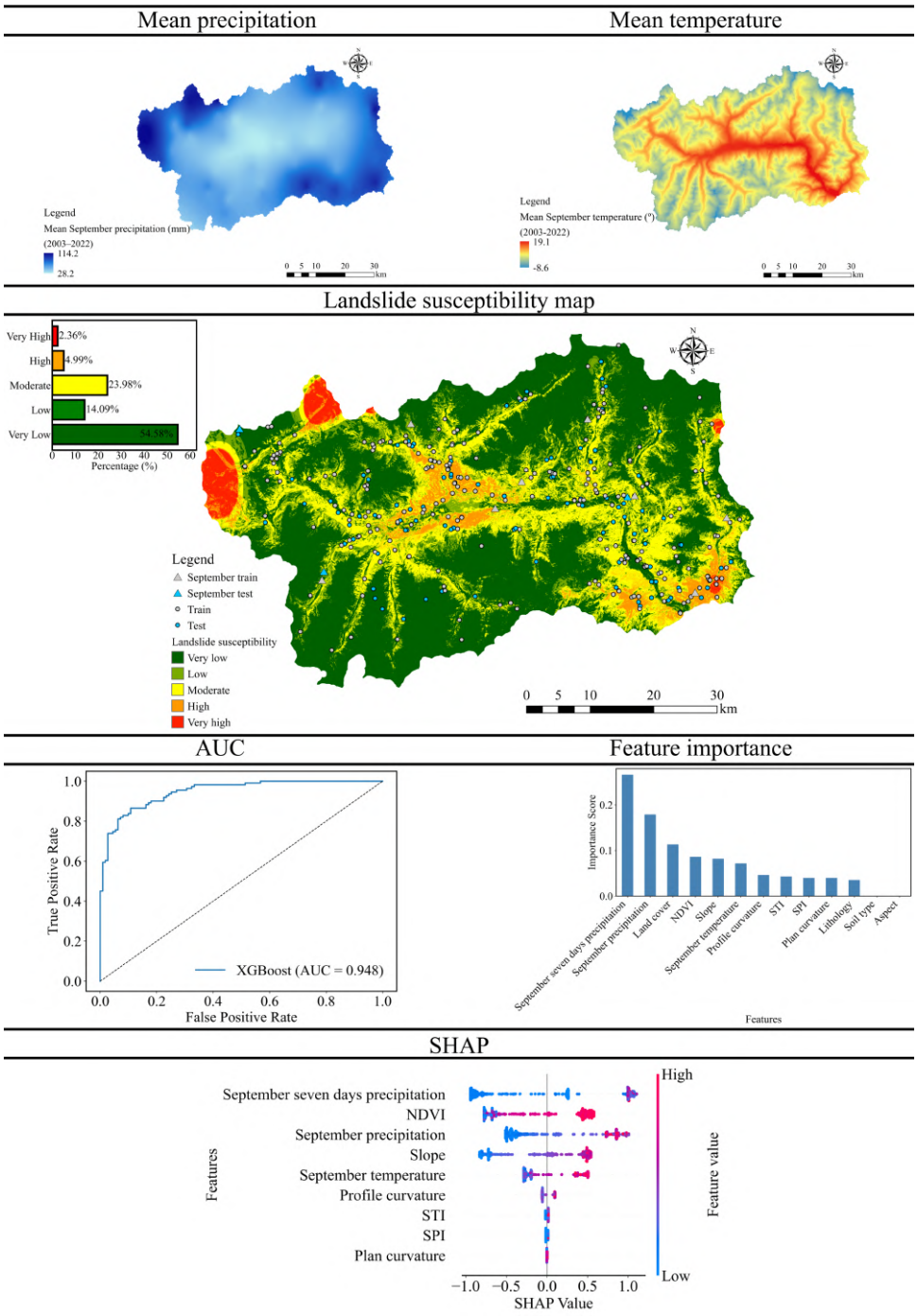

Figure 5-9 September mean precipitation (mm) and temperature (°C) maps, LSM, AUC, feature importance, and SHAP.

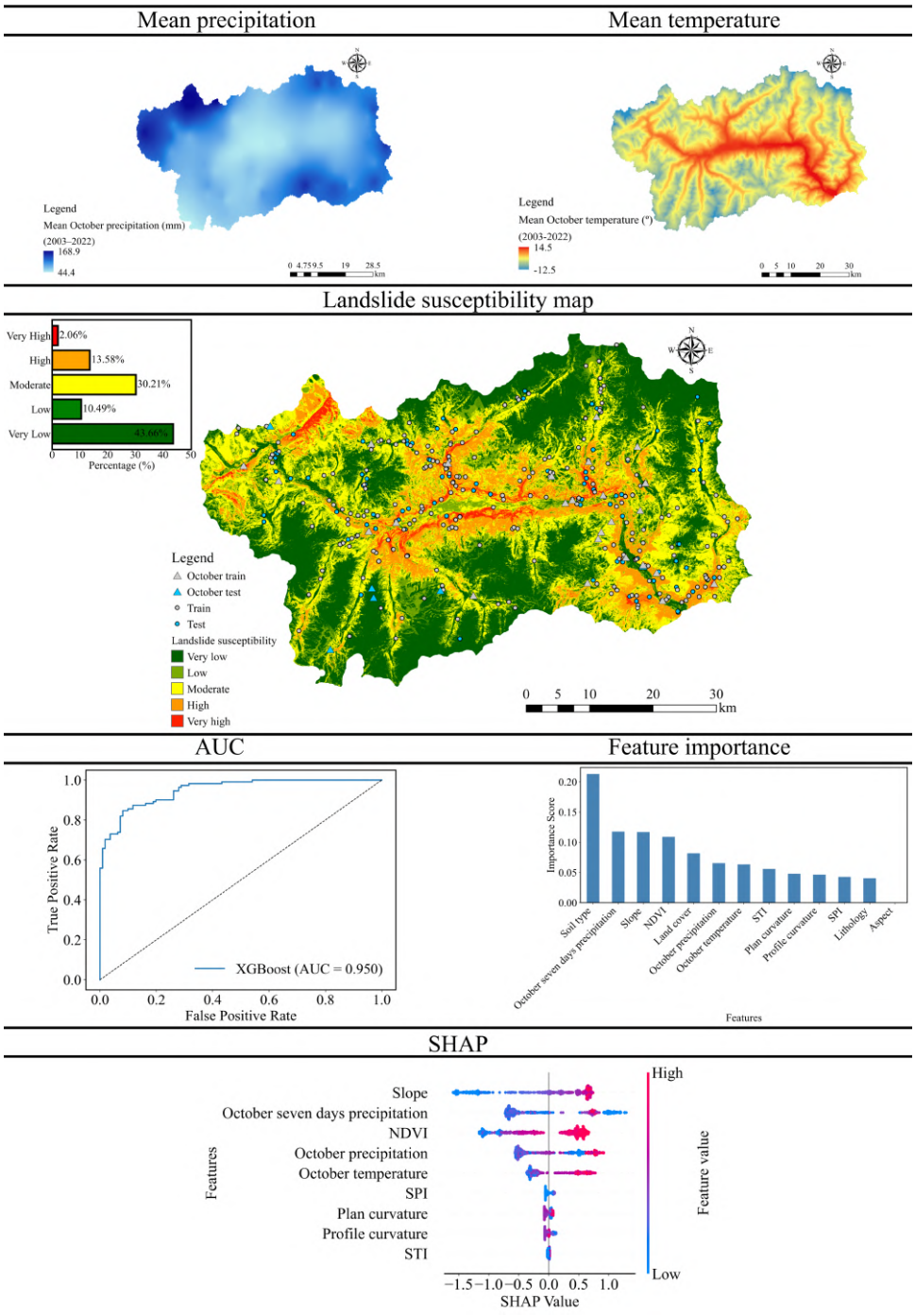

Figure 5-105-11 October mean precipitation (mm) and temperature (°C) maps, LSM, AUC, feature importance, and SHAP.

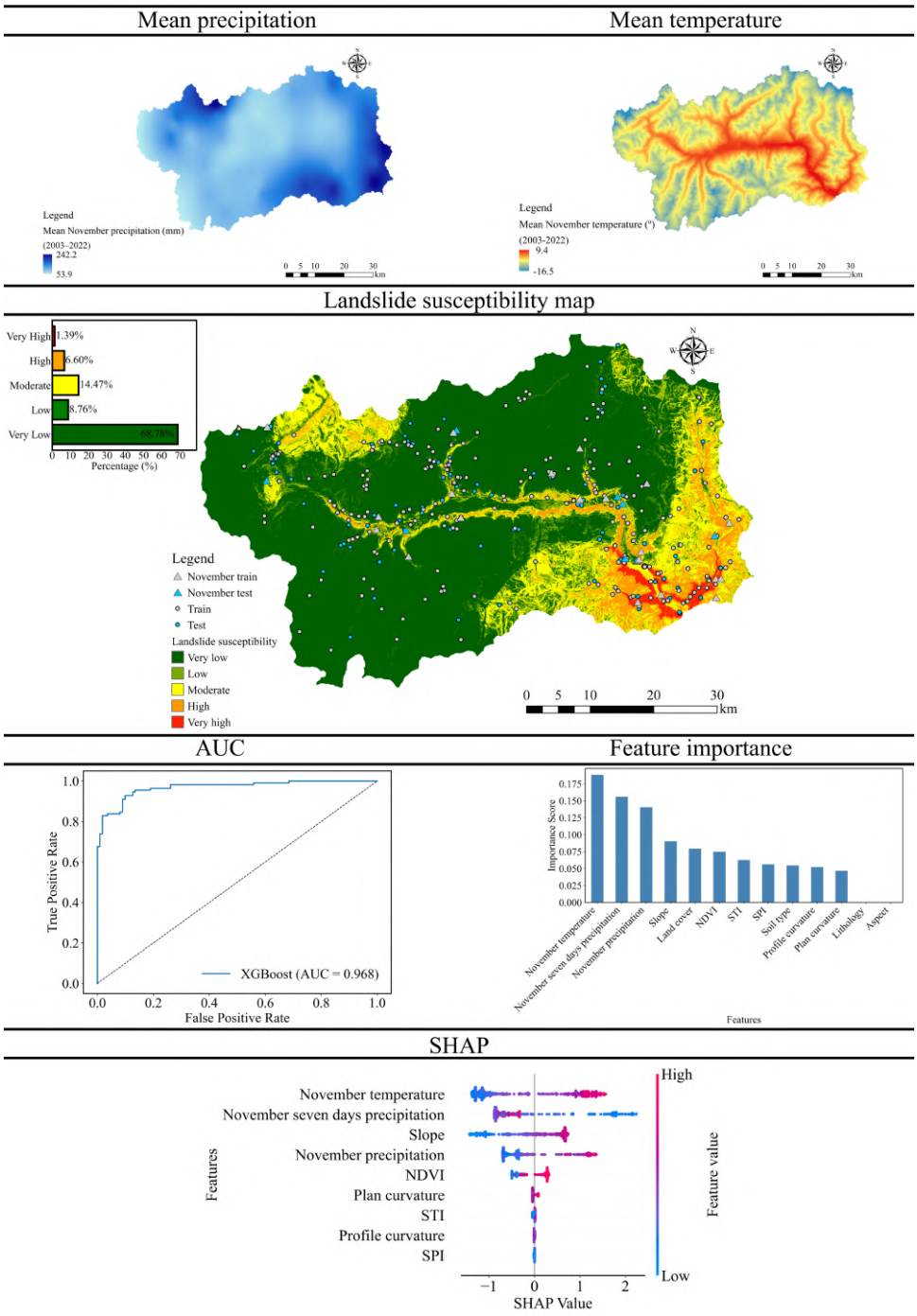

Figure 5-12 November mean precipitation (mm) and temperature (°C) maps, LSM, AUC, feature importance, and SHAP.

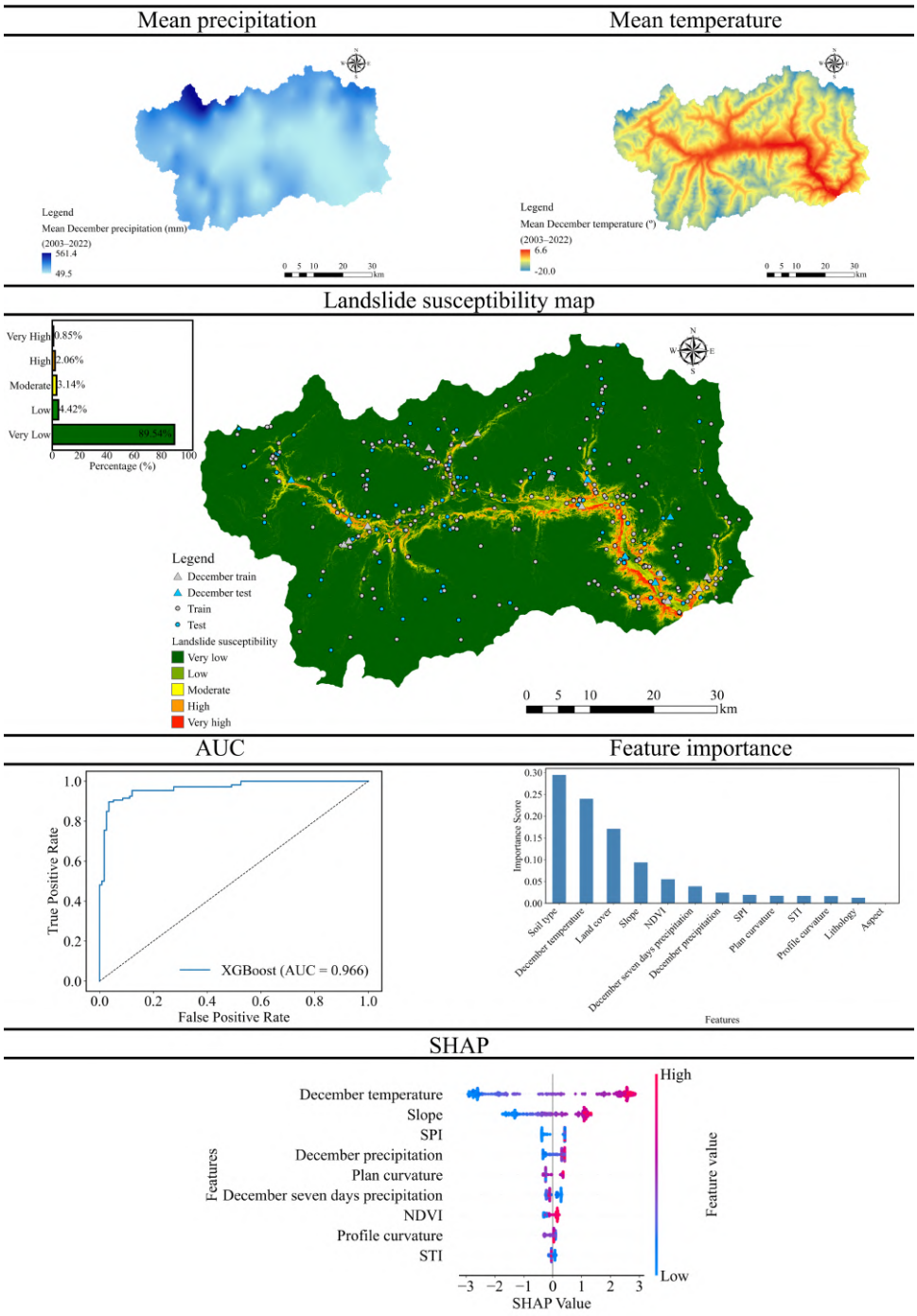

Figure 5-13 December mean precipitation (mm) and temperature (°C) maps, LSM, AUC, feature importance, and SHAP.

5.2.13 Summary of monthly AUC and feature importance

Figure 3-13 presents a comparison of the AUC values across all twelve months of the year. Although the variation is not significant, the AUC tends to be higher during the colder months. This may be because, at lower temperatures, the algorithm can more easily distinguish landslide from non-landslide events.

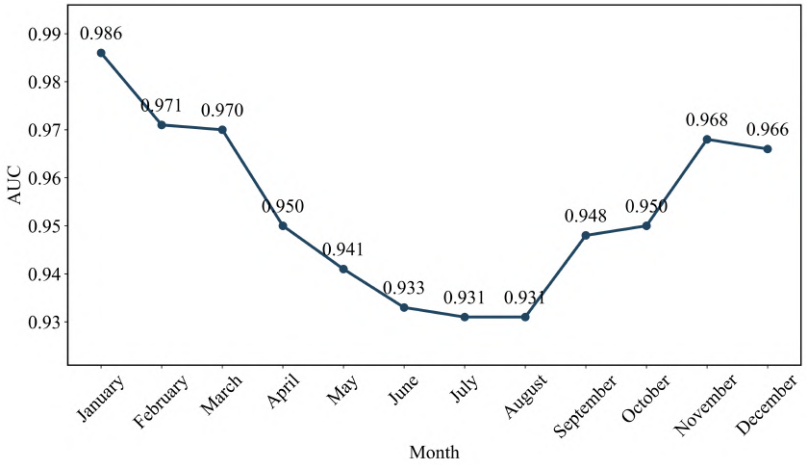

Figure 5-14 AUC variation across all twelve months.

Figure 5-15 presents the top three contributing features for each month. During warmer months, precipitation-related variables (monthly and short-term) dominate, whereas in colder months, temperature becomes the most influential factor. This reflects the strong control of temperature on ground freezing, snow accumulation, and hydrological activity. When temperatures fall below 0 °C, pore water freezes, increasing soil and rock strength and preventing deformation (Davies et al., 2001). Precipitation occurs mainly as snow, reducing infiltration and pore-pressure buildup (Daanen et al., 2011; Gruber and Haeberli, 2007). Consequently, temperature exerts a dominant stabilizing influence during cold months, explaining its high importance among the predictive features.

Secondary and tertiary factors also display distinct monthly patterns, reflecting the complex interplay of environmental conditions. Land cover appears most influential during the transition into spring (February to April), possibly coinciding with changes in vegetation or land use activities. Slope and Soil type, while intrinsic physical characteristics, fluctuate in their relative importance; they tend to peak in rank during the mid-year months when they interact with high precipitation levels to define susceptibile zones. Notably, NDVI only reaches the top three in April, suggesting a very specific window where vegetation density is a primary indicator of slope stability. This visualization effectively demonstrates that landslide susceptibility is not static; the "importance" of a factor is highly dependent on the specific climatic window of the year.

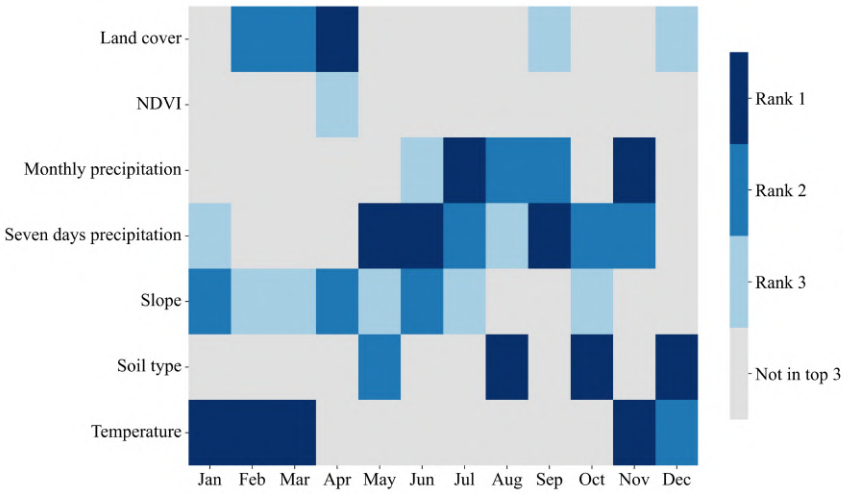

Figure 5-15 Top three features for each month.

5.2.14 Summary of monthly susceptibility distribution

To better understand the monthly variations in landslide susceptibility, it is useful to present all months together with their respective susceptibility class percentages. Figure 5-16 allows for an easy comparison of landslide susceptibility across different months. It can be observed that during the colder months (December to February), the region is not highly prone to landslides, with less than 3 percent of the area classified as “Very high” or “High” susceptibility. From March the susceptibility starts to increase, and for this month the combined “High” and “Very high” susceptible areas reach to around 6%. In April and May, however, susceptibility increases substantially, with the combined share of these two classes rising to around 20 percent. In the following months, from June to September, the proportion decreases to about 10 percent, reaching its lowest value in September at approximately 7 percent. From October to November, the share increases again to around 14 percent.

The higher susceptibility observed in April, May, and October can be explained by the critical combination of temperature and precipitation values during these months, which together create favorable conditions for landslide occurrence. In contrast, during the coldest months (December to February), even though precipitation levels are relatively high, the very low temperatures limit slope instability and reduce the likelihood of landslides. Similarly, in the warmer months (June to September), although temperatures are high, precipitation is low, making landslide events less probable.

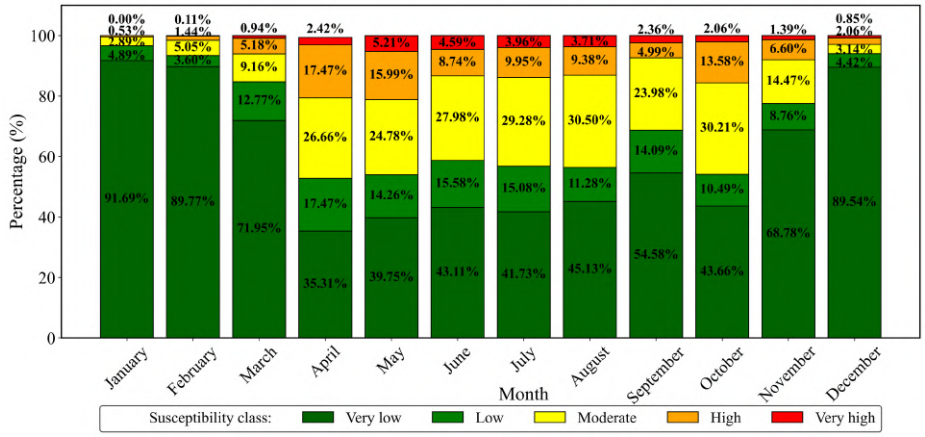

Figure 5-16 Monthly landslide susceptibility shares for 2003-2022.

5.2.15 Analyzing monthly landslide events

Figure 5-17 presents the monthly frequency of landslide occurrences from 2003 to 2022. A distinct seasonal pattern is evident, with a significant concentration of events in May, June, October, and April. Collectively, these four months account for 202 of the 369 recorded events, representing around 55% of the total landslide activity in the region.

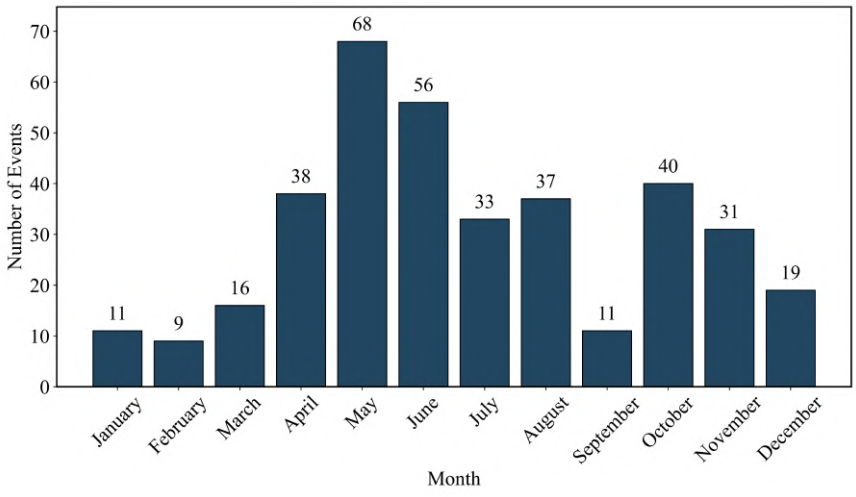

Figure 5-17 Landslide events from 2003-2022.

Comparing the percentage of monthly landslide events with the percentage of the region classified as “Very high” and “High” susceptibility provides insight into how well the generated maps correspond to real conditions. Figure 5-18 shows that the trend of susceptible areas closely aligns with the occurrence of actual landslide events, indicating good agreement between the model results and reality.

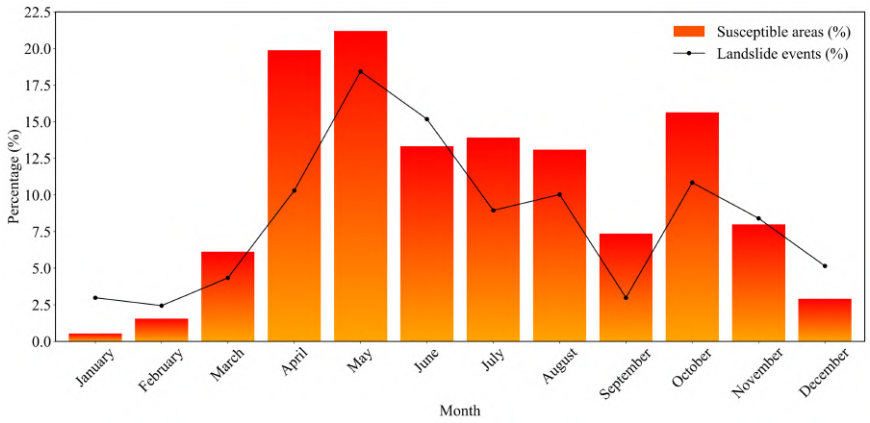

Figure 5-18 Comparison of susceptible areas and landslide event percentage.

5.2.16 Envelope map (2003-2022) and verification

To generate a single map representing the overall landslide susceptibility of the region across all twelve months, an "Envelope map" was created (Figure 5-19). In this map, the twelve-monthly landslide susceptibility maps were overlaid, and the highest value for each pixel was extracted. The resulting map was then classified into five categories: "Very Low," "Low," "Moderate," "High," and "Very High", using the natural Jenks method. The value ranges for each class were approximately 0–0.35, 0.35–0.5, 0.5–0.75, 0.75–0.9, and 0.9–1. To allow consistent comparison across months, the same classification ranges were applied to all twelve-monthly maps. Although no landslide events were recorded in the northwestern part of the study area during the 20-year observation period, this region is predominantly classified as having "High" to "Very high" susceptibility. Given that other areas with similar susceptibility classes contain documented landslide occurrences, it may be inferred that the absence of recorded events in the northwestern sector could be related to limited accessibility and sparse urban development in this high-elevation mountainous terrain, which may have hindered the detection and documentation of landslide events.

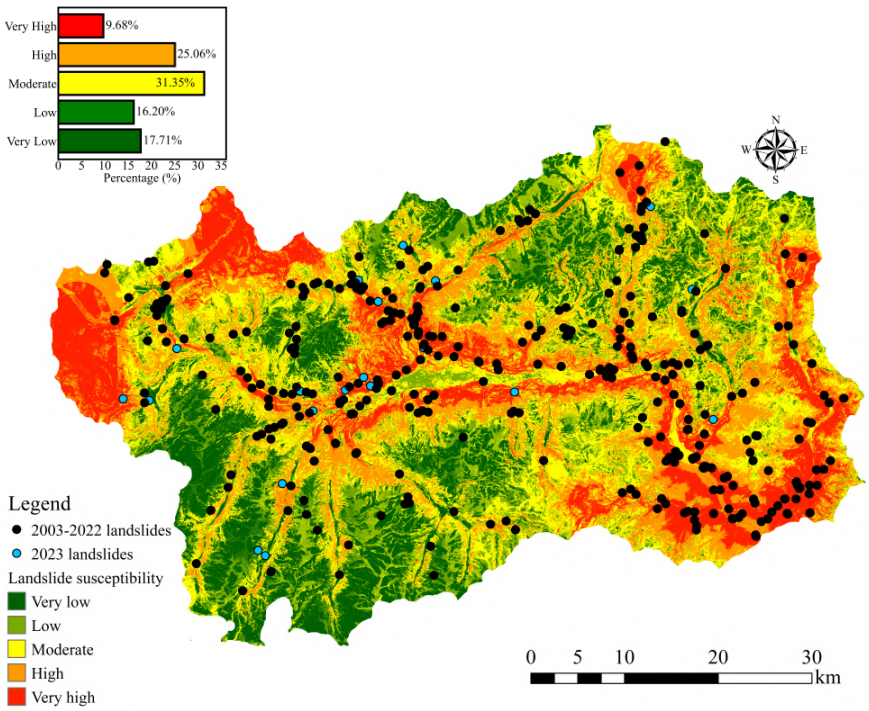

Figure 5-19 Landslide susceptibility envelope map for 2003-2022 and the classes percentage.

Figure 5-20 shows that 75 percent of the landslide points from 2003 to 2022, which were used for training and testing the model, fall within areas classified as "Very high" or "High" susceptibility. This finding suggests that, although these two classes represent only 35 percent of the total area, they successfully capture around 75 percent of the landslides that have occurred to date, demonstrating the model's strong spatial predictive capability.

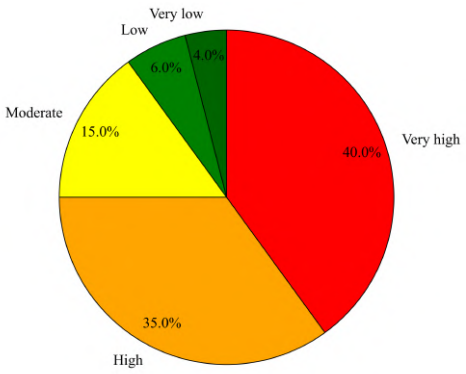

Figure 5-20 Classification of landslide events occurred in 2003–2022 based on the current envelope map.

To perform a "Geotechnical validation" of the Envelope map, the most recent landslide points, which were not used in training or testing the algorithm, were employed. These points corresponded to landslide events that occurred in 2023. Figure 5-21 illustrates that 72 percent of these events fall in the areas classified as "High" or "Very high" susceptibility.

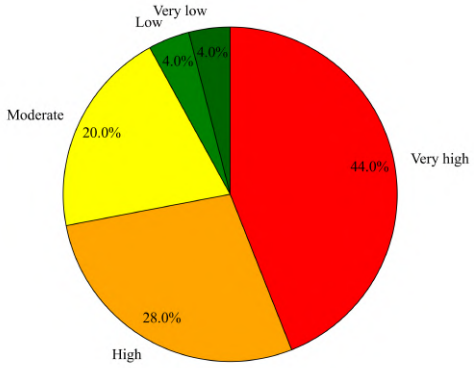

Figure 5-21 Classification of landslide events occurred in 2023 based on the current envelope map.

5.3 Future scenario (2021-2040)

After the algorithm was trained and tested for each month, the trained models were employed to generate monthly landslide susceptibility maps for future periods. To produce each susceptibility map, the inclusion of dynamic features was required. As described in section 4.4.3, the data corresponding to the future time frame was obtained from the WorldClim database (https://www.worldclim.org).

Figure 5-22 to Figure 5-33 illustrate the monthly precipitation and temperature distributions, the resulting landslide susceptibility maps, and the proportional area of each susceptibility class.

5.3.1 January

In January (Figure 5-22), precipitation and temperature conditions generally do not represent a substantial threat to slope stability. Although total precipitation is relatively high, with a spatial mean value of 96 mm, temperatures remain sufficiently low, with spatial mean of -4.19°C, which makes most the precipitation for most of the area to occur as snow rather than rainfall (Figure 4-32 and Figure 4-43). The results further indicate that only about 2% of the study area falls within the “High” and “Very High” susceptibility classes, whereas approximately 89% is classified as “Low” and “Very low.”

When compared with 2003–2022, the mean spatial precipitation is projected to decrease from 112 mm to 96 mm, while the mean spatial temperature is expected to rise from -5.94°C by approximately 1.75 °C, reaching −4.19 °C. This leads to a slight increase of 1.58% in susceptible areas, suggesting a marginal deterioration in slope stability. This change is primarily attributed to temperature variations, as temperature was identified as the most influential factor for January (Figure 5-1). Even a modest temperature increase can therefore lead to a minor expansion of landslide-susceptible zones during this month.

5.3.2 February

In February (Figure 5-23), the spatial mean precipitation is expected to increase marginally compared to January, to 101 mm. In addition, the mean spatial temperatures rise by approximately 1 °C, growing to -3.2 °C (Figure 4-32 and Figure 4-43). This combined increase in temperature and precipitation contributes to a less stable environment, with about 4.07% of the study area classified within the "High" and "Very high" susceptibility categories.

When compared with the same month during the 2003–2022 period (Figure 5-2), both the mean spatial temperature and precipitation are projected to increase by approximately 2 °C and 21 mm, respectively (Figure 4-29 and Figure 4-41). In this month, temperature represents the most influential factor contributing to slope instability. The observed increase in landslide-susceptible areas is therefore primarily attributed to the projected temperature rise. Consequently, the proportion of the area classified as "High" and "Very high" susceptibility is expected to increase from 1.55% to 4.07% during the 2021–2040 period.

5.3.3 March

In March (Figure 5-24), both precipitation and temperature (maximum and mean spatial) exhibit an increase compared to February (Figure 4-32 and Figure 4-43). Precipitation is projected to rise by approximately 4 mm in mean spatial values, while mean spatial temperature is expected to increase by 1.2 °C, reaching 105 mm and −2 °C, respectively. This concurrent rise in precipitation and temperature intensifies the potential for slope instability, resulting in an increase of 2.53% to 6.6% in the area classified as "High" and "Very high" susceptibility.

When compared with the 2003–2021 period, the proportion of landslide-susceptible areas is projected to increase slightly by only 0.48%, reaching 6.6% in the 2021–2040 period. This increase is primarily attributed to the rise in mean spatial precipitation, which is expected to grow from 93 mm in 2003–2021 to 105 mm in 2021–2040, while the mean temperature remains relatively stable on -2 °C.

5.3.4 April

In April (Figure 5-25), the mean spatial temperature increases compared to March, by approximately 2 °C to 0.2. In contrast, the mean spatial precipitation remains almost constant, with only a 5 mm decrease (Figure 4-32 and Figure 4-43). The rise in temperature is expected to further expand the "Very High" and "High" susceptibility classes, increasing their extent from 6.6% in March to 11.12% in April.

Furthermore, when comparing April in the periods 2003–2021 and 2021–2040, mean spatial precipitation and temperature are projected to decrease from 137.7 mm and 1.56 °C to 99.6 mm and 0.2 °C, respectively. This reduction in dynamic variables is expected to result in a decline in the "Very high" and "High" susceptibility classes, from 19.89% in 2003–2021 to approximately 11.12% in 2021–2040.

5.3.5 May

In May (Figure 5-26), compared to April of the same period, the mean spatial precipitation shows a slight increase from 99.6 to 102 mm (Figure 4-32). At the same time, the mean spatial temperature exhibits a notable rise of 5 °C, reaching 5 °C (Figure 4-43). This warming trend intensifies the conditions during this month and increases the proportion of areas classified as "Very high" and "High" susceptibility by 4.5%, reaching a total of 15.6%.

However, when comparing May 2021-2040 with May 2003- 2022, the mean spatial temperature remains relatively constant, while mean spatial precipitation decreases by 16 mm. These changes project a reduction in landslide susceptibility, with the shares of the "High" and "Very high" classes decreasing from 21.2% to 15.64%. This outcome is mainly explained by the reduction in precipitation, since the seven-day cumulative precipitation was identified as the first most important factors, for this month.

5.3.6 June

In June (Figure 5-27), although temperature increases by 4 to 9.13 °C relative to the previous month (Figure 4-43), mean spatial precipitation decreases by approximately 24 mm to 78 mm (Figure 4-32). This reduction in precipitation is projected to decrease the share of susceptible areas by 4.4%, reaching 11.2%.

Similarly, when comparing June in the period 2021–2040 with 2003–2022, the mean spatial precipitation remains nearly constant around 78 mm, while the mean spatial temperature shows a slight decrease of 1 °C, reaching 9 °C. These changes lead to a minor reduction in the proportion of susceptible areas, decreasing from 13% in 2003–2021 to 11.2% in 2021–2040.

5.3.7 July

In July (Figure 5-28), the mean spatial precipitation continues to decrease compared to the previous month, declining from 78 mm to 68 mm, which represents the lowest value projected for the 2021–2040 period (Figure 4-32). Meanwhile, the mean spatial temperature continues to rise, reaching 12.8 °C. However, the shares of areas classified as "Very high" and "High" susceptibility decrease from 11.23% to 8.9%.

In comparison, during the same month in the 2003–2022 period, the situation was more critical, with approximately 13.9% of the area categorized as "Very high" and "High." This indicates a moderate improvement in 2021–2040, as the share of susceptible areas is expected to decrease to 8.9%. The reduction is mainly attributed to the projected decline in precipitation for this month, with mean spatial precipitation decreasing by about 20 mm and reaching its lowest level of 68 mm.

5.3.8 August

In August (Figure 5-29), during the period 2021–2040, the mean spatial temperature reaches its highest value of 14.1 °C. The mean spatial precipitation also shows a slight increase of 5 mm compared to the previous month, reaching 73 mm. This gradual rise in precipitation and temperature may cause a minor deterioration in slope stability, leading to an increase of 5% in the "Very high" and "High" susceptibility classes, reaching a total of 13.9%.

When comparing August in 2003–2022 with 2021–2040, the share of areas classified as "Very high" and "High" increases only by approximately 1%. This occurs despite an expected decrease in mean spatial precipitation of about 10 mm. However, spatial mean temperature is projected to increase by 3 °C in 2021–2040 compared to 2003–2022.

5.3.9 September

From September (Figure 5-30) onward, precipitation begins to increase again, reaching a mean spatial value of 89 mm, while the mean spatial temperature reaches to 9.6 °C. Comparing these values with the previous month can show an increase in precipitation by 16 mm and a drop of 4.3°C in temperature. Yet still proportion of susceptible areas rises by 10.3% to 24.2%.

Furthermore, when comparing the period 2021–2040 with 2003–2022, the situation is expected to worsen remarkably, as the share of areas classified as "Very high" and "High" susceptibility increases from 7.31% to 24.2%. This deterioration is mainly due to simultaneous increases in both precipitation and temperature, with mean spatial precipitation rising from 57 to 89 mm and mean spatial temperature increasing from 7.8 to 9.6 °C.

5.3.10 October

In October (Figure 5-31), the mean spatial precipitation continues to increase compared to the previous month by approximately 30 mm, reaching a value of 108 mm. At the same time, the mean spatial temperature decreases markedly by 4.5 °C, reaching 5.1 °C. The increase in precipitation compensates for the effect of temperature reduction on landslide susceptibility. Although the temperature

decreases, it remains above the freezing point, maintaining conditions favorable for landslide occurrence. As a result, the overall susceptibility levels remain nearly constant, with the "High" and "Very high" susceptibility classes increasing by only 0.2%, reaching their maximum recorded value of 24.4%.

Compared with October 2003-2022, both mean spatial precipitation and temperature are projected to increase in 2021-2040, by about 22 mm and 1.7 °C, respectively. Consequently, the share of areas classified as "High" and "Very high" susceptibility is expected to rise from 15.6% to 24.4%.

5.3.11 November

In November (Figure 5-32), although precipitation reaches its highest value for the period 2021 to 2040, with a mean spatial value of 121.7 mm (Figure 4-32), the decrease in mean spatial temperature to 0.1 °C (Figure 4-43) leads to a reduction in landslide susceptibility by about 12.4%, reaching 11.9%. This occurs because, in November, temperature holds the first rank of importance while the seven-day precipitation is ranked second, making the effect of temperature reduction more dominant than the increase in precipitation.

A comparison between November 2021-2040 and November 2003-2022 indicates an increase in both mean spatial precipitation and temperature, by approximately 15.4 mm and 1.4 °C, respectively. As a result, the share of areas classified as "High" and "Very high" susceptibility is projected to increase from 9.8% by 2.1%,

5.3.12 December

In December (Figure 5-33), the mean spatial precipitation is projected to decrease by 7.8 mm compared to the previous month, reaching 113.9 mm (Figure 4-32). Similarly, the temperature is expected to drop by 2.7 °C to -2.65 °C (Figure 4-43). This reduction in dynamic features leads to a significant decrease in the "High" and "Very high" susceptibility classes, which decline by 5.7% to 6.2%. The reduction is mainly attributed to temperature, as it represents the most influential factor among the others, and once the mean spatial temperature approaches or falls below 0 °C, the area becomes less susceptible to landslides.

Comparing December 2021 to 2040 with 2003 to 2022, the mean spatial temperature is projected to increase by 2.23 °C, from -4.88 to -2.65 °C, while mean spatial precipitation is expected to decrease from 138 mm to 113 mm. Since temperature has the second highest rank among the influencing factors, this increase will cause the share of areas classified as "High" and "Very high" susceptibility to rise from 2.9% to 6.2%.

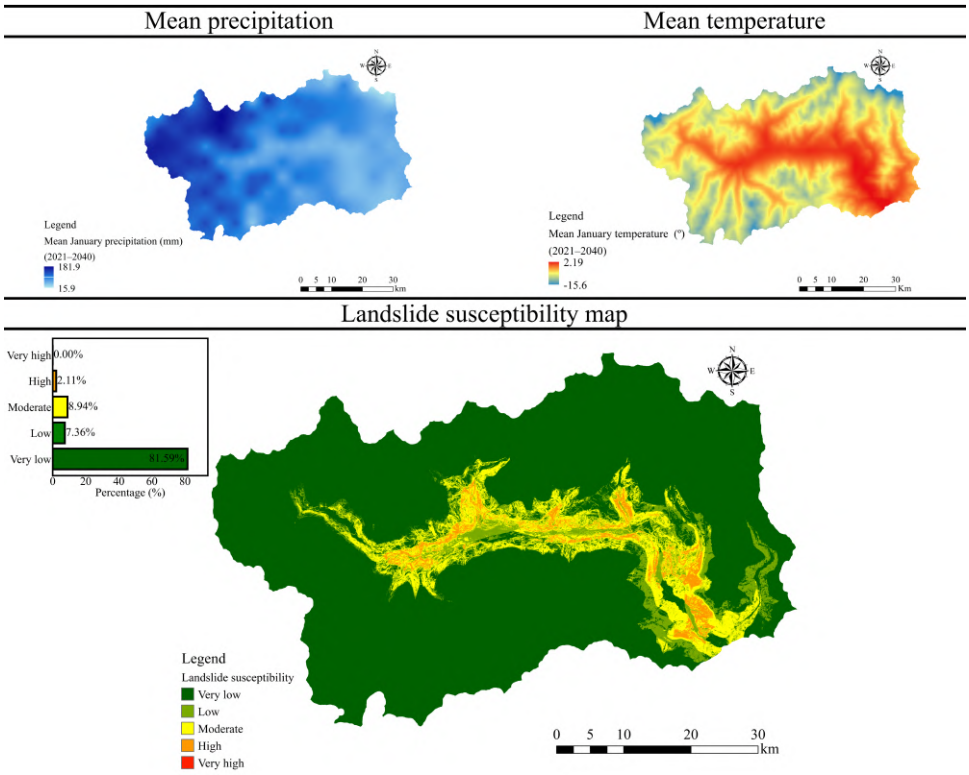

Figure 5-22 January mean precipitation and mean temperature, and LSM.

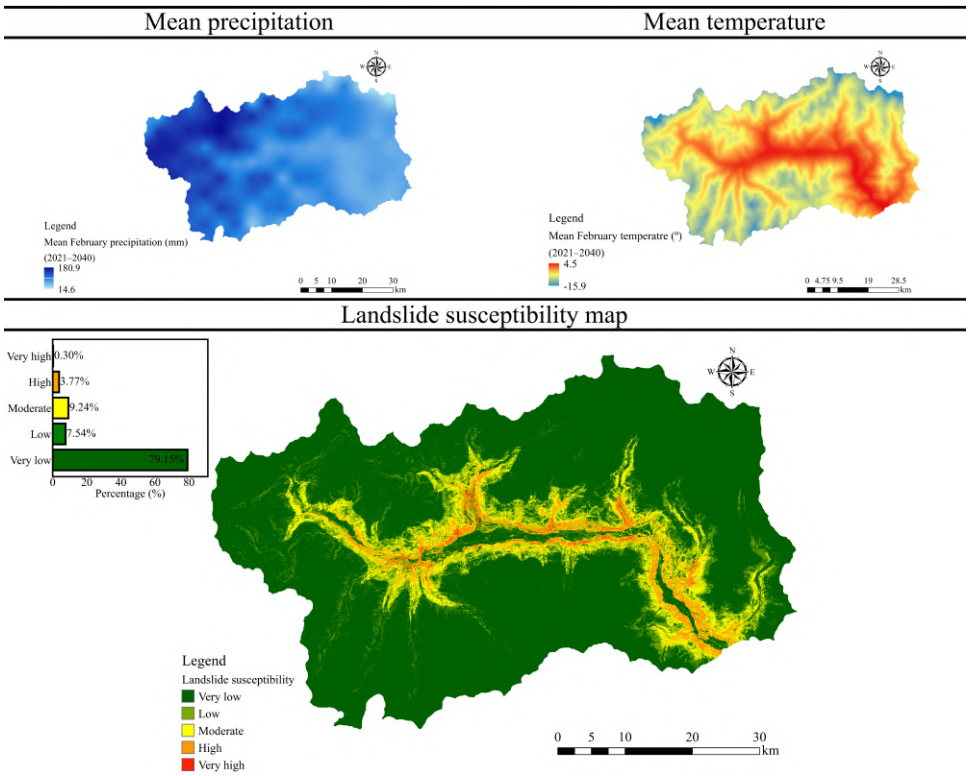

Figure 5-23 February mean precipitation and mean temperature, and LSM.

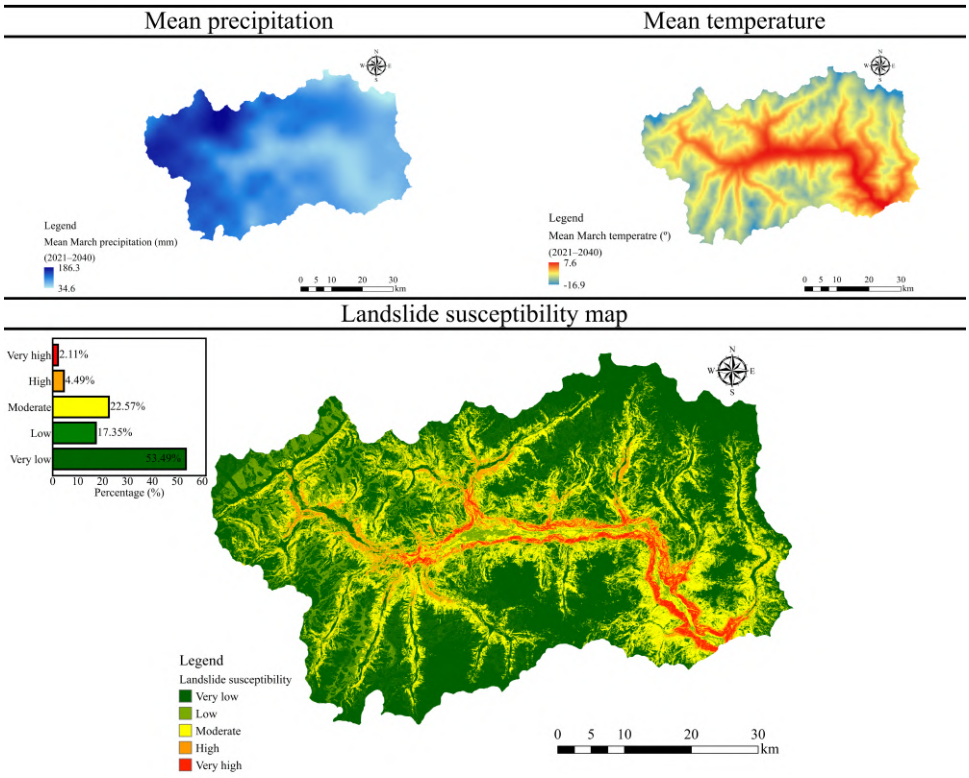

Figure 5-24 March mean precipitation and mean temperature, and LSM.

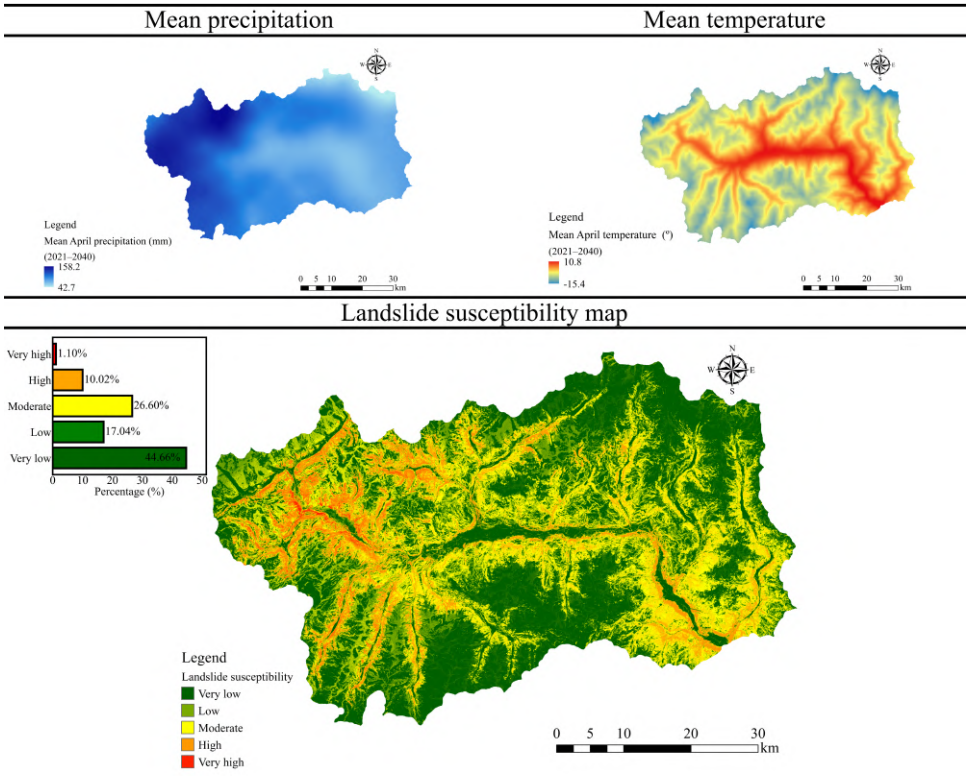

Figure 5-25 April mean precipitation and mean temperature, and LSM.

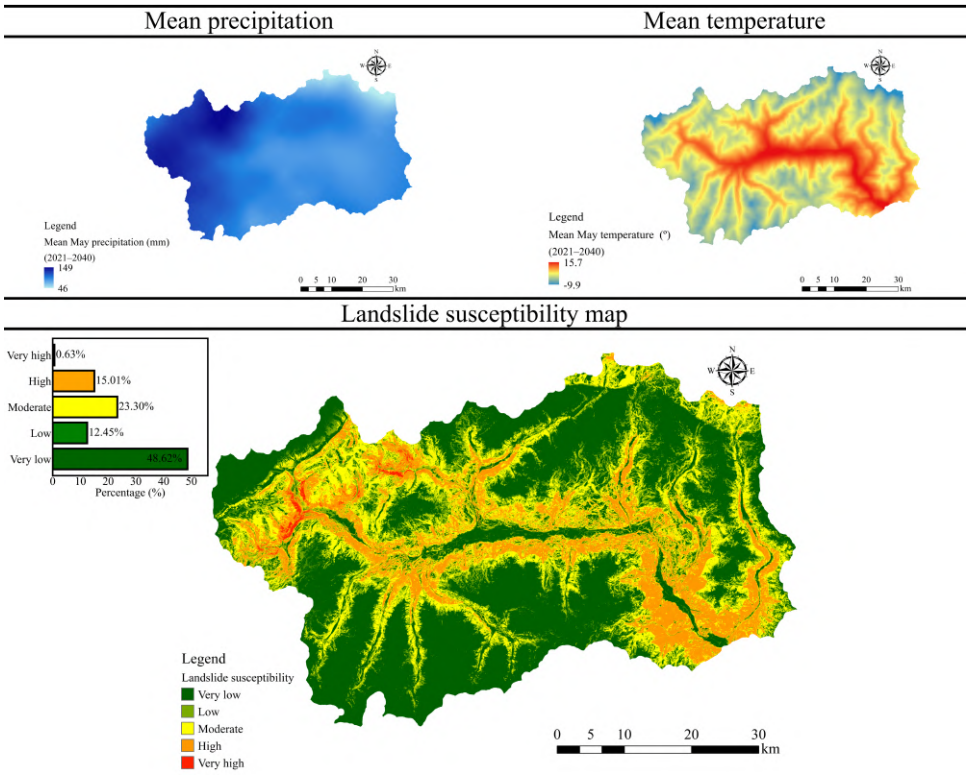

Figure 5-26 May mean precipitation and mean temperature, and LSM.

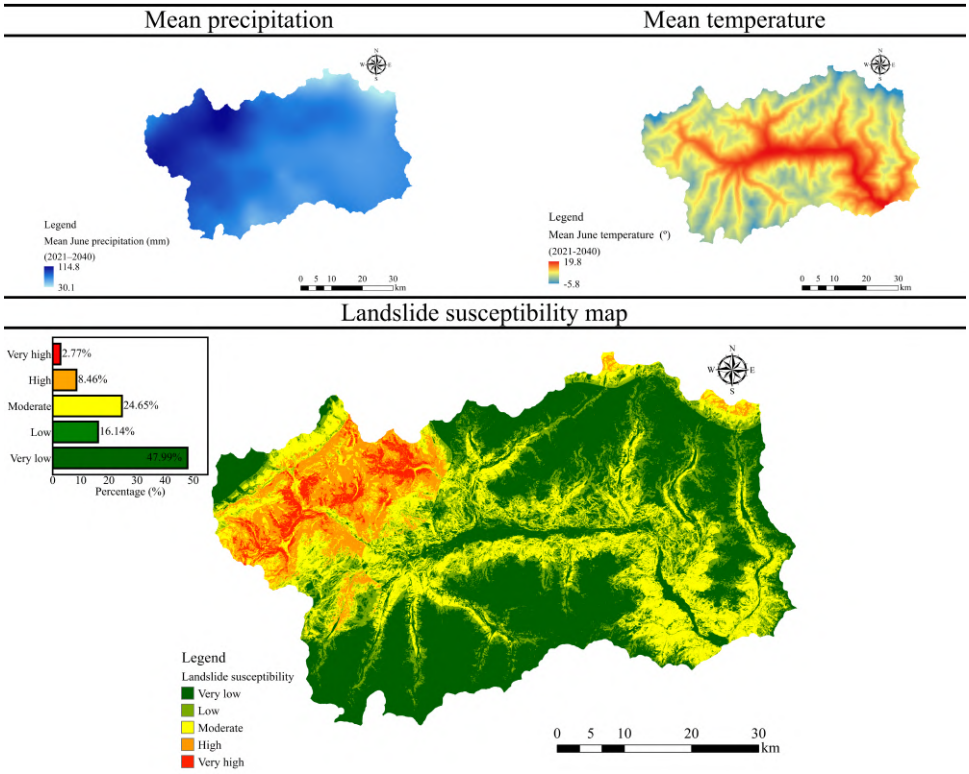

Figure 5-27 June mean precipitation and mean temperature, and LSM.

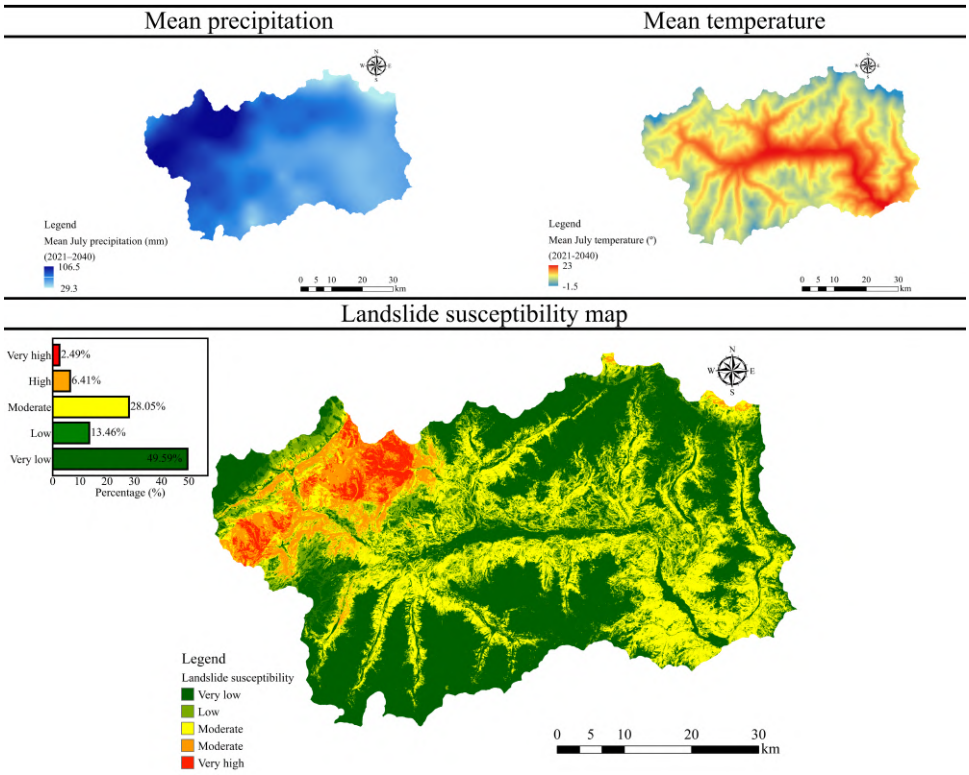

Figure 5-28 July mean precipitation and mean temperature, and LSM.

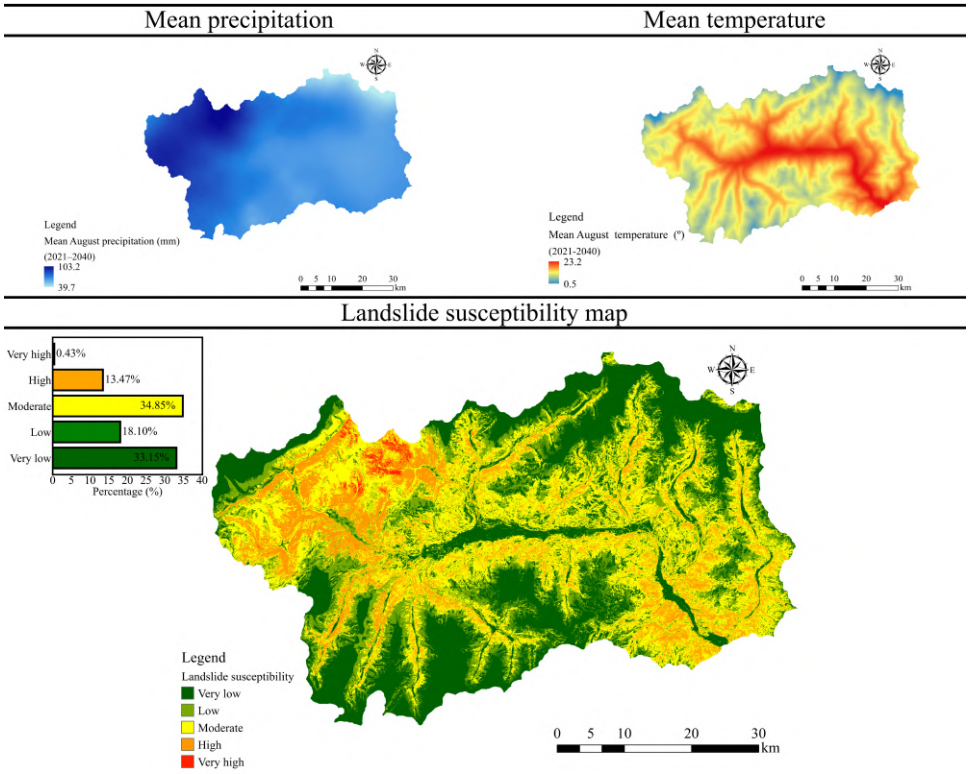

Figure 5-29 August mean precipitation and mean temperature, and LSM.

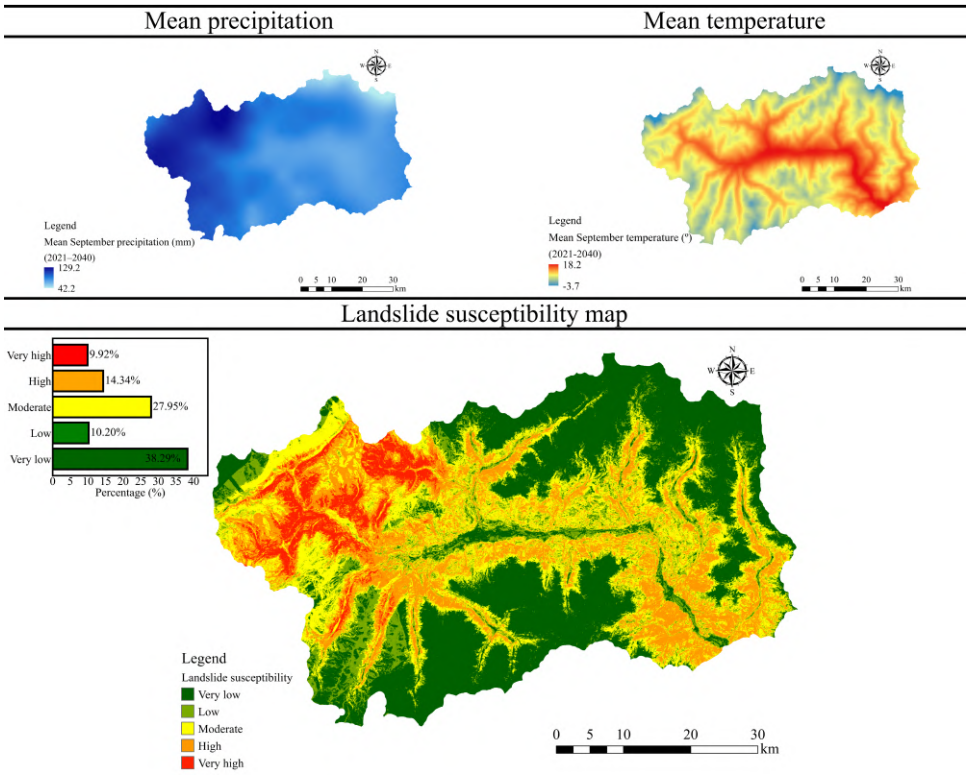

Figure 5-30 September mean precipitation and mean temperature, and LSM.

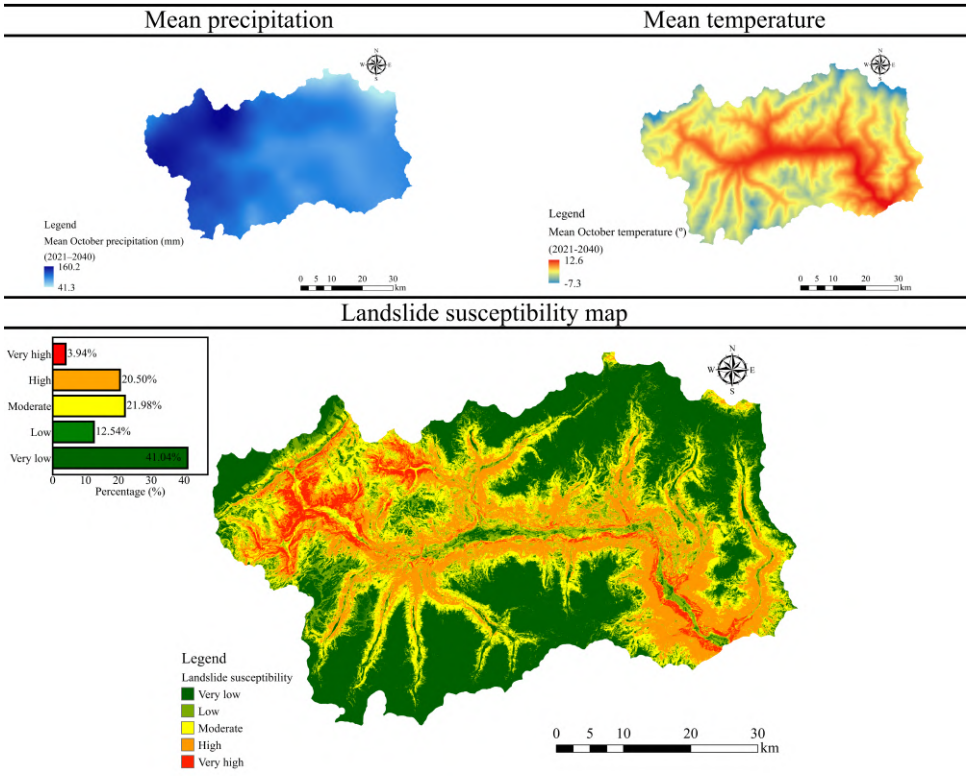

Figure 5-31 October mean precipitation and mean temperature, and LSM.

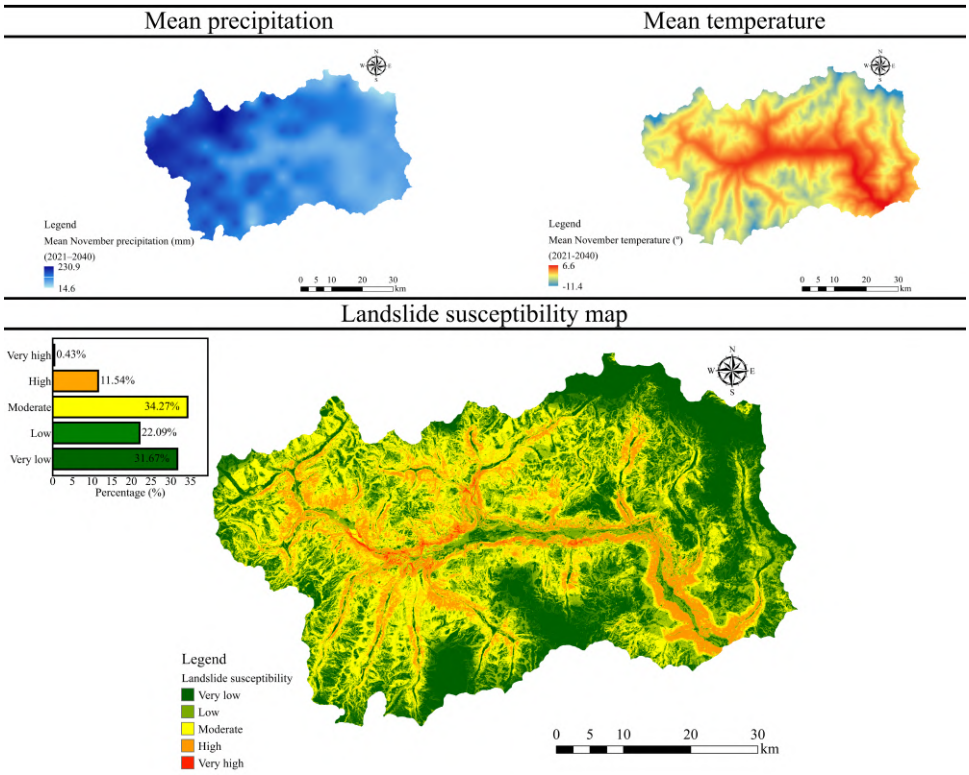

Figure 5-32 November mean precipitation and mean temperature, and LSM.

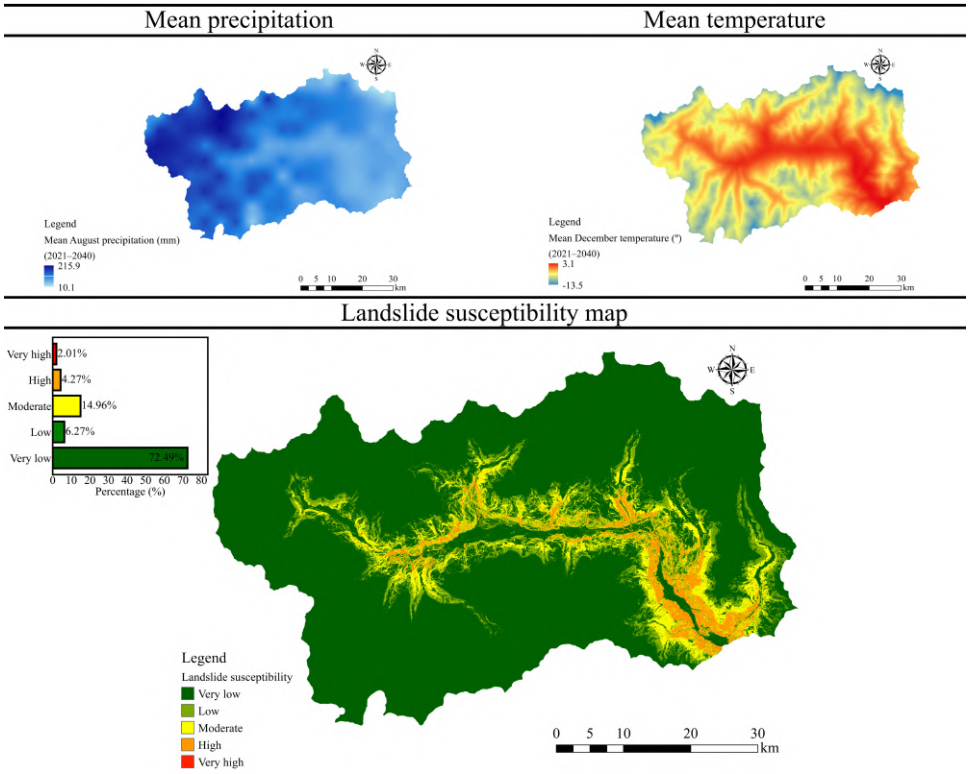

Figure 5-33 December mean precipitation and mean temperature, and LSM.

5.3.13 Summary of monthly susceptibility distribution

Figure 5-34 presents the percentage of each susceptibility class for each month during the period 2021-2040. It can be observed that in the colder months (December to February), only a marginal portion, up to about 6 percent of the region, is susceptible to landslides. From March to May, however, this share increases significantly, reaching around 15.6% percent. During the warmer months, the share decreases as precipitation values decline, but starting from September, a marked increase can again be seen, with susceptibility areas covering about 24 percent of the region. This trend continues to rise gradually, reaching its highest value of approximately 24.4 percent in October, after which it begins to decline.

The increased susceptibility observed in September and October is mainly attributed to the high precipitation levels (151 and 187 mm, respectively). Since the spatial mean temperature during these two months remains relatively high (9.6 and 5.1 °C, respectively), most of this precipitation occurs as rainfall, leading to a significant impact on slope stability. It is worth noting that October in the 2021–2040 period exhibits the highest proportion of "High" and "Very high" susceptibility classes, at approximately 24.6%, representing the maximum value observed across both current and future timeframes.

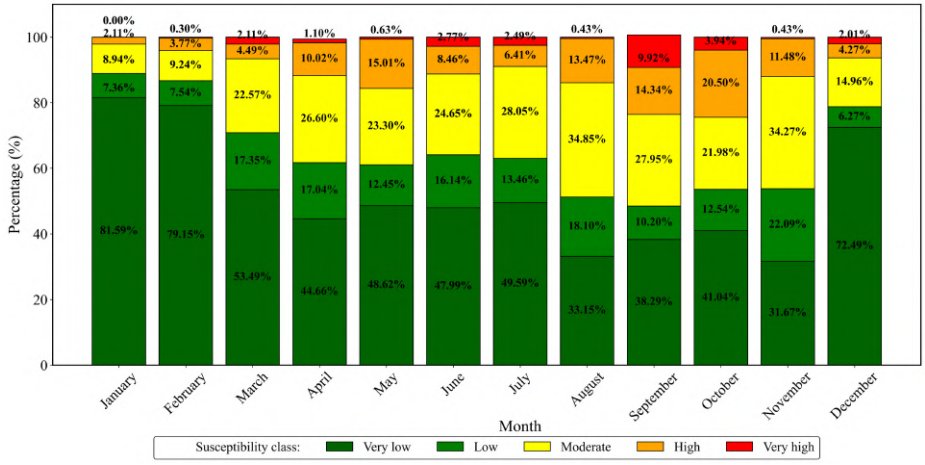

Figure 5-34 Monthly landslide susceptibility shares for 2021-2040.

5.3.14 Envelope map (2021-2040) and verification

To generate a single map representing the overall landslide susceptibility of the region across all twelve months, an "Envelope map" was created (Figure 5-35). In this map, the twelve-monthly landslide susceptibility maps were overlaid, and the highest susceptibility value for each pixel was extracted. The resulting map was then classified into five categories: "Very Low," "Low," "Moderate," "High," and "Very high," using the same class ranges that were applied to the envelope map of the current timeframe (Figure 5-19). Approximately 38% of the study area is

classified as “High” and “Very High” susceptibility, predominantly located in the western and northwestern parts of the region. The blue points represent the landslide events that occurred in 2023.

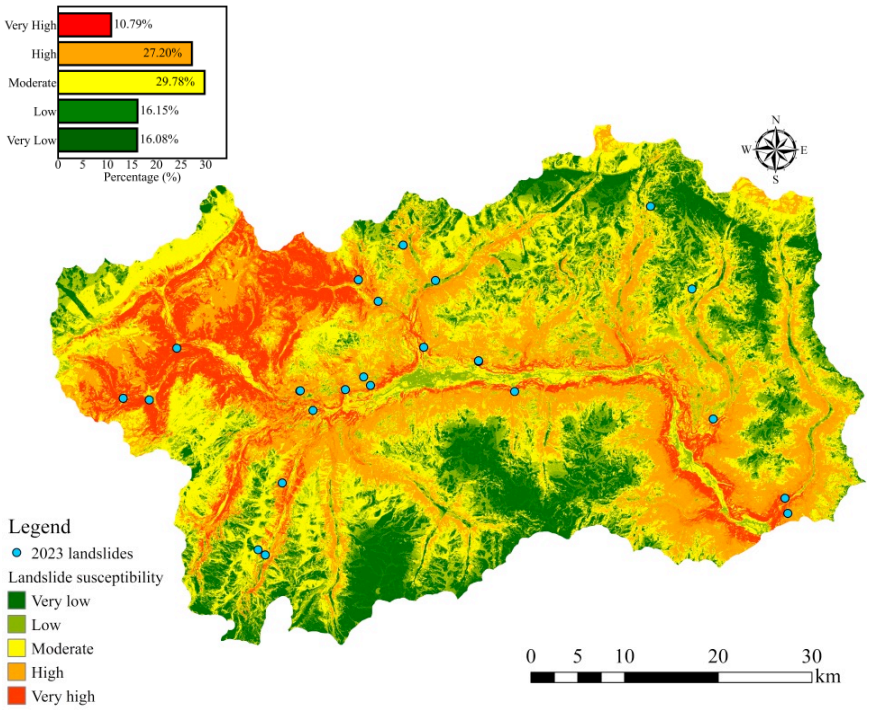

Figure 5-35 Landslide susceptibility envelope map for 2021-2040 and the classes percentage and landslide points in 2023.

The landslide events that occurred in 2023, as described in section 5.2.16, were not included in the training or testing datasets. The resulting map demonstrates improved validation performance for the 2023 events, with 80% of the landslide locations falling within areas classified as “High” or “Very high” susceptibility (Figure 5-36). This represents an approximate 8% improvement compared to the envelope map for the 2003–2022 period (Figure 5-21). Notably, none of the 2023 landslide events were located within the “Very low” susceptibility class.

Although the 2023 inventory contains 25 landslide events, which represents a relatively high number of occurrences within a single year, also compared to the whole dataset considered, the validation dataset remains limited in size. Therefore, additional validation is recommended as new landslide records become available. In particular, once landslide events occurring in 2024 and subsequent years are reported and incorporated into the inventory, the susceptibility map should be re-evaluated to further assess its predictive capability and long-term robustness.

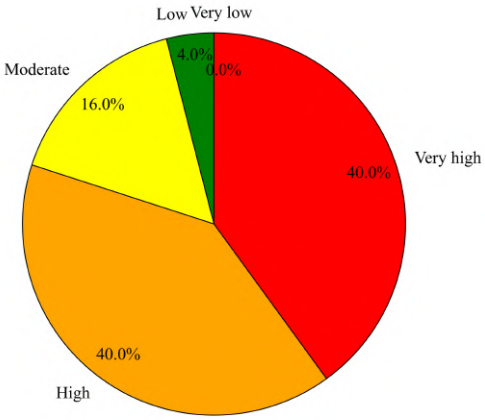

Figure 5-36 Classification of landslide events occurred in 2023 based on the future envelope map.

It should be noted that the 2023 landslide inventory was used primarily as an independent validation dataset to assess the credibility of the susceptibility map with respect to the future climatic period (2021-2040) for which the model was developed. However, this does not imply that landslides that occurred during the historical period (2003-2022) are irrelevant for evaluating model performance. Landslide occurrence is influenced by both persistent terrain characteristics and triggering factors, meaning that locations affected by landslides in the past may remain susceptible to future failures. Therefore, historical landslide events can also provide useful information regarding the spatial reliability of the predicted susceptibility distribution.

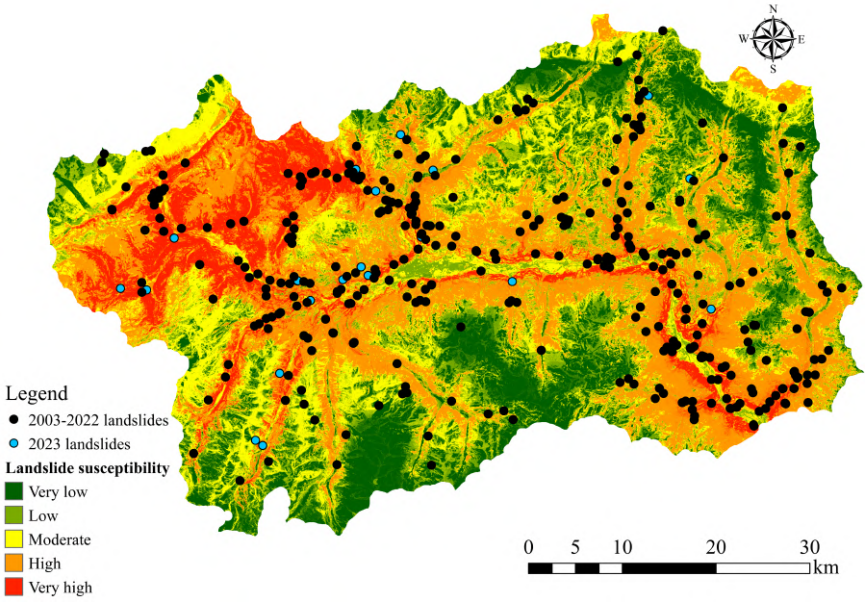

Figure 5-37 Landslide susceptibility envelope map for 2021-2040 and the classes percentage and landslide point from 2003-2023.

To further investigate this aspect, Figure 5-38 presents the classification of landslides that occurred during the 2003-2022 period using the future envelope

susceptibility map. The results indicate that approximately 70% of the historical landslide events fall within the "High" and "Very High" susceptibility classes. This demonstrates that the model is capable of capturing not only future validation events but also a substantial proportion of past landslide occurrences. Although the susceptibility map classifies approximately 38% of the study area as "High" or "Very high", this outcome is considered reasonable given the objective of identifying all potentially unstable areas under future climate conditions. The higher validation rate obtained for the 2023 landslide inventory (80%) compared with the historical inventory (70%) is also expected, as the envelope map was generated using projected climatic conditions for the 2021-2040 period. Consequently, the results suggest that the model provides a conservative yet effective representation of future landslide-prone areas, balancing broad spatial coverage with a strong ability to capture observed landslide occurrences.

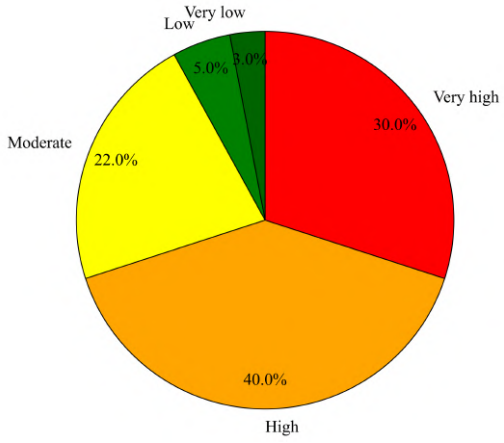

Figure 5-38 Classification of landslide events occurred in 2003-2021 based on the future envelope map.

5.4 Comparing dynamic features

Figure 5-39 illustrates the range and spatial mean of precipitation for the two timeframes, 2003–2022 and 2021–2040. It is evident that both the maximum and minimum precipitation values are projected to decrease in the near future, except for September, where the maximum value increases, while in October and November the maximum values remain approximately unchanged. However, since maximum or minimum values may represent only a limited number of pixels within the study area, a more reliable comparison can be achieved by examining the spatial mean, which accounts for the average value across all pixels in the region. In this regard, March and November show moderate increases of approximately 12 mm and 14 mm, rising from initial values of 93.4 mm and 106.4 mm, respectively. The increases in February, September, and October are more pronounced, with gains of 20 mm, 32 mm, and 23 mm from their initial mean spatial values of 79.3 mm, 57.8 mm, and 85.7 mm. The "seven day precipitation" feature, being a component of the monthly precipitation, is also expected to exhibit similar variations and trends.

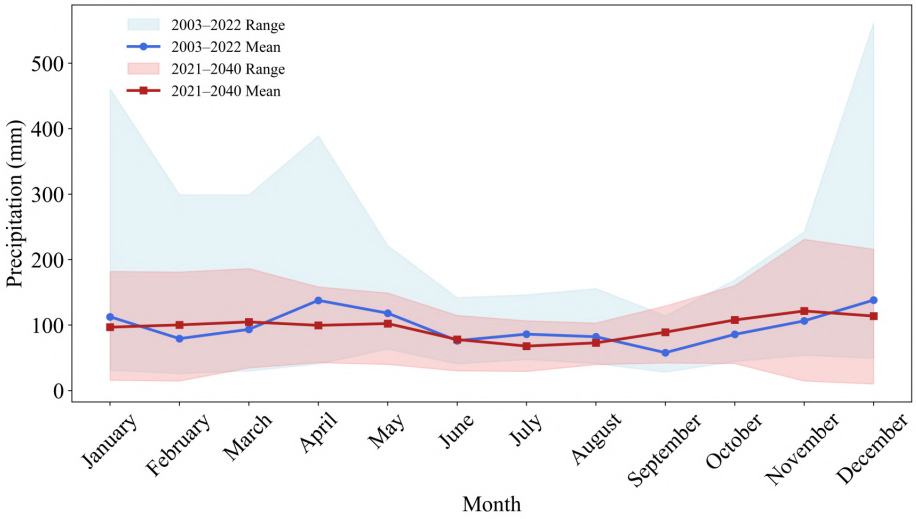

Figure 5-39 Monthly precipitation range and spatial mean for 2003-2022 and 2021-2040.

Figure 5-40 presents the range and spatial mean of temperature for the two timeframes, 2003–2022 and 2021–2040. It is evident that the minimum temperature for all months increases significantly, particularly from December to February, where it is projected to rise by approximately 7 °C. The maximum temperature shows an increase only in August, by 0.3 °C, reaching a peak of 23.2 °C. A more reliable indicator for comparison is the spatial mean temperature, which generally exhibits an increase across most months, except for April and June. The highest rise is observed in August, with an increase of 2.76 °C, reaching a record value of 14.13 °C.

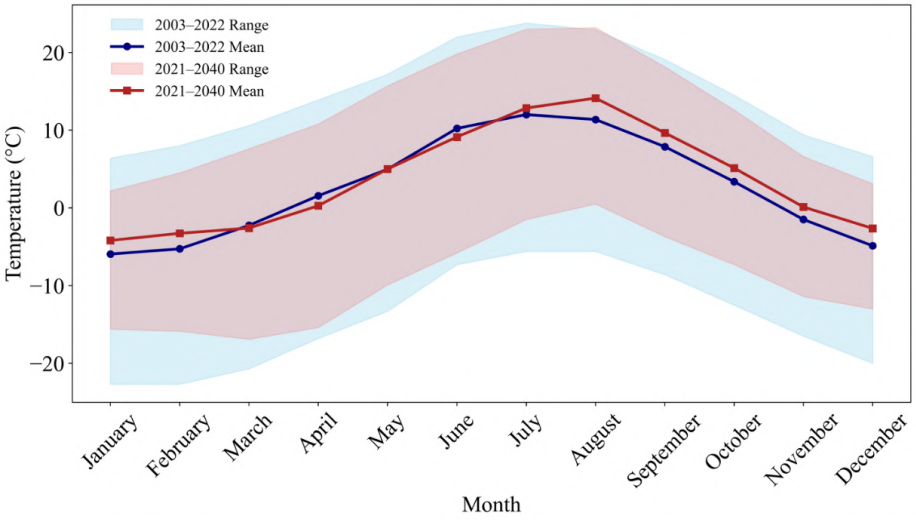

Figure 5-40 Monthly temperature range and spatial mean for 2003-2022 and 2021-2040.

5.5 Comparing envelope maps

Figure 5-41 compares the percentage of susceptibility classes for the current and future envelope maps. It is evident that, due to climate change, the area will become less safe, as the combined proportions of "Very low" and "Low" susceptibility classes are projected to decrease by 1.68%, respectively. This reduction is compensated by a considerable increase of 3.25% in the combined shares of "High" and "Very high" susceptibility classes. The "Moderate" class is also expected to decrease slightly, by approximately 1.5% over the next 20 years.

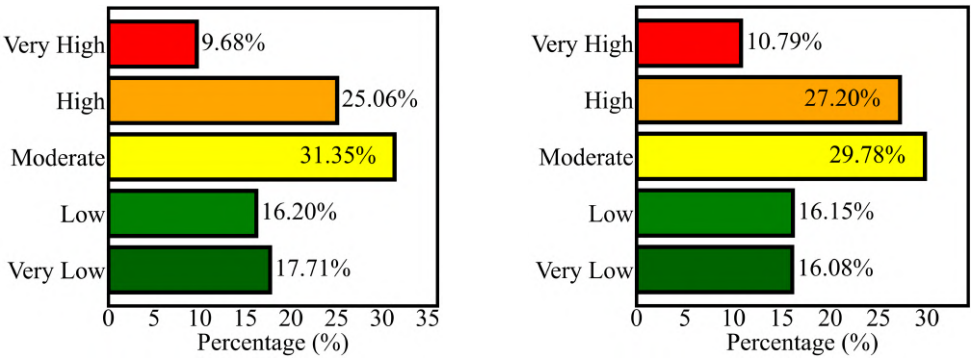

(a) (b)

Figure 5-41 Susceptibility classes for (a) 2003-2022 and, (b) 2021-2040.

5.6 Comparing monthly susceptibility distribution

Figure 5-42 illustrates the monthly variation in the percentage of susceptible areas (i.e., the sum of very high and high classes) for the current and future periods. It can be observed that the situation is not expected to worsen for every month. For instance, in April and May, the extent of susceptible areas is projected to decrease, mainly due to the reduced amount of precipitation anticipated under the SSP 5-8.5 scenario. However, the situation is expected to intensify during autumn, with October showing the highest value of 24.4% of the area classified as susceptible. This increase is attributed to the simultaneous rise in projected temperature and precipitation for that month.

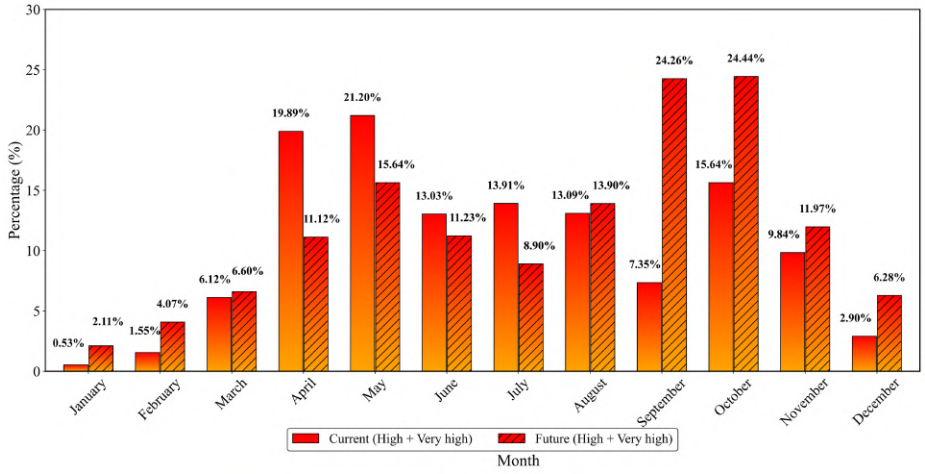

Figure 5-42 Comparison of monthly share of high and very high susceptible areas for the current and future time frames.

5.7 Monthly LSM as the optimal choice

Initially, precipitation and temperature were treated as static variables to generate a single landslide susceptibility map. Specifically, accumulated annual mean precipitation and mean annual temperature for the period 2003–2022 were used as representative climatic inputs (Figure 5-43). This approach is consistent with many previous studies, where precipitation is commonly considered in annual time windows due to its availability and the relative simplicity of implementation. By adopting annual aggregates, precipitation was effectively represented as a time-invariant factor, allowing the model to produce one spatially distributed susceptibility map for the entire study period. Temperature was also incorporated as a static variable using mean annual values. In several studies, temperature is often indirectly represented through elevation as a conditioning factor. However, in this case, temperature was explicitly included to better characterize the climatic conditions of the region, while still maintaining a static framework.

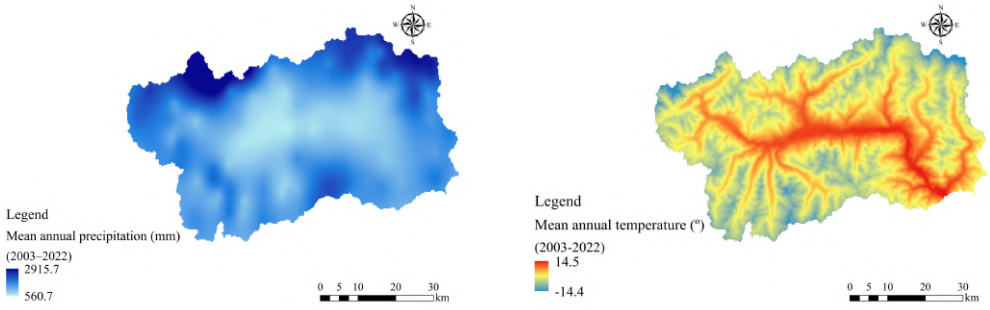

(a) (b)

Figure 5-43 Mean annual values of (a) precipitation and (b) temperature in 2003-2022, used in initial model.

LCFs were consistent with those described in Chapter 4, and the same algorithm, XGBoost, was employed. The number of landslides used for training and testing in this model was 542, which is higher than in the original model (369). This difference arises because, in several landslide records, only the year of occurrence was reported, while the exact month was not specified. Such events were excluded from the original model, which required temporal resolution at the monthly scale, but were retained in this static framework. In addition, the number of non-landslide points was set equal to the number of landslide points to ensure a balanced dataset.

Within this single-model framework, the importance scores of the LCFs were calculated and are presented in Figure 5-44. The results indicate that temperature, land cover, and slope are the three most influential factors. In contrast, mean annual precipitation, which is generally considered a primary triggering factor for landslides, ranks among the least important variables.

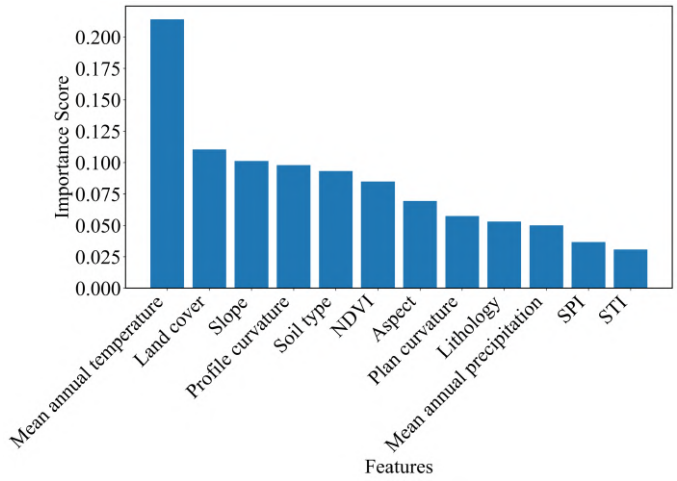

Figure 5-44 Importance scores of LCFs for the initial model.

Figure 5-45 presents the AUC of the model, which is 0.89. This value is lower than the lowest AUC obtained in the original model, which was 0.93.

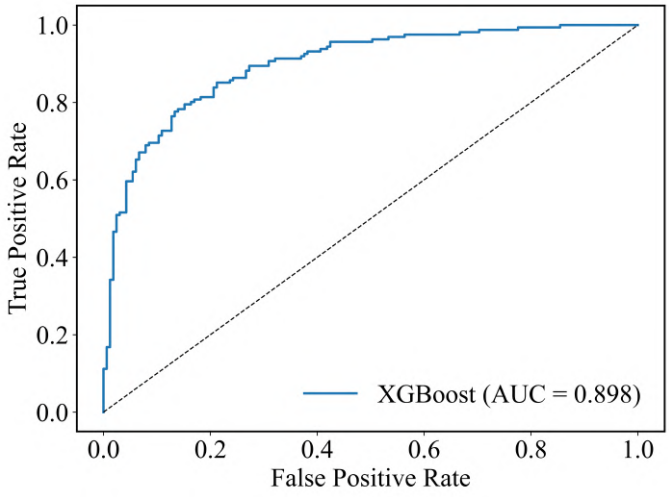

Figure 5-45 ROC curve and AUC score for the initial XGBoost model.

Finally, Figure 5-46 illustrates the LSM. The range of each susceptibility class is consistent with that of the original model described in section 5.2.16. The results indicate that approximately 20.3% of the study area is classified as "High" or "Very high" susceptibility, while 57.1% and 11.6% fall within the "Very low" and "Low" classes, respectively.

In comparison with the envelope map of 2003–2022 (Figure 5-19), an important limitation becomes evident. The model fails to identify the western and northwestern parts of the study area as "High" or "Very High" susceptibility zones, despite the presence of landslide events recorded during 2003–2022 (used as training and testing data) as well as in 2023 within these regions.

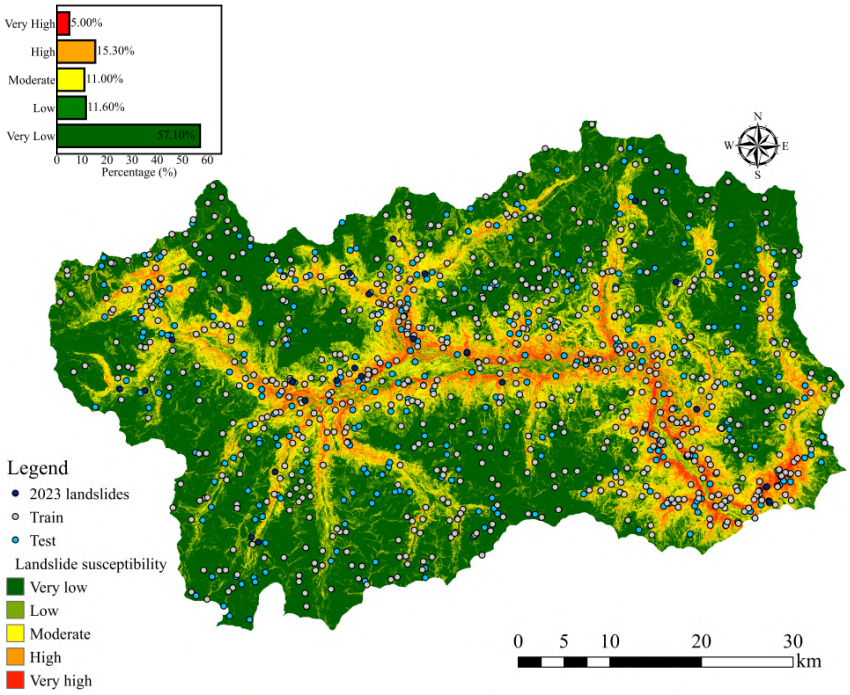

Figure 5-46 Initial LSM for 2003-2022, using annual precipitation and temperature.

It can be seen that, in the initial model, only 56% of the 2023 landslide events occurred within areas classified as “High” or “Very high” susceptibility (Figure 5-47), while a substantial proportion (28%) fell within the “Very low” or “Low” susceptibility classes, highlighting its limited predictive performance. This performance was significantly improved in the original model, where 72% of the landslides were located in “High” or “Very high” susceptibility zones (Figure 5-21), and only 8% occurred in the “Very low” or “Low” classes.

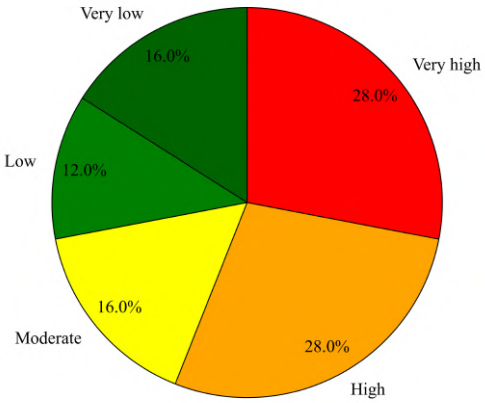

Figure 5-47 Classification of landslide events occurred in 2023 based on the initial susceptibility map.

The development of the monthly LSMs and the corresponding envelope map was motivated by the limitations observed in the initial model. As demonstrated, the initial model was not able to effectively capture the role of precipitation as a key landslide conditioning factor. More importantly, its performance in predicting landslide occurrences for 2023 was relatively weak, highlighting the inadequacy of representing climatic variables as static, annual inputs.

These limitations led to a reconsideration of how climatic variables should be incorporated into the modeling framework. In particular, it became evident that the temporal variability of precipitation and temperature, including their seasonal patterns, plays a critical role in landslide occurrence and should not be overlooked.

By adopting monthly LSMs, it becomes possible to account for the intra-annual variability of precipitation and temperature, allowing the model to capture both seasonal trends and short-term fluctuations within a given timeframe. This temporally resolved approach provides a more realistic representation of the hydro-meteorological conditions influencing slope stability.

Furthermore, the use of monthly LSMs offers a significant advantage when the objective is to assess the impacts of climate change. Training the model on monthly-scale data enables it to better capture the relationship between climatic variables and landslide occurrence over time, thereby allowing for a more reliable evaluation of potential changes under future climatic scenarios.

5.8 Summary

This chapter presents a comprehensive assessment of landslide susceptibility through monthly mapping for both the historical period (2003–2022) and a projected future scenario (2021–2040), complemented by an envelope map representing landslide susceptibility for each timeframe. For the 2003-2022 period, model performance, evaluated using the Area Under the Curve (AUC), exhibits limited seasonal variability, with slightly higher predictive accuracy during colder months, likely because the underlying conditions make it easier for the algorithm to distinguish between landslide and non-landslide events under low-temperature regimes. Analyzing feature importance reveals a clear seasonal pattern, with precipitation-related variables dominating during warmer months, while temperature emerges as the primary controlling factor in colder periods, reflecting its stabilizing influence through ground freezing and reduced pore-pressure development. The spatial distribution of susceptibility confirms this seasonal behavior, with minimal high-susceptibility areas in winter (less than 3%), increasing significantly in spring and peaking in April and May (approximately 20%), before declining in summer and rising moderately again in autumn. These patterns are consistent with observed landslide occurrences, of which approximately 55% are concentrated in April, May, June, and October, demonstrating strong agreement between modeled susceptibility and real events. The Envelope Map for the historical period further confirms the model's robustness, capturing approximately 75% of landslides within areas classified as "High" and "Very high" susceptibility, despite these zones covering only about 35% of the study area, while independent validation using 2023 events shows a similar agreement of about 72%. For the future scenario (2021–2040), landslide susceptibility maps were generated using the trained models and climate projections from the WorldClim database, revealing a comparable but intensified seasonal pattern. Susceptibility remains low during winter (up to approximately 6%), increases in spring (around 15.6%), decreases during summer due to reduced precipitation, and rises sharply in autumn, reaching a peak of approximately 24.4% in October, which represents the highest susceptibility observed across both periods. This intensification is primarily driven by the combined effect of increased precipitation and relatively high temperatures, leading to rainfall-dominated conditions that promote slope instability. Analysis of projected climate variables indicates an overall increase in spatial mean precipitation during some months, particularly February, September, and October, alongside a consistent rise in temperature, including significant increases in minimum winter temperatures and notable increases in mean temperatures. The future Envelope Map highlights a shift toward higher susceptibility levels, with a reduction of approximately 1.68% in "Very low" and "Low" classes and an increase of about 3.25% in "High" and "Very high" classes, indicating a general decline in slope stability under projected climate

conditions. However, this trend is not uniform across all months, as slight decreases in susceptibility are projected for spring months such as April and May, while autumn months, particularly October, exhibit a marked increase. Validation using the 2023 landslide events indicates that 80% of the observed landslides occurred within areas classified as “High” or “Very high” susceptibility. Overall, the results demonstrate that climate change is likely to amplify landslide susceptibility and modify its seasonal distribution in the alpine region, with a pronounced shift toward higher risk during specific periods of the year.

Chapter 6

Identification of landslides interaction with linear infrastructures

6.1 Introduction

In the previous chapter, landslide-susceptible areas were identified for both current conditions and future scenarios accounting for climate change over the next 20 years. Building on those results, the present chapter shifts the focus from regional susceptibility mapping to the assessment of landslide risk for linear infrastructure. The aim of this chapter is to demonstrate the applicability of the proposed methodology in evaluating the interaction between landslide susceptibility and infrastructure elements. To this end, electricity transmission lines are considered as a representative example of linear infrastructure, allowing the identification of those segments that are more exposed to landslide hazards within the study area.

To achieve this objective, the locations of power transmission towers first need to be mapped. Subsequently, the envelope current and future landslide susceptibility maps will be used to extract susceptibility values at each tower power across the entire region. This approach allows for a spatially consistent evaluation of landslide exposure affecting the electricity network. Finally, a case study will be performed to investigate cascading effects within the electricity transmission network, where damage to a single power tower caused by landslides may lead to functional disruption of connected transmission lines upstream and downstream.

6.2 Obtaining aerial power tower map

The technical map of the study area was obtained from the Geoportal of the Aosta Valley region (https://geoportale.regione.vda.it/). Figure 6-1a includes specific cartographic symbols identifying electricity transmission lines and power towers. The map was subsequently partitioned into 1 km × 1 km grid cells using QGIS. Based on this partitioning, vector shapefiles of the power transmission lines and power towers were extracted and generated and then stored for use in the subsequent analysis steps. Figure 6-1b shows the spatial distribution of electricity transmission lines and power towers across the study region. Figure 6-1c presents a zoomed-in aerial view highlighting the corresponding transmission line and tower shapefiles.

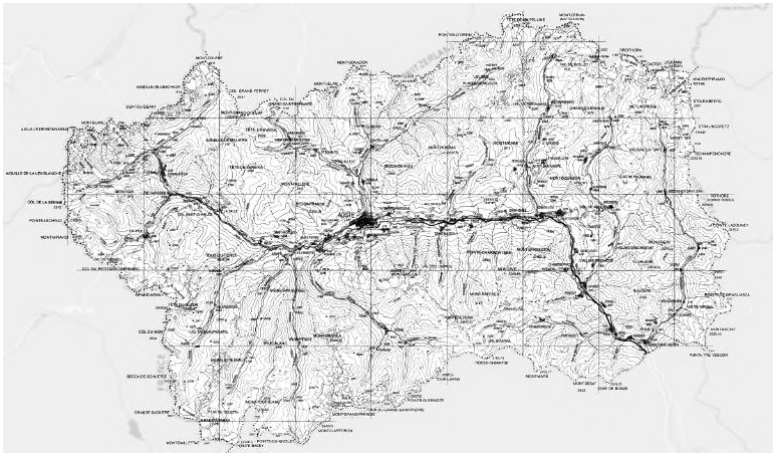

(a)

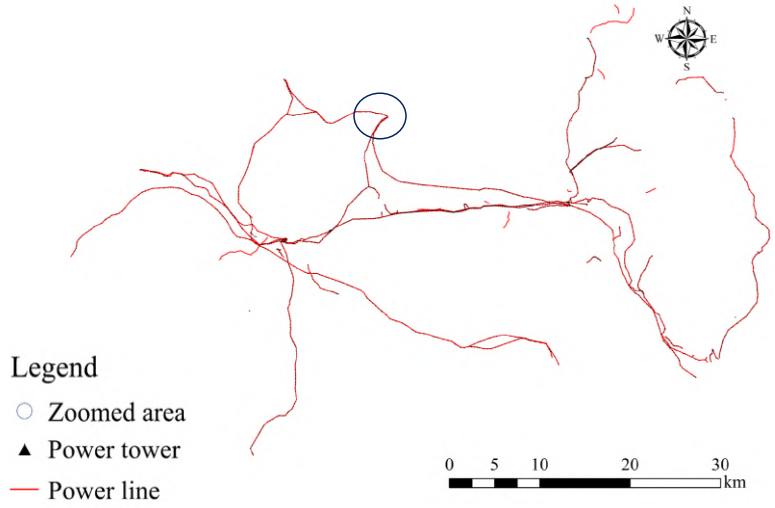

(b)

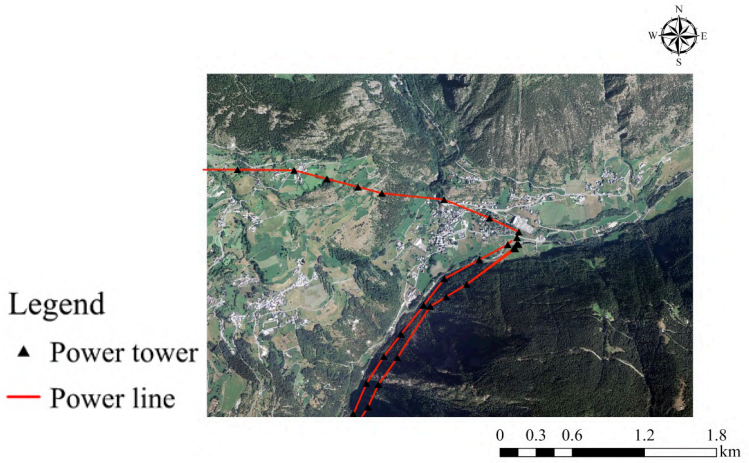

(c)

Figure 6-1(a) Cartographic map of the Aosta Valley region, (b) Spatial distribution of electricity transmission lines and power towers, and (c) zoomed-in aerial view showing the extracted transmission line and tower shapefiles.

6.3 Overlay analysis of power tower locations on landslide susceptibility maps

6.3.1 Current period (2003–2022)

After locating all power towers in the region, landslide susceptibility values were extracted from the 2003–2022 envelope map. Figure 6-2 illustrates the intersection between the power tower locations and the landslide susceptibility map. It can be seen that 18.31% of the power towers are located in areas identified as having "Very high" landslide susceptibility. A larger share of the power towers, 31.1%, fall within zones classified as "High" susceptibility.

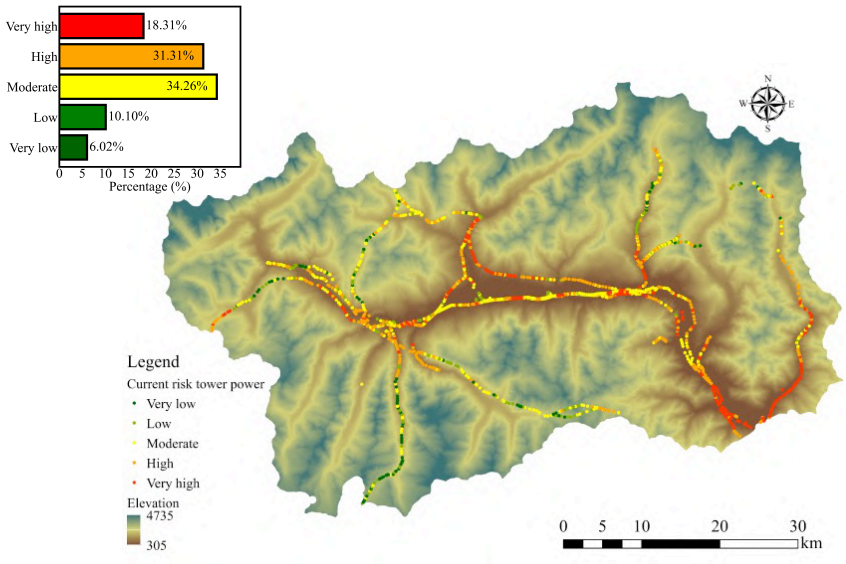

Figure 6-2 Landslide susceptibility intersection with power towers (2003-2022).

6.3.2 Future period (2021-2040)

The intersection of power towers with the future landslide susceptibility map is illustrated in Figure 6-3. The proportions of the "Very high" and "High" susceptibility classes increase by 1.61% and 1.16%, respectively. Most power towers exposed to landslide hazard are primarily concentrated in the western and northwestern parts of the region.

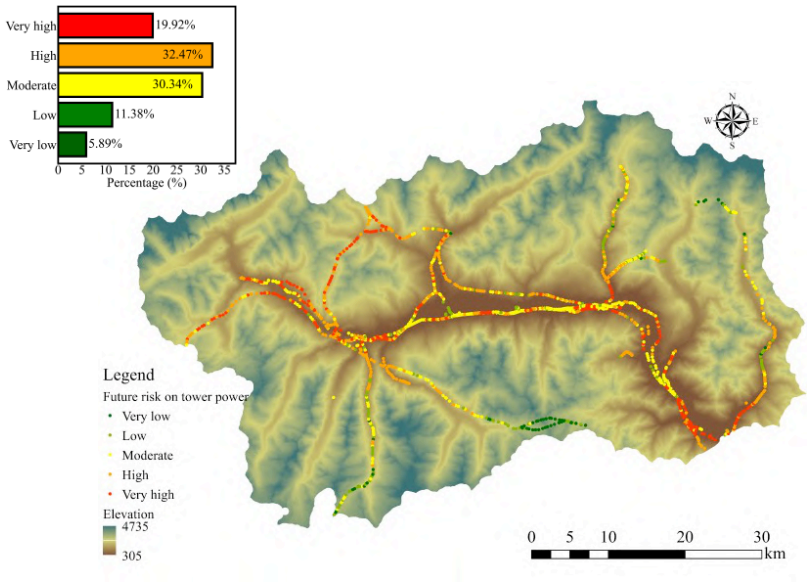

Figure 6-3 Landslide susceptibility intersection with power towers (2021-2040).

6.4 Investigating cascading failures in power grids

Cascading failures, characterized by long chains of interdependent events and outages, pose a serious threat to the reliable operation of power grids and can result in catastrophic blackouts with substantial economic and societal losses if not adequately understood, prevented, or mitigated.

Various methods have been proposed to investigate cascading failures in power grids. For instance, Liu et al. (2025) introduced a framework to assess the risks posed by natural hazards to power grid infrastructure. Meyur (2022) conducted a vulnerability analysis of power grids subjected to severe initiating events, including hurricanes, earthquakes, forest fires, and targeted cyber or physical attacks. Using reinforcement learning, Meng et al. (2025) argued that conventional mitigation strategies are largely "single-stage", whereas cascading failures are inherently dynamic, multi-stage processes that require continuous and adaptive intervention.

Another line of research models power grids as complex networks. Doostinia et al. (2025) and Doostinia and Falabretti (2025) represent physical components such as power towers and substations as nodes, and transmission lines as edges within a graph structure. The criticality of these components is quantified using

network centrality metrics, including Betweenness Centrality (BC) and Degree Centrality (DC), which rank elements based on their connectivity and topological importance. To evaluate operational risk, Node Removal Performance (NRP) and Edge Removal Analysis (ERA) are performed by simulating the complete failure of selected nodes or lines and analyzing the system response. Risk is quantified using the performance reduction percentage, defined as the proportion of remaining nodes that lose access to power following a component failure. By correlating these outcomes with centrality rankings, the most critical nodes and transmission lines for maintaining grid stability are identified, enabling targeted prioritization of maintenance and hardening measures.

In this study, the latter network-based approach is adopted, as detailed socio-economic data related to population access or economic dependence on individual power towers were not available. Nevertheless, this approach still requires an explicit representation of the power tower connectivity within the network. A specific area within the region was selected as the case study. This area was chosen because the distribution point could be clearly identified using aerial imagery, and the associated power tower network exhibits a relatively simple linear configuration. Accordingly, the risk associated with each power tower is calculated based on the risk of losing the power supply connected to that tower, as defined in Equation (6-1):

$$R_{P_i} = \frac{n_{i-1}}{n} \tag{6-1}$$

where R_{P_i}denotes the risk associated with power tower i, n_{i-1}represents the number of power towers located upstream of tower $i$along the transmission path toward the terminal points , and n is the total number of power towers connected to the power distributor. Figure 6-4 illustrates a selected area in which point A represents the location of the power distributor, while points B, C, and D correspond to the terminal points of the transmission lines.

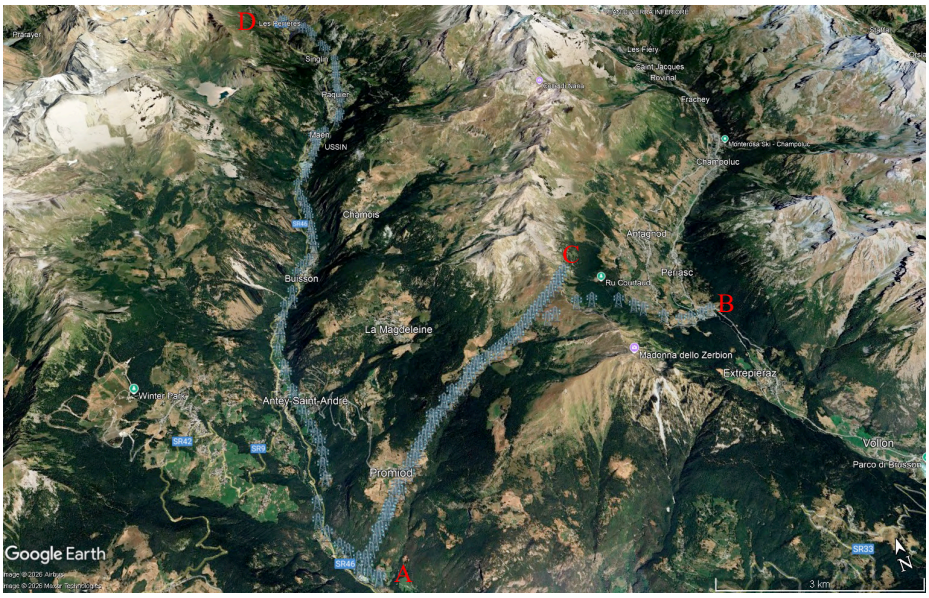

Figure 6-4 the aerial photo of selected area. Blue symbols are the power towers, A is where the power distributor located, while points B, C, and D are to the terminal points of the transmission lines.

Varnes (1981) proposed an equation to compute the risk on elements due to the landslide Equation (6-2):

$$R_L = H.V.E \tag{6-2}$$

where R_L is the risk on the considered element due to the landslide, E is the exposure of the element which can be the population, properties, economic activities, or public services potentially at risk, H is the hazard which is probability of occurrence within a specified period of time and within a given area of a potentially damaging phenomenon (the landslide), finally V is vulnerability which is the degree of loss to a given element or set of elements resulting from the occurrence of landslides.

In this study, triggering factors associated with LCFs, such as precipitation and temperature, are explicitly considered, and the analysis is conducted over a defined time frame. Under these conditions, landslide susceptibility is assumed to be equivalent to hazard. Furthermore, since power towers are fixed in location, the exposure term is set equal to 1. In addition, because the population surrounding each power tower is assumed to be uniform, the vulnerability term V is also taken as 1. Accordingly, the above equation can be simplified and rewritten in the form of Equation (6-3):

$$R_{L_i} = S_i \tag{6-3}$$

where, R_{L_i} is the risk due to landslide on element i, and S_i is the landslide susceptibility on element i, which has been obtained from the envelope map.

To account for the combined impacts of landslide-induced risk on power towers and the associated cascading effects, an integrated formulation is required in which both Equation (6-1) and Equation (6-3) are normalized. For this purpose, Equation (6-4) is employed:

$$R_{t_i} = \frac{R_{L_i} + R_{P_i}}{R_{L_{max}} + R_{p_{max}}} \tag{6-4}$$

Figure 6-5 illustrates the cascading impacts calculated using Equation (6-1). The results indicate that power towers located closer to the distributor exhibit higher risk levels. This is primarily because the failure of any tower in proximity to the distributor can disrupt power transmission to a large portion of the network, potentially leading to a shutdown of the entire system.

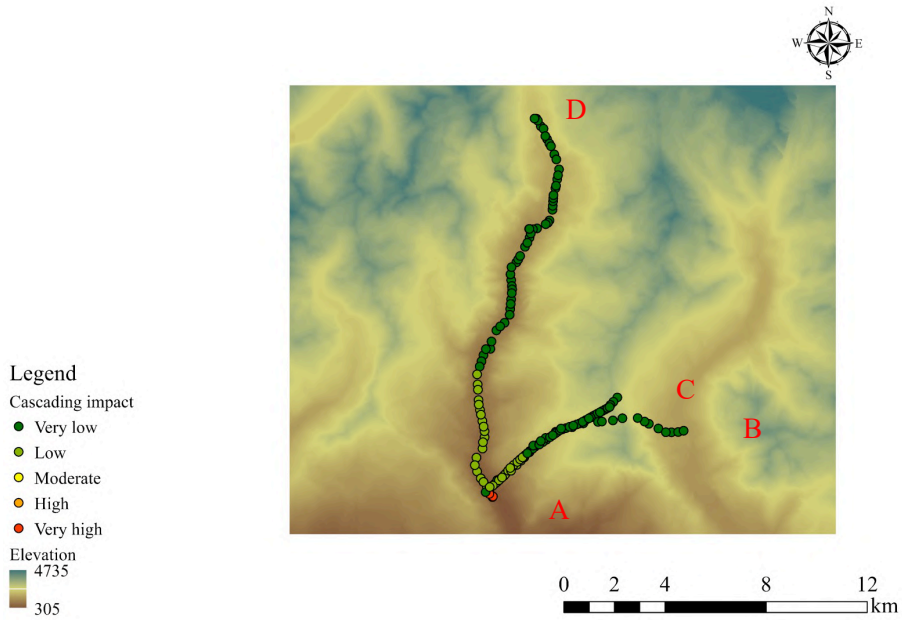

Figure 6-5 Cascading impacts of tower power failure.

Figure 6-6 illustrates the risk associated with landslides, which is assumed to be equal to landslide susceptibility (Equation (6-3)).

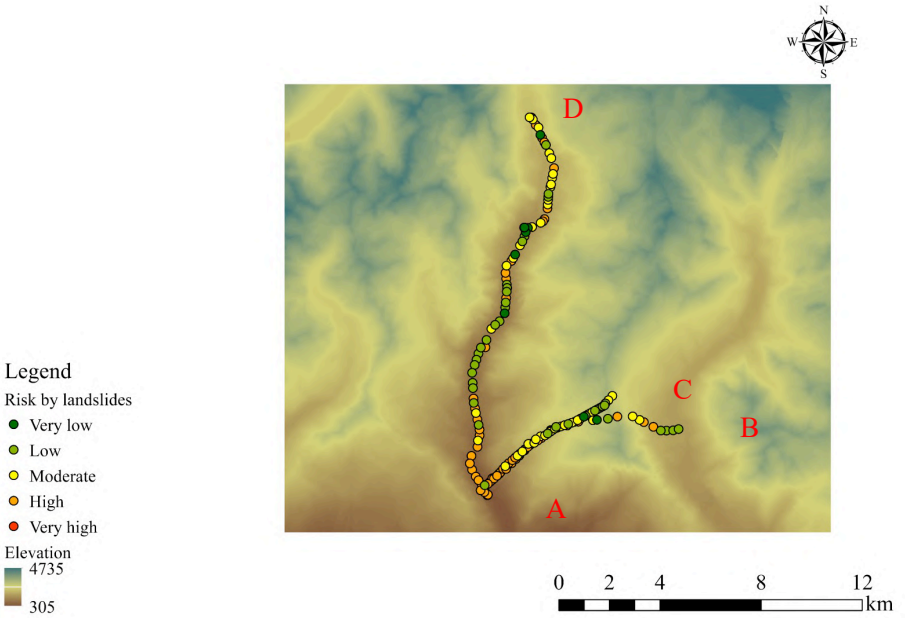

Figure 6-6 Risk by landslides on tower power in the selection area.

Finally, Figure 6-7 presents the combined risk resulting from landslides and cascading impacts. Power towers located near the distributor exhibit high risk values in both cascading effects and landslide susceptibility; consequently, these towers also show the highest combined risk values.

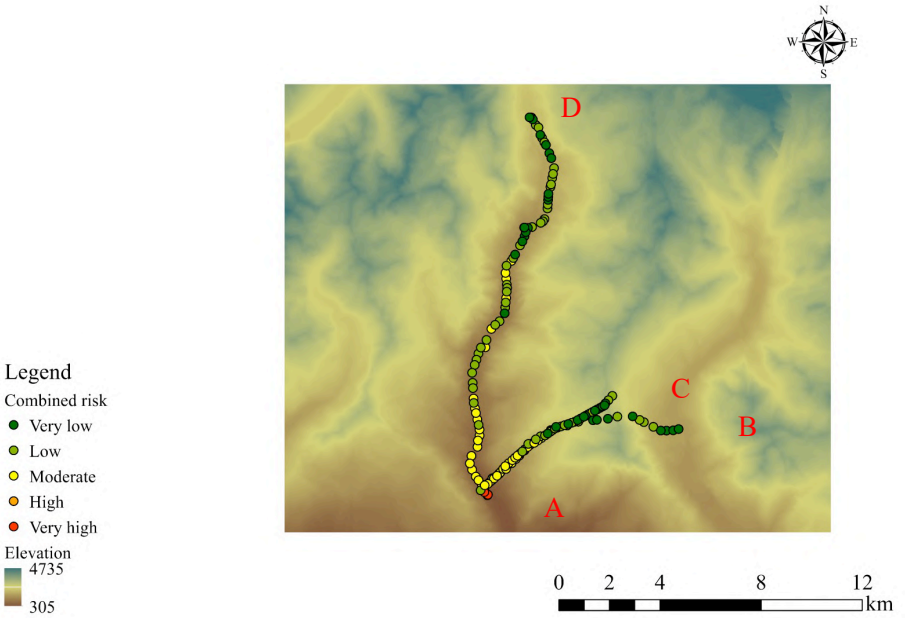

Figure 6-7 Combined risks (landslides and cascading effects) on power towers in the selected area.

6.5 Other applications with overlay analysis

In this study, the interaction between landslide susceptibility and power transmission towers has been investigated. Due to limited availability of detailed infrastructure data, all power towers were assumed to have equal importance within the network. However, in a more comprehensive framework, additional attributes such as transmitted power capacity, load distribution, and the number of end-users served by each tower could be incorporated. Inclusion of such parameters would enable a more realistic representation of infrastructure criticality and could significantly influence the resulting risk assessment.

The proposed methodology is transferable and can be extended to other types of infrastructure, including transportation networks (e.g., roads and railways), pipelines, and water conveyance systems. Each of these infrastructure systems is associated with its own intrinsic risk characteristics. For instance, road networks may be evaluated based on traffic volume and accessibility impacts, pipelines based on flow capacity and potential environmental consequences of failure, and waterways based on hydraulic connectivity and flood propagation effects. Similar to the cascading impacts observed in power networks, failures in these systems may also trigger secondary or interconnected disruptions.

By integrating these infrastructure-specific vulnerability and consequence metrics with landslide susceptibility maps, a more comprehensive multi-risk framework can be developed. This allows not only for the identification of exposed assets but also for the assessment of systemic impacts, thereby supporting more effective risk-informed planning and decision-making.

6.6 Summary

In this chapter, the study shifted focus from regional susceptibility mapping to the specific risk assessment of linear infrastructure, with a primary objective of identifying electricity transmission lines exposed to landslide hazards.

The analysis began by generating a detailed inventory of the electricity network. Using technical maps from the Geoportal of the Aosta Valley region, the spatial distribution of transmission lines and power towers was vectorized and partitioned into a grid format to facilitate spatial analysis.

Subsequently, an exposure analysis was conducted by overlaying the infrastructure locations onto the landslide susceptibility envelope maps. This was performed for two distinct time frames: current conditions (2003–2022) and future climate scenarios (2021–2040). The results indicated a significant exposure of the network, with over 49% of towers currently located in "High" or "Very high"

susceptibility zones. The future scenario analysis revealed a projected increase in these proportions, particularly in the western and northwestern sectors of the region.

To address the interdependence of the grid, the study also investigated cascading failures for a specific case study. Adopting a network-based approach, the topological importance of each tower was evaluated. A specific risk model was developed that adapted Varnes (1981) equation, simplifying the exposure and vulnerability terms to focus on susceptibility as the primary hazard. This physical risk was then integrated with a functional risk metric, defined by the tower's position relative to the power distributor. The final output produced a combined risk index, highlighting that towers located near the power distributor are the most critical due to both their proximity and the high landslide susceptibility in that area, which could trigger extensive downstream network disruptions if failure occurs.

Chapter 7

Summary and conclusions

7.1 Summary

This Thesis investigates the impact of climate change on landslide susceptibility in the Alpine region using a machine learning-based approach. To develop and test the methodology, the Aosta Valley, a region in the North of Italy was selected as a case study.

Thirteen landslide conditioning factors, representing key variables that potentially influence landslide occurrence, were considered in this study. For the baseline scenario, daily temperature and precipitation data covering the period 2003-2022 were used, resulting in approximately 7,200 raster layers for both variables. To better capture the role of short-term rainfall in triggering landslides, seven-day accumulated precipitation was also accounted for, representing the total rainfall in the seven days preceding each landslide event. In addition, a landslide inventory consisting of 369 events, occurred in the study region, over the same period was compiled and used for model training and validation.

Using the XGBoost algorithm, monthly landslide susceptibility maps were generated for the period 2003-2022, together with an envelope map representing the maximum susceptibility values across all twelve months. Each monthly model was evaluated independently using the Area Under the Curve (AUC) metric. The trained models were then used to project landslide susceptibility for the period 2021-2040 based on temperature and precipitation projections from CMIP6 under the SSP5-8.5 scenario. The results of the study suggest an overall increase of the "High" and "Very high" landslide susceptibility classes in the near future for the

study area. This occurs particularly during the autumn months, driven by the combined effect of rising temperature and increased precipitation.

Both envelope maps were validated using independent landslide events that were not included in the training and testing datasets. The envelope map for 2021-2040 was able to capture approximately 80% of the observed landslides within areas classified as "High" or "Very High" susceptibility, indicating a strong agreement between model predictions and real-world events.

In addition, the potential interaction between landslide susceptibility and linear infrastructures was analyzed. Specifically, as a general example, the spatial relationship between electric power lines and the susceptibility maps was assessed. The findings allow to quantify that a greater number of power towers may be exposed to landslide risk under future climate conditions. Finally, for a selected area within the study region, the potential cascading effects associated with landslide susceptibility were investigated, highlighting the compounding risks within localized systems.

7.2 Conclusions

This section presents the main conclusions of the Doctoral research, which develops a novel methodology to assess the impact of climate change on landslide susceptibility, while also examining the interaction between landslide-prone areas and linear infrastructure systems.

7.2.1 Landslide susceptibility assessment under climate variability

A novel machine learning-based framework is developed to investigate the impact of climate change on landslide susceptibility, accounting for the temporal variability of climatic drivers. A key advancement in the methodology is incorporating both temperature and precipitation data. The algorithm is trained on 2003-2022 climatic conditions, allowing it to reproduce present-day landslide patterns while remaining sensitive to future climatic variations. To better capture short-term triggering mechanisms, a seven-day accumulated precipitation parameter is introduced, representing rainfall conditions immediately preceding landslide events.

Another advancement of the proposed framework lies in its dynamic treatment of feature importance. Unlike conventional models that rely on static rankings, the methodology evaluates the relative importance of controlling factors on a monthly basis, thereby capturing seasonal variability in landslide drivers. As a result, model performance is shown to vary throughout the year, with higher predictive capability during colder months, when landslide and non-landslide conditions are more distinct, and slightly reduced performance during warmer periods due to increased

overlap in climatic signals. Nevertheless, the model consistently demonstrates high accuracy, with a minimum AUC of 0.93.

The generated monthly susceptibility maps reflect the seasonal distribution of landslide occurrence, with April and May exhibiting the highest proportions of "High" and "Very High" susceptibility classes, consistent with historical patterns. In contrast, winter months display significantly lower susceptibility levels. To provide a comprehensive representation of regional conditions, an envelope map is constructed by combining the maximum susceptibility values across all months. Validation against independent 2023 landslide events confirms the reliability of this approach, with 72% of events located within high-susceptibility zones.

The proposed monthly framework outperforms traditional annual models by effectively capturing seasonal climatic variability, increasing the predictive accuracy from approximately 56% to 72% in validation exercises. Furthermore, the methodology is extended to future climate scenarios by incorporating projected temperature and precipitation data. The results indicate a general decline in slope stability over the next two decades under SSP5-8.5 scenario, characterized by a reduction in low-susceptibility areas and a corresponding increase in "High" and "Very high" classes. Notably, the future envelope map (2021–2040) demonstrates even stronger predictive capability, capturing 80% of observed 2023 landslide events, thereby emphasizing the importance of integrating projected climate data in forward-looking susceptibility assessments.

7.2.2 Interaction between landslide susceptibility and infrastructures

Beyond susceptibility assessment, the study extends the analysis to evaluate the interaction between landslide-prone areas and critical infrastructure. The generated susceptibility maps provide a basis for identifying infrastructure elements exposed to landslide hazards. In particular, as a general example, an overlay analysis with electricity transmission networks reveals that a substantial proportion of power towers are currently located within areas classified as "High" and "Very High" susceptibility. These proportions are projected to increase under future climate conditions, highlighting a growing exposure of infrastructure to landslide risk.

Importantly, the assessment of infrastructure risk goes beyond simple spatial overlap by considering system-specific vulnerabilities. In the case of power transmission networks, it is important to incorporate the cascading failure mechanisms into the analysis, recognizing that the failure of a single element may propagate through the system. By integrating landslide susceptibility with infrastructure-specific risk characteristics, the study provides a more comprehensive evaluation of potential impacts.

Overall, the methodology establishes a robust foundation for coupling landslide susceptibility modeling with infrastructure risk assessment, offering a transferable approach for identifying and managing climate-induced geohazards in complex systems.

7.2.3 The impacts of this Doctoral research

This Doctoral research provides a significant advancement in the assessment of landslide susceptibility at regional scale by addressing the long-standing limitation of static methodologies that fail to account for climate variability. By developing a novel machine learning-based framework capable of evaluating both current and future susceptibility conditions, the study establishes a robust and transferable approach for incorporating climate change into landslide hazard assessment.

The implications of this work extend well beyond methodological innovation. The proposed framework enables stakeholders and decision-makers to identify landslide-prone areas with greater accuracy compared to conventional methodologies and temporal resolution, supporting more informed planning and risk mitigation strategies. In particular, the ability to generate monthly susceptibility maps allows practitioners to move from static representations toward dynamic assessments, reflecting the evolving nature of climatic forcing and its influence on slope stability.

From a practical perspective, the application of the methodology to the Aosta Valley demonstrates both its feasibility and effectiveness. The results indicate that the proposed framework can be successfully implemented to generate more accurate and dynamic landslide susceptibility maps compared to conventional static approaches. This improvement enhances its value for practical applications, particularly in supporting land-use planning and infrastructure management. Moreover, the integration of future climate projections increases its relevance by enabling forward-looking assessments, which are essential for long-term resilience planning.

A key contribution of this research lies in its ability to link landslide susceptibility with infrastructure exposure. The overlay analysis conducted on electricity transmission networks illustrates how the methodology can be used to identify critical assets located in high-risk areas, thereby supporting targeted mitigation and maintenance strategies. Moreover, the framework is not limited to a specific infrastructure type; it is inherently adaptable and can be extended to other linear systems such as roads, railways, and pipelines.

Overall, this research shifts the perspective of landslide susceptibility assessment from a static to a dynamic paradigm, emphasizing the necessity of incorporating climate variability and change into hazard evaluation. By combining methodological rigor with practical applicability, the study provides a valuable tool

for improving risk assessment, enhancing infrastructure resilience, and supporting evidence-based decision-making in the context of a changing climate.

7.3 Recommendations for future development

Several additional aspects could be considered in future studies to further improve the predictive performance of the applied algorithms.

First, regarding the monthly dataset, it would be preferable for each month to be trained and tested using only the landslide events that occurred within that specific month. However, due to the limited number of recorded landslides in certain months (e.g., January and February), the same landslide dataset was used across all months in the present study.

Second, incorporating projected land cover changes could significantly affect future landslide susceptibility, especially in months where land cover is an important factor. Although preliminary projections were attempted, they could not be verified and were excluded from the analysis.

Third, once landslide events occurring in 2024 and subsequent years are reported and incorporated into the inventory, the susceptibility map should be re-evaluated to further assess its predictive capability and long-term robustness.

In addition, incorporating permafrost thickness as a conditioning factor may enhance model performance, especially in mountainous regions such as the Aosta Valley. However, such data were not available for the time periods considered in this study.

The proposed approach is inherently data-driven and therefore strongly dependent on the quality and completeness of the input datasets, particularly the landslide inventory used for model training and validation. However, such inventories may not fully capture all landslide events within the considered time frame, especially in remote or inaccessible areas where reporting is limited. This may introduce some degree of bias into the model and influence the reliability of the resulting susceptibility maps. To address this, it is recommended that the landslide inventory be continuously updated as new events become available. In particular, incorporating newly recorded landslides from areas that were previously not identified by the model as belonging to the “high” or “very high” susceptibility classes can contribute to improving model performance and enhancing the robustness of future susceptibility assessments.

Moreover, for a more comprehensive infrastructure risk assessment, additional factors such as transmitted power capacity, load distribution, and number of end-users per tower could be included, but these data were unavailable in this study.

Finally, future developments of the proposed methodology may include its extension to other infrastructure networks, such as railways, road systems, and pipelines, to assess their susceptibility to landslides under changing environmental conditions.

References

Abe, S. (2005). *Support vector machines for pattern classification.* London: Springer London.

Abija, F. A., Nwosu, J., Ifedotun, A. I., & Osadebe, C. C. (2019). Landslide susceptibility assessment of Calabar, Nigeria using geotechnical, remote sensing and multi-criteria decision analysis: Implications for urban planning and development. *SDRP Journal of Earth Sciences & Environmental Studies*.

Ado, M., Kane, N., & Amitab, K. (2026). A stacked ensemble machine learning technique for landslide susceptibility mapping in Meghalaya, India. *Georisk: Assessment and Management of Risk for Engineered Systems and Geohazards*, 1–26. https://doi.org/10.1080/17499518.2026.2636068

Ahmed, M. F., Rogers, J. D., & Ismail, E. H. (2014). A regional level preliminary landslide susceptibility study of the upper Indus river basin. *European Journal of Remote Sensing*, 47(1), 343–373. https://doi.org/10.5721/EuJRS20144721

Aksoy, H. (2023). Determination of landslide susceptibility with analytic hierarchy process (AHP) and the role of forest ecosystem services on landslide susceptibility. *Environmental Monitoring and Assessment*, 195(12), 1525. https://doi.org/10.1007/s10661-023-12100-0

Aleotti, P., & Chowdhury, R. (1999). Landslide hazard assessment: Summary review and new perspectives. *Bulletin of Engineering Geology and the Environment*, 58(1), 21–44. https://doi.org/10.1007/s100640050066

Alexander, J. S., Buckley, R. M., & Whyte, S. A. (2024). Machine learning to expedite concept monopile design. In *Geotechnical Engineering Challenges to Meet Current and Emerging Needs of Society* (pp. 2760-2763). CRC Press.

Alin, A. (2010). Multicollinearity. *Wiley Interdisciplinary Reviews: Computational Statistics*, 2(3), 370–374. https://doi.org/10.1002/wics.84

Allen, M. R., & Ingram, W. J. (2002). Constraints on future changes in climate and the hydrologic cycle. *Nature*, 419(6903), 224-232. https://doi.org/10.1038/nature01092

Aminpour, M., Alaie, R., Khosravi, S., Kardani, N., Moridpour, S., & Nazem, M. (2023). Slope stability machine learning predictions on spatially variable random fields with and without factor of safety calculations. *Computers and Geotechnics*, 153, 105094. https://doi.org/10.1016/j.compgeo.2022.105094

Anbalagan, R., Kumar, R., Lakshmanan, K., Parida, S., & Neethu, S. (2015). Landslide hazard zonation mapping using frequency ratio and fuzzy logic approach, a case study of Lachung Valley, Sikkim. *Geoenvironmental Disasters*, 2(1), 6. https://doi.org/10.1186/s40677-014-0009-y

Arnell, N., Kram, T., Carter, T., Ebi, K., Edmonds, J., Hallegatte, S., Kriegler, E., Mathur, R., O'Neill, B., Riahi, K., Winkler, H., van Vuuren, D., & Zwickel, T. (2011). *A framework for a new generation of socioeconomic scenarios for climate change impact, adaptation, vulnerability, and mitigation research* (Report, 42 pp.). Potsdam Institute for Climate Impact Research.

Ayalew, L., & Yamagishi, H. (2005). The application of GIS-based logistic regression for landslide susceptibility mapping in the Kakuda-Yahiko Mountains, Central Japan. *Geomorphology*, 65(1-2), 15-31. https://doi.org/10.1016/j.geomorph.2004.06.010

Ayele, S., Raghuvanshi, T. K., & Kala, P. M. (2014). Application of remote sensing and GIS for landslide disaster management: A case from Abay Gorge, Gohatsion–Dejen section, Ethiopia. In M. Singh, R. B. Singh, & M. I. Hassan (Eds.), *Landscape ecology and water management* (pp. 15–32). Springer. https://doi.org/10.1007/978-4-431-54871-3_2

Ayenew, T., & Barbieri, G. (2005). Inventory of landslides and susceptibility mapping in the Dessie area, northern Ethiopia. *Engineering Geology*, 77(1), 1–15. https://doi.org/10.1016/j.enggeo.2004.07.002

Azarafza, M., Azarafza, M., Akgün, H., Atkinson, P. M., & Derakhshani, R. (2021). Deep learning-based landslide susceptibility mapping. *Scientific reports*, 11(1), 24112. https://doi.org/10.1038/s41598-021-03585-1

Bachri, S., & Shresta, R. P. (2010). Landslide hazard assessment using analytic hierarchy processing (AHP) and geographic information system in Kaligesing mountain area of Central Java Province Indonesia. In *Proceedings of the 5th Annual International Workshop & Expo on Sumatra Tsunami Disaster & Recovery* (pp. 107–112).

Barla, G., & Barla, M. (2001, June). Investigation and modelling of the Brenva Glacier rock avalanche on the Mont Blanc Range. In *Proceedings of the ISRM Regional Symposium Eurock* (pp. 35–40).

Barla, G., & Paronuzzi, P. (2013). The 1963 Vajont landslide: 50th anniversary. *Rock Mechanics and Rock Engineering*, 46(5), 1267–1270. https://doi.org/10.1007/s00603-013-0483-7

Barla, G., Antolini, F., & Barla, M. (2013). Slope stabilization in difficult conditions: The case study of a debris slide in NW Italian Alps. *Landslides*, 10(3), 343–355. https://doi.org/10.1007/s10346-013-0396-2

Barla, G., Dutto, F., & Mortara, G. (2000). Brenva glacier rock avalanche of 18 January 1997 on the Mount Blanc range, northwest Italy. *Landslide news*, 13, 2-5.

Barla, M. (2024). Managing climate change impacts on landslides in Alpine areas by using a machine learning-based approach and detection sensors. In *Proceedings of the 4th Macao International Conference on Smart City Technologies* (pp. 88–89), Macao, August 22–24, 2024.

Bayaraa, M., Rossi, C., Kalaitzis, F., & Sheil, B. (2023). Entity embeddings in remote sensing: application to deformation monitoring for infrastructure. *Remote Sensing*, 15(20), 4910. https://doi.org/10.3390/rs15204910

Bednarik, M., Magulová, B., Matys, M., & Marschalko, M. (2010). Landslide susceptibility assessment of the Kraľovany-Liptovský Mikuláš railway case study. *Physics and Chemistry of the Earth*, 35(3–5), 162–171. https://doi.org/10.1016/j.pce.2009.12.002

Bednarik, M., Yilmaz, I., & Kralovičová, L. (2024). Deterministic approach to assess landslide susceptibility and landslide activity in the Central-Western Region of Slovakia. *Bulletin of Engineering Geology and the Environment*, 83, 327. https://doi.org/10.1007/s10064-024-03795-7

Behera, I., Jain, N., Martha, T. R., & Bose, M. (2026). Optimising sampling strategies for AI-based landslide susceptibility mapping: A case study of Idukki, Kerala. *Natural Hazards*, 122(1), 18. https://doi.org/10.1007/s11069-025-07842-8

Behnia, P., & Blais-Stevens, A. (2018). Landslide susceptibility modelling using the quantitative random forest method along the northern portion of the Yukon Alaska Highway Corridor, Canada. *Natural hazards*, 90(3), 1407-1426. https://doi.org/10.1007/s11069-017-3104-z

Bera, A., Mukhopadhyay, B. P., & Das, D. (2019). Landslide hazard zonation mapping using multi-criteria analysis with the help of GIS techniques: A case study from Eastern Himalayas, Namchi, South Sikkim. *Natural Hazards*, 96(2), 935–959. https://doi.org/10.1007/s11069-019-03580-w

Bezak, N., & Mikoš, M. (2021). Changes in the rainfall event characteristics above the empirical global rainfall thresholds for landslide initiation at the pan-European level. *Landslides*, 18(5), 1859-1873. https://doi.org/10.1007/s10346-020-01579-0

Biswas, N., Islam, K. S., Efty, E. A., Das, S., Pathan, A. M., & Ferdaus, M. R. (2026). Ensemble deep learning framework for landslide susceptibility mapping and road vulnerability index development in the Chittagong Hill Tracts,

Bangladesh. Geomatics, *Natural Hazards and Risk*, 17(1), 2634207. https://doi.org/10.1080/19475705.2026.2634207

Boer, G. J. (1993). Climate change and the regulation of the surface moisture and energy budgets. *Climate Dynamics*, 8(5), 225-239. https://doi.org/10.1007/BF00198617

Bolan, S., Sharma, S., Mukherjee, S., Isaza, D. F. G., Rodgers, E. M., Zhou, P., Hou, D., Scordo, F., Chandra, S., Siddique, K. H. M., & Bolan, N. (2025). Wildfires under changing climate, and their environmental and health impacts. *Journal of Soils and Sediments*, 25(11), 3173–3197. https://doi.org/10.1007/s11368-025-04020-y

Bonham-Carter, G. F. (1994). *Geographic information systems for geoscientists: Modelling with GIS* (Vol. 13). Pergamon Press.

Bornaetxea, T., Rossi, M., Marchesini, I., & Alvioli, M. (2018). Effective surveyed area and its role in statistical landslide susceptibility assessments. *Natural Hazards and Earth System Sciences Discussions*, 2018, 1–22. https://doi.org/10.5194/nhess-18-2455-2018

Bousfield, C. G., Lindenmayer, D. B., & Edwards, D. P. (2023). Substantial and increasing global losses of timber-producing forest due to wildfires. *Nature Geoscience*, 16(12), 1145–1150. https://doi.org/10.1038/s41561-023-01323-y

Breiman, L. (1996). Bagging predictors. *Machine learning*, 24(2), 123-140. https://doi.org/10.1023/A:1018054314350

Breiman, L. (2001). Random forests. *Machine learning*, 45(1), 5-32.

Brideau, M.-A., Stead, D., & Couture, R. (2006). Structural and engineering geology of the East Gate Landslide, Purcell Mountains, British Columbia, Canada. *Engineering Geology*, 84(3), 183–206. https://doi.org/10.1016/j.enggeo.2006.01.004

Broeckx, J., Vanmaercke, M., Duchateau, R., & Poesen, J. (2018). A data-based landslide susceptibility map of Africa. *Earth-Science Reviews*, 185, 102-121. https://doi.org/10.1016/j.earscirev.2018.05.002

Buckley, R., Chen, Y. M., Sheil, B., Suryasentana, S., Xu, D., Doherty, J., & Randolph, M. (2023). Bayesian optimization for CPT-based prediction of impact pile drivability. *Journal of Geotechnical and Geoenvironmental Engineering*, 149(11), 04023100. https://doi.org/10.1061/JGGEFK.GTENG-11385

Camelo, J., Mayo, T. L., & Gutmann, E. D. (2020). Projected climate change impacts on hurricane storm surge inundation in the coastal United States. *Frontiers in Built Environment*, 6, 588049. https://doi.org/10.3389/fbuil.2020.588049

Cao, B. T., Obel, M., Freitag, S., Mark, P., & Meschke, G. (2020). Artificial neural network surrogate modelling for real-time predictions and control of building damage during mechanised tunnelling. *Advances in Engineering Software*, 149, 102869. https://doi.org/10.1016/j.advengsoft.2020.102869

Carrara, A., Cardinali, M., Guzzetti, F., & Reichenbach, P. (1995). GIS technology in mapping landslide hazard. In A. Carrara & F. Guzzetti (Eds.), *Geographical information systems in assessing natural hazards* (pp. 135–175). Springer Netherlands. https://doi.org/10.1007/978-94-015-8404-3

Casagli, N., Catani, F., Puglisi, C., Delmonaco, G., Ermini, L., & Margottini, C. (2004). An inventory-based approach to landslide susceptibility assessment and its application to the Virginio River Basin, Italy. *Environmental & Engineering Geoscience*, 10(3), 203–216. https://doi.org/10.2113/10.3.203

Cernuto, E., Salciarini, D., Ubertini, F., & Giardina, G. (2025). Landslide-bridge interaction: A combined approach based on InSAR data and numerical modelling. *International Journal of Disaster Risk Reduction*, 126, 105568. https://doi.org/10.1016/j.ijdrr.2025.105568

Chacón, J., Irigaray, C., Fernández, T., & El Hamdouni, R. (2006). Engineering geology maps: Landslides and geographical information systems. *Bulletin of Engineering Geology and the Environment*, 65(4), 341–411. https://doi.org/10.1007/s10064-006-0064-z

Chang, Z., Du, Z., Zhang, F., Huang, F., Chen, J., Li, W., & Guo, Z. (2020). Landslide susceptibility prediction based on remote sensing images and GIS: Comparisons of supervised and unsupervised machine learning models. *Remote Sensing*, 12(3), 502. https://doi.org/10.3390/rs12030502

Chang, Z., Huang, J., Huang, F., Bhuyan, K., Meena, S. R., & Catani, F. (2023). Uncertainty analysis of non-landslide sample selection in landslide susceptibility prediction using slope unit-based machine learning models. *Gondwana Research*, 117, 307–320. https://doi.org/10.1016/j.gr.2023.02.007

Charles, J. A., Gourvenec, S., & Vardy, M. E. (2023). Recovering shear stiffness degradation curves from classification data with a neural network approach. *Acta Geotechnica*, 18(10), 5619-5633. https://doi.org/10.1007/s11440-023-01879-4

Chatterjee, S., & Hadi, A. S. (2015). *Regression analysis by example*. John Wiley & Sons.

Chen, B., Maurer, J., & Gong, W. (2025). Applications of UAV in landslide research: a review: B. Chen et al. *Landslides*, 22(9), 3029-3048. https://doi.org/10.1007/s10346-025-02547-2

Chen, T., & Guestrin, C. (2016). XGBoost: A scalable tree boosting system. *Proceedings of the 22nd ACM SIGKDD International Conference on*

Knowledge Discovery and Data Mining, 785–794. https://doi.org/10.1145/2939672.2939785

Chen, T., He, T., Benesty, M., Khotilovich, V., Tang, Y., Cho, H., Chen, K., Mitchell, R., Cano, I., & Zhou, T. *(2015). XGBoost: Extreme gradient boosting* (R package version 0.4-2). https://CRAN.R-project.org/package=xgboost

Chen, W., Li, W., Hou, E., Zhao, Z., Deng, N., Bai, H., & Wang, D. (2014). Landslide susceptibility mapping based on GIS and information value model for the Chencang District of Baoji, China. *Arabian Journal of Geosciences*, 7(11), 4499–4511. https://doi.org/10.1007/s12517-014-1369-z

Chen, Wei, Huichan Chai, Zhou Zhao, Qiqing Wang, and Haoyuan Hong. Landslide susceptibility mapping based on GIS and support vector machine models for the Qianyang County, China. *Environmental Earth Sciences*,75, no. 6 (2016): 474. https://doi.org/10.1007/s12665-015-5093-0

Chen, Y. (2025). Spatial prediction and mapping of landslide susceptibility using machine learning models. *Natural Hazards*, 121(7), 8367-8385. https://doi.org/10.1007/s11069-025-07132-3

Chen, Z., & Wang, J. (2007). Landslide hazard mapping using logistic regression model in Mackenzie Valley, Canada. *Natural Hazards*, 42(1), 75–89. https://doi.org/10.1007/s11069-006-9061-6

Cherchi, A., Fogli, P. G., Lovato, T., Peano, D., Iovino, D., Gualdi, S., Masina, S., Scoccimarro, E., Materia, S., Bellucci, A., & Navarra, A. (2019). Global mean climate and main patterns of variability in the CMCC-CM2 coupled model. *Journal of Advances in Modeling Earth Systems*, 11(1), 185–209. https://doi.org/10.1029/2018MS001369

Chiang, S.-H., & Chang, K.-T. (2011). The potential impact of climate change on typhoon-triggered landslides in Taiwan, 2010–2099. *Geomorphology*, 133(3), 143–151. https://doi.org/10.1016/j.geomorph.2010.12.028

Chiarle, M., Nigrelli, G., & Provenzale, A. (2015). A system for assessing the past, present and future of glacial resources. In G. Lollino, A. Manconi, J. Clague, W. Shan, & M. Chiarle (Eds.), *Engineering geology for society and territory* (Vol. 1, pp. 69–72). Springer International Publishing. https://doi.org/10.1007/978-3-319-09300-0_13

Chimidi, G., Raghuvanshi, T. K., & Suryabhagavan, K. V. (2017). Landslide hazard evaluation and zonation in and around Gimbi town, western Ethiopia—a GIS-based statistical approach. *Applied Geomatics*, 9(4), 219–236. https://doi.org/10.1007/s12518-017-0195-x

Ching, J., Wang, J. S., Juang, C. H., & Ku, C. S. (2015). Cone penetration test (CPT)-based stratigraphic profiling using the wavelet transform modulus

maxima method. *Canadian Geotechnical Journal*, 52(12), 1993-2007. http://dx.doi.org/10.1139/cgj-2015-0027

Conoscenti, C., Rotigliano, E., Cama, M., Caraballo-Arias, N. A., Lombardo, L., & Agnesi, V. (2016). Exploring the effect of absence selection on landslide susceptibility models: a case study in Sicily, Italy. *Geomorphology*, 261, 222-235. http://dx.doi.org/10.1016/j.geomorph.2016.03.006

Corominas, J., van Westen, C., Frattini, P., Cascini, L., Malet, J.-P., Fotopoulou, S., Catani, F., Van Den Eeckhaut, M., Mavrouli, O., Agliardi, F., Pitilakis, K., Winter, M. G., Pastor, M., Ferlisi, S., Tofani, V., Hervás, J., & Smith, J. T. (2014). Recommendations for the quantitative analysis of landslide risk. *Bulletin of Engineering Geology and the Environment*, 73(2), 209–263. https://doi.org/10.1007/s10064-013-0538-8

Crespo Cuaresma, J. (2017). Income projections for climate change research: A framework based on human capital dynamics. *Global Environmental Change*, 42, 226–236. https://doi.org/10.1016/j.gloenvcha.2015.02.012

Crozier, M. J. (2010). Deciphering the effect of climate change on landslide activity: A review. *Geomorphology*, 124(3), 260–267. https://doi.org/10.1016/j.geomorph.2010.04.009

Cruden, D. M., & Varnes, D. J. (1993). Landslide types and processes. In A. K. Turner & R. L. Schuster (Eds.), *Landslides*: Investigation and mitigation (Transportation Research Board Special Report 247, pp. 36–75). National Academy Press.

Cuomo, S., Di Cola, V. S., Giampaolo, F., Rozza, G., Raissi, M., & Piccialli, F. (2022). Scientific machine learning through physics–informed neural networks: Where we are and what's next. *Journal of Scientific Computing*, 92(3), 88. https://doi.org/10.1007/s10915-022-01939-z

Cutler, A. (2005). Random Forests. In Encyclopedia of Statistics in Behavioral Science (eds B.S. Everitt and D.C. Howell). https://doi.org/10.1002/0470013192.bsa530

Daanen, R. P., Ingeman-Nielsen, T., Marchenko, S. S., Romanovsky, V. E., Foged, N., Stendel, M., Christensen, J. H., & Hornbech Svendsen, K. (2011). Permafrost degradation risk zone assessment using simulation models. *The Cryosphere*, 5(4), 1043–1056. https://doi.org/10.5194/tc-5-1043-2011

Dafalias, Y. F., & Manzari, M. T. (2004). Simple plasticity sand model accounting for fabric change effects. *Journal of Engineering mechanics*, 130(6), 622-634. https://doi.org/10.1061/(ASCE)0733-9399(2004)130:6(622)

Dai, F. C., & Lee, C. F. (2001). Terrain-based mapping of landslide susceptibility using a geographical information system: A case study. *Canadian Geotechnical Journal*, 38(5), 911–923. https://doi.org/10.1139/t01-021

Dai, F. C., Lee, C. F., & Ngai, Y. Y. (2002). Landslide risk assessment and management: An overview. *Engineering Geology*, 64(1), 65–87. https://doi.org/10.1016/S0013-7952(01)00093-X

Davies, M. C. R., Hamza, O., & Harris, C. (2001). The effect of rise in mean annual temperature on the stability of rock slopes containing ice-filled discontinuities. *Permafrost and Periglacial Processes*, 12(1), 137–144. https://doi.org/10.1002/ppp.378

Deline, P., Akçar, N., Ivy-Ochs, S., & Kubik, P. W. (2015). Repeated Holocene rock avalanches onto the Brenva Glacier, Mont Blanc massif, Italy: A chronology. *Quaternary Science Reviews*, 126, 186–200. https://doi.org/10.1016/j.quascirev.2015.09.004

Delmonaco, G., Margottini, C., & Spizzichino, D. (2013). Rock-fall hazard assessment in the Siq of Petra, Jordan. In *Landslide Science and Practice: Volume 6: Risk Assessment, Management and Mitigation* (pp. 441-449). Berlin, Heidelberg: Springer Berlin Heidelberg. https://doi.org/10.1007/978-3-642-31319-6_59

Dietrich, W. E., Reiss, R., Hsu, M.-L., & Montgomery, D. R. (1995). A process-based model for colluvial soil depth and shallow landsliding using digital elevation data. *Hydrological Processes*, 9(3–4), 383–400. https://doi.org/10.1002/hyp.3360090311

Ding, H., Liu, S., Cai, S., & Xia, Y. (2019, September). Big data analysis of structural defects and traffic accidents in existing highway tunnels. In *International Conference on Inforatmion technology in Geo-Engineering* (pp. 189-195). Cham: Springer International Publishing. https://doi.org/10.1007/978-3-030-32029-4_17

Dixon, N., & Brook, E. (2007). Impact of predicted climate change on landslide reactivation: Case study of Mam Tor, UK. *Landslides*, 4(2), 137–147. https://doi.org/10.1007/s10346-006-0071-y

Dohmen, K., Blum, P., Braun, A., & Fernandez-Steeger, T. M. (2025). Landslide-triggered tsunamis – a review. *Natural Hazards*, 121(19), 22341–22373. https://doi.org/10.1007/s11069-025-07551-2

Doostinia, M., & Falabretti, D. (2025). Assessing critical edges in cyber-physical power systems using complex network theory: A real-world case study. *Energies*, 18(18), 4803. https://doi.org/10.3390/en18184803

Doostinia, M., Falabretti, D., Verticale, G., & Bolouki, S. (2025). Critical node identification for cyber–physical power distribution systems based on complex network theory: A real case study. *Energies*, 18(11), 2937. https://doi.org/10.3390/en18112937

Driscoll, D. A., Macdonald, K. J., Gibson, R. K., Doherty, T. S., Nimmo, D. G., Nolan, R. H., Ritchie, E. G., Williamson, G. J., Heard, G. W., Tasker, E. M., Bilney, R., Porch, N., Collett, R. A., Crates, R. A., Hewitt, A. C., Pendall, E., Boer, M. M., Gates, J., Boulton, R. L., McLean, C. M., … Phillips, R. D. (2024). Biodiversity impacts of the 2019–2020 Australian megafires. *Nature*, 635(8040), 898–905. https://doi.org/10.1038/s41586-024-08174-6

Dunn, R. J. H., Alexander, L. V., Donat, M. G., Zhang, X., Bador, M., Herold, N., Lippmann, T., Allan, R., Aguilar, E., Barry, A. A., Brunet, M., Caesar, J., Chagnaud, G., Cheng, V., Cinco, T., Durre, I., de Guzman, R., Htay, T. M., Wan Ibadullah, W. M., … Yussof, M. N. (2020). Development of an updated global land in situ-based data set of temperature and precipitation extremes: HadEX3. *Journal of Geophysical Research: Atmospheres*, 125(16), e2019JD032263. https://doi.org/10.1029/2019JD032263

Eiras, C. G. S., Souza, J. R. G. de, Freitas, R. D. A. de, Barella, C. F., & Pereira, T. M. (2021). Discriminant analysis as an efficient method for landslide susceptibility assessment in cities with the scarcity of predisposition data. *Natural Hazards*, 107(2), 1427–1442. https://doi.org/10.1007/s11069-021-04638-4

El Brahimi, M., Benzougagh, B., Sbihi, A., Kadhim Tayyeh, H., Mageed Hussein, A., Bammou, Y., Kader S, Yahya Faqeih K, Mohamed Khedher, K. (2026). Landslide susceptibility assessment using feature selection-based machine learning models: RF, SVM, and LR applications in Rif, Morocco. *Geoscience* Letters, 13(1), 17. https://doi.org/10.1186/s40562-026-00458-1

Ellis, G. W., Yao, C., & Zhao, R. (1992). Neural network modeling of the mechanical behavior of sand. In *Engineering Mechanics* (pp. 421-424). ASCE.

Erener, A., & Düzgün, H. S. B. (2012). Landslide susceptibility assessment: What are the effects of mapping unit and mapping method? *Environmental Earth Sciences*, 66(3), 859–877. https://doi.org/10.1007/s12665-011-1297-0

Erener, A., Mutlu, A., & Düzgün, H. S. (2016). A comparative study for landslide susceptibility mapping using GIS-based multi-criteria decision analysis (MCDA), logistic regression (LR) and association rule mining (ARM). *Engineering Geology*, 203, 45–55. https://doi.org/10.1016/j.enggeo.2015.09.007

European Environment Agency. (2017). *Climate change adaptation and disaster risk reduction in Europe: Enhancing coherence of the knowledge base, policies and practices*. Publications Office of the European Union. https://doi.org/10.2800/938195

Fall, M., Azzam, R., & Noubactep, C. (2006). A multi-method approach to study the stability of natural slopes and landslide susceptibility mapping. *Engineering Geology*, 82(4), 241–263. https://doi.org/10.1016/j.enggeo.2005.11.007

Fan, X., Scaringi, G., Korup, O., West, A. J., van Westen, C. J., Tanyaş, H., et al. (2019). Earthquake-induced chains of geologic hazards: Patterns, mechanisms, and impacts. *Reviews of Geophysics*, 57(2), 421–503. https://doi.org/10.1029/2018RG000626

Feizizadeh, B., & Blaschke, T. (2012). Comparing GIS-multicriteria decision analysis for landslide susceptibility mapping for the lake basin, Iran. In *Proceedings of the 2012 IEEE International Geoscience and Remote Sensing Symposium (IGARSS)*, 5390–5393. https://doi.org/10.1109/IGARSS.2012.6352388

Feizizadeh, B., Jankowski, P., & Blaschke, T. (2014). A GIS based spatially-explicit sensitivity and uncertainty analysis approach for multi-criteria decision analysis. *Computers & Geosciences*, 64, 81–95. https://doi.org/10.1016/j.cageo.2013.11.009

Feng, Q., Liu, J., & Gong, J. (2015). Urban flood mapping based on unmanned aerial vehicle remote sensing and random forest classifier—A case of Yuyao, China. *Water*, 7(4), 1437-1455. https://doi.org/10.3390/w7041437

Fick, S. E., & Hijmans, R. J. (2017). WorldClim 2: new 1-km spatial resolution climate surfaces for global land areas. *International journal of climatology*, 37(12), 4302-4315. https://doi.org/10.1002/joc.5086

Flaschel, M., Kumar, S., & De Lorenzis, L. (2021). Unsupervised discovery of interpretable hyperelastic constitutive laws. *Computer Methods in Applied Mechanics and Engineering*, 381, 113852. https://doi.org/10.1016/j.cma.2021.113852

Fowler, H. J., Lenderink, G., Prein, A. F., Westra, S., Allan, R. P., Ban, N., Barbero, R., Berg, P., Blenkinsop, S., Do, H. X., Guerreiro, S., Haerter, J. O., Kendon, E. J., Lewis, E., Schaer, C., Sharma, A., Villarini, G., Wasko, C., & Zhang, X. (2021). Anthropogenic intensification of short-duration rainfall extremes. *Nature Reviews Earth & Environment*, 2(2), 107–122. https://doi.org/10.1038/s43017-020-00128-6

Fredlund, D. G., & Rahardjo, H. (1993). *Soil mechanics for unsaturated soils*. John Wiley & Sons.

Friedman, J. H. (2001). Greedy function approximation: A gradient boosting machine. *Annals of Statistics*, 29, 1189–1232.

Garcia, L., Hafezi, M., Lima, L., Millett, C., Thompson, J., Wang, R., Akaraci, S., Goel, R., Reis, R., Nice, K. A., Zapata-Diomedi, B., Hallal, P. C., Moro, E., Amoako, C., & Hunter, R. F. (2025). Future-proofing cities against negative

city mobility and public health impacts of impending natural hazards: A system dynamics modelling study. *The Lancet Planetary Health*, 9(3), e207–e218. https://doi.org/10.1016/S2542-5196(25)00026-9

Gariano, S. L., & Guzzetti, F. (2016). Landslides in a changing climate. *Earth-Science Reviews*, 162, 227–252. https://doi.org/10.1016/j.earscirev.2016.08.011

Gariano, S. L., & Rianna, G. (2025). How will the projected climate change influence rainfall-induced landslides in Europe? A review of modelling approaches. *Landslides*, 22, 3011–3027. https://doi.org/10.1007/s10346-025-02550-7

Ge, Q., Li, C., & Yang, F. (2023). Support vector machine to predict the pile settlement using novel optimization algorithm. *Geotechnical and Geological Engineering*, 41(7), 3861–3875. https://doi.org/10.1007/s10706-023-02487-5

Gensini, V. A., & Brooks, H. E. (2018). Spatial trends in United States tornado frequency. *npj Climate and Atmospheric Science*, 1(1), 38. https://doi.org/10.1038/s41612-018-0048-2

Ghaboussi, J., Garrett Jr, J. H., & Wu, X. (1991). Knowledge-based modeling of material behavior with neural networks. *Journal of engineering mechanics*, 117(1), 132-153. https://doi.org/10.1061/(ASCE)0733-9399(1991)117:1(132)

Ghaboussi, J., Garrett, J. H., & Wu, X. (1990, January). Material modeling with neural networks. In *Proceedings of the international conference on numerical methods in engineering: theory and applications, Swansea*, UK (pp. 701-717).

Girma, F., Raghuvanshi, T. K., Ayenew, T., & Hailemariam, T. (2015). Landslide hazard zonation in Ada Berga District, Central Ethiopia–a GIS based statistical approach. *Journal of Geomorphology*, 9(1), 25–38.

Girolami, M., Febrianto, E., Yin, G., & Cirak, F. (2021). The statistical finite element method (statFEM) for coherent synthesis of observation data and model predictions. Computer Methods in Applied Mechanics and Engineering, 375, 113533. https://doi.org/10.1016/j.cma.2020.113533

Gitirana Jr., G., Santos, M. A., & Fredlund, M. D. (2012). Three-dimensional slope stability model using finite element stress analysis. In *GeoCongress 2008: Proceedings* (pp. 191–198). https://doi.org/10.1061/40971(310)24

Gnyawali, K., Dahal, K., Talchabhadel, R., & Nirandjan, S. (2023). Framework for rainfall-triggered landslide-prone critical infrastructure zonation. Science of the *Total Environment*, 872, 162242. https://doi.org/10.1016/j.scitotenv.2023.162242

Goetz, J. N., Brenning, A., Petschko, H., & Leopold, P. (2015). Evaluating machine learning and statistical prediction techniques for landslide susceptibility modeling. *Computers & Geosciences*, 81, 1–11. https://doi.org/10.1016/j.cageo.2015.04.007

Gonzalez-Ollauri, A., & Mickovski, S. B. (2017). Hydrological effect of vegetation against rainfall-induced landslides. *Journal of Hydrology*, 549, 374-387. https://doi.org/10.1016/j.jhydrol.2017.04.014

Gorsevski, P. V., & Jankowski, P. (2010). An optimized solution of multi-criteria evaluation analysis of landslide susceptibility using fuzzy sets and Kalman filter. *Computers & Geosciences*, 36(8), 1005–1020. https://doi.org/10.1016/j.cageo.2010.03.001

Gorsevski, P. V., Gessler, P. E., & Jankowski, P. (2003). Integrating a fuzzy k-means classification and a Bayesian approach for spatial prediction of landslide hazard. *Journal of Geographical Systems*, 5(3), 223–251. https://doi.org/10.1007/s10109-003-0113-0

Gorsevski, P. V., Gessler, P., & Foltz, R. B. (2000). Spatial prediction of landslide hazard using discriminant analysis and GIS. In *Proceedings of the GIS in the Rockies 2000 Conference and Workshop: Applications for the 21st century*, Denver, CO, United States.

Görüm, T., Tanyas, H., Karabacak, F., Yılmaz, A., Girgin, S., Allstadt, K. E., Süzen, M. L., & Bürgi, P. (2023). Preliminary documentation of coseismic ground failure triggered by the February 6, 2023 Türkiye earthquake sequence. *Engineering Geology*, 327, 107315. https://doi.org/10.1016/j.enggeo.2023.107315

Gruber, S., & Haeberli, W. (2007). Permafrost in steep bedrock slopes and its temperature-related destabilization following climate change. *Journal of Geophysical Research: Earth Surface*, 112(F2), F02S18. https://doi.org/10.1029/2006JF000547

Gu, T., Duan, P., Wang, M., et al. (2024). Effects of non-landslide sampling strategies on machine learning models in landslide susceptibility mapping. *Scientific Reports*, 14, 7201. https://doi.org/10.1038/s41598-024-57964-5

Guardiani, C., Soranzo, E., & Wu, W. (2022). Time-dependent reliability analysis of unsaturated slopes under rapid drawdown with intelligent surrogate models. *Acta Geotechnica*, 17(4), 1071-1096. https://doi.org/10.1007/s11440-021-01364-w

Gutmann, E. D., et al. (2018). Changes in hurricanes from a 13-yr convection-permitting pseudo–global warming simulation. *Journal of Climate*, 31(9), 3643–3657. https://doi.org/10.1175/JCLI-D-17-0391.1

Guzzetti, F., Carrara, A., Cardinali, M., & Reichenbach, P. (1999). Landslide hazard evaluation: A review of current techniques and their application in a multi-scale study, Central Italy. *Geomorphology*, 31(1), 181–216. https://doi.org/10.1016/S0169-555X(99)00078-1

Guzzetti, F., Galli, M., Reichenbach, P., Ardizzone, F., & Cardinali, M. (2006). Landslide hazard assessment in the Collazzone area, Umbria, Central Italy. *Natural Hazards and Earth System Sciences*, 6(1), 115–131. https://doi.org/10.5194/nhess-6-115-2006

Guzzetti, F., Mondini, A. C., Cardinali, M., Fiorucci, F., Santangelo, M., & Chang, K.-T. (2012). Landslide inventory maps: New tools for an old problem. *Earth-Science Reviews*, 112(1), 42–66. https://doi.org/10.1016/j.earscirev.2012.02.001

Guzzetti, F., Reichenbach, P., Cardinali, M., Galli, M., & Ardizzone, F. (2005b). Probabilistic landslide hazard assessment at the basin scale. *Geomorphology*, 72(1–4), 272–299. https://doi.org/10.1016/j.geomorph.2005.06.002

Guzzetti, F., Stark, C. P., & Salvati, P. (2005a). Evaluation of flood and landslide risk to the population of Italy. *Environmental management*, 36(1), 15-36. https://doi.org/10.1007/s00267-003-0257-1

Han, H., Shi, B., & Zhang, L. (2021). Prediction of landslide sharp increase displacement by SVM with considering hysteresis of groundwater change. *Engineering Geology*, 280, 105876. https://doi.org/10.1016/j.enggeo.2020.105876

Haque, U., Blum, P., da Silva, P. F., Andersen, P., Pilz, J., Chalov, S. R., Malet, J.-P., Auflič, M. J., Andres, N., Poyiadji, E., Lamas, P. C., Zhang, W., Peshevski, I., Pétursson, H. G., Kurt, T., Dobrev, N., García-Davalillo, J. C., Halkia, M., Ferri, S., Gaprindashvili, G., Engström, J., & Keellings, D. (2016). Fatal landslides in Europe. *Landslides*, 13(6), 1545–1554. https://doi.org/10.1007/s10346-016-0689-3

Haraguchi, M., Nishino, A., Kodaka, A., Allaire, M., Lall, U., Kuei-Hsien, L., Onda, K., Tsubouchi, K., & Kohtake, N. (2022). Human mobility data and analysis for urban resilience: A systematic review. *Environment and Planning B: Urban Analytics and City Science*, 49(5), 1507–1535. https://doi.org/10.1177/23998083221075634

Harmouzi, H., Nefeslioglu, H. A., Rouai, M., Sezer, E. A., Dekayir, A., & Gokceoglu, C. (2019). Landslide susceptibility mapping of the Mediterranean coastal zone of Morocco between Oued Laou and El Jebha using artificial neural networks (ANN). *Arabian Journal of Geosciences*, 12(22), 696. https://doi.org/10.1007/s12517-019-4892-0

Hashash, Y. M., Jung, S., & Ghaboussi, J. (2004). Numerical implementation of a neural network based material model in finite element analysis. International *Journal for numerical methods in engineering*, 59(7), 989-1005. https://doi.org/10.1002/nme.905

Hayashi, H., Miyanaka, M., Gomi, H., Tatsumi, J., Kawabe, N., & Shinji, M. (2019, September). Prediction of forward tunnel face score of rock mass classification for stability by applying machine learning to drilling data. In *International Conference on Inforatmion technology in Geo-Engineering* (pp. 268-278). Cham: Springer International Publishing. https://doi.org/10.1007/978-3-030-32029-4_23

He, S. H., Shan, H. F., Xia, T. D., et al. (2021). The effect of temperature on the drained shear behavior of calcareous sand. *Acta Geotechnica*, 16, 613–633. https://doi.org/10.1007/s11440-020-01030-7

He, S.-Y., Tang, C., Pan, M., & Zhou, W.-H. (2025). Settlement-based triple factor framework for long-term safety assessment of immersed tunnel. Tunnelling and *Underground Space Technology*, 162, 106597. https://doi.org/10.1016/j.tust.2025.106597

Hearn, G. J. (1995). Landslide and erosion hazard mapping at Ok Tedi copper mine, Papua New Guinea. *Quarterly Journal of Engineering Geology*, 28(1), 47–60. https://doi.org/10.1144/GSL.QJEGH.1995.028.P1.05

Highland, L. M., & Bobrowsky, P. (2008). The landslide handbook: *A guide to understanding landslides* (No. 1325). US Geological Survey.

Hoek, E., & Brown, E. T. (1980). Empirical strength criterion for rock masses. *Journal of the Geotechnical Engineering Division*, 106(9), 1013–1035. https://doi.org/10.1061/AJGEB6.0001029

Hong, H., Ilia, I., Tsangaratos, P., Chen, W., & Xu, C. (2017). A hybrid fuzzy weight of evidence method in landslide susceptibility analysis on the Wuyuan area, China. *Geomorphology*, 290, 1–16. https://doi.org/10.1016/j.geomorph.2017.04.002

Hu, J. Z., Zhang, J., Huang, H. W., & Zheng, J. G. (2021). Value of information analysis of site investigation program for slope design. *Computers and Geotechnics*, 131, 103938. https://doi.org/10.1016/j.compgeo.2020.103938

Huang, Y., & Zhao, L. (2018). Review on landslide susceptibility mapping using support vector machines. *Catena*, 165, 520–529. https://doi.org/10.1016/j.catena.2018.03.003

Hueckel, T., Francois, B., & Laloui, L. (2009). Explaining thermal failure in saturated clays. *Géotechnique*, 59(3), 197–212. https://doi.org/10.1680/geot.2009.59.3.197

Huggel, C. (2009). Recent extreme slope failures in glacial environments: Effects of thermal perturbation. *Quaternary Science Reviews*, 28(11), 1119–1130. https://doi.org/10.1016/j.quascirev.2008.06.007

Hutchinson, J. N. (1995). Keynote paper: Landslide hazard assessment. In Proceedings of the 6th International Symposium on Landslides (pp. 1805–1841). A.A. Balkema.

Ilia, I., Tsangaratos, P. Applying weight of evidence method and sensitivity analysis to produce a landslide susceptibility map. *Landslides,* 13, 379–397 (2016). https://doi.org/10.1007/s10346-015-0576-3

Ingram, W. (2016). Increases all round. *Nature Climate Change*, 6(5), 443–444. https://doi.org/10.1038/nclimate2966

Insana, A., Beroya-Eitner, M. A., Barla, M., Zachert, H., Žlender, B., van Marle, M., Kalsnes, B., Bračko, T., Pereira, C., Prodan, I., Szymkiewicz, F., & Löfroth, H. (2021). Climate change adaptation of geo-structures in Europe: Emerging issues and future steps. *Geosciences*, 11(12), 488. https://doi.org/10.3390/geosciences11120488

Insana, A., Uzielli, M., Bračko, T., Pourfatollah, A., Vitale, P., Žlender, B., Barla, M., Capobianco, V., Jelušič, P., Mahmoudi, E., Nik, L., Ruopp, J.-I., Szymkiewicz, F., Zachert, H., & Löfroth, H. (2025). A framework for climate-adaptive geotechnical analysis and design. *Bulletin of Engineering Geology and the Environment*, 84(12), 590. https://doi.org/10.1007/s10064-025-04628-x

Intarawichian, N., & Dasananda, S. (2010). Analytical hierarchy process for landslide susceptibility mapping in lower Mae Chem watershed, northern Thailand. *Suranaree Journal of Science and Technology*, 17(3), 277–292.

Intergovernmental Panel on Climate Change (IPCC). (2007). *Climate change 2007: The physical science basis. Summary for policymakers. Contribution of Working Group I to the Fourth Assessment Report of the Intergovernmental Panel on Climate Change*. Cambridge University Press.

Intergovernmental Panel on Climate Change (IPCC). (2012). *Managing the risks of extreme events and disasters to advance climate change adaptation: A special report of Working Groups I and II of the Intergovernmental Panel on Climate Change.* Cambridge University Press.

Intergovernmental Panel on Climate Change (IPCC). (2014). Summary for policymakers. In C. B. Field, V. R. Barros, D. J. Dokken, K. J. Mach, M. D. Mastrandrea, T. E. Bilir, M. Chatterjee, K. L. Ebi, Y. O. Estrada, R. C. Genova, B. Girma, E. S. Kissel, A. N. Levy, S. MacCracken, P. R. Mastrandrea, & L. L. White (Eds.), *Climate change 2014: Impacts, adaptation, and vulnerability. Part A: Global and sectoral aspects. Contribution of Working Group II to the*

Fifth Assessment Report of the Intergovernmental Panel on Climate Change (pp. 1–32). Cambridge University Press.

Intergovernmental Panel on Climate Change (IPCC). (2022). *Climate change 2022: Impacts, adaptation and vulnerability: Contribution of Working Group II to the Sixth Assessment Report*. Cambridge University Press. https://doi.org/10.1017/9781009325844

Jaedicke, C., Van Den Eeckhaut, M., Nadim, F., Hervás, J., Kalsnes, B., Vangelsten, B. V., Smith, J. T., Tofani, V., Ciurean, R., Winter, M. G., Sverdrup-Thygeson, K., Syre, E., & Smebye, H. (2014). Identification of landslide hazard and risk 'hotspots' in Europe. *Bulletin of Engineering Geology and the Environment*, 73(2), 325–339. https://doi.org/10.1007/s10064-013-0541-0

Jain, P., Barber, Q. E., Taylor, S. W., Flannigan, M. D., & Parisien, M.-A. (2024). Drivers and impacts of the record-breaking 2023 wildfire season in Canada. *Nature Communications*, 15, 6764. https://doi.org/10.1038/s41467-024-51154-7

Jakob, M., & Lambert, S. (2009). Climate change effects on landslides along the southwest coast of British Columbia. *Geomorphology*, 107(3), 275–284. https://doi.org/10.1016/j.geomorph.2008.12.009

Janizadeh, S., Bateni, S. M., Jun, C., Pal, S. C., Band, S. S., Chowdhuri, I., ... & Mosavi, A. (2023). Potential impacts of future climate on the spatio-temporal variability of landslide susceptibility in Iran using machine learning algorithms and CMIP6 climate-change scenarios. *Gondwana Research*, 124, 1-17. https://doi.org/10.1016/j.gr.2023.05.003

Janizadeh, S., Kim, D., Jun, C., Bateni, S. M., Pandey, M., & Mishra, V. N. (2024). Impact of climate change on future flood susceptibility projections under shared socioeconomic pathway scenarios in South Asia using artificial intelligence algorithms. *Journal of Environmental Management*, 366, 121764. https://doi.org/10.1016/j.jenvman.2024.121764

Javadi, A. A., & Rezania, M. (2009). Applications of artificial intelligence and data mining techniques in soil modeling. *Geomechanics and Engineering*, 1(1), 53-74. https://doi.org/10.12989/gae.2009.1.1.053

Ji, J., Tong, B., Cui, H.-Z., Tang, X.-T., Hürlimann, M., & Du, S. (2025). A QGIS framework for physically-based probabilistic modelling of landslide susceptibility: QGIS-FORM. *Environmental Modelling & Software*, 183, 106258. https://doi.org/10.1016/j.envsoft.2024.106258

Jiang, L., & O'Neill, B. C. (2017). Global urbanization projections for the Shared Socioeconomic Pathways. *Global Environmental Change*, 42, 193–199. https://doi.org/10.1016/j.gloenvcha.2015.03.008

Jiang, S., Li, J., Zhang, S., Gu, Q., Lu, C., & Liu, H. (2022). Landslide risk prediction by using GBRT algorithm: Application of artificial intelligence in disaster prevention of energy mining. *Process Safety and Environmental Protection*, 166, 384–392. https://doi.org/10.1016/j.psep.2022.08.043

K, B., & Kumaraswamy, K. (2013). Application of geospatial technology and information value technique in landslide hazard zonation mapping: A case study of Giri Valley, Himachal Pradesh. *Disaster Advances*, 6(1), 38–47.

Kannangara, K. K. P. M., Zhou, W., Ding, Z., & Hong, Z. (2022). Investigation of feature contribution to shield tunneling-induced settlement using Shapley additive explanations method. *Journal of Rock Mechanics and Geotechnical Engineering*, 14(4), 1052–1063. https://doi.org/10.1016/j.jrmge.2022.01.002

Kanungo, D. P., Arora, M. K., Sarkar, S., & Gupta, R. P. (2006). A comparative study of conventional, ANN black box, fuzzy and combined neural and fuzzy weighting procedures for landslide susceptibility zonation in Darjeeling Himalayas. *Engineering Geology*, 85(3), 347–366. https://doi.org/10.1016/j.enggeo.2006.03.004

Kanungo, D. P., Arora, M. K., Sarkar, S., & Gupta, R. P. (2009). Landslide susceptibility zonation (LSZ) mapping: A review. *Journal of South Asia Disaster Studies*, 2, 81–105.

Karaman, K., Ercikdi, B., & Kesimal, A. (2013). The assessment of slope stability and rock excavatability in a limestone quarry. *Earth Sciences Research Journal*, 17(2), 169–181.

Kasmalkar, I. G., Serafin, K. A., & Dawson, T. E. (2020). When floods hit the road: Resilience to flood-related traffic disruption in the San Francisco Bay Area and beyond. *Science Advances*, 6(32), eaba2423. https://doi.org/10.1126/sciadv.aba2423

KC, S., & Lutz, W. (2017). The human core of the shared socioeconomic pathways: Population scenarios by age, sex and level of education for all countries to 2100. *Global Environmental Change*, 42, 181–192. https://doi.org/10.1016/j.gloenvcha.2014.06.004

Kennedy, M. C., & O'Hagan, A. (2001). Bayesian calibration of computer models. *Journal of the Royal Statistical Society: Series B (Statistical Methodology)*, 63(3), 425–464. https://doi.org/10.1111/1467-9868.00294

Khabiri, S., Crawford, M. M., Koch, H. J., Haneberg, W. C., & Zhu, Y. (2023). An assessment of negative samples and model structures in landslide susceptibility characterization based on Bayesian network models. *Remote Sensing*, 15(12), 3200. https://doi.org/10.3390/rs15123200

Khan, S., Siddique, T., Haris, P. M., Gupta, K., Ahamad, A., & Mondal, M. E. A. (2026). Comparative landslide susceptibility mapping along national highway

109 using analytical hierarchy process and frequency ratio method. *Discover Geoscience*, 4(1), 89. https://doi.org/10.1007/s44288-026-00456-y

Kharin, V. V., Flato, G. M., Zhang, X., Gillett, N. P., Zwiers, F., & Anderson, K. J. (2018). Risks from climate extremes change differently from 1.5°C to 2.0°C depending on rarity. *Earth's Future*, 6(5), 704–715. https://doi.org/10.1002/2018EF000813

Kharin, V. V., Zwiers, F. W., Zhang, X., & Wehner, M. (2013). Changes in temperature and precipitation extremes in the CMIP5 ensemble. *Climatic change*, 119(2), 345-357. https://doi.org/10.1007/s10584-013-0705-8

Khatti, J., Samadi, H., & Grover, K. S. (2024). Estimation of settlement of pile group in clay using soft computing techniques. *Geotechnical and Geological Engineering*, 42(3), 1729-1760. https://doi.org/10.1007/s10706-023-02643-x

Khetwal, S., Pei, S., & Gutierrez, M. (2019, September). A data-driven approach for direct assessment and analysis of traffic tunnel resilience. In *International Conference on Inforatmion technology in Geo-Engineering* (pp. 168-177). Cham: Springer International Publishing. https://doi.org/10.1007/978-3-030-32029-4_15

Kim, J. C., Lee, S., Jung, H. S., & Lee, S. (2018). Landslide susceptibility mapping using random forest and boosted tree models in Pyeong-Chang, Korea. *Geocarto international*, 33(9), 1000-1015. https://doi.org/10.1080/10106049.2017.1323964

Kimura, Y., Hirabayashi, Y., Kita, Y., Zhou, X., & Yamazaki, D. (2023). Methodology for constructing a flood-hazard map for a future climate. *Hydrology and Earth System Sciences*, 27(8), 1627–1644. https://doi.org/10.5194/hess-27-1627-2023

Kocaman, S., Cetinkaya, S., Tunar Özcan, N., Karakaş, G., Karakaş, V. E., & Gökçeoğlu, C. (2025). Landslides triggered by the 6 February 2023 Kahramanmaraş earthquakes (Türkiye). *Turkish Journal of Earth Sciences*, 34(1), 47-67. https://doi.org/10.55730/1300-0985.1945

Koks, E. E., Rozenberg, J., Zorn, C., Tariverdi, M., Vousdoukas, M., Fraser, S. A., Hall, J. W., & Hallegatte, S. (2019). A global multi-hazard risk analysis of road and railway infrastructure assets. *Nature Communications*, 10(1), 2677. https://doi.org/10.1038/s41467-019-10442-3

Kong, J., Zhuang, J., Peng, J., Ma, P., Zhan, J., Mu, J., Wang, J., Zhang, D., Zheng, J., Fu, Y., Wang, S., & Du, C. (2023). Failure mechanism and movement process of three loess landslides due to freeze-thaw cycle in the Fangtai village, Yongjing County, Chinese Loess Plateau. *Engineering Geology*, 315, 107030. https://doi.org/10.1016/j.enggeo.2023.107030

König, T., Kux, H. J., & Mendes, R. M. (2019). Shalstab mathematical model and WorldView-2 satellite images to identification of landslide-susceptible areas. *Natural Hazards*, 97(3), 1127-1149. https://doi.org/10.1007/s11069-019-03691-4

Korup, O. (2012). Earth's portfolio of extreme sediment transport events. *Earth-Science Reviews*, 112(3), 115–125. https://doi.org/10.1016/j.earscirev.2012.02.006

Kossin, J. P. (2018). A global slowdown of tropical-cyclone translation speed. *Nature*, 558, 104–107. https://doi.org/10.1038/s41586-018-0158-3

Kotlarski, S., Gobiet, A., Morin, S., Olefs, M., Rajczak, J., & Samacoïts, R. (2023). 21st century alpine climate change. *Climate Dynamics*, 60(1), 65–86. https://doi.org/10.1007/s00382-022-06303-3

Kriegler, E., O'Neill, B. C., Hallegatte, S., Kram, T., Lempert, R. J., Moss, R. H., & Wilbanks, T. (2012). The need for and use of socio-economic scenarios for climate change analysis: a new approach based on shared socio-economic pathways. *Global Environmental Change*, 22(4), 807-822. https://doi.org/10.1016/j.gloenvcha.2012.05.005

La Porta, G., Leonardi, A., Pirulli, M., Cafaro, F., & Castelli, F. (2024). Time-resolved triggering and runout analysis of rainfall-induced shallow landslides. *Acta Geotechnica*, 19(4), 1873–1889. https://doi.org/10.1007/s11440-023-01996-0

Laloui, L. (2001). Thermo-mechanical behaviour of soils. Revue Française de Génie Civil, 5(6), 809–843. https://doi.org/10.1080/12795119.2001.9692328

Lan, H. X., Zhou, C. H., Wang, L. J., Zhang, H. Y., & Li, R. H. (2004). Landslide hazard spatial analysis and prediction using GIS in the Xiaojiang watershed, Yunnan, China. *Engineering Geology*, 76(1–2), 109–128. https://doi.org/10.1016/j.enggeo.2004.06.009

Lari, S., Frattini, P., & Crosta, G. B. (2014). A probabilistic approach for landslide hazard analysis. *Engineering Geology*, 182, 3–14. https://doi.org/10.1016/j.enggeo.2014.07.015

Lawal, A. I., & Kwon, S. (2023). Development of mathematically motivated hybrid soft computing models for improved predictions of ultimate bearing capacity of shallow foundations. *Journal of Rock Mechanics and Geotechnical Engineering*, 15(3), 747–759. https://doi.org/10.1016/j.jrmge.2022.04.005

Lee, C. T. (2015). Review and perspectives on methodology for landslide hazard analysis. In *Proceedings of the 10th Asian Regional Conference of the International Association for Engineering Geology and the Environment* (IAEG).

Lee, M. L., Ng, K. Y., Huang, Y. F., & Li, W. C. (2014). Rainfall-induced landslides in Hulu Kelang area, Malaysia. *Natural hazards*, 70(1), 353-375. https://doi.org/10.1007/s11069-013-0814-8

Lee, S. (2007). Application and verification of fuzzy algebraic operators to landslide susceptibility mapping. *Environmental Geology*, 52(4), 615–623. https://doi.org/10.1007/s00254-006-0491-y

Lee, S., Roh, M., Jo, H. W., Joon, K., & Lee, W. K. (2025). Machine learning-based rainfall-induced landslide susceptibility model and short-term early warning assessment in South Korea. *Landslides*, 22(8), 2809-2827. https://doi.org/10.1007/s10346-025-02513-y

Lee, S., Ryu, J.-H., Won, J.-S., & Park, H.-J. (2004). Determination and application of the weights for landslide susceptibility mapping using an artificial neural network. *Engineering Geology*, 71(3–4), 289–302. https://doi.org/10.1016/S0013-7952(03)00142-X

Li, C., Zwiers, F., Zhang, X., Li, G., Sun, Y., & Wehner, M. (2021). Changes in annual extremes of daily temperature and precipitation in CMIP6 models. *Journal of Climate*, 34(9), 3441–3460. https://doi.org/10.1175/JCLI-D-19-1013.1

Li, J., Cassidy, M. J., Huang, J., Zhang, L., & Kelly, R. (2016). Probabilistic identification of soil stratification. *Géotechnique*, 66(1), 16-26. https://doi.org/10.1680/jgeot.14.P.242

Li, L., Lan, H., Guo, C., Zhang, Y., Li, Q., & Wu, Y. (2017). A modified frequency ratio method for landslide susceptibility assessment. *Landslides*, 14(2), 727–741. https://doi.org/10.1007/s10346-016-0771-x

Li, Y., Chen, G., Wang, B., Zheng, L., Zhang, Y., & Tang, C. (2013). A new approach of combining aerial photography with satellite imagery for landslide detection. *Natural hazards*, 66(2), 649-669. https://doi.org/10.1007/s11069-012-0505-x

Likitlersuang, S., Takahashi, A., & Eab, K. H. (2017). Modeling of root-reinforced soil slope under rainfall condition. *Engineering Journal*, 21(3), 123–132. https://doi.org/10.4186/ej.2017.21.3.123

Lin, M.-L., & Tung, C.-C. (2004). A GIS-based potential analysis of the landslides induced by the Chi-Chi earthquake. *Engineering Geology*, 71(1–2), 63–77. https://doi.org/10.1016/S0013-7952(03)00126-1

Lin, Z., Ling, S., Luo, F., Gao, F., Pu, Y., Li, M., ... & Wu, X. (2026). Comparisons of machine learning models for landslide susceptibility mapping in the Jiuzhaigou earthquake-affected area, China. *Bulletin of Engineering Geology and the Environment*, 85(1), 68. https://doi.org/10.1007/s10064-025-04737-7

Linardatos, P., Papastefanopoulos, V., & Kotsiantis, S. (2021). Explainable AI: A review of machine learning interpretability methods. *Entropy*, 23(1), 18. https://doi.org/10.3390/e23010018

Liu, H., Liu, H., Xiao, Y., & McCartney, J. S. (2018). Effects of temperature on the shear strength of saturated sand. *Soils and Foundations*, 58(6), 1326–1338. https://doi.org/10.1016/j.sandf.2018.07.010

Liu, P., Liu, P., Yang, Y., Wu, J., Tian, G., Zhang, Z., & Chai, L. (2025). Risk analysis and mitigation strategy of power system cascading failure under the background of weather disaster. *Processes*, 13(1), 45. https://doi.org/10.3390/pr13010045

Liu, Q., Tang, A., Huang, D., Huang, Z., Zhang, B., & Xu, X. (2022). Total probabilistic measure for the potential risk of regional roads exposed to landslides. Reliability *Engineering & System Safety*, 228, 108822. https://doi.org/10.1016/j.ress.2022.108822

Liu, Y., & Hou, S. (2019, September). Rockburst prediction based on particle swarm optimization and machine learning algorithm. In *International Conference on Inforatmion technology in Geo-Engineering* (pp. 292-303). Cham: Springer International Publishing. https://doi.org/10.1007/978-3-030-32029-4_25

Liu, Y.-C., & Chen, C.-S. (2007). A new approach for application of rock mass classification on rock slope stability assessment. *Engineering Geology*, 89(1–2), 129–143. https://doi.org/10.1016/j.enggeo.2006.09.017

Longoni, L., Scaioli, A., Panzeri, L., Arosio, D., Corti, M., Hojat, A., & Papini, M. (2025). A new landslide investigation and simulation archive through downscaled landslide experiments. *Scientific Data*, 12(1), 1668. https://doi.org/10.1038/s41597-025-05948-z

Lundberg, S. M., & Lee, S.-I. (2017). A unified approach to interpreting model predictions. In U. von Luxburg, I. Guyon, S. Bengio, H. Wallach, & R. Fergus (Eds.), *Proceedings of the 31st International Conference on Neural Information Processing Systems* (NeurIPS) (pp. 4768–4777). Curran Associates.

Luo, H., Zhou, G. G. D., Lu, X., Cui, K. F. E., Zhao, Y., Xie, Y., Zhong, W., Zhou, J., & Pasuto, A. (2025). Experimental investigation on the formation and failure of landslide dams considering the landslide mobility and river flow. *Engineering Geology*, 346, 107873. https://doi.org/10.1016/j.enggeo.2024.107873

MacKay, D. J. C. (2003). *Information theory, inference and learning algorithms*. Cambridge University Press.

Mahmoodzadeh, A., Mohammadi, M., Farid Hama Ali, H., Hashim Ibrahim, H., Nariman Abdulhamid, S., & Nejati, H. R. (2022). Prediction of safety factors

for slope stability: comparison of machine learning techniques. *Natural Hazards*, 111(2), 1771-1799. https://doi.org/10.1007/s11069-021-05115-8

Major, J. J., & Yamakoshi, T. (2005). Decadal-scale change of infiltration characteristics of a tephra-mantled hillslope at Mount St Helens, Washington. *Hydrological Processes: An International Journal*, 19(18), 3621-3630. https://doi.org/10.1002/hyp.5863

Malsawmzuali, Das, S., & Bhowmik, D. (2025). Landslide susceptibility mapping of Aizawl District using a multi factor frequency ratio approach. *Geotechnical and Geological Engineering*, 44(1), 62. https://doi.org/10.1007/s10706-025-03561-w

Mandaglio, M. C., Moraci, N., Rosone, M., & Farulla, C. A. (2016). Experimental study of a naturally weathered stiff clay. *Canadian Geotechnical Journal*, 53(12), 2047–2057. https://doi.org/10.1139/cgj-2016-0175

Manning, R. (1891). On the flow of water in open channels and pipes. *Transactions of the Institution of Civil Engineers of Ireland*, 20, 161–207.

Martinez-Villalobos, C., & Neelin, J. D. (2023). Regionally high risk increase for precipitation extreme events under global warming. *Scientific Reports*, 13, 5579. https://doi.org/10.1038/s41598-023-32372-3

Masi, E. B., Tofani, V., Rossi, G., Cuomo, S., Wu, W., Salciarini, D., Caporali, E., & Catani, F. (2023). Effects of roots cohesion on regional distributed slope stability modelling. *Catena*, 222, 106853. https://doi.org/10.1016/j.catena.2022.106853

Masi, F., & Stefanou, I. (2022). Multiscale modeling of inelastic materials with Thermodynamics-based Artificial Neural Networks (TANN). *Computer Methods in Applied Mechanics and Engineering*, 398, 115190. https://doi.org/10.1016/j.cma.2022.115190

Masi, F., Stefanou, I., Vannucci, P., & Maffi-Berthier, V. (2021). Thermodynamics-based artificial neural networks for constitutive modeling. *Journal of the Mechanics and Physics of Solids*, 147, 104277. https://doi.org/10.1016/j.jmps.2020.104277

Mataveli, G., de Oliveira, G., Silva-Junior, C. H. L., Aragão, L. E. O. C., & Anderson, L. O. (2022). Record-breaking fires in the Brazilian Amazon associated with uncontrolled deforestation. *Nature Ecology & Evolution*, 6(12), 1792–1793. https://doi.org/10.1038/s41559-022-01945-2

Menard, Scott. Applied logistic regression analysis. SAGE publications, 2001.

Meng, B., Xu, C., & Zhu, Y. (2025). *Deep reinforcement learning for power grid multi-stage cascading failure mitigation.* arXiv preprint arXiv:2505.09012. https://doi.org/10.48550/arXiv.2505.09012

Mengistu, F., Suryabhagavan, K. V., Raghuvanshi, T. K., & Lewi, E. (2019). Landslide hazard zonation and slope instability assessment using optical and InSAR data: A case study from Gidole Town and its surrounding areas, southern Ethiopia. *Remote Sensing of Land*, 3(1), 1–14. https://doi.org/10.21523/gcj1.19030101

Meten, M., Bhandary, N. P., & Yatabe, R. (2015). Application of GIS-based fuzzy logic and rock engineering system (RES) approaches for landslide susceptibility mapping in Selelkula area of the lower Jema River gorge, Central Ethiopia. *Environmental Earth Sciences*, 74(4), 3395–3416.

Meyur, R. (2022). *Cascading failures in power grids*. arXiv preprint arXiv:2209.08116. https://doi.org/10.48550/arXiv.2209.08116

Miao, F., Wu, Y., Li, L., Wang, X., & Zhang, H. (2019). Risk assessment of snowmelt-induced landslides based on GIS and an effective snowmelt model. *Natural Hazards*, 97, 1151–1173. https://doi.org/10.1007/s11069-019-03693-2

Milan, L., Napoli, M. L., Barbero, M., & Castelli, M. (2023). A novel approach to assess the influence of rockfall source areas: The case study of Bardonecchia (Italy). *Geosciences*, 13(12), 386. https://doi.org/10.3390/geosciences13120386

Mitchell, J. K. (1969). Temperature effects on the engineering properties and behavior of soils (pp. 9–28). https://onlinepubs.trb.org/Onlinepubs/sr/sr103/103-002.pdf

Mohammady, M., Pourghasemi, H. R., & Pradhan, B. (2012). Landslide susceptibility mapping at Golestan Province, Iran: A comparison between frequency ratio, Dempster–Shafer, and weights-of-evidence models. *Journal of Asian Earth Sciences*, 61, 221–236. https://doi.org/10.1016/j.jseaes.2012.10.005

Mokhtari, M., & Abedian, S. (2019). Spatial prediction of landslide susceptibility in Taleghan basin, Iran. *Stochastic Environmental Research and Risk Assessment*, 33(7), 1297–1325. https://doi.org/10.1007/s00477-019-01696-w

Mokhtari, S., & Mooney, M. A. (2020). Feasibility study of EPB shield automation using deep learning. In *Tunnels and Underground Cities: Engineering and Innovation Meet Archaeology, Architecture and Art* (pp. 2691-2699). CRC Press.

Moore, I. D., Grayson, R. B., & Ladson, A. R. (1991). Digital terrain modelling: A review of hydrological, G*eomorphological*, and biological applications. Hydrological Processes, 5, 3–30.

Morita, T., Nakićenović, N., & Robinson, J. (2000). Overview of mitigation scenarios for global climate stabilization based on new IPCC emission scenarios

(SRES). *Environmental Economics and Policy Studies*, 3(2), 65-88. https://doi.org/10.1007/BF03354031

Moss, R. H., Edmonds, J. A., Hibbard, K. A., Manning, M. R., Rose, S. K., van Vuuren, D. P., Carter, T. R., Emori, S., Kainuma, M., Kram, T., Meehl, G. A., Mitchell, J. F. B., Nakicenovic, N., Riahi, K., Smith, S. J., Stouffer, R. J., Thomson, A. M., Weyant, J. P., & Wilbanks, T. J. (2010). The next generation of scenarios for climate change research and assessment. *Nature*, 463(7282), 747–756. https://doi.org/10.1038/nature08823

Moung-Jin L, Won-Kyong S, Joong-Sun W, Inhye P, Saro L (2014). Spatial and temporal change in landslide hazard by future climate change scenarios using probabilistic-based frequency ratio model. *Geocarto International*, 29(6), 639–662. https://doi.org/10.1080/10106049.2013.826739

Næs, T., Kvaal, K., Isaksson, T., & Miller, C. (1993). Artificial neural networks in multivariate calibration. *Journal of Near Infrared Spectroscopy*, 1(1), 1-11. https://doi.org/10.1255/jnirs.1

Nandi, A., & Shakoor, A. (2010). A GIS-based landslide susceptibility evaluation using bivariate and multivariate statistical analyses. *Engineering Geology*, 110(1–2), 11–20. https://doi.org/10.1016/j.enggeo.2009.10.001

Napoli, M. L., Barbero, M., Minuto, D., Morandi, L., & Ullah, H. (2023). The relict landslide in bimsoils in downtown Genova, Italy: A new modeling approach. *IOP Conference Series: Earth and Environmental Science, 1124*(1), 012124. https://doi.org/10.1088/1755-1315/1124/1/012124

Nhu, V. H., Shirzadi, A., Shahabi, H., Singh, S. K., Al-Ansari, N., Clague, J. J., Ahmad, B. B., et al. (2020). Shallow landslide susceptibility mapping: A comparison between logistic model tree, logistic regression, naïve Bayes tree, artificial neural network, and support vector machine algorithms. *International Journal of Environmental Research and Public Health*, 17(8), 2749

Nikolopoulos, E. I., Borga, M., Marra, F., Crema, S., & Marchi, L. (2015). Debris flows in the eastern Italian Alps: Seasonality and atmospheric circulation patterns. *Natural Hazards and Earth System Sciences*, 15(3), 647–656. https://doi.org/10.5194/nhess-15-647-2015

Ninić, J., Gamra, A., & Ghiassi, B. (2024). Real-time assessment of tunnelling-induced damage to structures within the building information modelling framework. *Underground Space*, 14, 99-117. https://doi.org/10.1016/j.undsp.2023.05.010

Niraj, K. C., Singh, A., & Shukla, D. P. (2023). Effect of the normalized difference vegetation index (NDVI) on GIS-enabled bivariate and multivariate statistical models for landslide susceptibility mapping. *Journal of the Indian Society of*

Remote Sensing, 51(8), 1739–1756. https://doi.org/10.1007/s12524-023-01738-5

Nocentini, N., Rosi, A., Segoni, S., & Fanti, R. (2023). Towards landslide space-time forecasting through machine learning: The influence of rainfall parameters and model setting. *Frontiers in Earth Science*, 11, 1152130. https://doi.org/10.3389/feart.2023.1152130

Nossin, J. J. (1989). On rock slope stability assessment. *Engineering Geology*, 89, 129–143.

O'Neill, B. C., Kriegler, E., Ebi, K. L., Kemp-Benedict, E., Riahi, K., Rothman, D. S., van Ruijven, B. J., van Vuuren, D. P., Birkmann, J., Kok, K., Levy, M., & Solecki, W. (2017). The roads ahead: Narratives for shared socioeconomic pathways describing world futures in the 21st century. *Global Environmental Change*, 42, 169–180. https://doi.org/10.1016/j.gloenvcha.2015.01.004

Öztürk, Ş. (2025). Comparative landslide susceptibility mapping using local inventories: A case study from Trabzon, Türkiye. *Natural Hazards*, 121, 14655–14676. https://doi.org/10.1007/s11069-025-07371-4

Pack, R. T., Tarboton, D. G., & Goodwin, C. N. (1998). The SINMAP approach to terrain stability mapping. In *Proceedings of the 8th Congress of the International Association for Engineering Geology and the Environment*.

Pardeshi, S. D., Autade, S. E., & Pardeshi, S. S. (2013). Landslide hazard assessment: Recent trends and techniques. SpringerPlus, 2, 523. https://doi.org/10.1186/2193-1801-2-523

Parizia, F., Roberti, G., Clague, J. J., Alberto, W., Giardino, M., Ward, B., & Perotti, L. (2024). Landslide deposit erosion and reworking documented by geomatic surveys at Mount Meager, BC, Canada. *Remote Sensing*, 16(9), 1599. https://doi.org/10.3390/rs16091599

Pasqua, A., Leonardi, A., & Pirulli, M. (2025). A multiscale framework for simulating landslide runout and impact with barriers. *Canadian Geotechnical Journal*, 62, 1–19. https://doi.org/10.1139/cgj-2025-0034

Pawluszek, K., & Borkowski, A. (2017). Impact of DEM-derived factors and analytical hierarchy process on landslide susceptibility mapping in the region of Rożnów Lake, Poland. Natural Hazards, 86(2), 919–952. https://doi.org/10.1007/s11069-016-2725-y

Pedone, G., Tsiampousi, A., Cotecchia, F., & Zdravkovic, L. (2016). Effects of soil-vegetation-atmosphere interaction on the stability of a clay slope: A case study. In 3rd European Conference on Unsaturated Soils (E-UNSAT) (Vol. 9, pp. 1–4). *E3S Web of Conferences*. https://doi.org/10.1051/e3sconf/20160915002

Penumadu, D., & Zhao, R. (1999). Triaxial compression behavior of sand and gravel using artificial neural networks (ANN). *Computers and Geotechnics*, 24(3), 207-230. https://doi.org/10.1016/S0266-352X(99)00002-6

Peterson, B. J., McClelland, J., Curry, R., Holmes, R. M., Walsh, J. E., & Aagaard, K. (2006). Trajectory shifts in the Arctic and Subarctic freshwater cycle. *Science*, 313(5790), 1061–1066. https://doi.org/10.1126/science.1122593

Petley, D. (2012). Global patterns of loss of life from landslides. *Geology*, 40(10), 927–930. https://doi.org/10.1130/G33217.1

Pham, B. T., Bui, D. T., & Prakash, I. (2018). Landslide susceptibility modelling using different advanced decision trees methods. Civil Engineering and *Environmental Systems*, 35(1–4), 139–157. https://doi.org/10.1080/10286608.2019.1568418

Piacentini, D., Troiani, F., Soldati, M., Notarnicola, C., Savelli, D., Schneiderbauer, S., & Strada, C. (2012). Statistical analysis for assessing shallow-landslide susceptibility in South Tyrol (south-eastern Alps, Italy). *Geomorphology*, 151–152, 196–206. https://doi.org/10.1016/j.geomorph.2012.02.003

Pierson, T. C., Major, J. J., Amigo, Á., et al. (2013). Acute sedimentation response to rainfall following the explosive phase of the 2008–2009 eruption of Chaitén volcano, Chile. *Bulletin of Volcanology*, 75, 723. https://doi.org/10.1007/s00445-013-0723-4

Potter, S., Solvik, K., Erb, A., Stenzel, J. E., Turetsky, M. R., & Mack, M. C. (2020). Climate change decreases the cooling effect from postfire albedo in boreal North America. *Global Change Biology*, 26(3), 1592–1607. https://doi.org/10.1111/gcb.14888

Pourfatollah, A., Insana, A., De Biagi, V., & Barla, M. (2025). Assessing the impacts of climate change on landslide susceptibility in Northwestern Alps. In *Proceedings of the 9th International Symposium for Geotechnical Safety and Risk (ISGSR 2025),* Oslo, Norway, August 25–28, 2025. DOI: 10.3850/GRF-25280825_isgsr-104-P173-cd

Pourfatollah, A., Insana, A., De Biagi, V., & Barla, M. (2025). Landslide susceptibility maps in alpine areas subjected to climate change by using a machine learning-based approach. In *Proceedings of the Incontro Annuale dei Ricercatori di Geotecnica* (IARG) (pp. 85–90), Florence, Italy.

Previtali, M., Ciantia, M. O., Spadea, S., Castellanza, R., & Crosta, G. (2022, July). Assessing Rockfall barrier performance through block propagation codes and meta-models. In *International Conference of the International Association for Computer Methods and Advances in Geomechanics* (pp. 291-298). Cham: Springer International Publishing. https://doi.org/10.1007/978-3-031-12851-6_35

Promper, C., Puissant, A., Malet, J. P., & Glade, T. (2014). Analysis of land cover changes in the past and the future as contribution to landslide risk scenarios. *Applied Geography*, 53, 11-19. https://doi.org/10.1016/j.apgeog.2014.05.020

Qi, J., Ma, W., & Song, C. (2008). Influence of freeze–thaw on engineering properties of a silty soil. *Cold Regions Science and Technology*, 53(3), 397–404. https://doi.org/10.1016/j.coldregions.2007.05.010

Raghuvanshi, T. K. (2019). Governing factors influence on rock slope stability – Statistical analysis for plane mode of failure. *Journal of King Saud University – Science*, 31(4), 1254–1263. https://doi.org/10.1016/j.jksus.2019.01.002

Raghuvanshi, T. K., Ibrahim, J., & Ayalew, D. (2014a). Slope stability susceptibility evaluation parameter (SSEP) rating scheme–an approach for landslide hazard zonation. *Journal of African Earth Sciences*, 99, 595-612. https://doi.org/10.1016/j.jafrearsci.2014.05.004

Raghuvanshi, T. K., Kala, P. M., & Singh, M. (2014b). Landslide disaster management and reduction: An approach through remote sensing and GIS. In M. Singh, R. B. Singh, & M. I. Hassan (Eds.), *Landscape Ecology and Water Management* (pp. 33–40). Springer Japan. https://doi.org/10.1007/978-4-431-54871-3_3

Raghuvanshi, T. K., Negassa, L., & Kala, P. M. (2015). GIS based grid overlay method versus modeling approach – A comparative study for landslide hazard zonation (LHZ) in Meta Robi District of West Showa Zone in Ethiopia. *The Egyptian Journal of Remote Sensing and Space Sciences*, 18(2), 235–250. https://doi.org/10.1016/j.ejrs.2015.08.001

Rana, H., Mushtaq, T., & Anburaj, R. (2025). Impact of geofactors on landslide susceptibility using weighted overlay method: An integrated GIS and field-based analysis on NH-07, Chamoli, Uttarakhand. *Geosystems and Geoenvironment*, 4(4), 100420. https://doi.org/10.1016/j.geogeo.2025.100420

Ratto, S., Bonetto, F., & Comoglio, C. (2003). The October 2000 flooding in Valle d'Aosta (Italy): Event description and land planning measures for the risk mitigation. *International Journal of River Basin Management*, 1(2), 105–116. https://doi.org/10.1080/15715124.2003.9635197

Raymond, C., Horton, R. M., Zscheischler, J., Martius, O., AghaKouchak, A., Balch, J., Bowen, S. G., Camargo, S. J., Hess, J., Kornhuber, K., Oppenheimer, M., Ruane, A. C., Wahl, T., & White, K. (2020). Understanding and managing connected extreme events. *Nature Climate Change*, 10(7), 611–621. https://doi.org/10.1038/s41558-020-0790-4

Razifard, M., Shoaei, G., & Zare, M. (2019). Application of fuzzy logic in the preparation of hazard maps of landslides triggered by the twin Ahar-Varzeghan

earthquakes (2012). *Bulletin of Engineering Geology and the Environment*, 78(1), 223–245. https://doi.org/10.1007/s10064-018-1235-4

Regmi, N. R., Giardino, J. R., & Vitek, J. D. (2010). Modeling susceptibility to landslides using the weight of evidence approach: Western Colorado, USA. *Geomorphology*, 115(1–2), 172–187. https://doi.org/10.1016/j.geomorph.2009.10.002

Reichenbach, P., Rossi, M., Malamud, B. D., Mihir, M., & Guzzetti, F. (2018). A review of statistically-based landslide susceptibility models. *Earth-Science Reviews*, 180, 60–91. https://doi.org/10.1016/j.earscirev.2018.03.001

Ren, T., Gao, L., & Gong, W. (2024). An ensemble of dynamic rainfall index and machine learning method for spatiotemporal landslide susceptibility modeling. *Landslides*, 21(2), 257-273. https://doi.org/10.1007/s10346-023-02152-1

Riahi, K., van Vuuren, D. P., Kriegler, E., Edmonds, J., O'Neill, B. C., Fujimori, S., Bauer, N., Calvin, K., Dellink, R., Fricko, O., Lutz, W., Popp, A., Crespo Cuaresma, J., KC, S., Leimbach, M., Jiang, L., Kram, T., Rao, S., Emmerling, J., … Tavoni, M. (2017). The shared socioeconomic pathways and their energy, land use, and greenhouse gas emissions implications: An overview. Global *Environmental Change*, 42, 153–168. https://doi.org/10.1016/j.gloenvcha.2016.05.009

Rianna, G., Zollo, A., Tommasi, P., Paciucci, M., Comegna, L., & Mercogliano, P. (2014). Evaluation of the effects of climate changes on landslide activity of Orvieto clayey slope. *Procedia Earth and Planetary Science*, 9, 54–63. https://doi.org/10.1016/j.proeps.2014.06.017

Roderick, T. P., Wasko, C., & Sharma, A. (2019). Atmospheric moisture measurements explain increases in tropical rainfall extremes. *Geophysical Research Letters*, 46(3), 1375–1382. https://doi.org/10.1029/2018GL080833

Rokach, L. (2010). Ensemble-based classifiers. *Artificial intelligence review*, 33(1), 1-39.

Rong, G., Alu, S., Li, K., Su, Y., Zhang, J., Zhang, Y., & Li, T. (2020). Rainfall induced landslide susceptibility mapping based on Bayesian optimized random forest and gradient boosting decision tree models—A case study of Shuicheng County, China. *Water*, 12(11), 3066. https://doi.org/10.3390/w12113066

Rossi, M., Guzzetti, F., Salvati, P., Donnini, M., Napolitano, E., & Bianchi, C. (2019). A predictive model of societal landslide risk in Italy. *Earth-Science Reviews*, 196, 102849. https://doi.org/10.1016/j.earscirev.2019.04.021

Ruff, M., & Czurda, K. (2008). Landslide susceptibility analysis with a heuristic approach in the Eastern Alps (Vorarlberg, Austria). *Geomorphology*, 94(3), 314–324. https://doi.org/10.1016/j.geomorph.2006.10.032

Russell, S. J., & Norvig, P. (2010). Artificial intelligence: A modern approach. Pearson.

Saaty, T. L. (2008). Decision making with the analytical hierarchy process. *International Journal of Services Sciences*, 1(1), 83–98. https://doi.org/10.1504/IJSSci.2008.01759

Saaty, T. L., & Vargas, L. G. (2006). *Decision making with the analytic network process: Economic, political, social and technological applications with benefits, opportunities, costs and risks*. Springer.

Saez, J. L., Corona, C., Stoffel, M., & Berger, F. (2013). Climate change increases frequency of shallow spring landslides in the French Alps. *Geology*, 41(5), 619-622. https://doi.org/10.1130/G34098.1

Safaei, M., Omar, H., Huat, B. K., Yousof, Z. B. M., & Ghiasi, V. (2011). Deterministic rainfall induced landslide approaches, advantage and limitation. *Electronic Journal of Geotechnical Engineering*, 16, 1619–1650.

Saffer, D. M., Frye, K. M., Marone, C., et al. (2001). Laboratory results indicating complex and potentially unstable frictional behavior of smectite clay. *Geophysical Research Letters*, 28(12), 2297–2300. https://doi.org/10.1029/2001GL012869

Saha, S., & Bera, B. (2026). Preliminary assessment of heavy rainfall-induced landslides and reactivation of old landslides in the Garhwal Himalayas. *Landslides*, 23, 899–908. https://doi.org/10.1007/s10346-025-02691-9

Saha, S., Roy, J., Pradhan, B., & Hembram, T. K. (2021). Hybrid ensemble machine learning approaches for landslide susceptibility mapping using different sampling ratios at East Sikkim Himalayan, *India. Advances in Space Research*, 68(7), 2819-2840. https://doi.org/10.1016/j.asr.2021.05.018

Sahin, E. K. (2022). Comparative analysis of gradient boosting algorithms for landslide susceptibility mapping. *Geocarto International*, 37(9), 2441–2465. https://doi.org/10.1080/10106049.2020.1831623

Sahin, E. K., Colkesen, I., & Kavzoglu, T. (2020). A comparative assessment of canonical correlation forest, random forest, rotation forest and logistic regression methods for landslide susceptibility mapping. *Geocarto International*, 35(4), 341-363. https://doi.org/10.1080/10106049.2018.1516248

Salciarini, D., Volpe, E., Kelley, S. A., Brocca, L., Camici, S., Fanelli, G., & Tamagnini, C. (2016). Modeling the effects induced by the expected climatic trends on landslide activity at large scale. Procedia Engineering, 158, 541–545. https://doi.org/10.1016/j.proeng.2016.08.486

Salvati, P., Petrucci, O., Rossi, M., Bianchi, C., Pasqua, A. A., & Guzzetti, F. (2018). Gender, age and circumstances analysis of flood and landslide fatalities in Italy. *Science of the Total Environment*, 610, 867–879. https://doi.org/10.1016/j.scitotenv.2017.08.061

Sameen, M. I., Pradhan, B., & Lee, S. (2020). Application of convolutional neural networks featuring Bayesian optimization for landslide susceptibility assessment. *Catena*, 186,104249. https://doi.org/10.1016/j.catena.2019.104249

Sasahara, K., & Sakai, N. (2014). Development of shear deformation due to the increase of pore pressure in a sandy model slope during rainfall. *Engineering Geology*, 170, 43–51. https://doi.org/10.1016/j.enggeo.2013.12.005

Sassa, K. (2021). The Kyoto Landslide Commitment 2020: Launched. *Landslides*, 18(1), 5–20. https://doi.org/10.1007/s10346-020-01575-4

Sayedi, S. S., Abbott, B. W., Vannière, B., Leys, B., Colombaroli, D., Romera, G. G., Słowiński, M., Aleman, J. C., Blarquez, O., Feurdean, A., Brown, K., Aakala, T., Alenius, T., Allen, K., Andric, M., Bergeron, Y., Biagioni, S., Bradshaw, R., Bremond, L., … Daniau, A.-L. (2024). Assessing changes in global fire regimes. *Fire Ecology*, 20(1), 18. https://doi.org/10.1186/s42408-023-00237-9

Schicker, R., & Moon, V. (2012). Comparison of bivariate and multivariate statistical approaches in landslide susceptibility mapping at a regional scale. Geomorphology, 161–162, 40–57. https://doi.org/10.1016/j.geomorph.2012.03.036

Shafique, M. (2020). Spatial and temporal evolution of co-seismic landslides after the 2005 Kashmir earthquake. *Geomorphology*, 362, 107228. https://doi.org/10.1016/j.geomorph.2020.107228

Shapley, L. S. (1953). Stochastic games. Proceedings of the National Academy of Sciences, 39(10), 1095–1100. https://doi.org/10.1073/pnas.39.10.1095

Sharma, S., Raghuvanshi, T. K., & Anbalagan, R. (1995). Plane failure analysis of rock slopes. *Geotechnical & Geological Engineering*, 13(2), 105–111. https://doi.org/10.1007/BF00421876

Sheil, B. B., Suryasentana, S. K., Mooney, M. A., Zhu, H., McCabe, B. A., & O'Dwyer, K. G. (2021). Discussion: Machine learning to inform tunnelling operations: recent advances and future trends. *Proceedings of the Institution of Civil Engineers-Smart Infrastructure and Construction*, 173(1), 180-181. https://doi.org/10.1680/jsmic.2020.173.1.180

Sheil, B., Anagnostopoulos, C., Buckley, R., Ciantia, M. O., Febrianto, E., Fu, J., Gao, Z., Geng, X., Gong, B., Hanley, K., He, P., Kolomvatsos, K., de C. F. L. Lopes, B., Ninic, J., Previtali, M., Rezania, M., Ruiz-Lopez, A., Sun, J., Suryasentana, S., Taborda, D., Utili, S., Whyte, S., & Zhang, P. (2026).

Artificial intelligence transformations in geotechnics: Progress, challenges and future enablers. *Computers and Geotechnics*, 189, 107604. https://doi.org/10.1016/j.compgeo.2025.107604

Shen, P., Wei, S., Shi, H., Gao, L., & Zhou, W.-H. (2023). Coastal flood risk and smart resilience evaluation under a changing climate. *Ocean-Land-Atmosphere Research*, 2, 0029. https://doi.org/10.34133/olar.0029

Shi, Y., Lin, Q., & Hong, H. (2026). Enhancing Landslide Susceptibility and Dynamic Exposure Assessment Using Interpretable Machine Learning: A Case Study of the Qinba Mountain Area, China. *Transactions in GIS*, 30(2), e70228. https://doi.org/10.1111/tgis.70228

Shuku, T., Phoon, K. K., & Yoshida, I. (2020). Trend estimation and layer boundary detection in depth-dependent soil data using sparse Bayesian lasso. *Computers and Geotechnics*, 128, 103845. https://doi.org/10.1016/j.compgeo.2020.103845

Simoni, S., Zanotti, F., Bertoldi, G., & Rigon, R. (2008). Modelling the probability of occurrence of shallow landslides and channelized debris flows using GEOtop-FS. *Hydrological Processes*, 22(4), 532–545. https://doi.org/10.1002/hyp.6886

Skempton, A. W., & deLory, F. A. (1957). Stability of natural slopes in London clay. In *Proceedings of the 4th International Conference on Soil Mechanics and Foundation Engineering* (London).

Sobel, A. H., & Emanuel, K. A. (2025). Hurricane risk in a changing climate: The role of uncertainty. *Nature*, 641(8064), 848–851. https://doi.org/10.1038/d41586-025-01552-8

Stead, D., Eberhardt, E., & Coggan, J. S. (2006). Developments in the characterization of complex rock slope deformation and failure using numerical modelling techniques. *Engineering Geology*, 83(1), 217–235. https://doi.org/10.1016/j.enggeo.2005.06.033

Steger, S., Brenning, A., Bell, R., & Glade, T. (2016). The propagation of inventory-based positional errors into statistical landslide susceptibility models. *Natural Hazards and Earth System Sciences*, 16(12), 2729–2745. https://doi.org/10.5194/nhess-16-2729-2016

Stoffel, M., Tiranti, D., & Huggel, C. (2014). Climate change impacts on mass movements — Case studies from the European Alps. *Science of the Total Environment*, 493, 1255–1266. https://doi.org/10.1016/j.scitotenv.2014.02.102

Straub, D., & Schubert, M. (2008). Modeling and managing uncertainties in rock-fall hazards. *Georisk: Assessment and Management of Risk for Engineered Systems and Geohazards*, 2(1), 1–15. https://doi.org/10.1080/17499510701835696

Sun, Y., Hu, T., & Zhang, X. (2018). Substantial increase in heat wave risks in China in a future warmer world. *Earth's Future*, 6(11), 1528–1538. https://doi.org/10.1029/2018EF000963

Suryasentana, S. K., & Sheil, B. B. (2023a). Demystifying the connections between Gaussian process regression and kriging. In *Proceedings of the 9th International SUT OSIG Conference* (pp. 1–8).

Suryasentana, S. K., Lawler, M., Sheil, B. B., & Lehane, B. M. (2023b). Probabilistic soil strata delineation using DPT data and Bayesian changepoint detection. *Journal of Geotechnical and Geoenvironmental Engineering*, 149(4), 06023001. https://doi.org/10.1061/JGGEFK.GTENG-10843

Süzen, M. L., & Doyuran, V. (2004). Data driven bivariate landslide susceptibility assessment using geographical information systems: A method and application to Asarsuyu catchment, Turkey. *Engineering Geology*, 71(3), 303–321. https://doi.org/10.1016/S0013-7952(03)00143-1

Tabari, H., Hosseinzadehtalaei, P., AghaKouchak, A., & Willems, P. (2019). Latitudinal heterogeneity and hotspots of uncertainty in projected extreme precipitation. *Environmental Research Letters*, 14(12), 124032. https://doi.org/10.1088/1748-9326/ab55fd

Taherkhani, A. H., Mei, Q., & Han, F. (2023). Capacity prediction and design optimization for laterally loaded monopiles in sandy soil using hybrid neural network and sequential quadratic programming. *Computers and Geotechnics*, 163, 105745. https://doi.org/10.1016/j.compgeo.2023.105745

Take, W. A., Bolton, M. D., Wong, P. C. P., & Yeung, F. J. (2004). Evaluation of landslide triggering mechanisms in model fill slopes. *Landslides*, 1(3), 173–184. https://doi.org/10.1007/s10346-004-0025-1

Tang, C., Van Westen, C. J., Tanyaş, H., & Jetten, V. G. (2016). Analysing post-earthquake landslide activity using multi-temporal landslide inventories near the epicentral area of the 2008 Wenchuan earthquake. *Natural Hazards and Earth System Sciences*, 16(12), 2641–2655. https://doi.org/10.5194/nhess-16-2641-2016

Tang, H., Yong, R., & Ez Eldin, M. A. M. (2017). Stability analysis of stratified rock slopes with spatially variable strength parameters: The case of Qianjiangping landslide. *Bulletin of Engineering Geology and the Environment*, 76(3), 839–853. https://doi.org/10.1007/s10064-016-0876-4

Tanyaş, H., Kirschbaum, D., Görüm, T., van Westen, C. J., & Lombardo, L. (2021). New insight into post-seismic landslide evolution processes in the tropics. *Frontiers in Earth Science*, 9, 700546. https://doi.org/10.3389/feart.2021.700546

Taylor, K. E., Stouffer, R. J., & Meehl, G. A. (2012). An overview of CMIP5 and the experiment design. *Bulletin of the American meteorological Society*, 93(4), 485-498. https://doi.org/10.1175/BAMS-D-11-00094.1

Tsangaratos, P., & Ilia, I. (2016). Landslide susceptibility mapping using a modified decision tree classifier in the Xanthi Perfection, Greece. *Landslides*, 13(2), 305–320. https://doi.org/10.1007/s10346-015-0565-6

UNEP & GRID-Arendal. (2022). Spreading like wildfire: The rising threat of extraordinary landscape fires – A rapid response assessment. https://wedocs.unep.org/handle/20.500.11822/38372

Uzielli, M., Rianna, G., Ciervo, F., Mercogliano, P., & Eidsvig, U. K. (2018). Temporal evolution of flow-like landslide hazard for a road infrastructure in the municipality of Nocera Inferiore (southern Italy) under the effect of climate change. *Natural Hazards and Earth System Sciences*, 18(11), 3019-3035. https://doi.org/10.5194/nhess-18-3019-2018

van Vuuren, D. P., & Carter, T. R. (2014). Climate and socio-economic scenarios for climate change research and assessment: Reconciling the new with the old. *Climatic Change*, 122(3), 415–429. https://doi.org/10.1007/s10584-013-0974-2

van Vuuren, D. P., Edmonds, J., Kainuma, M., Riahi, K., Thomson, A., Hibbard, K., Hurtt, G. C., Kram, T., Krey, V., Lamarque, J.-F., Masui, T., Meinshausen, M., Nakicenovic, N., Smith, S. J., & Rose, S. K. (2011). The representative concentration pathways: An overview. *Climatic Change*, 109(1), 5–31. https://doi.org/10.1007/s10584-011-0148-z

van Vuuren, D. P., Riahi, K., Moss, R., Edmonds, J., Thomson, A., Nakicenovic, N., Kram, T., Berkhout, F., Swart, R., Janetos, A., Rose, S. K., & Arnell, N. (2012). A proposal for a new scenario framework to support research and assessment in different climate research communities. *Global Environmental Change*, 22(1), 21–35. https://doi.org/10.1016/j.gloenvcha.2011.08.002

van Westen, C. J. (2002). *Use of weights of evidence modeling for landslide susceptibility mapping* (p. 21). International Institute for Geoinformation Science and Earth Observation.

van Westen, C. J., Rengers, N., & Soeters, R. (2003). Use of geomorphological information in indirect landslide susceptibility assessment. *Natural Hazards*, 30(3), 399–419. https://doi.org/10.1023/B:NHAZ.0000007097.42735.9e

van Westen, C. J., Rengers, N., Terlien, M. T. J., & Soeters, R. (1997). Prediction of the occurrence of slope instability phenomena through GIS-based hazard zonation. *Geologische Rundschau*, 86(2), 404–414. https://doi.org/10.1007/s005310050149

Vapnik, Vladimir. *The nature of statistical learning theory*. Springer science & business media, 2013.

Varnes, D. J., & Commission on Landslides and Other Mass Movements. (1981). The principles and practice of landslide hazard zonation. *Bulletin of the International Association of Engineering Geology*, 23, 13–14. https://doi.org/10.1007/BF02594720

Varnes, D. J., & International Association of Engineering Geology (IAEG). (1984). *Landslide hazard zonation: A review of principles and practice* (pp. 1–6). UNESCO.

Verstappen, H. T. (1983). *Applied geomorphology: Geomorphological survey for environmental development* (Vol. 11, p. 437). Elsevier Scientific Publishing Co.

Vichi, M., Manzini, E., Fogli, P. G., Alessandri, A., Patara, L., Scoccimarro, E., Masina, S., & Navarra, A. (2011). Global and regional ocean carbon uptake and climate change: Sensitivity to a substantial mitigation scenario. *Climate Dynamics*, 37(9–10), 1929–1947. https://doi.org/10.1007/s00382-011-1079-0

Vitaletti, A., Cernuto, E., & Salciarini, D. (2026). Coupling finite element modelling and InSAR data for enhanced understanding of landslide behaviour along highway infrastructures. *Landslides*, 23, 231–246. https://doi.org/10.1007/s10346-025-02610-y

Wang, F., Xu, P., Wang, C., Wang, N., & Jiang, N. (2017). Application of a GIS-based slope unit method for landslide susceptibility mapping along the Longzi River, Southeastern Tibetan Plateau, China. *ISPRS International journal of Geo-information*, 6(6), 172. https://doi.org/10.3390/ijgi6060172

Wang, Haojie, Limin Zhang, Hongyu Luo, Jian He, and Raymond Wai Man Cheung. "AI-powered landslide susceptibility assessment in Hong Kong." *Engineering Geology*, 288 (2021): 106103. https://doi.org/10.1016/j.enggeo.2021.106103

Wang, S., Hou, Q., Demisa, M. G., Gao, Z., & Chunyuk, D. (2025). Snowmelt and rainfall-induced slope failure mechanisms and post-failure behavior in Yili Valley, Xinjiang. *Natural Hazards*, 121(18), 21911–21933. https://doi.org/10.1007/s11069-025-07671-9

Wang, X., & Niu, R. (2009). Spatial forecast of landslides in Three Gorges based on spatial data mining. *Sensors*, 9(3), 2035–2061. https://doi.org/10.3390/s90302035

Wang, Y., Hu, Y., & Zhao, T. (2020). Cone penetration test (CPT)-based subsurface soil classification and zonation in two-dimensional vertical cross section using Bayesian compressive sampling. *Canadian Geotechnical Journal*, 57(7), 947–958. https://doi.org/10.1139/cgj-2019-0131

Wang, Y., Huang, K., & Cao, Z. (2013). Probabilistic identification of underground soil stratification using cone penetration tests. *Canadian Geotechnical Journal*, 50(7), 766-776. https://doi.org/10.1139/cgj-2013-0004

Wang, Y., Wang, R., Chen, J., Wang, H., & Cheng, R. (2026). Numerical simulation of deposit-landslide instability induced by water level decrease: a case study of RS deposit in Lancang River. *European Journal of Environmental and Civil Engineering*, 30(1), 1–14. https://doi.org/10.1080/19648189.2024.2417677

Wartenburger, R., Hirschi, M., Donat, M. G., Greve, P., Pitman, A. J., & Seneviratne, S. I. (2017). Changes in regional climate extremes as a function of global mean temperature: An interactive plotting framework. *Geoscientific Model Development*, 10, 3609–3634. https://doi.org/10.5194/gmd-10-3609-2017

Weier, J., & Herring, D. (2000). *Measuring vegetation (NDVI & EVI)*. NASA Earth Observatory.

Westra, S., Alexander, L. V., & Zwiers, F. W. (2013). Global increasing trends in annual maximum daily precipitation. *Journal of climate*, 26(11), 3904-3918. https://doi.org/10.1175/JCLI-D-12-00502.1

Wilson, J. P., & Gallant, J. C. (2000). Digital terrain analysis. In J. C. Gallant & J. P. Wilson (Eds.), *Terrain analysis: Principles and applications*. John Wiley & Sons.

Wischmeier, W. H., & Smith, D. D. (1965). *Predicting rainfall-erosion losses from cropland east of the Rocky Mountains: Guide for selection of practices for soil and water conservation* (No. 282). U.S. Department of Agriculture, Agricultural Research Service.

Wold, S., Sjöström, M., & Eriksson, L. (2001). PLS-regression: A basic tool of chemometrics. *Chemometrics and Intelligent Laboratory Systems*, 58(2), 109–130. https://doi.org/10.1016/S0169-7439(01)00155-1

Woods, M. J., Trapp, R. J., & Mallinson, H. M. (2023). The impact of human-induced climate change on future tornado intensity as revealed through multi-scale modeling. *Geophysical Research Letters*, 50, e2023GL104796. https://doi.org/10.1029/2023GL104796

Wu LZ, Huang RQ, Xu Q, Zhang LM, Li HL (2015) Analysis of physical testing of rainfall-induced soil slope failures. Environ Earth Sci 73(12):8519–31

Wu, Y., Ke, Y., Chen, Z., Liang, S., Zhao, H., & Hong, H. (2020). Application of alternating decision tree with AdaBoost and bagging ensembles for landslide susceptibility mapping. *Catena*, 187, 104396. https://doi.org/10.1016/j.catena.2019.104396

Wubalem, A., & Meten, M. (2020). Landslide susceptibility mapping using information value and logistic regression models in Goncha Siso Eneses area, northwestern Ethiopia. *SN Applied Sciences*, 2(5), 807. https://doi.org/10.1007/s42452-020-2563-0

Xing, X., Wu, C., Li, J., Li, X., Zhang, L., & He, R. (2021). Susceptibility assessment for rainfall-induced landslides using a revised logistic regression method. *Natural Hazards*, 106(1), 97–117. https://doi.org/10.1007/s11069-020-04452-4

Xu, J., Li, Y., Lan, W., & Wang, S. (2019). Shear strength and damage mechanism of saline intact loess after freeze-thaw cycling. *Cold Regions Science and Technology*, 164, 102779. https://doi.org/10.1016/j.coldregions.2019.05.005

Xu, K., Zhao, Z., Chen, W., Ma, J., Liu, F., Zhang, Y., & Ren, Z. (2024). Comparative study on landslide susceptibility mapping based on different ratios of training samples and testing samples by using RF and FR-RF models. *Natural Hazards Research*, 4(1), 62–74. https://doi.org/10.1016/j.nhres.2023.07.004

Xu, X., He, Y., Liu, H., Shi, Q., Yao, X., & Tang, K. (2026). Landslide susceptibility assessment in a reservoir area using integrated models based on time-series InSAR. *Journal of Applied Geophysics*, 246, 106115. https://doi.org/10.1016/j.jappgeo.2026.106115

Xue, Y. D., & Zhang, S. (2019, September). A fast metro tunnel profile measuring method based on close-range photogrammetry. In *International Conference on Inforatmion technology in Geo-Engineering* (pp. 57-69). Cham: Springer International Publishing. https://doi.org/10.1007/978-3-030-32029-4_5

Yalçın, A. (2008). GIS-based landslide susceptibility mapping using analytical hierarchy process and bivariate statistics in Ardeşen (Turkey): Comparisons of results and confirmations. *Catena*, 72(1), 1–12. https://doi.org/10.1016/j.catena.2007.01.003

Yalcin, A., & Bulut, F. (2007). Landslide susceptibility mapping using GIS and digital photogrammetric techniques: A case study from Ardesen (NE-Turkey). *Natural Hazards*, 41(1), 201–226. https://doi.org/10.1007/s11069-006-9030-0

Yang, C., Liu, L. L., Huang, F., Huang, L., & Wang, X. M. (2023). Machine learning-based landslide susceptibility assessment with optimized ratio of landslide to non-landslide samples. *Gondwana Research*, 123, 198-216. https://doi.org/10.1016/j.gr.2022.05.012

Yang, W., Ge, Q., Tao, Z., Xu, D., Wang, Y., & Hao, Z. (2026). Landslide susceptibility on the Qinghai-Tibet Plateau: Key driving factors identified through machine learning. *Journal of Geographical Sciences*, 36(1), 199-218.https://doi.org/10.1007/s11442-026-2444-6

Yatim Mustapa, M., & Tahar, K. (2025). Landslide Susceptibility Mapping Utilizing the Weighted Frequency Ratio Technique: A Case Study of Klang Valley, Malaysia. *International Journal of Geoinformatics*, 21(2), 70–86. https://doi.org/10.52939/ijg.v21i2.3939

Ye, W., & Li, C. (2019). The consequences of changes in the structure of loess as a result of cyclic freezing and thawing. *Bulletin of Engineering Geology and the Environment*, 78(3), 2125–2138. https://doi.org/10.1007/s10064-018-1252-3

Yeon, Y.-K., Han, J.-G., & Ryu, K. H. (2010). Landslide susceptibility mapping in Injae, Korea, using a decision tree. *Engineering Geology*, 116(3–4), 274–283. https://doi.org/10.1016/j.enggeo.2010.09.009

Yilmaz, I. (2010). The effect of the sampling strategies on the landslide susceptibility mapping by conditional probability and artificial neural networks. *Environmental Earth Sciences*, 60, 505–519. https://doi.org/10.1007/s12665-009-0191-5

Yin, K. L., & Yan, T. Z. (1990). Statistical prediction models for slope instability of metamorphosed rocks. *International Journal of Rock Mechanics and Mining Sciences & Geomechanics Abstracts*, 27(1), 43. https://doi.org/10.1016/0148-9062(90)90358-9

Yoshida, I., Tasaki, Y., & Tomizawa, Y. (2022). Optimal placement of sampling locations for identification of a two-dimensional space. *Georisk: Assessment and Management of Risk for Engineered Systems and Geohazards*, 16(1), 98-113. https://doi.org/10.1080/17499518.2021.1971255

Youssef, A. M., Pourghasemi, H. R., Pourtaghi, Z. S., & Al-Katheeri, M. M. (2016). Landslide susceptibility mapping using random forest, boosted regression tree, classification and regression tree, and general linear models and comparison of their performance at Wadi Tayyah Basin, Asir Region, Saudi Arabia. *Landslides*, 13(5), 839-856. https://doi.org/10.1007/s10346-015-0614-1

Yuan, F., & Bauer, M. E. (2007). Comparison of impervious surface area and normalized difference vegetation index as indicators of surface urban heat island effects in Landsat imagery. *Remote Sensing of Environment*, 106(3), 375–386. https://doi.org/10.1016/j.rse.2006.09.003

ZainAlabideen, K., & Helal, M. (2016). Determination of the safe orientation and dip of a rock slope in an open pit mine in Syria using kinematic analysis. Al-*Nahrain University College of Engineering Journal*, 91(1), 33–45.

Zeng, P., Zhang, T., Li, T., Jimenez, R., Zhang, J., & Sun, X. (2022). Binary classification method for efficient and accurate system reliability analyses of layered soil slopes. *Georisk: Assessment and Management of Risk for*

Engineered Systems and Geohazards, 16(3), 435-451. https://doi.org/10.1080/17499518.2020.1861635

Zêzere, J. L., Reis, E., Garcia, R., Oliveira, S., Rodrigues, M. L., Vieira, G., & Ferreira, A. B. (2004). Integration of spatial and temporal data for the definition of different landslide hazard scenarios in the area north of Lisbon (Portugal). *Natural Hazards and Earth System Sciences*, 4(1), 133–146. https://doi.org/10.5194/nhess-4-133-2004

Zhang, J., Ma, X., Zhang, J., Sun, D., Zhou, X., Mi, C., & Wen, H. (2023a). Insights into geospatial heterogeneity of landslide susceptibility based on the SHAP-XGBoost model. *Journal of environmental management*, 332, 117357. https://doi.org/10.1016/j.jenvman.2023.117357

Zhang, J., Wang, Z., Hu, J., Xiao, S., & Shang, W. (2022a). Bayesian machine learning-based method for prediction of slope failure time. *Journal of Rock Mechanics and Geotechnical Engineering*, 14(4), 1188-1199. https://doi.org/10.1016/j.jrmge.2021.09.010

Zhang, K., Li, D., Mu, Y., Li, G., Wu, H., Mao, Y., Li, L., & Zhang, Q. (2023b). Field observations on hydro-thermal regimes of loess cut slopes in cold and arid regions: A comparative study of sunny and shady slopes. *Cold Regions Science and Technology*, 215, 103981. https://doi.org/10.1016/j.coldregions.2023.103981

Zhang, K., Wang, L., Dai, Z., Huang, B., & Zhang, Z. (2022b). Evolution trend of the Huangyanwo rock mass under the action of reservoir water fluctuation. *Natural Hazards*, 113(3), 1583-1600. https://doi.org/10.1007/s11069-022-05359-y

Zhang, P., Karapiperis, K., & Weeger, O. (2025). t-PiNet: A thermodynamics-informed hierarchical learning for discovering constitutive relations of geomaterials. *Journal of the Mechanics and Physics of Solids*, 197, 106049. https://doi.org/10.1016/j.jmps.2025.106049

Zhang, P., Yin, Z. Y., & Sheil, B. (2023c). Interpretable data-driven constitutive modelling of soils with sparse data. Computers and Geotechnics, 160, 105511. https://doi.org/10.1007/s11069-021-04638-4

Zhang, S., Liu, H., Chen, W., Niu, F., & Niu, Z. (2020). Strength deterioration model of remolded loess contaminated with acid and alkali solution under freeze-thaw cycles. *Bulletin of Engineering Geology and the Environment*, 79(6), 3007–3018. https://doi.org/10.1007/s10064-019-01721-w

Zhang, W., Gu, X., Tang, L., Yin, Y., Liu, D., & Zhang, Y. (2022). Application of machine learning, deep learning and optimization algorithms in geoengineering and geoscience: Comprehensive review and future challenge. *Gondwana Research*, 109, 1-17. https://doi.org/10.1016/j.gr.2022.03.015

Zhang, X., Duan, X., Khalil, U., Muhammadi, M. A., Elmannai, H., Algarni, A. D., & Kucher, D. E. (2026). Multi-Type Landslide Susceptibility Modeling Using Ensemble Machine Learning Approaches: A Case Study from the Karakoram Highway, Northern Pakistan. *Physics and Chemistry of the Earth, Parts A/B/C*, 104305. https://doi.org/10.1139/cgj-2018-0286

Zhao, T., & Wang, Y. (2019). Determination of efficient sampling locations in geotechnical site characterization using information entropy and Bayesian compressive sampling. *Canadian Geotechnical Journal*, 56(11), 1622–1637. https://doi.org/10.1139/cgj-2018-0286

Zhao, T., & Wang, Y. (2020). Interpolation and stratification of multilayer soil property profile from sparse measurements using machine learning methods. *Engineering Geology*, 265, 105430. https://doi.org/10.1016/j.enggeo.2019.105430

Zhao, W., Wei, Y., Liu, B., Liu, S., & Xiao, L. (2019, September). Design and application of automatic monitoring and BIM technology to the construction of shield-bored underneath building. In *International Conference on Inforatmion technology in Geo-Engineering* (pp. 493-501). Cham: Springer International Publishing. https://doi.org/10.1007/978-3-030-32029-4_43

Zhou, W., Zhou, Y., Liang, S., Zhang, C., Dai, H., & Sun, X. (2025). A new framework for landslide susceptibility mapping in contiguous impoverished areas using machine learning and catastrophe theory. *Scientific Reports*, 15(1), 10620. https://doi.org/10.1038/s41598-025-88070-9

Zhou, X., Shi, P., Sheil, B., & Suryasentana, S. (2024). Knowledge-based U-Net and transfer learning for automatic boundary segmentation. *Advanced Engineering Informatics*, 59, 102243. https://doi.org/10.1016/j.aei.2023.102243

Zhou, X., Wen, H., Zhang, Y., Xu, J., & Zhang, W. (2021). Landslide susceptibility mapping using hybrid random forest with GeoDetector and RFE for factor optimization. *Geoscience Frontiers*, 12(5), 101211. https://doi.org/10.1016/j.gsf.2021.101211

Zhou, Z., Ma, W., Zhang, S., Mu, Y., & Li, G. (2018). Effect of freeze-thaw cycles in mechanical behaviors of frozen loess. *Cold Regions Science and Technology*, 146, 9–18. https://doi.org/10.1016/j.coldregions.2017.11.011

Zhu, M., Zhu, H., Guo, F., Chen, X., & Ju, J. W. (2021). Tunnel condition assessment via cloud model-based random forests and self-training approach. *Computer-Aided Civil and Infrastructure Engineering*, 36(2), 164-179.https://doi.org/10.1111/mice.12601

Zimmermann, H.-J. (1996). Fuzzy sets and expert systems. In *Fuzzy set theory—and its applications* (pp. 173–201). Springer Netherlands. https://doi.org/10.1007/978-94-015-8702-0_10